



**University of
Sheffield**

**Thermodynamic and kinetic modelling on the
microstructure and mechanical behaviour of Mg-Zn-
Ca(-Ag) alloys based on CALPHAD approach**

Yanheng Xie

A thesis submitted in partial fulfilment of the requirements for the degree of
Doctor of Philosophy

The University of Sheffield
Faculty of Engineering
Department of Chemical, Materials and Biological Engineering

May, 2025

● Abstract

Advances in lightweight structural materials have intensified interest in magnesium alloys, particularly those strengthened by Zn, Ca, and Ag additions. This research presents a comprehensive study of the thermodynamic and kinetic behaviour of Mg-Zn-Ca and Mg-Zn-Ca-Ag alloys using an integrated CALPHAD-based modelling and experimental approach. The solidification process is analysed using an extended Scheil model, capturing non-equilibrium phase evolution and solute segregation during casting. A mean-field model is developed to simulate the nucleation, growth, and coarsening of strengthening phases during heat treatment, enabling the prediction of precipitate evolution over time. Together, these models provide a framework for simulating phase transformations across the entire processing route from casting to homogenisation and ageing treatment.

The modelling results are supported and validated by advanced characterisation and mechanical experiments. Zn is shown to play a central role in age-hardening by promoting the formation of fine strengthening precipitates. Ca is beneficial in refining grain structure and modifying texture and tends to form Laves phases during solidification. These coarse particles are thermodynamically stable and dissolve slowly during homogenisation, limiting solute uniformity. Ag additions can promote mechanical performance by accelerating the nucleation of fine precipitates, improving strengthening responses. By linking CALPHAD predictions with observed microstructure and mechanical behaviour, this work establishes a predictive design strategy for magnesium alloys.

These findings are directly applicable to the development of lightweight structural materials, aligning with Industry 4.0 schemes that include data-driven materials design and digital manufacturing. By integrating Scheil-based solidification modelling and mean-field simulations within a CALPHAD framework, this research shows how computational tools can aid digital alloy development. These simulation frameworks enable virtual prototyping, optimise thermal processing routes, and reduce experimental workload, which accelerates the transition from concept to application in smart manufacturing environments.

● Acknowledgements

First and foremost, I would like to express my heartfelt gratitude to my primary supervisor, Prof. Hector Basoalto. His support, insightful advice and encouragement to pursue my own ideas have been crucial throughout my PhD journey. I'm especially grateful for the countless hours he spent discussing research, solving problems, and celebrating small victories along the way, and it was a privilege to study under his supervision.

I would also like to sincerely thank my co-supervisors, for their valuable contributions in thoughtful discussions, feedback and constructive suggestions at key stages of this project. I am particularly grateful to Dr. Magnus Anderson for his guidance in computational simulations and programming, to Dr. Dikai Guan for his expertise in magnesium alloys and experimental support, to Dr. Claire Utton for her guidance in phase diagram calculations and methodology, and to Dr. Matthew Murphy for his support in magnesium experiment and industrial insight.

I would also like to sincerely thank many researchers who have supported me throughout my PhD journey in various ways. I am grateful to Prof. Mark Rainforth for guiding me towards a PhD and for his patient mentorship during the challenging early days of the COVID-19 pandemic. I would like to thank Dr. Le Ma, Dr. Ian Ross, Stuart Creasey-Gray, Dr. Lisa Hollands, Neil Hind, Dean Haylock, Dr. Yunus Azakli, Dr. Oday Hussein, Tesoro Monaghan, Sylwester Mikula, Dr. Mingwen Bai, Dr. Joanna Bates, and Elisa Alonso Lopez for their invaluable technical support across different laboratories. I am also thankful to Dr. Xun Zeng, Dr. Liang Yuan, Xingjian Zhao, Haoran Yi, Zhiyu Quan, Dr. Miguel Espadero, Dr. Lucia Scotti, Dr. Sourabh Supanekar, Prashant Jadhav, Hugh Banes, Connor Cladingboel, Zeyu Cao, Bonaventure Ugwuanyi, Mostafa Salem, Conor McVeigh, and Dr. Andrew Hutchinson for their helpful discussions throughout the project. I would also like to acknowledge the financial support provided by the Great Britain-China Educational Trust and the Larry Kaufman CALPHAD Scholarship.

I would like to express my appreciation to my families. To my parents, for their unwavering love, support, and encouragement throughout my academic journey. To my wife Shurou, for standing by me through every high and low, for bringing light into my journey, and for all the experiences and growth with me. Finally, to my grandparents, who passed away during my PhD journey, they would be proud.

- **Declaration**

I, Yanheng Xie, confirm that the Thesis is my own work. I am aware of the University's Guidance on the Use of Unfair Means. This work has not been previously been presented for an award at this, or any other, university.

● **Table of Contents**

| | | |
|-------|--|-----------|
| ● | Abstract | 2 |
| ● | Acknowledgements | 3 |
| ● | Declaration | 5 |
| ● | Table of Contents | 1 |
| ● | List of Figures | 4 |
| ● | List of Tables | 10 |
| | Chapter 1: Introduction | 1 |
| 1.1 | Background and Motivation | 1 |
| 1.2 | Aim, Objectives and Scope | 2 |
| | Chapter 2: Literature Review | 5 |
| 2.1 | General Properties and Application of Magnesium Alloys..... | 5 |
| 2.1.1 | Brief History of Magnesium Alloys..... | 5 |
| 2.1.2 | Physical Properties of Pure Magnesium | 6 |
| 2.1.3 | Application of Magnesium Alloys..... | 8 |
| 2.2 | Deformation Mechanisms of Magnesium Alloys..... | 11 |
| 2.2.1 | Critical Resolved Shear Stress (CRSS) and Schmid Factor..... | 11 |
| 2.2.2 | Slip Systems..... | 12 |
| 2.2.3 | Twinning | 13 |
| 2.2.4 | Grain Boundary Sliding | 14 |
| 2.3 | Alloying Elements in Magnesium Alloys | 15 |
| 2.3.1 | Aluminium (Al)..... | 15 |
| 2.3.2 | Zinc (Zn) | 15 |
| 2.3.3 | Calcium (Ca)..... | 16 |
| 2.3.4 | Rare-Earth Metals (REs)..... | 16 |
| 2.3.5 | Silver (Ag)..... | 17 |
| 2.4 | Strengthening Mechanisms of Magnesium Alloys | 17 |
| 2.4.1 | Solid Solution strengthening..... | 17 |

| | | |
|-------------------|---|-----------|
| 2.4.2 | Precipitation strengthening | 18 |
| 2.4.3 | Grain Refinement | 18 |
| 2.5 | Texture of Magnesium Alloys | 19 |
| 2.5.1 | Basal Texture | 20 |
| 2.5.2 | Rare-Earth Texture | 21 |
| 2.5.3 | Calcium (Ca) Effects on Texture | 21 |
| 2.6 | Heat and Mass Transfer in Materials | 21 |
| 2.6.1 | Heat Transfer | 21 |
| 2.6.2 | Mass Transport | 23 |
| 2.7 | Precipitation Theory | 25 |
| 2.7.1 | Nucleation | 26 |
| 2.7.2 | Growth | 27 |
| 2.7.3 | Age-Hardening Response | 29 |
| 2.8 | General Precipitation Hardening in Magnesium Alloys | 31 |
| 2.8.1 | Mg-Zn Alloys | 31 |
| 2.8.2 | Mg-Ca Alloys | 35 |
| 2.8.3 | Mg-Zn-Ca Alloys | 36 |
| 2.8.4 | Mg-Zn-Ca-Ag Alloys | 37 |
| 2.9 | Calculation of Phase Diagram (CALPHAD) | 39 |
| 2.10 | Mean-field Approaches | 42 |
| 2.11 | Summary | 44 |
| Chapter 3: | Experimental Methodology | 46 |
| 3.1 | Alloy Preparation | 46 |
| 3.1.1 | Alloy Compositions | 46 |
| 3.1.2 | Cast and Wrought Procedures | 46 |
| 3.1.3 | Heat Treatment | 47 |
| 3.1.4 | Grinding and polishing | 48 |
| 3.2 | Phase and Composition Characterisation | 49 |

| | | |
|-------------------|---|-----------|
| 3.2.1 | X-ray Analysis (XRD) | 49 |
| 3.3 | Mechanical Properties | 49 |
| 3.3.1 | Hardness Micro Indentation | 49 |
| 3.3.2 | Tensile Test | 49 |
| 3.4 | Microstructure Characterisation | 50 |
| 3.4.1 | Optical Microscopy (OM)..... | 50 |
| 3.4.2 | Scanning Electron Microscopy (SEM) | 51 |
| 3.4.3 | Energy-dispersive X-ray spectroscopy based on SEM (SEM-EDS) | 51 |
| 3.4.4 | Electron Backscatter Diffraction (EBSD)..... | 52 |
| 3.4.5 | Electron Probe Micro-analyser (EPMA)..... | 52 |
| 3.4.6 | Scanning Transmission Electron Microscopes (STEM) | 52 |
| 3.5 | Error Measurements | 53 |
| Chapter 4: | Modelling Methodology | 54 |
| 4.1 | Calculation of Phase Diagram | 54 |
| 4.1.1 | Extended Scheil-Gulliver Solidification Models | 54 |
| 4.1.2 | Diffusion and Homogenisation (DICTRA) Simulations..... | 59 |
| 4.2 | Mean-field Theory | 64 |
| 4.2.1 | Thermodynamic preparatory calculations..... | 65 |
| 4.2.2 | Mean-field Model..... | 66 |
| 4.2.2.1 | <i>Continuity</i> | 66 |
| 4.2.2.2 | <i>Growth</i> | 67 |
| 4.2.2.3 | <i>Nucleation</i> | 69 |
| 4.3 | Mechanical Properties Model..... | 72 |
| Chapter 5: | Numerical Implementation..... | 74 |
| 5.1 | Finite Difference Method (FDM)..... | 74 |
| 5.2 | Scheil-Gulliver Solidification Model in Ternary Alloy System..... | 78 |
| 5.3 | Diffusion Couple between Mg Matrix and second Phases..... | 79 |
| 5.4 | Mean-field Model..... | 81 |

| | | |
|-------------------|--|------------|
| 5.4.1 | Mean-field Model in Solidification..... | 84 |
| 5.4.2 | Mean-field Model in Precipitation..... | 85 |
| Chapter 6: | Solidification, segregation and second phases formation of Mg-Zn- | |
| Ca alloys | | 89 |
| 6.1 | Introduction | 89 |
| 6.2 | Materials and Methods | 90 |
| 6.2.1 | Methodology..... | 90 |
| 6.2.2 | Preparation of Mg alloys | 91 |
| 6.2.3 | Thermal model set-up | 92 |
| 6.2.4 | Mean field approach | 93 |
| 6.3 | Microstructure of As-cast ZX10 and ZX70 Alloys..... | 95 |
| 6.4 | Scheil solidification..... | 97 |
| 6.5 | Mean-field Results of Second Phase Precipitation..... | 101 |
| 6.6 | Discussion | 107 |
| 6.6.1 | Quantitative Analysis of Particles Size Distribution..... | 107 |
| 6.6.2 | Second Phases Formation in Scheil Solidification Model..... | 109 |
| 6.6.3 | Solidification Segregation and Composition Map..... | 110 |
| 6.6.4 | Precipitation Sequences of Mg-Zn precipitates | 111 |
| 6.7 | Conclusion to this chapter | 112 |
| Chapter 7: | Homogenisation, diffusion and second phases dissolution of Mg-Zn- | |
| Ca alloys | | 114 |
| 7.1 | Introduction | 114 |
| 7.2 | Materials and Method..... | 115 |
| 7.2.1 | Methodology..... | 115 |
| 7.2.2 | Materials preparation | 118 |
| 7.3 | Microstructure of As-Cast and Homogenised ZX10 Alloys..... | 118 |
| 7.4 | DICTRA Simulation of ZX10 Alloys | 122 |
| 7.4.1 | Self-Diffusion in Mg Matrix | 122 |
| 7.4.2 | Diffusion Couple Between Mg Matrix and Second Phases..... | 125 |

| | | |
|---|--|------------|
| 7.5 | Discussion | 128 |
| 7.5.1 | Precipitates in ZX10 Alloy | 128 |
| 7.5.2 | The limitation of Initial Segregation | 130 |
| 7.6 | Conclusion to this chapter | 131 |
| Chapter 8: Precipitation, mechanical properties and microstructure of Mg-Zn-Ca(-Ag) alloys | | 133 |
| 8.1 | Introduction | 133 |
| 8.2 | Materials and Method..... | 135 |
| 8.2.1 | Methodology | 135 |
| 8.2.2 | Materials Preparation..... | 136 |
| 8.2.3 | Mean-field Approach..... | 137 |
| 8.2.4 | Dislocation Orowan Bowing Model..... | 138 |
| 8.3 | Microstructure of Mg-3Zn-0.2Ca(-xAg) Alloys | 139 |
| 8.4 | Mechanical Properties of Ageing Mg-3Zn-0.2Ca(-xAg) Alloys | 150 |
| 8.5 | Mean-field Predictions of Second Phase Precipitation during Ageing | 154 |
| 8.6 | Precipitation-Property Model..... | 158 |
| 8.7 | Discussion | 161 |
| 8.7.1 | Microstructure Evolution of Mg-3Zn-0.2Ca(-xAg) Alloys | 161 |
| 8.7.2 | Precipitation Sequences of β -type Phases | 164 |
| 8.7.3 | Dislocation Pinning for Non-spherical Precipitates..... | 166 |
| 8.8 | Conclusion to this chapter | 167 |
| Chapter 9: Conclusion..... | | 169 |
| Chapter 10: Future Work | | 172 |
| 10.1 | Extending computational models and alloy composition optimisation..... | 172 |
| 10.2 | Develop multi-scale digital twin models for industrial applications..... | 172 |
| 10.3 | Expanding mechanical performance and environmental adaptability..... | 173 |
| 10.4 | Advanced characterisation techniques for microstructural evolution..... | 173 |
| • | References | 174 |

● List of Figures

| | |
|---|----|
| Figure 2.1 Average annual crude oil prices for the last 18 years in U.S. dollars per barrel [9]. | 6 |
| Figure 2.2 Primary magnesium metal consumption each year from 1999 to 2019 [10]. | 6 |
| Figure 2.3 Hexagonal close-packed structure unit cell [59]. | 11 |
| Figure 2.4 CRSS values for basal slip, prismatic slip, pyramidal slip, extension twinning, and contraction twinning and their variation with increased temperature of pure Mg [10]. | 12 |
| Figure 2.5 Basal, prismatic, and pyramidal slip systems in Mg [10]. | 13 |
| Figure 2.6 Extension and contraction twinning systems in Mg [10]. | 14 |
| Figure 2.7 Schematic diagram showing orientation of grains of rolled Mg alloy [100]. | 20 |
| Figure 2.8 Molecular distribution in solid, liquid, and gas state. | 22 |
| Figure 2.9 Thermodynamic solver workflow. | 25 |
| Figure 2.10 Free energy versus radius of nuclei in classical nucleation theory [132]. | 27 |
| Figure 2.11 Schematic representation of Ostwald ripening [135]. | 29 |
| Figure 2.12 Schematic diagram showing the Orowan Bowing mechanism [138]. | 30 |
| Figure 2.13 The shear strength τ variation with dislocation cutting mechanism and bowing mechanism, the cross point is the critical radius of precipitates [139]. | 31 |
| Figure 2.14 Age-hardening response of Mg-8Zn (wt. %) and Mg-5Zn (wt. %) alloys at 423 K and 473 K [99]. | 32 |
| Figure 2.15 Mg-Zn phase diagram [164]. | 33 |
| Figure 2.16 TEM micrographs showing precipitates in samples aged for 2 h (a, b) and 1000 h (c, d) at 200 °C. The electron beam was approximately parallel to 1010α (a, c) and 0001α (b, d) [151]. | 34 |
| Figure 2.17 Precipitation sequences for supersaturated Mg-Zn solid solution during ageing [164]. | 34 |
| Figure 2.18 Mg-Zn phase diagram [171]. | 35 |
| Figure 2.19 Effect of Ca content on the hardness of Mg-Ca alloy under as-cast condition [171]. | 36 |
| Figure 2.20 (a) Ageing curves of Mg-Ca based alloy at 200 °C and (b) Guinier-Preston (GP) in Mg-0.6Zn-0.3Ca (at. %) alloy at 200 °C [99]. | 37 |
| Figure 2.21 Age-hardening response of Mg-2.4Zn (at. %) during isothermal ageing at 160 °C [99]. | 38 |

| | |
|---|-----|
| Figure 2.22 SEM-EDS mapping results of as-extruded Mg-2Zn-0.2Ca-xAg (x=0, 0.1, 0.3 and 0.5 wt. %) alloys: (a) ZX20, (b) ZXQ0.1, (c) ZXQ0.3 and (d) ZXQ0.5 [183]. | 39 |
| Figure 3.1 As-cast ZX10 and ZX70 samples solidification process | 47 |
| Figure 3.2 Equilibrium phase diagram of (a) ZX10, (b) ZX30 and (c) ZX70 alloys | 47 |
| Figure 3.3 ZX10 samples after homogenisation at (a) 500°C, (b) 520°C and (c) 540°C for 48 hours | 48 |
| Figure 3.4 Extruded ZX30 tensile flat sample schematics with 2 mm thick dimension | 50 |
| Figure 4.1 Scheil solidification path (marked in red) for a binary alloy system | 57 |
| Figure 4.2 (a) Mg-Ca binary phase diagram and (b) Scheil solidification curve of Mg-1wt. %Ca, Mg-5wt. %Ca, and Mg-10wt. %Ca by Thermo-Calc | 57 |
| Figure 4.3 Scheil solidification path in ternary alloy system | 59 |
| Figure 4.4 Tracer Diffusion Coefficient of Ca and Zn element in liquid and primary solid phase of Mg-Zn-Ca alloys | 60 |
| Figure 5.1 (a) One-dimensional heat transfer approximation of a three-dimensional cylindrical billet from surface to core solidification process. (b) Space difference in One-dimensional heat transfer model | 75 |
| Figure 5.2 Space and time difference in One-dimensional heat transfer model | 76 |
| Figure 5.3 FDM model of composition and liquidus map | 79 |
| Figure 5.4 Mean-field model solver algorithm | 86 |
| Figure 6.1. Hypothesis of precipitation sequences by (a) Scheil and (b) Mean-field model of Mg-Zn-Ca alloys | 91 |
| Figure 6.2 Schematic diagram of the cut area of the ZX10 and ZX70 samples | 92 |
| Figure 6.3. Sample rapid cooling process | 92 |
| Figure 6.4. Approximate thermal history of ZX10 and ZX70 alloys cooling process in Figure 6.3 | 93 |
| Figure 6.5. SEM-BSE and EDS map results of as-cast (a) ZX10 and (b) ZX70 alloys from surface (1) to core (6) | 96 |
| Figure 6.6. SEM-BSE and EDS line scan analysis of as-cast (a) ZX10 and (b) ZX70 alloys | 97 |
| Figure 6.7. Scheil solidification curve of (a, b) ZX10 and (c, d) ZX70 alloy. Figure (a, c) are generated from the liquidus-minimising Scheil in this study, and figure (b, d) are generated from Thermo-Calc Scheil module | 98 |
| Figure 6.8. Equilibrium phase diagram of Mg-xZn-yCa (wt %) alloys, x=0.8, 1.0, 1.2, and y=0.2, 0.3, 0.4. | 100 |

| | |
|--|-----|
| Figure 6.9. Particles volume fraction with variation of nucleation site fraction and cooling time in ZX10 (a, b) and ZX70 (c, d) alloys; (a) is Mg ₂ Ca phase, (b) is Ca ₂ Mg ₆ Zn ₃ phase in ZX10; (c) is MgZn phase, (d) is Ca ₂ Mg ₆ Zn ₃ phase in ZX70..... | 103 |
| Figure 6.10. Time evolution of second phase volume fractions in ZX10 and ZX70 alloys under different nucleation site fractions: (a) Mg ₂ Ca and (b) Ca ₂ Mg ₆ Zn ₃ in ZX10; (c) MgZn and (d) Ca ₂ Mg ₆ Zn ₃ in ZX70..... | 104 |
| Figure 6.11. Particles mean radius with variation of nucleation site fraction and cooling time in ZX10 (a, b) and ZX70 (c, d) alloys; (a) is Mg ₂ Ca phase, (b) is Ca ₂ Mg ₆ Zn ₃ phase in ZX10; (c) is MgZn phase, (d) is Ca ₂ Mg ₆ Zn ₃ phase in ZX70..... | 106 |
| Figure 6.12. Time evolution of second phase mean radius in ZX10 and ZX70 alloys under different nucleation site fractions: (a) Mg ₂ Ca and (b) Ca ₂ Mg ₆ Zn ₃ in ZX10; (c) MgZn and (d) Ca ₂ Mg ₆ Zn ₃ in ZX70..... | 107 |
| Figure 6.13. Composition map of Mg-Zn-Ca alloys solidification segregation pathway | 111 |
| Figure 6.14. Phase diagram of Mg-Zn system [274] | 112 |
| Figure 7.1. The overall process and geometry for self-diffusion DICTRA model..... | 117 |
| Figure 7.2. The overall process and geometry for Interface diffusion couple DICTRA model..... | 117 |
| Figure 7.3. SEM-BSE and EDS map results of ZX10 alloy at (a) as-cast condition and at (b) 520 °C heat-treated for 4 hours, from surface (1) to core (6)..... | 119 |
| Figure 7.4. SEM-BSE images and EBSD phases index of ZX10 alloy at (a) as-cast condition and at (b) 520 °C heat-treated for 4 hours..... | 120 |
| Figure 7.5. SEM-BSE and EPMA map results of ZX10 alloy at (a-c) as-cast condition and at (d-f) 520 °C heat-treated for 4 hours | 122 |
| Figure 7.6. The self-diffusion DICTRA compositional distribution of (a) Mg, (b) Ca, and (c) Zn at heat-treated at 520°C conditions for 10s, 100s, 1000s, and 10000s in ZX10 alloy. | 124 |
| Figure 7.7. The self-diffusion DICTRA compositional distribution of (a) Mg, (b) Ca, and (c) Zn at as-cast and heat-treated at 520°C, 4 hours conditions in ZX10 alloy. | 125 |
| Figure 7.8. The diffusion couple DICTRA of (a) interface movement and (b,c) compositional distribution of (b) Ca, and (c) Zn at as-cast and heat-treated at 520°C for 100, 1000, and 2000 seconds conditions in ZX10 alloy. | 127 |
| Figure 7.9. The diffusion couple DICTRA of (a) interface movement and (b) compositional distribution of Ca at as-cast and heat-treated at 520°C for 100, 1000, and 100000 seconds conditions in ZX10 alloy. | 128 |

Figure 7.10. ZX20 extruded at 330°C. (a) HAADF STEM image, revealing grains of a few microns and precipitates of about 50 to 200 nm in size. The arrow points at a precipitate that pins a grain boundary, as shown by the bowing of the latter. (b) Corresponding STEM EDS map, exhibiting Zn-, Ca-, and Zn+Ca-rich regions; Mg is omitted for clarity. It reveals the (green) binary Mg–Ca and (yellow) ternary Ca–Mg–Zn precipitates. (c) Binary Mg–Ca precipitate and (d) ternary Ca–Mg–Zn precipitate, both taken at the very edge of the thin sample to avoid matrix overlap, with their corresponding EDS spectrum on the right. [283] 130

Figure 8.1. The overall framework for precipitation modelling 136

Figure 8.2. Mg-Zn-Ca(-Ag) alloy optical micrographs in the as-extruded conditions; (a,d) are ZX30, (b,e) are ZXQ300a, (c,f) are ZXQ300b; (a,b,c) are at the edge of extruded samples, (d,e,f) are at the centre of extruded samples. 140

Figure 8.3. EBSD maps and pole figures for as-extruded (a) ZX30, (b) ZXQ300a, (c) ZXQ300b alloys. The extrusion direction is aligned horizontally on all EBSD maps, but the grains are coloured with respect to the crystal directions aligned parallel with the extrusion direction..... 142

Figure 8.4. EBSD maps and pole figures for extruded and solution treated (a) ZX30, (b) ZXQ300a, (c) ZXQ300b alloys. The extrusion direction is aligned horizontally on all EBSD maps, but the grains are coloured with respect to the crystal directions aligned parallel with the extrusion direction..... 143

Figure 8.5. Grain boundaries (GBs) character distribution map of as-extruded ZX30 specimen, the extrusion direction is aligned horizontally on all EBSD maps. HAGBs plus LAGBs map (a), the corresponding grain boundary misorientation distribution (b), grain orientation spread (GOS) map (c), and grain diameter distribution (d). 144

Figure 8.6. Grain boundaries (GBs) character distribution map of extruded and solution treated ZX30 specimen, the extrusion direction is aligned horizontally on all EBSD maps. HAGBs plus LAGBs map (a), the corresponding grain boundary misorientation distribution (b), grain orientation spread (GOS) map (c), and grain diameter distribution (d). 145

Figure 8.7. Grain boundaries (GBs) character distribution map of as-extruded ZXQ300a specimen, the extrusion direction is aligned horizontally on all EBSD maps. HAGBs plus LAGBs map (a), the corresponding grain boundary misorientation distribution (b), grain orientation spread (GOS) map (c), and grain diameter distribution (d). 146

Figure 8.8. Grain boundaries (GBs) character distribution map of extruded and solution treated ZXQ300a specimen, the extrusion direction is aligned horizontally on all EBSD

| | |
|--|-----|
| maps. HAGBs plus LAGBs map (a), the corresponding grain boundary misorientation distribution (b), grain orientation spread (GOS) map (c), and grain diameter distribution (d)..... | 147 |
| Figure 8.9. Grain boundaries (GBs) character distribution map of as-extruded ZXQ300b specimen, the extrusion direction is aligned horizontally on all EBSD maps. HAGBs plus LAGBs map (a), the corresponding grain boundary misorientation distribution (b), grain orientation spread (GOS) map (c), and grain diameter distribution (d)..... | 148 |
| Figure 8.10. Grain boundaries (GBs) character distribution map of extruded and solution treated ZXQ300b specimen, the extrusion direction is aligned horizontally on all EBSD maps. HAGBs plus LAGBs map (a), the corresponding grain boundary misorientation distribution (b), grain orientation spread (GOS) map (c), and grain diameter distribution (d)..... | 148 |
| Figure 8.11. High-magnification SEM micrographs and results of EDS mapping and compositional analysis of the solution treated (a, c, e) and peak aged (b, d, f) samples. ZX30 alloy (a, b), ZXQ300a (c, d), and ZXQ300b (e, f)..... | 150 |
| Figure 8.12. Engineering stress-strain curves for T4 treated and T6 treated (a) ZX30, (b) ZXQ300a, and (c) ZXQ300b alloys..... | 152 |
| Figure 8.13. Age-hardening response curve of ZX30, ZXQ300a, and ZXQ300b alloys when aged at 160 °C. | 154 |
| Figure 8.14. Liquidus-minimising Scheil solidification curve of ZX30 alloy..... | 156 |
| Figure 8.15. Equilibrium phase diagram of (a) ZX30, (b) ZXQ300a, (c) ZXQ300b alloys | 156 |
| Figure 8.16. Particles volume fraction with variation of nucleation site fraction and ageing time of (a) Ca ₂ Mg ₆ Zn ₃ phase and (b) MgZn phase in ZX30 alloy | 156 |
| Figure 8.17. Mean-field results of (a,c) particles volume fraction and (b,d) particle mean radius in ZX30 alloy aged at 160°C; (a,b) are Ca ₂ Mg ₆ Zn ₃ phase and (c,d) are β1' and β2' phases..... | 158 |
| Figure 8.18. Mean-field results of (a,c) particles volume fraction and (b,d) particle mean radius in ZXQ300a alloy aged at 160°C; (a,b) are Ca ₂ Mg ₆ Zn ₃ phase and (c,d) are β1' and β2' phases. | 158 |
| Figure 8.19. Mean-field results of (a,c) particles volume fraction and (b,d) particle mean radius in ZXQ300b alloy aged at 160°C; (a,b) are Ca ₂ Mg ₆ Zn ₃ phase and (c,d) are β1' and β2' phases. | 158 |

Figure 8.20. The predicted yield stress of (a) ZX30, (b) ZXQ300a, (c) ZXQ300b alloys aged at 160°C compared with the experimental hardness data..... 160

Figure 8.21. Higher magnification dark field images (a, c) with corresponding selected-area electron diffraction (SAED) images of the precipitates of yellow box, lower magnification dark field images and corresponding EDS maps (b, d): ZX20 (a, b) and ZXQ0.3 (c, d) [297]. 164

Figure 8.22. TTT diagram of the formation of Mg_4Zn_7 and $MgZn_2$ phases in Mg-1.7at.%Zn alloy [268]. 166

● List of Tables

| | |
|--|-----|
| Table 2.1 Physical Properties of Pure Magnesium [6]..... | 7 |
| Table 2.2 Mechanical properties of pure magnesium, magnesium alloys and alternative metals [3]..... | 7 |
| Table 2.3 Maximum solubility data for binary magnesium alloys [67]..... | 15 |
| Table 3.1 Composition of magnesium Mg-Zn-Ca alloys..... | 46 |
| Table 3.2 Mg-Zn-Ca(-Ag) alloys extrusion parameters..... | 46 |
| Table 3.3 Homogenisation process of ZX10 alloy | 48 |
| Table 5.1 Model parameters for heat transfer calculation..... | 77 |
| Table 5.2 Pre-processing input key files | 87 |
| Table 5.3 Solver input key files | 87 |
| Table 6.1 Chemical composition of as-received Mg-Zn-Ca alloy | 91 |
| Table 6.2 Model parameters for heat transfer calculation, where Temperature is given by T with units of K | 93 |
| Table 6.3 Interfacial energy of precipitates in Mg-Zn-Ca Mg system rich corner | 94 |
| Table 6.4 Phase transition during Liquidus-minimising Scheil solidification for both ZX10 (Figure 6.7a) and ZX70 (Figure 6.7c) alloys | 100 |
| Table 6.5 Amount of particles simulated from liquidus-minimising Scheil solidification model..... | 101 |
| Table 6.6 Quantitative analysis of the area fraction of second phase particles, in comparison with the volume fraction predicted by the mean-field model and the Scheil model, was conducted for both ZX10 and ZX70 alloys. | 108 |
| Table 6.7 Quantitative analysis of the mean radius of second phase particles, in comparison with the mean radius predicted by the mean-field model, was conducted for both ZX10 and ZX70 alloys..... | 109 |
| Table 7.1 Chemical composition of Zn-free Mg ₂ Ca and Zn-containing Mg ₂ Ca phases | 118 |
| Table 7.2 Chemical composition of as-received ZX10 alloy..... | 118 |
| Table 7.3 Quantitative analysis of the area fraction of second phase particles for as-cast and heat-treated at 520 °C for 4 hours in ZX10 alloys. | 121 |
| Table 7.4 Average composition of as-cast and heat-treated sample in Figure 7.5..... | 122 |
| Table 8.1 Composition of Mg-Zn-Ca(-Ag) alloys | 136 |
| Table 8.2 Mg-Zn-Ca(-Ag) alloys extrusion parameters..... | 136 |
| Table 8.3 Mg-Zn-Ca(-Ag) alloys heat-treatment parameters | 137 |
| Table 8.4 Model parameters..... | 139 |

Table 8.5 Composition of Mg-Zn-Ca(-Ag) alloys 152

Chapter 1: Introduction

1.1 Background and Motivation

Magnesium (Mg) alloys are lightweight materials of particular interest in the automotive, aerospace and biomedical sectors. These alloys have unique advantages in reducing energy consumption in transportation and as biodegradable implants in the medical field applications due to their low density, high specific strength and excellent biocompatibility. Among magnesium alloys, Mg-Zn-Ca alloys are of particular interest due to their excellent mechanical properties, good corrosion resistance and biocompatibility. The addition of trace amounts of silver (Ag) to these alloys is expected to further expand their application fields by improving their mechanical performance and functional properties.

The growing demand for high-performance materials requires a deeper understanding of the complex relationships between alloy composition, processing conditions, microstructural evolution, and the resulting mechanical properties. However, the development of new magnesium alloys often relies heavily on empirical trial-and-error approaches, which are both time and resource intensive. This challenge highlights the need for an integrated framework that combines computational modelling with experimental validation to accelerate the discovery and optimisation of Mg-Zn-Ca(-Ag) alloys.

The CALPHAD (Calculation of Phase Diagrams) approach has emerged as a powerful computational framework for thermodynamic and kinetic modelling to accurately predict phase equilibrium, solidification paths and microstructural evolution. In addition, it can combine these predictions with mechanical behaviour simulations to provide a comprehensive view of material properties. When combined with experimental methods such as Scanning Electron Microscopy (SEM), Energy Dispersive X-ray Spectroscopy (EDS), and mechanical testing, CALPHAD provides a reliable method to the design of magnesium alloys.

The motivation for this research arises from the serious challenges faced in engineering and biomedical applications. In automotive and aerospace industry sectors, reducing material weight without compromising structural integrity is a major goal for improving energy efficiency and reducing carbon emissions. In the biomedical field, the development of degradable implants made of magnesium alloys offers a promising alternative to traditional permanent implants. However, achieving the ideal balance between mechanical properties, corrosion behaviour and biocompatibility of magnesium

alloys, such as Mg-Zn-Ca(-Ag) alloys requires an in-depth understanding of the mechanisms driving microstructure and mechanical behaviour, which is the main focus of this research.

1.2 Aim, Objectives and Scope

The aim of this study is to investigate the thermodynamic and kinetic mechanisms that govern the microstructural evolution and mechanical performance of Mg-Zn-Ca(-Ag) alloys, with a particular focus on three key stages of alloy processing: solidification, diffusion, and precipitation. Each of these stages plays a critical role in determining the final properties of the material. By integrating computational modelling with experimental validation, this research seeks to establish a predictive framework for the optimisation of magnesium alloy compositions and thermal processing routes.

Objectives of this study are as follows:

1. The solidification behaviour of Mg-Zn-Ca alloys will be investigated with a focus on solute redistribution, segregation phenomena, and the formation of intermetallic phases. The CALPHAD method, extended Scheil model, and mean-field model will be employed to predict the solidification path and phase evolution during cooling. The influence of Zn and Ca concentrations on solidification behaviour will be systematically evaluated. In parallel, finite difference methods (FDM) will be used to simulate both elemental and phase segregation. The resulting microstructures of the as-cast alloys will be characterised using SEM-EDS analysis to validate the model predictions and to gain insight into the solidification mechanisms.
2. The diffusion-controlled processes occurring during the homogenisation of Mg-Zn-Ca alloys will be studied to understand the dissolution behaviour of segregation phases and to achieve a more uniform solute distribution. Computational simulations will be conducted using DICTRA, diffusion couple approaches, and mean-field models to examine the redistribution of alloying elements and the dissolution of second phases. Particular attention will be paid to the effects of thermal treatment parameters, including temperature and time, on the kinetics of homogenisation and the evolution of grain boundary structures. Experimental characterisation of both the as-cast and homogenised microstructures will be performed using SEM-EDS, EBSD, and EPMA to validate the diffusion models and assess the degree of microstructural homogenisation.

3. The precipitation behaviour of Mg-Zn-Ca(-Ag) alloys during the ageing process will be investigated to establish the kinetic mechanisms that govern the nucleation, growth, and coarsening of strengthening phases. A CALPHAD-based mean-field precipitation model will be used to simulate the temporal evolution of multiple precipitate species and to predict the precipitation sequence. The interactions between precipitates and dislocations will be analysed to understand their role in precipitation strengthening, with a particular emphasis on dislocation pinning mechanisms. Model predictions will be validated through a combination of ageing treatments, mechanical testing, and microstructural analyses using SEM, TEM, and EBSD techniques, thereby linking precipitation behaviour to mechanical property development.

By addressing the critical stages of solidification, diffusion, and precipitation, this study provides a comprehensive understanding of the interrelationship between alloy composition, thermal processing, microstructural evolution, and mechanical properties in Mg-Zn-Ca(-Ag) systems. The combination of computational modelling and experimental techniques ensures that the outcomes of this work are both predictive and directly applicable to the design of high-performance magnesium alloys.

This study combines thermodynamic and kinetic modelling with experimental studies to explore the solidification behaviour, phase stability, precipitation mechanisms, particle evolution and mechanical properties of several Mg-Zn-Ca(-Ag) alloys. In order to provide a comprehensive study of these materials, the thesis is divided into several key sections in following Chapters:

Chapter 2 provides a detailed literature review of magnesium alloys, their physical properties and their applications in industries such as automotive, aerospace and biomedical. In addition, deformation and strengthening mechanisms, alloying effects and texture evolution are presented to provide a strong background foundation for the study. Moreover, the precipitation theory has discussed and linked to the precipitation hardening mechanism in Mg-Zn-Ca(-Ag) alloy system. Also provided a general overview of CALPHAD (Calculation of Phase Diagrams) and mean-field approaches and their development in computational thermodynamic modelling.

The methodology and numerical implementation of this study are presented in three key chapters. Chapter 3 provides an overview of the experimental methods employed in this study, ranging from alloy preparation and heat treatment to advanced characterisation

techniques such as Scanning Electron Microscopy (SEM) and Energy-dispersive X-ray spectroscopy (EDS). These methods are essential to validate the computational models developed in the subsequent chapters. Chapter 4 focuses on modelling methods, which include CALPHAD-based phase diagram calculations, diffusion simulations and mean-field theory of microstructure evolution. The combination of these techniques forms the backbone of the computational framework in this study. Chapter 5 then provides an overview of the numerical implementation of the modelling approaches described in Chapter 4.

The results of this study are also presented in three key chapters. Chapter 6 investigates the solidification process and the formation of intermetallic phases in Mg-Zn-Ca alloys using experimental observations and mainly using the Scheil model. Chapter 7 explores diffusion mechanisms and second phase dissolution during homogenisation and uses diffusion simulations to illustrate the kinetics of these processes. Chapter 8 explores the role of precipitate evolution, precipitation hardening, and mechanical behaviour in modifying the microstructure and properties of Mg-Zn-Ca(-Ag) alloys, focusing on precipitation and the effect of precipitates on mechanical properties under the mean-field modelling approach.

The thesis concludes in Chapter 9 with a summary of the findings, highlighting the contribution of this work to the field of magnesium alloy research. Chapter 10 outlines future research directions, highlighting the potential for further innovation in alloy design and application.

Chapter 2: Literature Review

2.1 General Properties and Application of Magnesium Alloys

Magnesium alloys are increasingly becoming key materials in modern engineering due to their excellent lightweight and mechanical properties. These alloys offer an excellent balance of strength-to-weight ratio, processability and energy efficiency, making them ideal for a wide range of industries from automotive to biomedical [1–3]. However, there are still limitations to the industrial application of magnesium alloys. Challenges such as corrosion resistance, low ductility and high processing costs have driven extensive research to enhance their properties and expand their application range [4]. Although progress has been made in the development of magnesium alloys, some challenges remain. This section provides an overview of the general properties and application fields of magnesium alloys.

2.1.1 Brief History of Magnesium Alloys

Magnesium's history as an industrial material began in the 19th century, when it was first isolated in metallic form. It makes up 2.7% of the earth's crust and is the eighth most abundant element [5]. Magnesium does not occur naturally as an element, but only as magnesium compounds. The most common compounds are magnesite MgCO_3 (27% magnesium), dolomite $\text{MgCO}_3 \cdot \text{CaCO}_3$ (13% magnesium) and carnallite $\text{KCl} \cdot \text{MgCl}_2 \cdot 6\text{H}_2\text{O}$ (8% magnesium) [6]. Magnesium alloys are the lightest metallic structural materials in practical use today, the density of pure magnesium is 1.74 g/cm^3 , about 2/3 that of aluminium alloys, 1/3 that of zinc alloys, 1/4 that of steel and 2/5 that of titanium alloys and therefore the use of magnesium alloys can significantly reduce weight and improve efficiency in many industries [7]. Magnesium alloys have emerged as a promising material in the global transition towards sustainability and net zero carbon emissions, their unique properties align with strategies to reduce environmental impact, energy consumption and enable circular economy practices [8]. For example, the use of lightweight materials such as magnesium alloys directly reduces vehicle weight, improving fuel efficiency and lowering emissions. The price of crude oil rose sharply in the around 20 years from the beginning of the 21st century, as shown in Figure 2.1, which made manufacturers aware of the need to take measures to use lightweight materials to reduce energy consumption [9]. During this period, commercial production of magnesium metal increased from 277,000 tons per year to about 1,100,000 tons per year, as shown in Figure 2.2 [10]. With advances in processing technology and alloy design, it

is possible to create high-performance alloys for specific applications, and the market for magnesium alloys is also expanding [11].

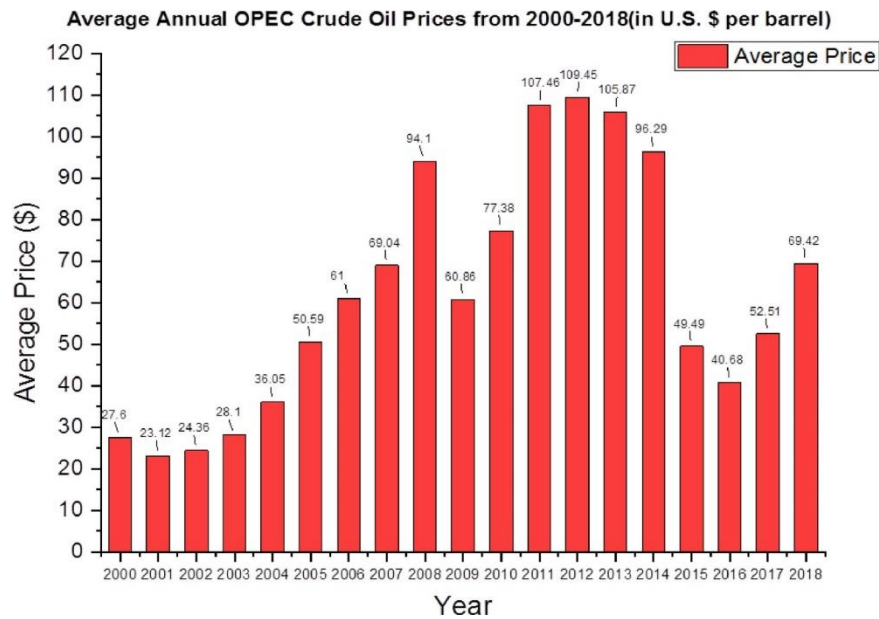


Figure 2.1 Average annual crude oil prices for the last 18 years in U.S. dollars per barrel [9].

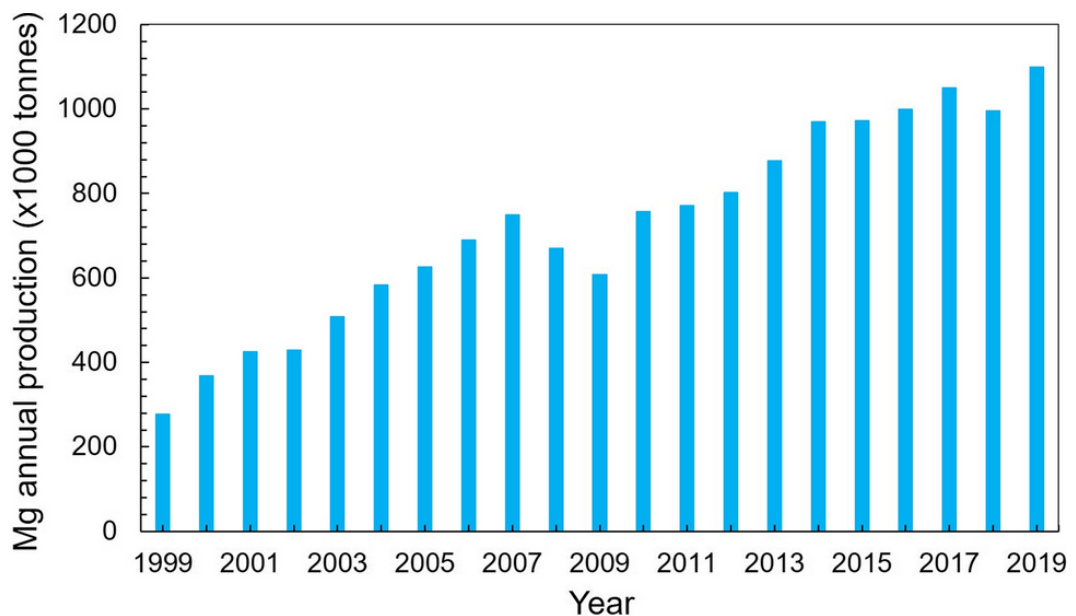


Figure 2.2 Primary magnesium metal consumption each year from 1999 to 2019 [10].

2.1.2 Physical Properties of Pure Magnesium

The crystal structure of pure magnesium is hexagonal close packed (HCP) and its physical properties are shown in Table 2.1 [6]. Mg crystallizes in an HCP structure with crystal lattice parameters giving a c/a ratio of 1.6236 that is almost identical to the ideal close packed ratio of 1.633. This will increase the asymmetric tensile-compressive yield, limiting its ductility and formability at room temperature, the details of which will be

discussed in the following Chapter 2.2. Table 2.2 lists some of the mechanical properties of pure magnesium and compares them with commonly used commercial magnesium alloys and other alternative metals [3]. It can be seen that the strength of AZ31 and AZ91 is slightly improved compared to pure magnesium, but there is still a strength gap compared to other currently available commercial metals. Pure magnesium and magnesium alloys have low density and high specific strength which makes them widely used in weight critical applications. In addition to this, magnesium is the most reactive of all engineering materials, and its lack of corrosion resistance limits its use in many applications [12–14]. Therefore, even though magnesium alloys have a relatively low density, it is necessary to continuously develop new alloy compositions to replace materials such as aluminium alloys or stainless steel in more engineering applications [12,13].

Table 2.1 Physical Properties of Pure Magnesium [6].

| Material Property | Numerical Value |
|---|------------------------------|
| Density (at 20 °C) | 1.738 g/cm ³ |
| Melting Point | (650 ± 1) °C |
| Boiling Point | 1090 °C |
| Thermal Conductivity (at 27 °C) | 156 W / m K |
| Specific heat capacity (at 20 °C) | 1.025 kJ / kg K |
| Latent heat of fusion | 360 to 377 kJ / kg |
| Latent heat of vaporization | 5150 to 5400 kJ / kg |
| Latent heat of sublimation (at 25 °C) | 6113 to 6238 kJ / kg |
| Heat of combustion | 24.9 to 25.2 MJ / kg |
| Linear coefficient of thermal expansion | 29.9 × 10 ⁻⁶ / °C |

Table 2.2 Mechanical properties of pure magnesium, magnesium alloys and alternative metals [3].

| Materials | Density (g/cm ³) | Compressive Strength (MPa) | Tensile Strength (MPa) | Elastic Modulus (GPa) | References |
|------------------------|------------------------------|----------------------------|------------------------|-----------------------|------------|
| Magnesium | | | | | |
| Pure Magnesium | 1.74 | 20-115 | 90-190 | 45 | [15] |
| AZ31 Alloy (Extruded) | 1.78 | 83-97 | 241-260 | 45 | [15] |
| AZ91D Alloy (Die Cast) | 1.81 | 160 | 230 | 45 | [15] |
| Alternative Metals | | | | | |
| Aluminium Alloys | 2.7 | - | 170-560 | 70 | [16] |
| Stainless Steel | 7.9-8.1 | - | 480-620 | 189-205 | [15,17] |
| Cobalt-Chrome Alloys | 7.8-9.2 | - | 450-960 | 195-230 | [15,17] |
| Titanium Alloys | 4.4-4.5 | - | 550-985 | 100-125 | [15,17] |

2.1.3 Application of Magnesium Alloys

2.1.3.1 Automotive/Aerospace Industry

Magnesium alloys are widely used in the automotive and aerospace industries due to their light weight and excellent mechanical properties. Porsche Classic introduced a magnesium crankcase for the classic 911 model, while Honda used magnesium alloys in the oil pan and ignition cover of its CBR1000RR motorcycle to reduce engine weight [18,19]. Meridian Lightweight Technologies, in collaboration with Honda, has developed the AM60B magnesium alloy steering hanger beam for the Acura-TLX model. This high-pressure die-cast design significantly reduces weight and enhances energy absorption during frontal collisions [11]. Brunel University London, in collaboration with Husqvarna AB, has developed a high-temperature magnesium alloy for small engine cylinders that can withstand temperatures of 300–350°C without deformation. This innovation enables the use of precision die-cast magnesium alloy parts for engine blocks, meeting the requirements for high precision and wear resistance [20]. Another milestone was the production of the largest magnesium die-cast part for an electric vehicle, which offers a weight reduction of 32% compared to aluminium. Developed by Chongqing University using Millison's 8800T Giga-Press, these oversized parts demonstrate the potential of magnesium alloys in large automotive applications [21]. Aerospace structural materials must withstand harsh environments such as vibration, vacuum and radiation during launch and missions [22,23]. Magnesium alloys meet these requirements with tailored properties such as strength, modulus and corrosion resistance [24,25]. The range of magnesium alloys used in aerospace technology has expanded significantly. These alloys are now used in spacecraft structures, rocket components and during planetary missions [26–28].

2.1.3.2 Mg-based Biomedical Implants

The earliest biomedical application of magnesium alloys dates back to 1878, when they were used as tourniquets [29]. Today, magnesium alloys are mainly used for cardiovascular stents and bone implants due to their unique combination of mechanical properties and biodegradability. In cardiovascular applications, magnesium stents offer various advantages: they can regulate heart rhythm, improve blood flow, inhibit platelet activation and prevent vasoconstriction [30]. These stents provide temporary structural support to dilate stenotic arteries until vascular remodelling is complete, after which the stents gradually degrade and are replaced by new tissue [31]. As orthopaedic implants, magnesium alloys have superior mechanical properties to traditional materials such as titanium and stainless steel, and are very similar to human bone. They reduce the risk of

stress shielding and gradually degrade into non-toxic products that are excreted by the body without the need for secondary removal surgery [32,33]. In addition, magnesium implants promote bone healing and remodelling [34,35]. Magnesium's biocompatibility, bone-like density (1.74 g/cm^3) and elastic modulus of 41 – 45 *GPa* further enhance its attractiveness as a biomaterial [36,37].

The biodegradability of magnesium alloys makes them an attractive alternative to traditional implant materials such as stainless steel, cobalt-chromium and titanium alloys, which need to be removed after healing, causing additional discomfort for the patient [38,39]. However, the rapid degradation of magnesium alloys in physiological environments poses challenges, such as the loss of mechanical integrity before healing and the build-up of hydrogen, which can separate tissue layers [40,41]. To address these issues, researchers have explored metallurgical and surface modification techniques. Metallurgical methods such as alloying and heat treatment can improve mechanical properties and corrosion resistance, but may release toxic elements [42]. Surface modification, including coating and structural alteration, has shown great potential in enhancing biocompatibility and biodegradability without compromising mechanical property [43,44]. These advances have made magnesium alloys highly promising materials for biomedical applications, especially in the fields of cardiovascular and bone implants.

2.1.3.3 Additive Manufacturing

Additive manufacturing (AM) holds significant potential for advancing medical applications, particularly in the manufacture of biodegradable magnesium implants. However, the reactivity of magnesium poses challenges to AM processes, such as the risk of burning and the difficulty of achieving fully dense structures with optimal mechanical and corrosion properties. The high chemical reactivity of magnesium alloys, combined with their low vaporisation temperatures and reactive alloying elements, complicates their use in AM. Pure magnesium is highly oxidisable and requires careful treatment in an inert environment to prevent burning. The lack of readily available technology and dedicated equipment further limits progress in manufacturing fully functional magnesium parts. Despite these challenges, various AM techniques have been adapted for magnesium alloys, including Laser powder bed fusion (LPBF) [45–47], wire arc additive manufacturing (WAAM) [48,49], paste extrusion deposition and jetting [50–52], and stir friction additive manufacturing [53].

The design flexibility of additive manufacturing is beneficial for creating highly complex geometries, which include porous scaffolds that replicate the structure of natural bone. These scaffolds enhance cell proliferation, tissue adhesion and bone regeneration. For example, magnesium alloy WE43 scaffolds with pore sizes as small as $600\ \mu\text{m}$ have demonstrated low toxicity and structural stability in vitro [54]. By adjusting the printing parameters, the porosity of magnesium implants can be optimised to optimise corrosion rates and cell interactions. AM can also produce patient-specific implants that closely match the individual's anatomical geometry, thereby reducing manufacturing time and costs. Eliminating traditional processing steps simplifies production and improves efficiency in batch processing.

The development of additive manufacturing techniques for reactive materials such as magnesium is focused on solving challenges such as oxidation and burning. The development of an inert gas processing environment and improved material processing techniques is critical for the widespread adoption of magnesium in additive manufacturing. As these barriers are overcome, additive manufacturing is expected to realise the full potential of magnesium alloys in the manufacture of innovative biodegradable medical implants.

Beyond biomedical applications, additive manufacturing of magnesium alloys is gaining attention for lightweight structural components in aerospace, automotive, and defence industries. Magnesium's high strength-to-weight ratio makes it an attractive alternative to aluminium and titanium for reducing overall weight while maintaining mechanical integrity. AM techniques, such as laser powder bed fusion (LPBF) and wire arc additive manufacturing (WAAM), enable the fabrication of complex, topology-optimised structures that maximise load-bearing capacity while minimising material usage. For example, LPBF-processed Mg-Al-Zn (AZ91) alloys have demonstrated improved tensile strength and fatigue resistance through precise microstructural control and post-processing treatments [55]. Additionally, the ability to tailor grain structures and phase distributions through AM processing allows for enhanced mechanical properties, corrosion resistance, and thermal stability, which are crucial for structural reliability. By integrating AM with computational modelling and process optimisation, magnesium alloys can be further refined to meet the demanding requirements of next-generation lightweight structures.

2.1.3.4 *Computer, Communication, and Consumer Electronics (Thermal Conductivity)*
 Magnesium alloys are used in the electronics and consumer goods sectors due to their excellent electromagnetic shielding and heat dissipation properties [56]. These alloys are also increasingly replacing plastics and polymers in electronic casings, as well as steel and aluminium, in applications where low density is a key factor, thereby extending the lifespan of the product [57]. Mg is 100 times more thermally conductive than plastic, and its recyclability, shock absorption and machinability make it ideal for electronic products. Common electronic device applications include audio and video players, mobile phones, cameras, laptops, radar and rechargeable batteries [58]. Mg's combination of low density and high strength has encouraged manufacturers to use it to create lightweight, portable consumer electronic products.

2.2 Deformation Mechanisms of Magnesium Alloys

Magnesium alloys have unique deformation mechanisms due to their hexagonal close-packed (HCP) crystal structure. These mechanisms include slip, twins and grain boundary sliding (GBS), which together accommodate plastic deformation. The slip systems in single crystals require a certain amount of applied shear stress to be activated, which is known as the critical resolved shear stress (CRSS). The close-packed hexagonal structure is shown in Figure 2.3. Each deformation mechanism in magnesium alloys is discussed in this chapter.

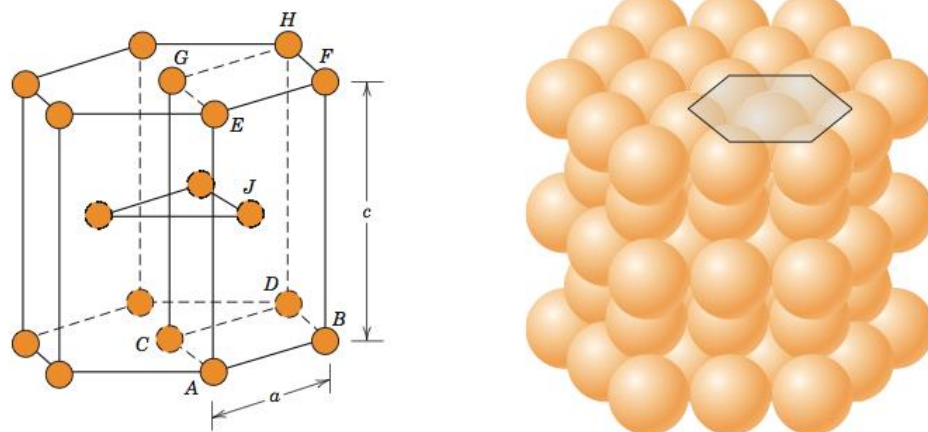


Figure 2.3 Hexagonal close-packed structure unit cell [59].

2.2.1 Critical Resolved Shear Stress (CRSS) and Schmid Factor

Critical resolved shear stress (CRSS) is a key parameter determining the activation energy of slip systems, as shown in Figure 2.4. The lowest CRSS is required for basal $\langle a \rangle$ slip and extension $\{10\bar{1}2\}$ twinning, followed by prismatic $\langle a \rangle$ slip, pyramidal $\langle a + c \rangle$ slip and contraction $\{10\bar{1}1\}$ twinning. CRSS is temperature dependent, and in particular the non-

basal slip CRSS decreases with increasing temperature, indicating the key role of thermal activation in increasing the plasticity of magnesium alloys.

The geometrical relationship between the applied stress, the slip plane and the slip direction determines whether a slip system can be activated. For a given applied stress σ , the analytical shear stress τ along the slip or twin plane in the slip or twin direction is given by Equation (2.1).

$$\sigma = \tau \cos\alpha \cos\beta \quad (2.1)$$

where α is the angle between the applied stress axis and the slip or twin direction, β is the angle between the applied stress axis and the normal to the slip or twin plane. The orientation factor $\cos\alpha \cos\beta$, also known as the Schmid factor, is crucially influenced by the texture. A strong base texture reduces the Schmid factor for base slip in certain loading directions, thus promoting anisotropic behaviour. By optimising the texture during processing, the distribution of the Schmid factor can be enhanced, promoting more uniform deformation.

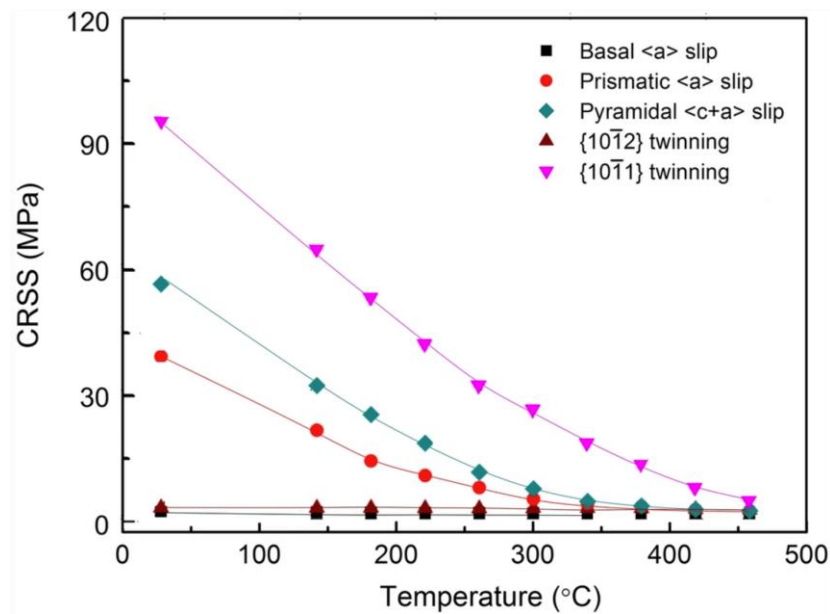


Figure 2.4 CRSS values for basal slip, prismatic slip, pyramidal slip, extension twinning, and contraction twinning and their variation with increased temperature of pure Mg [10].

2.2.2 Slip Systems

Slip is the fundamental mechanism of plastic deformation and occurs through the movement of dislocations along specific crystalline surfaces. In magnesium alloys, the activation of the slip system is controlled by the hcp structure, which has limited symmetry compared to the cubic system. As shown in Figure 2.5 [10], the basal plane

$(0001)[\bar{1}2\bar{1}0]$ is the most favourable slip plane, and main slip direction, following with prismatic planes $(10\bar{1}0)[2\bar{1}\bar{1}0]$, first-order pyramidal planes $(10\bar{1}1)[\bar{1}\bar{1}23]$, and second-order pyramidal planes $(11\bar{2}2)[\bar{1}\bar{1}23]$.

Base plane $(0001)[\bar{1}2\bar{1}0]$ slip is the main slip system in magnesium alloys because of its low CRSS. Basal plane slip dominates the deformation at room temperature and can accommodate strains along the basal plane. However, the dominance of basal slip leads to anisotropic behaviour in the properties of magnesium alloys.

Non-basal slip systems, which include prismatic $(10\bar{1}0)[2\bar{1}\bar{1}0]$ and pyramidal $(10\bar{1}1)[\bar{1}\bar{1}23]$ and $(11\bar{2}2)[\bar{1}\bar{1}23]$ slip systems, are activated at higher temperatures or higher stresses. These systems are essential to accommodate deformation vertical to the basal plane and to increase ductility and isotropy. The CRSS of non-basal slip can be reduced by alloying with elements such as Ca and rare earth metals [60–62]. Higher temperatures can reduce the CRSS of non-basal slip systems, resulting in more isotropic deformation. This temperature dependence is critical for applications requiring increased ductility and toughness.

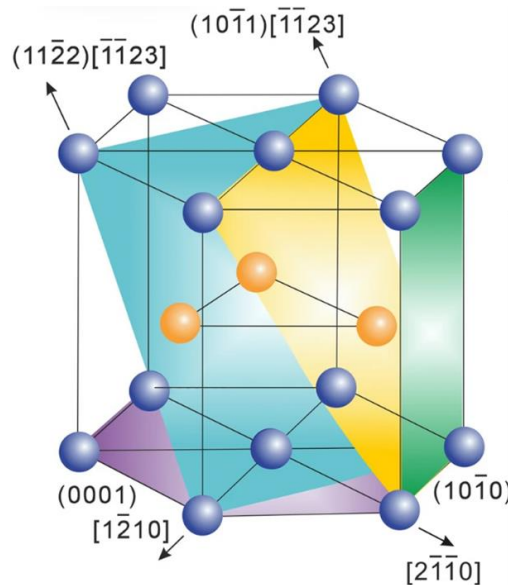


Figure 2.5 Basal, prismatic, and pyramidal slip systems in Mg [10].

2.2.3 Twinning

Twins complement the slip system to accommodate plastic deformation, especially at room temperature where conditions are not sufficient to activate enough slip systems [10]. As shown in Figure 2.6, extension twins $(10\bar{1}2)[\bar{1}011]$ are the most common type of twin, and their formation and growth result in the extension of the crystal

lattice along the c-axis. In contrast, contraction twins $(10\bar{1}1)[\bar{1}012]$ are formed under stress conditions that favour contraction of the crystal lattice along the c-axis. Twinning is strongly dependent on the direction of loading, grain orientation and texture. It is particularly common in coarse-grained materials and at low temperatures, where the limited number of available slip systems requires alternative deformation mechanisms. Although twinning can help with deformation, excessive twinning localises strain and can lead to premature failure, limiting its ability to act as an independent deformation mechanism. Twinning is prone to occur where stress is concentrated, such as at grain boundaries or extending from another twinning, or secondary twinning is generated inside twinning [63]. The appearance of twinning can largely change the orientation of the crystals, thereby changing the texture of magnesium alloys. Twinning has a great influence on the macroscopic mechanical properties of magnesium alloys, especially extension twinning. Because of the combination of the strong basal texture typically developed in wrought magnesium alloys and the inherent directional asymmetry of twinning, tensile-compression asymmetry is observed in the mechanical properties of magnesium alloys [64].

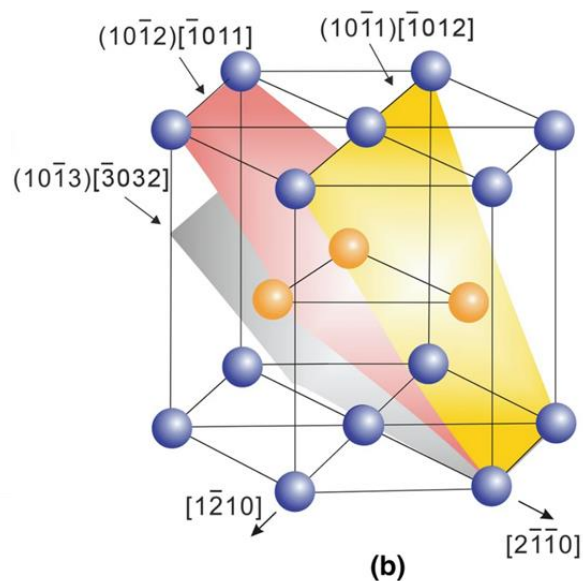


Figure 2.6 Extension and contraction twinning systems in Mg [10].

2.2.4 Grain Boundary Sliding

In addition to dislocation slip and twinning, grain boundary sliding and dynamic recrystallization during deformation can also be observed during plastic deformation, which is important when the grain size in polycrystalline magnesium and its alloys is less than 1 μm . However, in the production process of traditional magnesium alloys, the grain

size of wrought magnesium alloys is usually larger than 5 μm , so grain boundary sliding is usually not investigated. Therefore, how to control the plastic deformation process of magnesium alloys has become a key factor in enhancing the strength of magnesium alloys and improving the anisotropy of mechanical properties [65,66].

2.3 Alloying Elements in Magnesium Alloys

Magnesium alloys are strengthened and modified by alloying with various elements to improve their mechanical, thermal and corrosion resistance properties. The alloying elements discussed in this chapter include aluminium (Al), zinc (Zn), calcium (Ca), rare earth metals (REs) and silver (Ag). Each element has unique benefits, when alloyed with magnesium, to improve the physical and mechanical properties to meet specific industrial applications. The maximum solubility of common alloying elements is shown in Table 2.3 [67].

Table 2.3 Maximum solubility data for binary magnesium alloys [67].

| Element | at. % | wt. % | System |
|-----------------|-------|-------|------------|
| Aluminium (Al) | 11.8 | 12.7 | Eutectic |
| Zinc (Zn) | 2.4 | 6.2 | Eutectic |
| Calcium (Ca) | 0.82 | 1.35 | Eutectic |
| Silver (Ag) | 3.8 | 15.0 | Eutectic |
| Yttrium (Y) | 3.75 | 12.5 | Eutectic |
| Cerium (Ce) | 0.1 | 0.5 | Eutectic |
| Gadolinium (Gd) | 4.53 | 23.49 | Eutectic |
| Neodymium (Nd) | ~1 | ~3 | Eutectic |
| Gallium (Ga) | 3.1 | 8.4 | Eutectic |
| Zirconium (Zr) | 1.0 | 3.8 | Peritectic |

2.3.1 Aluminium (Al)

Aluminium is one of the most widely used alloying elements in Mg alloys because it improves both mechanical strength and corrosion resistance [68–70]. Mg-Al alloys (e.g. AZ series alloys such as AZ91) have better castability and wear resistance, making them ideal for automotive and aerospace components. Aluminium promotes the formation of the $Mg_{17}Al_{12}$ phase, which improves strength at room temperature, but limits performance at high temperatures due to phase coarsening. The amount of aluminium added is usually limited to 10 wt.%, as higher concentrations reduce ductility. However, aluminium is a neurotoxin that causes a variety of neurological diseases such as Alzheimer's disease and dementia, limiting its use in the biomedical field [71].

2.3.2 Zinc (Zn)

Zinc is a key alloying element in magnesium alloys. The maximum solubility of zinc in magnesium is 6.2 wt.%, which decreases to 0.8 wt.% at room temperature, which makes

magnesium-zinc alloys able to be age-hardened, thereby significantly increasing tensile strength [67,72,73]. In the Mg-Zn system, zinc can refine grain size and improve the age-hardening response of the material. The strengthening can be further improved in the Mg-Zn system by adding alloying elements such as Ag and Ca [74,75]. However, the zinc content needs to be carefully optimised as too high a zinc content can decrease the melting temperature and also lead to brittleness.

2.3.3 Calcium (Ca)

Calcium is becoming increasingly popular in magnesium alloys because of its dual role as a grain refiner and corrosion inhibitor, and that it is inexpensive and readily available compared to Rare-Earth elements [76,77]. The maximum solubility of Ca in Mg is only 1.4 wt. % at 517°C, and drops to 0 wt. % at 200°C [67]. Mg-Ca alloys are therefore age-hardening, and Mg-Ca-Zn alloys are particularly interesting for development due to their excellent strength-ductility balance [78–80]. The addition of Ca to magnesium alloys reduces grain size and leads to a weakening of the texture in wrought magnesium alloys [81–83]. In addition, Ca improves the biocompatibility of magnesium alloys, making them suitable for use in biodegradable implants in the biomedical field. However, excessive amounts of Ca can lead to the formation of brittle intermetallic compounds, which reduces ductility.

2.3.4 Rare-Earth Metals (REs)

Rare earth magnesium alloys, which include Mg-Y, Mg-Gd, Mg-Nd and many others, can significantly improve the mechanical properties and thermal stability of magnesium alloys [84–86]. Rare earth elements have a high valence state, strong interatomic bonding and a slow diffusion rate in the magnesium matrix. Adding rare earths to magnesium alloys has many benefits, such as: (1) forming high-melting-point and highly stable precipitates to improve high-temperature properties; (2) forming low-melting-point eutectics to improve fluidity and casting properties; (3) purifying the melt, improving the microstructure and increasing the heat distortion capacity; (4) producing stronger precipitation strengthening and dispersion strengthening effects [87]. Although Mg-RE alloys are more expensive than non-rare earth magnesium alloys, these properties make them ideal for demanding applications in the aerospace and automotive industries [88,89]. For example, WE43 and Mg-Nd-Zn-Zr alloys have been studied and used as orthopaedic implants, and WE43C alloys can also be used as structural parts for aircraft seats, integrated gearboxes, etc. [90].

2.3.5 Silver (Ag)

Silver is not very commonly used, but it has unique advantages in magnesium alloys. It improves strength and corrosion resistance while maintaining good ductility [91,92]. Mg-Ag alloys are particularly valuable in biomedical applications due to their antimicrobial properties and biocompatibility [93–95]. The addition of silver also promotes grain refinement and improves the fatigue resistance of magnesium alloys, but its high cost limits its widespread application [96].

2.4 Strengthening Mechanisms of Magnesium Alloys

Magnesium alloys achieve enhanced mechanical properties through a variety of strengthening mechanisms, each of which contributes uniquely to their overall performance. The main strengthening mechanisms include solid solution strengthening, precipitation strengthening, and grain refinement strengthening. The strengthening contributions from different sources in magnesium alloys can be given in Equation (2.2) [97],

$$\sigma = \sigma_0 + \sigma_g + \sigma_s + \sigma_p \quad (2.2)$$

where σ is total strength, σ_0 is the initial strength, σ_g is the grain size strengthening contribution, σ_s is the solid solution strengthening contribution, and σ_p is the precipitation strengthening contribution.

2.4.1 Solid Solution strengthening

Solid solution strengthening is achieved by adding alloying elements that dissolve into the magnesium matrix. The difference in size between the alloying elements and magnesium atoms causes lattice distortion, which produces local deformation and restricts dislocation movement. When the alloying elements dissolve into the magnesium alloy matrix they cause lattice distortion, which increases the resistance of dislocation movement, making it difficult for a slip to proceed. This increases the strength and hardness of the alloy solid solution, which is the solid solution strengthening effect inside the magnesium alloy [98]. The effect of solid solution strengthening depends on the size difference between alloying element atoms and magnesium atoms and the type of added elements. In general, the greater the difference in the size of the dissolved alloying atoms, the more alloying elements are added, and the greater the effect of solid solution strengthening. In magnesium alloys, the contribution of solid solution strengthening of each alloying element can be expressed by the following Equation (2.3),

$$\sigma_s = \sum_i K_i C_i \quad (2.3)$$

where C_i is the average concentration of a single alloying element, k_i is the alloying element correlation coefficient.

2.4.2 Precipitation strengthening

In addition to solid solution strengthening, the addition of alloying elements can also cause second phase particle strengthening effects, which include precipitation strengthening and dispersion strengthening. As the temperature of the heat-treated sample changes, the second phase in the magnesium alloy with alloying elements will gradually precipitate into the magnesium matrix with the decrease in solubility, and these precipitates will lead to the increase in the strength of the magnesium alloy [99]. The effect of the second phase strengthening depends on the strength, volume fraction, particle shape, distribution state of the second phase precipitate, and the nature of the interface. The strengthening principle is that the precipitates hinder the movement of dislocations in the magnesium matrix, which increases the energy required for deformation, thereby enhancing the strength of magnesium alloys. Therefore, the more precipitates and the smaller the particle spacing, the more obvious the improvement of the strength of the magnesium alloy. The more dispersed the particles of the precipitate are, the more uniform the strength enhancement will be in each part of the magnesium alloy. In general, the strengthening effect of the second-phase particles is more significant than that of solid solution strengthening. Therefore, by adding alloying elements to design the composition of magnesium alloys, the combination of solid solution strengthening and second-phase particle strengthening has become the key to improving the strength and plasticity of magnesium alloys. The details of precipitation strengthening will be discussed in Chapter 2.7.

2.4.3 Grain Refinement

Grain refinement strengthening can not only improve the strength of magnesium alloys, but more importantly, can improve the shortcomings of easy fracture at room temperature. In general, forged magnesium alloys show higher fracture toughness than cast-processed magnesium alloys, because the forged magnesium alloys obtain a finer and more uniform grain structure during the deformation process. The room temperature formability of magnesium alloys increases significantly as the average grain size becomes smaller. Therefore, controlling the microstructure of magnesium alloys is an effective method to improve their strength and fracture toughness [98]. From the strengthening mechanism,

grain refinement increases grain boundaries in magnesium alloy. Due to the different orientations of grains, the resistance required for dislocation movement on both sides of the grain boundary increases, and the slip movement cannot directly enter grains on the other side of the grain boundary. Deformation on the grain boundary requires the simultaneous action of multiple deformation systems, so dislocations cannot easily pass through the grain boundary and thus accumulate at the grain boundary. Because magnesium is a metal with HCP structure, deformation twins, especially extension twins, are easily generated when non-basal plane slip is difficult to generate. Deformation twinning plays a very important role in the study of the microstructure of magnesium alloys, and its influence on the material properties may be more significant than that of slip. Since twinning greatly changes the orientation within the crystal, intragranular boundaries are introduced, which increase the movement of dislocations sliding within the grain and within the twin. Therefore, it is generally believed that deformation twinning is an important factor affecting the strength, ductility, formability, and failure of magnesium [20]. The relationship between the grain size and the yield strength σ_s of magnesium alloys follows the Hall-Petch method in Equation (2.4),

$$\sigma_g = \sigma_0 + kd^{-1/2} \quad (2.4)$$

where σ_0 is the yield strength of a single crystal, d is the average diameter of each grain in the polycrystal, and k is the Hall-Petch constant. The way to achieve fine-grain strengthening is to plastically deform magnesium alloy materials. Because of the limited formability of magnesium alloys at room temperature, the common way to manufacture deformed magnesium alloys is thermomechanical processing, so the processing cost is relatively high. Wrought magnesium alloys are generally divided into rolled magnesium alloys and extruded magnesium alloys. For rolled magnesium alloy sheets, different mechanical properties and formability tend to be exhibited in different directions. For extruded magnesium alloys, the asymmetry of tensile-compression yield strength is usually a problem to be considered.

2.5 Texture of Magnesium Alloys

The texture of magnesium alloys is characterised by the orientation of grains, which is a key factor affecting their mechanical properties, which include ductility, strength and anisotropy. As magnesium has a hexagonal close-packed (HCP) structure, textures such as basal texture and rare earth (RE) texture can significantly affect deformation mechanisms [100]. Recently, calcium (Ca) has been shown to have potential for

improving the texture of magnesium alloys as a cost-effective alternative to rare earth elements [101].

2.5.1 Basal Texture

The basal texture of magnesium alloys is formed during thermomechanical processing, such as extrusion or rolling. For rolled sheets with a strong basal texture, the c axes of individual grains are almost parallel to each other and also parallel to the direction normal to the sheet surface (ND), as shown in Figure 2.7. In addition, $\langle 10\bar{1}0 \rangle$ under deformation conditions, the majority of grains align in the direction of rolling (RD). This texture is abbreviated as $(0002)\langle 10\bar{1}0 \rangle$ and is called the deformed basal texture. But in a sheet with complete recrystallisation, the orientation of the majority of the grains of $\langle 11\bar{2}0 \rangle$ is along the rolling direction, and this texture, $(0002)\langle 11\bar{2}0 \rangle$, is called the recrystallised basal texture [10].

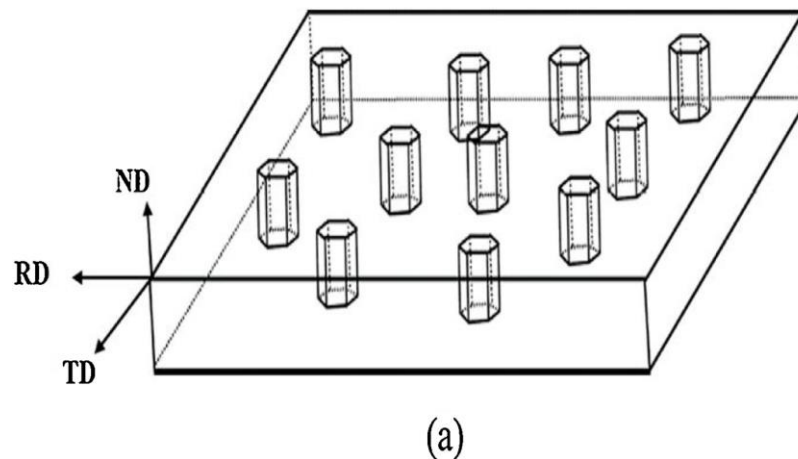


Figure 2.7 Schematic diagram showing orientation of grains of rolled Mg alloy [100].

Strong basal texture results in significant anisotropy in mechanical behaviour. The slip systems activated during deformation are primarily basal $\langle a \rangle$ slip, which are easily activated along the basal plane rather than along the c or $c + a$ axes [102]. This limitation results in poor ductility and formability of magnesium alloys at room temperature. In addition, strong basal texture also leads to asymmetric tensile-compressive yield and limits the practicality of magnesium alloys in structural applications. This is due to the significant difference in critical resolved shear stress (CRSS) between the basal and non-basal slip systems, which results in basal slip dominating the plastic deformation process [103]. Measures to weaken basal texture include the use of advanced processing techniques such as cross rolling and dynamic recrystallisation (DRX) during annealing. Alloying elements, in particular rare earth metals and calcium, also play a key role in weakening basal texture by modifying the recrystallisation behaviour.

2.5.2 Rare-Earth Texture

Rare earth elements such as yttrium (Y), neodymium (Nd) and cerium (Ce) have been shown to effectively modify the texture of magnesium alloys [100]. The texture modified by rare earth elements is characterised by a reduction in basal plane orientation and a more random orientation of the grains. Rare earth elements affect texture through mechanisms such as particle stimulated nucleation (PSN) [104,105], shear band nucleation [106,107], dynamic strain ageing [108], deformation twinning nucleation (DTN) [109], preferred growth of oriented nuclei [110], modification of c/a ratio and stacking fault energy [111,112], and solute drag [113–115]. RE textures minimise anisotropy and improve ductility by enabling the activation of non-basal slip systems, such as prismatic $\langle a \rangle$ and pyramidal $\langle c + a \rangle$ slip. Despite their effectiveness, the limitations of rare earth elements, such as their high price and rarity, restrict their commercial use [116]. This has prompted the search for alternative elements, such as calcium, to provide similar texture improvement effects.

2.5.3 Calcium (Ca) Effects on Texture

Calcium (Ca) has attracted attention as a low-cost alternative to rare earth elements because it can weaken the basal texture in magnesium alloys [101]. It exhibits similar mechanisms to rare earth elements, promoting texture randomisation and improving ductility, both Ca and RE additions can introduce new non-basal texture components that contribute to more isotropic mechanical behaviour [117]. The predominant cause of Ca-induced texture modification is its fundamental effect on deformation system activity and recrystallisation behaviour, enhancing non-basal slip activity and redirecting recrystallisation pathways towards RE-like non-basal orientations [118]. The grain refinement caused by the addition of Ca further suppresses the strong basal plane alignment typical of Mg alloys, thereby improving ductility and isotropy, making them suitable for commercial applications where rare earth alloys are not economically viable [119]. By reducing the cost of texture improvement, the addition of Ca can expand the applicability of Mg alloys in the industrial applications [120].

2.6 Heat and Mass Transfer in Materials

2.6.1 Heat Transfer

Heat transfer refers to the exchange of thermal energy between objects and is governed by the second law of thermodynamics, which states that heat naturally flows from a hotter object to a colder one. Thermal equilibrium is achieved when all participating objects and their surroundings reach the same temperature [121]. At the molecular level, heat transfer

can be understood as the transmission of vibrational energy from one molecule to another. As illustrated in Figure 2.8, this mechanism varies with the physical state of matter. In solids, particularly metals, atoms are closely packed according to the crystal structure, enabling efficient vibrational energy transfer. In liquids, increased thermal energy leads to stronger molecular vibrations and greater intermolecular distances, reducing heat transfer efficiency. In gases, molecular separation increases further, and heat is transferred primarily through collisions. These variations in medium and molecular arrangement give rise to three primary modes of heat transfer: conduction, convection, and thermal radiation.

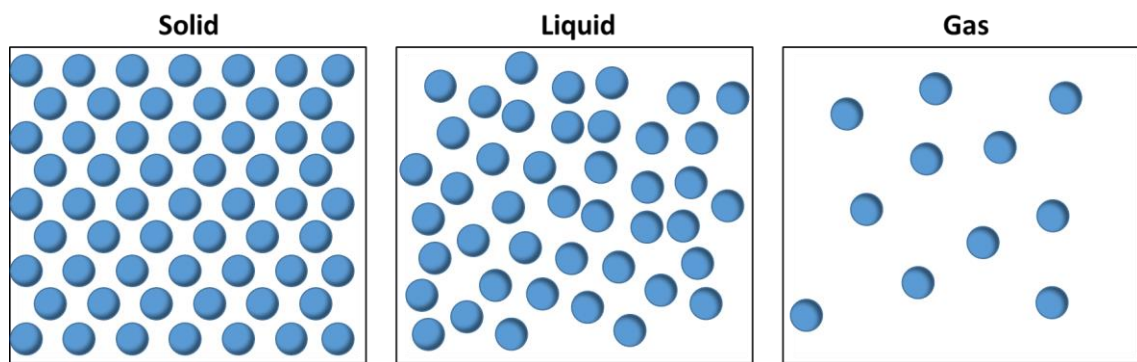


Figure 2.8 Molecular distribution in solid, liquid, and gas state.

Thermal conduction transfers heat through direct molecular collisions and energy is transferred from high to low. The process of heat transfer depends on the following factors: temperature gradient, cross sectional area of the material, transfer distance and physical material properties, which shown in Eq.(2.5).

$$Q = \frac{kA\Delta T}{d} \quad (2.5)$$

where Q is heat transferred per unit time, k is thermal conductivity, A is cross sectional area, ΔT is temperature gradient, d is transfer distance.

Convection is the process by which a liquid or gas transfers heat from one place to another by fluid motion, and the heat loss from an object is proportional to the difference in heat between that object and the surrounding medium. If convection occurs normally, it is called natural convection. Fluid disturbance by means of fans, agitation, etc., is called forced convection. The energy transfer due to heat convection is given by

$$Q = hA(T_s - T_a) \quad (2.6)$$

where Q is heat transferred per unit time, h is convection coefficient, A is cross sectional area, T_s is surface temperature, T_a is ambient temperature. Typically, forced convection provides a stronger heat exchange than natural convection and therefore has a higher convection coefficient.

Thermal radiation is produced by the emission of electromagnetic waves that travel through a vacuum or any transparent medium, such as air or water. All substances radiate heat energy according to their temperature and follow the relation.

$$Q = \epsilon\sigma A\Delta T^4 \quad (2.7)$$

where Q is heat transferred per unit time, ϵ is emissivity, σ is Stefan-Boltzmann constant, A is cross sectional area, ΔT is temperature gradient.

In this study, the heat transfer is mainly focused on the solidification of the metal billet and its heat treatment process. During the solidification and heat treatment of the samples, the heat conduction inside the samples and the convection between the sample surface and the environment are mainly considered. Considering the efficiency of heat transfer, the effect caused by thermal radiation is negligible.

2.6.2 Mass Transport

Mass transfer is the transport of mass due to a gradient in the concentration of a substance in a mixture, and diffusion is the macroscopic result of the random movement of molecules on a microscopic scale. For solid-state diffusion with no plastic deformation and a stationary component, the concentration of solute at location (x, y, z) and time t within the volume $\Delta x\Delta y\Delta z$ be given by $c(x, y, z, t)$

$$\frac{\partial c}{\partial t} + \frac{\partial(J_x)}{\partial x} + \frac{\partial(J_y)}{\partial y} + \frac{\partial(J_z)}{\partial z} = \dot{Q}^+ - \dot{Q}^- \quad (2.8)$$

where c is concentration of solute, J is flux of solute, \dot{Q}^+ and \dot{Q}^- are the rate at which solute enters or leaves the system. By following Fick's first rule, the flux of solute J is given by the following Eq.(2.9), which is corresponding to Eq.(4.7).

$$J_i = -D_i \text{grad}(c_i) = -D_i \nabla c_i \quad (2.9)$$

where D_i is diffusivity of i th element, ∇c_i is the concentration of i th element. We can now enter the flux into the equation of mass transport. Let us assume there is no source or sink of the alloying element A in Eq.(2.8), we can have following Eq.(2.10).

$$\frac{\partial c_A}{\partial t} + \frac{\partial(J_{A,x})}{\partial x} + \frac{\partial(J_{A,y})}{\partial y} + \frac{\partial(J_{A,z})}{\partial z} = 0 \quad (2.10)$$

By combining Eq.(2.9) and Eq.(2.10), we can have,

$$\frac{\partial c_A}{\partial t} - \frac{\partial}{\partial x} \left(D_A \frac{\partial c_A}{\partial x} \right) - \frac{\partial}{\partial y} \left(D_A \frac{\partial c_A}{\partial y} \right) - \frac{\partial}{\partial z} \left(D_A \frac{\partial c_A}{\partial z} \right) = 0 \quad (2.11)$$

And apply the chain rule,

$$\frac{\partial c_A}{\partial t} - \frac{\partial D_A}{\partial x} \frac{\partial c_A}{\partial x} - D_A \frac{\partial^2 c_A}{\partial x^2} - \frac{\partial D_A}{\partial y} \frac{\partial c_A}{\partial y} - D_A \frac{\partial^2 c_A}{\partial y^2} - \frac{\partial D_A}{\partial z} \frac{\partial c_A}{\partial z} - D_A \frac{\partial^2 c_A}{\partial z^2} = 0 \quad (2.12)$$

If the diffusivity does not change as a function of position, the Fick's second law can be calculated in the following Eq.(2.13), which is corresponding to Eq.(4.8).

$$\frac{\partial c_A}{\partial t} - D_A \left(\frac{\partial^2 c_A}{\partial x^2} + \frac{\partial^2 c_A}{\partial y^2} + \frac{\partial^2 c_A}{\partial z^2} \right) = 0 \quad (2.13)$$

The chemical potential μ describes the rate of change in the free energy as a response to a change in the composition.

$$\mu_A = \left(\frac{\partial G}{\partial n_A} \right)_{T,P,n_B} \quad (2.14)$$

where G is the Gibbs free energy, n_A is the number of moles of A, n_B is the number of moles of B. This is an important parameter, which we will use in the kinetics of diffusion. For a small change in composition, the Gibbs free energy can be expressed as a function of the chemical potential. For a multi-component alloy with n many alloying elements, the Gibbs free energy is given by

$$G = \sum_{i=1}^n X_i \mu_i \quad (2.15)$$

where X_i is the atomic fraction of element i . The chemical potential can be used to describe the energy of state. Differences in the energy between possible states can be used to calculate chemical driving forces for phase transformations. At equilibrium, the chemical potentials of all species in all stable phases are equal.

In multi-component alloy system, the Gibbs free energy for the α phase for a multi component alloy with n many alloying elements may be approximated by the following Eq.(2.16),

$$G^\alpha = \sum_{i=1}^n X_i^\alpha G_{0,i}^\alpha(T, P, B) + \sum_{i=1}^n X_i^\alpha R_g T \ln X_i^\alpha + \sum_{i=1}^{n-1} X_i^\alpha \sum_{j=2}^n X_j^\alpha \sum_{l=0}^n L_{l,i,j}^\alpha(T) (X_i^\alpha - X_j^\alpha)^l \quad (2.16)$$

Thermodynamic databases such as TCMG6 and MOBMG1 were used in this study. These databases have calibrated the parameters for $L_{l,i,j}^\alpha(T)$ for the phases present in the alloy systems. Thermodynamic solvers show in Figure 2.9 perform equilibrium calculations to determine the equilibrium phases present for a given composition, number of moles, pressure, and temperature.

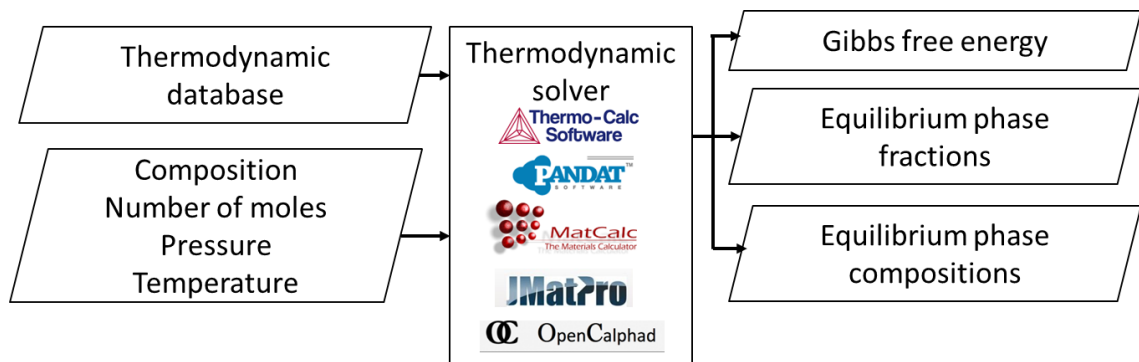


Figure 2.9 Thermodynamic solver workflow.

2.7 Precipitation Theory

Precipitation processes play an essential role in the development of high-strength materials, particularly in alloys, where the control of microstructural evolution can enhance mechanical properties. Precipitation theory involves three key stages: nucleation, particle growth and age hardening. These stages explain how the precipitates in an alloy interact with each other and influence the final properties of the material. Understanding these processes is important for designing alloys of a range of compositions and for different applications. Over the years, theoretical models have been developed to describe these stages, provide insight into the mechanisms involved and guide alloy development. Classical nucleation theory, particle growth mechanisms and age-hardening reactions provide a powerful framework for understanding how microstructural evolution affects material properties. Classical nucleation theories [122–125], particle growth mechanisms [126–129] and age-hardening mechanisms [130,131]. provide a strong

framework for understanding how microstructural evolution affects material properties. As research continues to develop these models, particularly through the integration of advanced CALPHAD thermodynamic and kinetic simulations, the accuracy of predicting and controlling the precipitation process will continue to improve, driving the development of the next generation of materials, particularly in magnesium alloys where strength, weight reduction and corrosion resistance are critical.

2.7.1 Nucleation

Classical nucleation theory (CNT) provides a fundamental framework for understanding the initiation of phase transitions, such as the formation of precipitates from supersaturated matrix. The concept of CNT is based on the first quantitative treatment of nucleation by Volmer and Weber [123], proposed by Becker and Döring [122], and improved by Gibbs [124] and Farka [125]. In CNT, the nucleation of new phases is regarded as a statistical process in which solute atoms clusters to form small particles or nuclei. The process is driven by a balance between the bulk free energy gain from precipitate formation and the interfacial energy associated with solid-solid interface formation as showing in Figure 2.10, where red curve ΔG_V and green curve ΔG_S are representing volume energy and surface energy, respectively. The blue curve is the Gibbs free energy ΔG of this system in Eq. (2.17). Stable nuclei are formed when the free energy of the system decreases, as determined by the critical nucleus size R_c in Eq. (2.18), nuclei larger than the critical size R_c will grow indefinitely and smaller nuclei will dissolve.

$$\Delta G = \Delta G_S - \Delta G_V = 4\pi R^2\gamma - \frac{4\pi}{3}R^3\Delta G_c \quad (2.17)$$

$$R_c = \frac{2\gamma}{\Delta G_c} \quad (2.18)$$

where ΔG_c is the chemical driving force, γ is interfacial energy. The nucleation rate is governed by the supersaturation level of the solute and the temperature of the system. As the supersaturation increases, the driving force for nucleation is enhanced, and the nucleation rate I increases in Eq. (2.19),

$$I = Z\beta^*(t)N_c(R, t) \exp\left(\frac{-\Delta G^*}{k_b T}\right) P_{inc} \quad (2.19)$$

where I is the nucleation rate, Z is the Zeldovich parameter, $\beta^*(t)$ is atomic attachment rate, $N_c(R, t)$ is nuclei radius distribution function, ΔG^* is energy barrier to nuclei

formation, k_b is Boltzmann constant, and P_{inc} is nuclei incubation probability. Nucleation is more likely to occur at high supersaturation, but CNT assumes a homogeneous nucleation environment, which simplifies the problem but may not fully capture the complexity of the material in the real world, where heterogeneities such as grain boundaries and dislocations typically lower the nucleation barriers and thus promote heterogeneous nucleation.

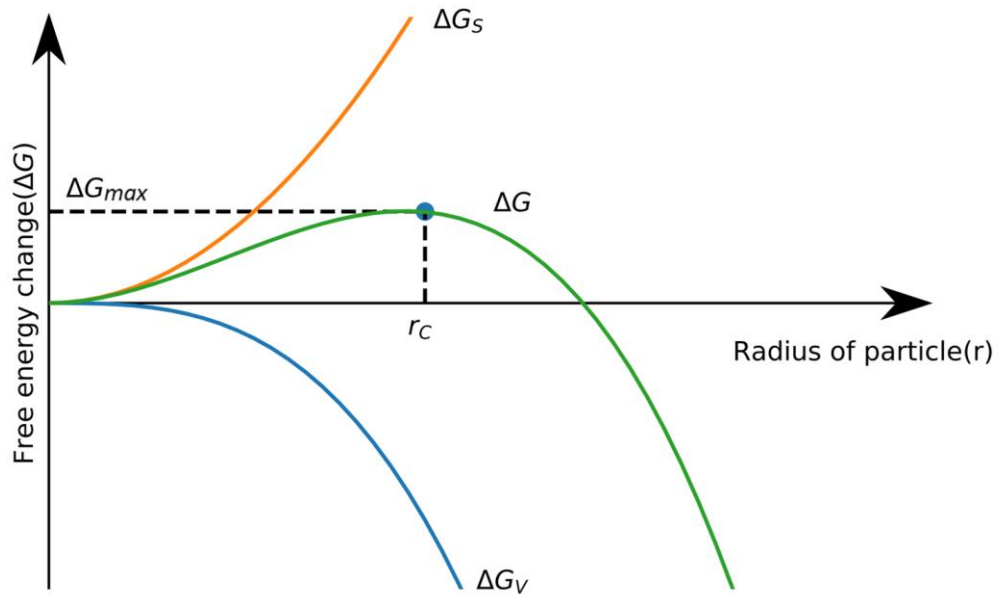


Figure 2.10 Free energy versus radius of nuclei in classical nucleation theory [132].

2.7.2 Growth

Once nucleation has occurred, the precipitate begins to grow, and the growth process usually proceeds by diffusion-controlled growth, in which solute atoms diffuse from the matrix into the growing precipitate. The rate of particle growth is determined by the concentration gradient between the precipitate and the matrix, which is governed by Fick's law of diffusion [129]. In the early stages of growth, the growth rate is proportional to the difference between the solute concentration in the matrix and the equilibrium concentration in the precipitate, which showing in Eq. (2.20),

$$J = 4\pi r^2 D \frac{dC}{dr} \quad (2.20)$$

where J is the total flux through a sphere particle of radius r , D is diffusion coefficient, and $\frac{dC}{dr}$ is the concentration gradient between the precipitate and the matrix.

In the later stages of growth, Ostwald ripening becomes significant. At this stage, due to differences in chemical potentials, larger particles grow at the cost of consuming smaller particles, the smaller particles dissolve and their solute atoms diffuse into the larger particles [126,133], shown in Figure 2.11. This thermodynamically driven self-generated process occurs because the energy on the surface of the particles is less stable than the energy inside, and therefore the larger particles are energetically favoured over the smaller particles [127]. This process leads to an overall coarsening of the sediment distribution and an increase in the average particle size with time. Lifshitz and Slyozov [128] provided a mathematical description of Ostwald ripening which is known as the Lifshitz-Slyozov-Wagner (LSW) theory. The LSW theory defines the boundary between the shrinkage of small particles and the growth of large particles, described by Eq. (2.21)

$$\langle R \rangle^3 - \langle R \rangle_0^3 = \frac{8\gamma S V_m D t}{9R_g T} \quad (2.21)$$

where $\langle R \rangle$ is average radius and $\langle R \rangle_0$ is average initial radius of all the particles, γ is interfacial energy of the particle, S is solubility of the particle, V_m is molar volume of the particle, D is diffusion coefficient of the particle, R_g is gas constant, T is temperature in Kelvin (K), and t is time. The coarsening process continues until the precipitate size reaches a steady-state value or the system is subject to changes in temperature or composition. In addition to diffusion-controlled growth, interface-controlled growth can also occur under conditions where the rate of atom attachment at the precipitate-matrix interface is slower than diffusion. In this case, the precipitate growth is limited by the kinetics of atoms diffusing to the interface and attaching to the particle surface, rather than by the concentration gradient in the bulk matrix [134].

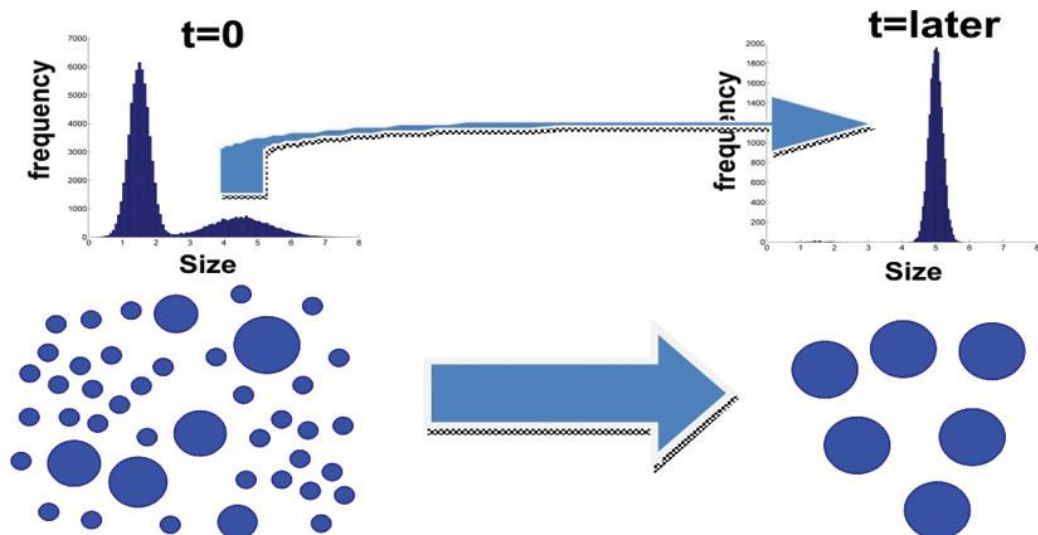


Figure 2.11 Schematic representation of Ostwald ripening [135].

2.7.3 Age-Hardening Response

The age-hardening process is a direct result of the precipitation of solute atoms, which strengthen the material by suppressing dislocation motion, which is also called precipitation hardening or particle hardening. Age hardening is usually divided into three stages: solid solution treatment, quenching and ageing. During solid solution treatment, the alloy is heated to a temperature below the solidus line but above the solvus to allow the solute atoms to dissolve into the matrix, forming a supersaturated solution. Then, the alloy is fast cooled (quenched) to suppress immediate precipitation, with the solute atoms remaining in solution. During ageing, controlled temperature leads to nucleation and growth of precipitates in the supersaturated solution, which hinders dislocation motion and increases the strength of the material. This is because the precipitates create barriers to dislocation motion and the interaction between dislocations and precipitates is one of the main strengthening mechanisms [130]. The coherent strengthening mechanism occurs when small, coherent precipitates induce an elastic strain field that resists dislocation motion [136]. As the size of the precipitates grows and coherence is lost, the Orowan bowing mechanism is dominant, in which dislocations bend around the precipitates due to their inability to pass through the precipitates, as shown in Figure 2.12, which improves the strength by increasing the energy required for the dislocations to bypass the precipitates [131].

In Mg alloys, ageing results in the formation of fine precipitates that hinder dislocation motion, leading to improved strength and hardness. However, the ageing response in Mg alloys is highly dependent on factors such as temperature and time, which must be carefully controlled to achieve the desired balance between precipitate size, distribution, and mechanical properties. In general, fine and dispersed precipitates can improve the strength of the magnesium alloy. The more dispersed the particles of the precipitate are, the more uniform the strength enhancement will be in each part of the magnesium alloy. But it should be noted that the ideal size of the precipitate is not as small as possible. The hindering effect of precipitates on dislocations can be divided into two types: dislocation cutting mechanism and dislocation bowing mechanism (Orowan mechanism). Hutchinson et al. [137] mentioned that in AZ91 (Mg-9Al-1Zn, wt.%), the precipitates with particle radii larger than 3 nm would be bowed by the Orowan mechanism rather than sheared. The effects of these two precipitations strengthening mechanisms on

strength as the particle radius changes are shown in Figure 2.13 [138], with the maximum strengthening effect occurring at the critical radius, and it would also depend on the particle separation, as that affects how easy or not the Orowan mechanism is. The critical radius is usually 5nm-30nm for precipitates [139]. As ageing progresses, precipitate coarsening can occur, which eventually results in a decrease in strength. The peak hardness is typically achieved when the precipitate size is small and uniformly distributed, optimizing the resistance to dislocation movement. However, if the alloy is overaged, precipitates become larger and more widely spaced, reducing the strength. In addition to strengthening, the ageing process in magnesium alloys also affects their ductility, as finer precipitates tend to maintain higher ductility compared to coarser precipitates [140]. This balance between strength and ductility is a critical factor in the design of magnesium-based alloys for structural applications, as it determines their suitability for high-performance uses.

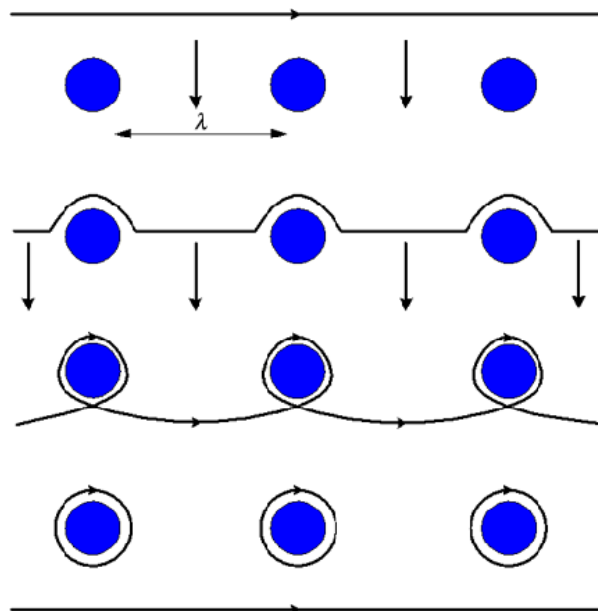


Figure 2.12 Schematic diagram showing the Orowan Bowing mechanism [138].

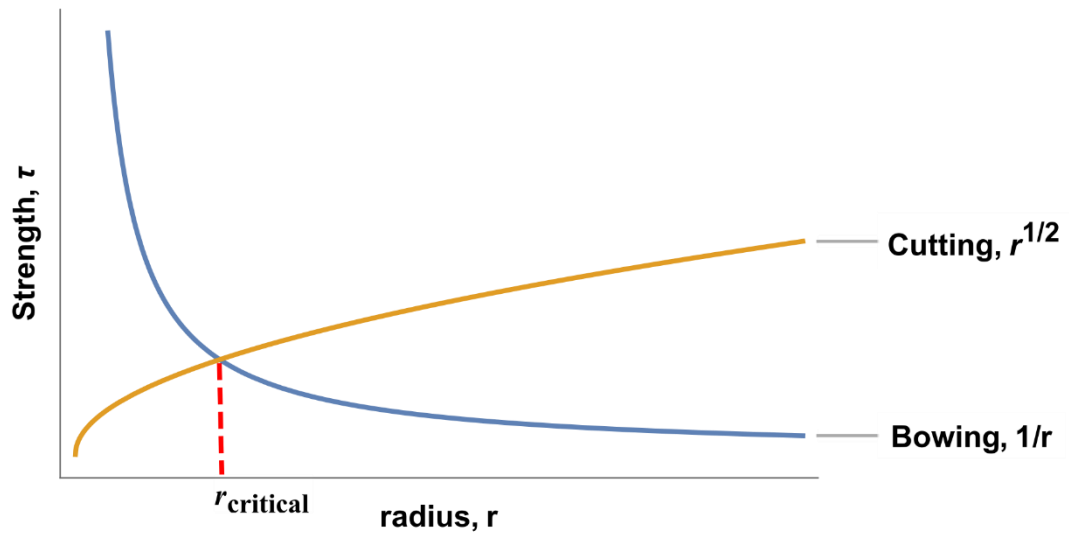


Figure 2.13 The shear strength τ variation with dislocation cutting mechanism and bowing mechanism, the cross point is the critical radius of precipitates [139].

2.8 General Precipitation Hardening in Magnesium Alloys

2.8.1 Mg-Zn Alloys

In magnesium alloys, Mg-Zn alloys are of particular interest due to their excellent precipitation strengthening ability, biocompatibility and low production costs [99,141–143]. Precipitation during ageing treatment increases the strength of the alloy by hindering dislocation movement. In addition to their mechanical properties, Mg-Zn alloys also have good biocompatibility because the body can absorb magnesium and zinc ions, which are essential to the human body, so these alloys have potential applications in biomedical implants [144–146]. From an economic perspective, the abundant and low-cost reserves of Mg and Zn compared to rare earth (RE)-based Mg alloys make these alloys more advantageous [143,147]. In addition, the Mg-Zn system is an important basis for commercial Mg alloys because zinc can form stable precipitates with magnesium. Figure 2.14 shows the age-hardening curve of Mg-Zn alloys. Over the years, researchers have made considerable efforts to understand and optimise the microstructure of Mg-Zn alloys, focusing mainly on their age-hardening properties [99,142]. Despite significant progress, challenges remain in understanding the structure and stability of the various phases in the Mg-Zn system, particularly metastable precipitates that form during the early stages of age-hardening treatment [99].

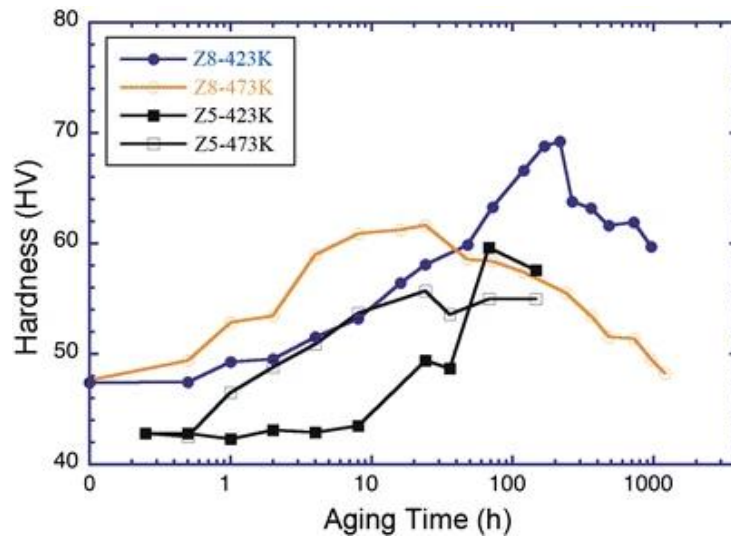


Figure 2.14 Age-hardening response of Mg-8Zn (wt. %) and Mg-5Zn (wt. %) alloys at 423 K and 473 K [99].

The Mg-Zn system consists of several intermetallic compounds as shown in the Mg-Zn phase diagram in Figure 2.15, which have a significant effect on its microstructure and mechanical properties. The key intermetallic phases include:

1. $Mg_{51}Zn_{20}$ (Mg_7Zn_3): This compound has the lowest Zn concentration (around 30 at. %), a stable temperature from 325 to 341 °C, and a crystal structure ($Immm$, $a = 14.083 \text{ \AA}$, $b = 14.486 \text{ \AA}$, $c = 14.025 \text{ \AA}$) similar to a Mackay icosahedron (MI)-type quasicrystal approximant [148–151].
2. $MgZn$ ($Mg_{21}Zn_{25}$): Commonly referred to as the equilibrium β phase at low temperature, this phase has a stoichiometry of around 50 at. % Zn and a hexagonal crystal structure ($R\bar{3}c$, $a = b = 25.7758 \text{ \AA}$, $c = 8.7624 \text{ \AA}$) [152–154].
3. Mg_4Zn_7 (Mg_2Zn_3): With a Zn concentration from 60 to 63.6 at. %, this phase is a Frank-Kasper topologically close packed phase with a monoclinic structure ($B/2m$, $a = 25.96 \text{ \AA}$, $b = 14.28 \text{ \AA}$, $c = 5.24 \text{ \AA}$) [155,156]. Gao and Nie confirmed the structure with an orientation relationship of $[001]_{Mg_4Zn_7} \sim \parallel [0001]_{\alpha}$, $[001]_{Mg_4Zn_7} \sim \parallel [0001]_{\alpha}$ and $(630)_{Mg_4Zn_7} \sim \parallel (01\bar{1}0)_{\alpha}$, $(630)_{Mg_4Zn_7} \sim \parallel (01\bar{1}0)_{\alpha}$ [151].
4. Laves phases ($MgZn_2$): These phases are structurally related to the icosahedral cluster and represent stable (C14 Laves) and metastable (C15 Laves) states of $MgZn_2$. The C14 Laves phase has a hexagonal structure ($P6_3/mmc$, $a = 5.221 \text{ \AA}$, $c = 8.57 \text{ \AA}$), while the C15 Laves phase has a face-centered cubic structure ($Fd\bar{3}m$, $a = b = c = 5.234 \text{ \AA}$) [156–161].

5. Mg_2Zn_{11} : This phase has a cubic packing structure ($Pm\bar{3}$, $a = b = c = 8.54 \text{ \AA}$) determined by Samson [162]. The structure is similar to the C14 Laves $MgZn_2$ phase [163].

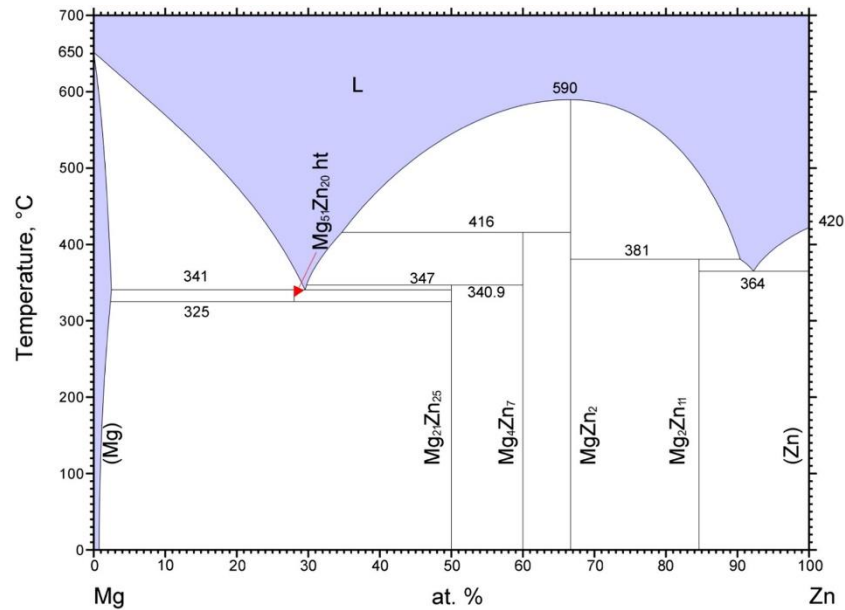


Figure 2.15 Mg-Zn phase diagram [164].

The order of precipitation in Mg-Zn alloys has a significant effect on their mechanical properties. In recent literature, the generally accepted order is S.S.S.S. \rightarrow Guinier-Preston (GP) zone $\rightarrow \beta'_1 \rightarrow \beta'_2 \rightarrow \beta$ [79,165]. However, the precipitation sequence of metastable precipitates in Mg-Zn alloys is still controversial. The precipitate morphology during ageing of Mg-Zn alloys is shown in Figure 2.16, where it can be found that both β'_1 and β'_2 precipitates are present in the early ageing precipitates. Possible precipitation sequences have been proposed by Cheng et al [164] by first-principles calculation methods, which are shown in Figure 2.17.

The GP zones in the Mg-Zn system are coherent nanometer-scale precipitates that form on specific crystal planes in the Mg matrix. These regions were initially detected using Laue XRD and later confirmed using high-resolution TEM and atom probe techniques (APT) [165,166]. GP zones play a key role in early hardening. Bhattacharjee et al. believe that GP zones can act as heterogeneous nucleation sites for the early β'_1 phase, but direct imaging of GP zones remains challenging [167].

The β'_1 precipitates are characterised by rod-like/lath-like structures, and these metastable precipitates form during early to peak ageing. Although β'_1 has traditionally been considered to be a C14 Laves phase, recent evidence suggests that it is a monoclinic structure similar to Mg_4Zn_7 [151,156]. Several studies have reported that β'_1 is a

composite of the Mg_4Zn_7 and C14 $MgZn_2$ phases, with occasional occurrences of C15 $MgZn_2$ [156,159]. β'_2 precipitates are characterised by a plate-like structure, which forms on the basal surface of the Mg matrix during over-ageing. Their structure is consistent with that of C14 $MgZn_2$ and their morphology usually overlaps with that of β'_2 precipitates [151,168]. β precipitate, as an equilibrium phase, are usually present in the form of sphere or blocks.

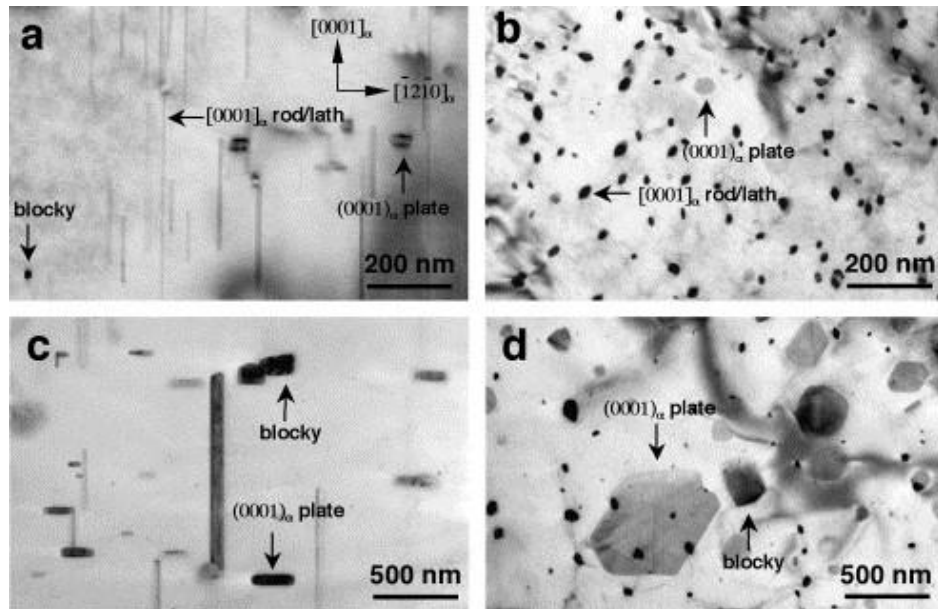


Figure 2.16 TEM micrographs showing precipitates in samples aged for 2 h (a, b) and 1000 h (c, d) at 200 °C. The electron beam was approximately parallel to $\langle 10\bar{1}0 \rangle_\alpha$ (a, c) and $[0001]_\alpha$ (b, d) [151].

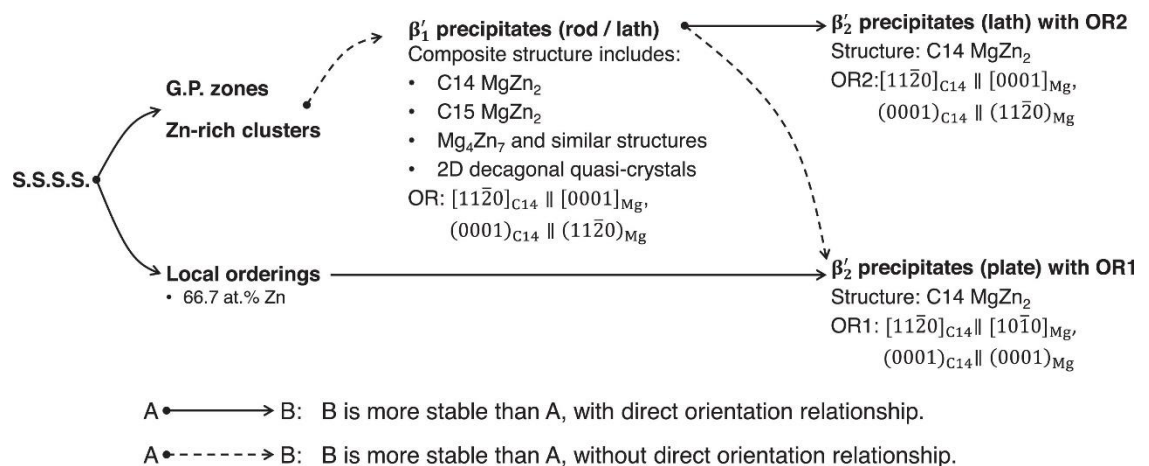


Figure 2.17 Precipitation sequences for supersaturated Mg-Zn solid solution during ageing [164].

2.8.2 Mg-Ca Alloys

The Mg-Ca system allows the development of precipitation-hardened alloys that have potential for biomaterial applications, and its phase diagram is shown in Figure 2.18. Calcium is an essential element for the human body, in addition, the low density of calcium (1.55 g/cm^3) helps to maintain the density of Mg-Ca alloys similar to that of bone. Calcium also acts as a grain refiner in magnesium and improves the mechanical properties of the alloy [169]. At the Mg-rich end of the Mg-Ca phase diagram, the equilibrium intermetallic phase is C14 Laves Mg_2Ca , which shares a similar crystal structure ($P6_3/mmc, a = 6.23 \text{ \AA}, c = 10.12 \text{ \AA}$) with the magnesium matrix phase ($P6_3/mmc, a = 3.21 \text{ \AA}, c = 5.21 \text{ \AA}$). This structural similarity may increase the nucleation rate and density of precipitates in Mg-Ca alloys [99].

Rad et al. observed that the hardness of as-cast Mg-Ca alloys increased with increasing calcium content due to the formation of intermetallic Mg_2Ca phase and was harder compared to the α Mg matrix phase. As shown in Figure 2.19, the hardness of pure magnesium is 28.9 HV, while Mg-10Ca (wt. %) alloys can reach 78.8 HV [170]. However, the Mg_2Ca phase tends to increase the brittleness of magnesium alloys. Wan et al. demonstrated that the bending and compression elastic modulus of heat-treated Mg-Ca alloys improved with increasing calcium content. Among the Mg-xCa ($x = 0.6, 1.2, 1.6, 2.0$ wt. %) alloys, Mg-0.6Ca (wt. %) exhibited excellent bending and compressive strengths due to the lower content of Mg_2Ca phase [77].

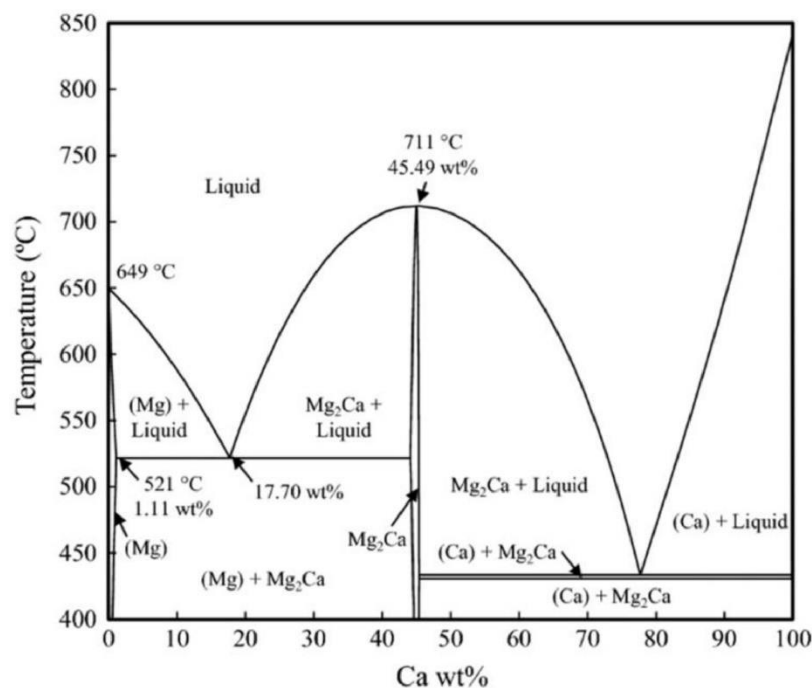


Figure 2.18 Mg-Zn phase diagram [171].

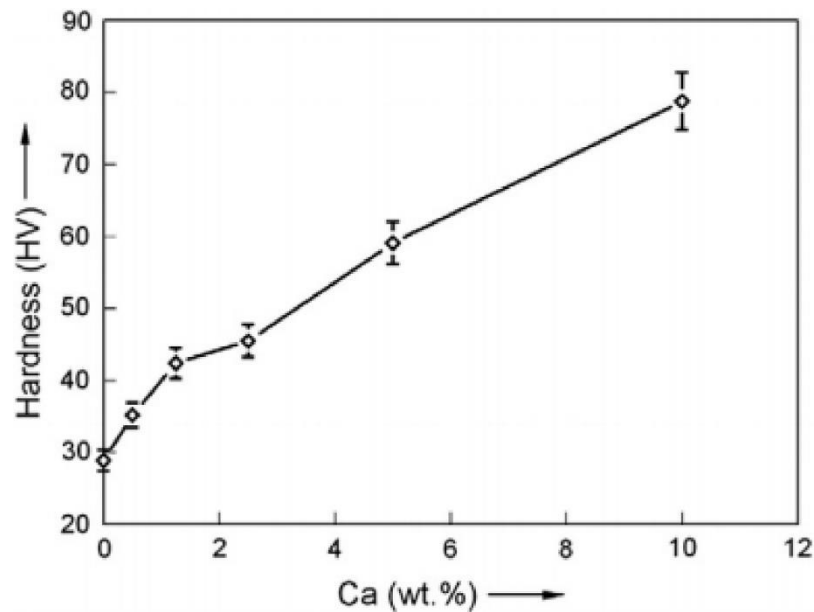


Figure 2.19 Effect of Ca content on the hardness of Mg-Ca alloy under as-cast condition [171].

2.8.3 Mg-Zn-Ca Alloys

Nie et al. showed that Mg-1 wt. % Ca alloys exhibit only a moderate age-hardening response during isothermal ageing at 200 °C, but the addition of 1 wt. % Zn to binary alloys leads to a significant increase in peak hardness and an accelerated ageing response, as shown in Figure 2.20a [79,172]. In contrast to the binary Mg-Ca phase with a C14 hexagonal structure, the ternary Mg-Zn-Ca precipitated phase is still a controversial topic because its structure and composition depend on factors such as the alloy composition, the Zn-Ca ratio, and the processing conditions. This long-standing discussion has developed over several decades.

In 1933, Paris reported the first discoveries concerning the Mg-Zn-Ca system, studying 189 different alloys [173]. After heat treatment, Paris found a ternary compound, $Ca_2Mg_5Zn_5$, with a melting point of 495°C, but no crystallographic data were provided. Later in 1961, Clark [174] gave isothermal profiles of the Mg-Zn-Ca phase diagram at 335°C based on 76 alloys. Using X-ray diffraction (XRD) and metallography, he observed two ternary phases, $Ca_2Mg_6Zn_3$ and $Ca_2Mg_5Zn_{13}$, with structural features different from those found by Paris.

Nie et al [79] demonstrated in 1997 that the addition of Zn to Mg-1Ca (wt. %) resulted in the formation of Zn-containing Mg_2Ca precipitates, which significantly enhanced precipitation hardening. The addition of Zn reduced the lattice mismatch between the precipitates and the Mg matrix, and facilitated homogeneous nucleation and a finer distribution of precipitates. Jardim et al [166,175] analysed the composition of the Mg-

6Zn-1.5Ca (wt. %) precipitates and found the composition to be close to $Ca_2Mg_4Zn_3$, but attributed this difference to EDS uncertainties.

Levi et al [176] and Bamberger et al [177] attributed the isothermal age-hardening of various Mg-Zn-Ca alloys to $Ca_2Mg_6Zn_3$ precipitates, but Oh-ishi et al [80] found that the Guinier-Preston (GP) zone is the main contributor to the age-hardening response of the Mg-0.6Zn-0.3Ca (at. %) alloy at 200 °C, as shown in Figure 2.20b. APT analyses showed that these GP zones consist of Mg-18Ca-8Zn (at. %). They found that the GP zone is the only contributor to age-hardening in Mg-1.6Zn-0.5Ca (wt.%), but the formation of $Ca_2Mg_6Zn_3$ suppresses the GP zone in high-Zn alloys [79]. Studies of precipitation sequences in Mg-Ca-Zn alloys have shown that monolayer GP zones, $Ca_2Mg_6Zn_3$ and $Mg_2Ca(Zn)$ phases depend on Zn content and ageing conditions.

Although the Mg-Zn-Ca ternary precipitation phase remains controversial, the generally accepted order today is S.S.S.S. → Guinier-Preston (GP) zone → η' ($Ca_2Mg_6Zn_3$) → η ($Mg_2Ca(Zn)$). Compared to binary Mg-Ca and Mg-Zn alloys, Mg-Zn-Ca alloys have a better age-hardening response, and heat treatment leads to a finer distribution of precipitates (mainly $Ca_2Mg_6Zn_3$), which improves the mechanical properties [78,167].

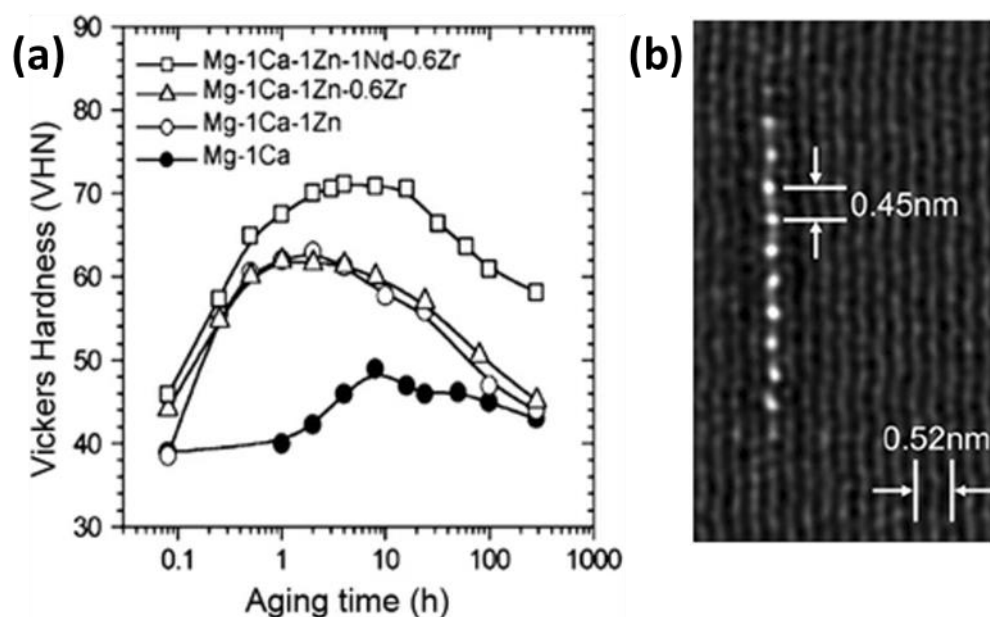


Figure 2.20 (a) Ageing curves of Mg-Ca based alloy at 200 °C and (b) Guinier-Preston (GP) in Mg-0.6Zn-0.3Ca (at. %) alloy at 200 °C [99].

2.8.4 Mg-Zn-Ca-Ag Alloys

Mg-Zn-Ca based alloys have excellent biocompatibility and high mechanical properties, while Ag is a good additive for them due to its good bacteriostatic effect and strong solid solution strengthening [178]. Ag also promotes the precipitation of the second phase to

strengthen the magnesium alloys, reduces the c/a ratio, and improves the ductility and deformability [179,180]. Quaternary Mg-Zn-Ca-Ag alloys have been extensively studied to develop biodegradable magnesium alloys [181,182].

It has been shown that the addition of Ag or both Ag and Ca to Mg-6Zn (wt.%) alloys significantly improves the age-hardening response and tensile yield strength (TYS), as shown in Figure 2.21 [99]. Microstructural analyses by Yin et al. showed that the addition of Ag to Mg-2Zn-0.2Ca (wt.%) alloys does not significantly alter the microstructure, although it promotes dynamic recrystallisation, refines the second phase and reduces its volume fraction. As a result, the mechanical properties of these alloys remain relatively consistent, exhibiting tensile yield strengths (TYS) of ~140 MPa, ultimate tensile strengths (UTS) of ~240 MPa and excellent elongations of ~30% [183]. EDS analysis shown in Figure 2.22 indicates that in as-extruded Mg-2Zn-0.2Ca-xAg (x=0, 0.1, 0.3 and 0.5 wt. %) alloys, most of the Ag is uniformly distributed in the Mg matrix, and a small portion of it tends to be attached to the precipitates containing Zn and Ca [183]. During the pre-precipitation stage, Ca and Zn atoms are co-segregated, whereas Ag atoms remain homogeneously distributed in the Mg matrix until they are segregated into the precipitates under peak ageing conditions. However, the exact mechanisms by which Ca and Ag co-promote nucleation remain unclear, and their exact roles need to be clarified through characterisation of the solute vacancy binding energy in magnesium and the distribution and orientation relationships of Ca and Ag atoms in the precipitates [184,185].

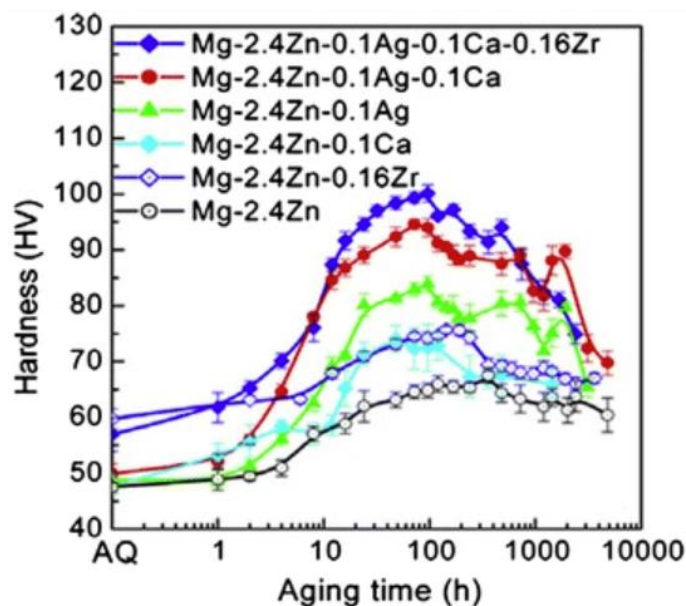


Figure 2.21 Age-hardening response of Mg-2.4Zn (at. %) during isothermal ageing at 160 °C [99].

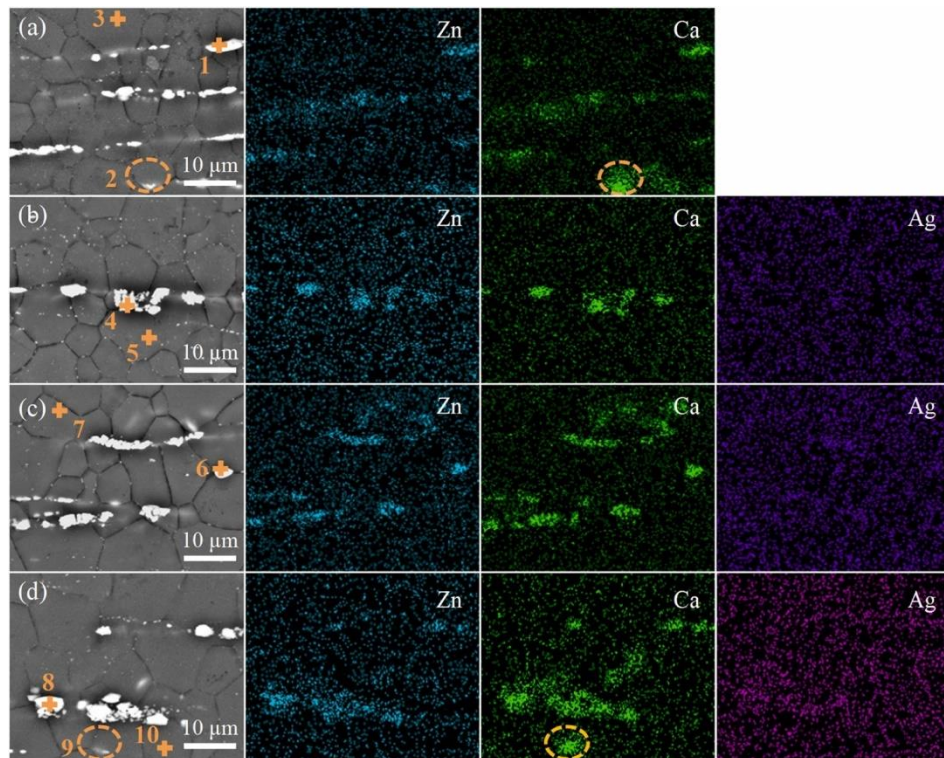


Figure 2.22 SEM-EDS mapping results of as-extruded Mg-2Zn-0.2Ca-xAg ($x=0, 0.1, 0.3$ and 0.5 wt. %) alloys: (a) ZX20, (b) ZXQ0.1, (c) ZXQ0.3 and (d) ZXQ0.5 [183].

2.9 Calculation of Phase Diagram (CALPHAD)

From the chapters above, the effect of improving the formability and mechanical properties can be achieved by controlling the size of the grains in the magnesium alloy and the solid solution and precipitation of the alloying element compositions. However, despite the great efforts made by researchers in the process of developing new magnesium alloys, the process of obtaining experimental results still requires a considerable investment of time and money. Designing alloys using traditional experimental methods generally require a long development cycle to develop alloys through trial-and-error and modification [186].

The Calculation of Phase Diagrams (CALPHAD) approach is a computational method that has evolved into a cornerstone of materials science, enabling the prediction and understanding of phase equilibrium and thermodynamic properties in complex multicomponent systems. Initially developed to address the challenges of constructing phase diagrams, the CALPHAD method has since expanded to integrate thermodynamics, kinetics, and advanced modelling techniques, driving innovation in alloy design, process optimization, and materials discovery. The development of CALPHAD has been driven by advancements in thermodynamic theory, computational techniques, and experimental validation, enabling its application to increasingly complex materials systems [187,188].

In the design of multicomponent materials, with each addition of an alloying element, the alloy may have different microstructure and properties, and this information is rarely obtained through experiments or manuals. Therefore, the CALPHAD method has attracted the attention of alloy composition design researchers as the method for efficient calculations in multicomponent, multiphase systems with the precision required for practical applications. In addition, CALPHAD calculations can be used to obtain information about the metastable equilibrium and the driving forces for the formation of stable phases. Since phases are the basic components of materials, in the CALPHAD method, the properties of each phase are modelled as a function of composition, temperature, and sometimes pressure, so the CALPHAD method is also called the genetic design of materials [189]. The origins of the CALPHAD method are in the establishment of the principles of thermodynamics and the realisation that phase equilibria can be described in terms of free energy functions. In the 1960s, Kaufman [190] and Hillert [191] pioneered the CALPHAD method by combining experimental phase diagram data with thermodynamic models to compute phase equilibria for binary and ternary systems. Their work highlighted Gibbs energy minimisation as a fundamental principle in determining equilibrium states. The method was initially limited to simple systems due to computational limitations and the lack of a comprehensive thermodynamic database.

A major milestone in the evolution of CALPHAD was the creation of comprehensive thermodynamic databases. These databases compile critically assessed parameters for Gibbs energy functions, derived from experimental data and ab-initio calculations. The 1980s and 1990s saw the emergence of software tools such as Thermo-Calc [192], Pandat [193], and FactSage [194], which integrate thermodynamic models with these databases. With the development of thermodynamic databases, the CALPHAD approach has now been incorporated into ICME (Integrated Computational Materials Engineering), which is the integration of material information captured in computational tools with engineering product performance analysis and manufacturing process simulation [186]. In 2011, the Materials Genome Initiative (MGI) in the United States of America was announced, in which the CALPHAD method was used to develop and manufacture advanced multicomponent materials faster and more cost-effectively [195].

Thermodynamics is the basis of the CALPHAD approach, centred on the first and second laws of thermodynamics and the combined laws of thermodynamics [196,197]. The first law of thermodynamics in Eq.(2.22) describes the interactions between a system and its

surroundings and states that the exchange of energy between the system and its surroundings is balanced by changes in the system's internal energy. The second law of thermodynamics in Eq.(2.23) governs the system in the context of these interactions internal processes and states that any self-generated internal process is irreversible and necessarily generates entropy. The Gibbs free energy (G) is a thermodynamic potential that expresses the maximum reversible work that can be performed by a system at constant pressure (P) and temperature (T), and is defined in Eq.(2.24) [121]. At equilibrium, the Gibbs free energy of the system is minimised, and in multicomponent systems, the free energy of each phase is calculated based on composition, temperature and pressure. The phase, or mixture of phases with the lowest free energy is stable, and the chemical potential (μ_i) of each component in all co-existing phases at equilibrium is equal. The molar Gibbs energy of a phase, which represents its stability relative to other phases in a multicomponent system, is expressed in Eq.(2.25) [198]. The Gibbs energy of Solution phase φ for liquid and the terminal solid solution phases is represented by ${}^\circ G_m^\varphi$ [199], which is the sum of contributions from pure component mechanical mixtures [200]. idG_m^φ and exG_m^φ are ideal configurational entropy and excess Gibbs energy respectively, which are described and extrapolated by the mean of Redlich -Kister-Muggianu polynomials [201]. $magG_m^\varphi$ is the magnetic contribution to the Gibbs energy, which is described by the Indeen model [202]. The advantage of the CALPHAD approach is that the descriptions of the constituent subsystems can be combined in the process to describe a multi-component system, thus improving the efficiency of the component design.

$$\Delta U = Q - W \quad (2.22)$$

$$\Delta S \geq \frac{Q}{T} \quad (2.23)$$

$$G = H - TS \quad (2.24)$$

$$G_m^\varphi = {}^\circ G_m^\varphi + idG_m^\varphi + exG_m^\varphi + magG_m^\varphi \quad (2.25)$$

where U is the internal energy of the system, Q is heat added to the system, W is the work done by the system, S is the entropy. In addition to equilibrium calculations, the Gibbs free energy serves as a driving force for phase transformations. The difference in Gibbs

energy between phases determines the supersaturation or undercooling, which influences nucleation, growth, and coarsening kinetics. Coupling CALPHAD with kinetic models such as DICTRA for diffusion-controlled transformations, uses this information to predict microstructural evolution in alloys [203–205].

The Gibbs thermodynamics form the backbone of the CALPHAD approach. By accurately modelling the Gibbs free energy of phases and ensuring consistency with experimental data, CALPHAD provides a framework for predicting phase equilibrium, thermodynamic properties, and material behaviour under various conditions. As computational methods and databases continue to evolve, the predictive power of CALPHAD will further expand, enabling the design of advanced materials with tailored properties. CALPHAD has been extended from equilibrium to non-equilibrium calculations by combining thermodynamic calculations with kinetic and physical property modelling. The study of precipitation kinetics has been a cornerstone of materials science, enabling the prediction of microstructural evolution and optimisation of material properties. Early theoretical developments laid the foundations for understanding nucleation, growth and coarsening processes, and subsequent advances have combined these kinetic models with a thermodynamic framework to improve the accuracy of predictions for complex alloy systems.

2.10 Mean-field Approaches

The combination of mean-field models with CALPHAD greatly improves the prediction of material precipitation kinetics, which enables the prediction of microstructural evolution and the optimisation of material properties. Mean-field models are widely used to describe precipitation processes in alloy systems, which is the simplest description of the evolution of particle dispersion. These models assume that the interactions between individual particles and the surrounding matrix can be expressed in terms of mean-field variables without the need to consider the interactions between different particles. The main mean-field models include the Langer-Schwartz-Wagner (LSW) model, the Kampmann-Wagner numerical (KWN) model, and the Svoboda-Fischer-Faulkner-Kozeschnik (SFFK) model.

The first comprehensive approach to modelling particle evolution was derived by Greenwood [206], Lifshitz and Slyozov [128] and Wagner [207] to modelling particle evolution, which is the LSW mean-field model. The LSW model describes the mechanism of Oswald ripening, where particle coarsening is driven by a reduction in interfacial energy. It assumes diffusion control of growth and predicts the evolution of

the precipitate size distribution. The model is derived by considering binary alloys and dilute particle dispersion.

Kampmann and Wagner developed a mean-field numerical model, the KWN model, which predicts the simultaneous nucleation, growth and coarsening of precipitates [208]. The model can be easily coupled with thermodynamic and kinetic databases to simulate the evolution of mean precipitate parameters in multi-component alloy systems. The KWN model describes precipitate evolution by discretizing the particle size distribution into a series of size classes and tracking their evolution over discrete time steps. Nucleation rates are calculated using classical nucleation theory, while particle growth and size-class transitions are modelled assuming solute diffusion as the rate-limiting process and spherical particle morphology. The Gibbs–Thomson relationship is applied to adjust interfacial compositions for each size class. Additionally, the mean-field approximation is employed to account for changes in matrix solute concentration caused by precipitation or dissolution at each time step [209–211].

The Svoboda-Fischer-Fratzl-Kozeschnik (SFFK) model not only simulates the nucleation, growth, coarsening and chemical composition evolution of precipitates [212,213], but also predicts the growth kinetics of both spherical and non-spherical precipitates [214–217]. Moore et al [218] described the growth kinetics of differently shaped precipitates using the shape factor of Kozeschnik et al [219] and the aspect ratio kinetics of Svoboda et al [220] on the basis of the SFFK model. The SFFK approach emphasises the coupling of thermodynamics and kinetics by explicitly combining diffusion and interfacial growth, enabling the modelling of precipitation in complex alloys.

The development of mean-field models, from the classical LSW theory to the advanced SFFK models, reflects the advances in precipitation kinetic modelling. Combining these models with CALPHAD enhances their predictive capabilities by providing thermodynamic and kinetic parameters from a reliable database. This integration makes it possible to design and optimise materials with tailored microstructures and properties, demonstrating the key role of mean-field models and CALPHAD in modern materials engineering. As computational methods and databases continue to evolve, the role between mean-field modelling and CALPHAD will further advance the design of high-performance alloys.

2.11 Summary

This literature review provides a comprehensive discussion of the historical development, general properties, deformation mechanisms, alloying, strengthening mechanisms and computational modelling of magnesium alloys, and provides guidance on the potential applications and materials design of magnesium alloys.

The low density and high thermal conductivity of magnesium make it an ideal material for applications in the automotive and aerospace industries, where weight reduction is critical, while biocompatibility and biodegradability are advantages in biomedical implants. The deformation behaviour of magnesium alloys is strongly influenced by their hexagonal close-packed (HCP) crystal structure, which is restricted by the slip systems. Alloying elements play a key role in tailoring mechanical properties, corrosion resistance and thermal stability, and their mechanical properties can be improved by combining strengthening mechanisms, which include solid solution strengthening, precipitation strengthening and grain refinement. In addition, texture evolution has a strong influence on anisotropy. The addition of rare earth elements can weaken the basal texture and thus exhibit improvements in ductility and strength, while the addition of calcium elements has the potential to replace rare earth elements in randomising the texture.

Precipitation strengthening, which is controlled by nucleation, growth and coarsening, remains the central mechanism for improving mechanical properties. Understanding the thermodynamic evolution of precipitates is fundamental to the study of precipitation strengthening mechanisms. Computational methods have become important tools in the research and development of magnesium alloys. The CALPHAD method can predict phase equilibrium and thermodynamic properties to accelerate alloy design by identifying optimal compositions and processing conditions. This approach links experimental and theoretical investigations by integrating thermodynamic and kinetic models to support the development of tailored alloys. On the other hand, mean-field models provide a framework for simulating microstructural evolution, capturing behaviour such as precipitation, grain growth and deformation on a continuum scale. These models complement experimental work by providing predictive insights into material behaviour, reducing the reliance on extensive empirical experimentation.

Despite these advances, several gaps remain in the current understanding of magnesium alloy systems. One of the major gaps lies in the limited understanding of precipitation behaviour in multicomponent Mg-Zn-Ca(-Ag) systems. Although various strengthening mechanisms have been reported, the role of complex precipitate interactions in such

alloys remains inadequately explored. Moreover, the validation of computational models under non-equilibrium solidification conditions is insufficient, especially for ternary and quaternary magnesium alloys that exhibit strong solute segregation. In addition, the impact of minor Ag additions on recrystallisation, grain growth, and mechanical strengthening in Mg-Zn-Ca alloys is still not clearly understood, particularly under thermomechanical processing conditions. There is also a lack of studies that integrate CALPHAD-based simulations with experimental microstructural characterisation methods such as SEM, EBSD, and EDX to validate the dissolution behaviour of thermally stable intermetallic phases like Mg_2Ca during homogenisation heat treatment. There is also a need for clear design strategies to balance precipitation strengthening with microstructural stability, particularly in systems where Ag affects both precipitation and recrystallisation kinetics. These gaps motivate the present study, which aims to bridge modelling and experimental efforts to better understand and optimise Mg-Zn-Ca(-Ag) alloy systems.

In response, this research combines microstructure control with advanced computational modelling, specifically CALPHAD and mean-field approaches to investigate the thermodynamic and kinetic evolution of Mg-Zn-Ca(-Ag) alloys. The goal is to guide alloy design and processing optimisation, accelerating the development of high-performance magnesium alloys.

Chapter 3: Experimental Methodology

3.1 Alloy Preparation

3.1.1 Alloy Compositions

The Mg-Zn-Ca(-Ag) alloy was supplied by Luxfer MEL Technology (UK) with a composition given in Table 3.1, where the actual Mg, Zn, Ca, Ag content was measured by Inductively coupled plasma optical emission spectroscopy (ICP-OES), and the local Mg, Zn, Ca content was measured by Energy-dispersive X-ray spectroscopy (SEM-EDS).

Table 3.1 Composition of magnesium Mg-Zn-Ca alloys

| Alloy | Mg (wt.%) | Zn (wt.%) | Ca (wt.%) | Ag (wt.%) | Measure by |
|---------|-----------|-----------|-----------|-----------|------------|
| ZX10 | Bal. | 0.8 | 0.2 | - | ICP-OES |
| ZX70 | Bal. | 6.8 | 0.2 | - | ICP-OES |
| ZX30 | Bal. | 3.11 | 0.22 | - | ICP-OES |
| ZXQ300a | Bal. | 3.10 | 0.21 | 0.14 | ICP-OES |
| ZXQ300b | Bal. | 3.11 | 0.21 | 0.33 | ICP-OES |

3.1.2 Cast and Wrought Procedures

The ZX10, ZX70 alloys was received in the as-cast condition. An as-cast cylindrical billet of dimension 110×75 mm was cooled in a water circulating steel mould, the solidification process shown in Figure 3.1. Material was cast at 750 °C into 75 mm diameter water-cooled billets, the melt was puddled and stirred in between adding additions and left for 15 minutes to settle prior to taking OES blocks and then casting. ZX30, ZXQ300a, and ZXQ300b were cast at 740 °C into 3.0-inch diameter water-cooled billets, the melt was puddled and stirred in between adding additions and left for 15 minutes to settle prior to taking OES blocks and then casting. Billets were homogenised at 370 °C for 24 hours, then extruded using a 10×40 mm die, the extrusion parameters are shown in Table 3.2.

Table 3.2 Mg-Zn-Ca(-Ag) alloys extrusion parameters

| | |
|---------------------------------|---------------------------|
| Cast Temperature (°C) | 740 °C, then Water-cooled |
| Homogenization Temperature (°C) | 370 °C for 24hrs |
| Extrusion temperature (°C) | 350°C |
| Extrusion ratio | 1:15 |
| Extrusion speed | 0.2 ~ 0.3 mm/s |

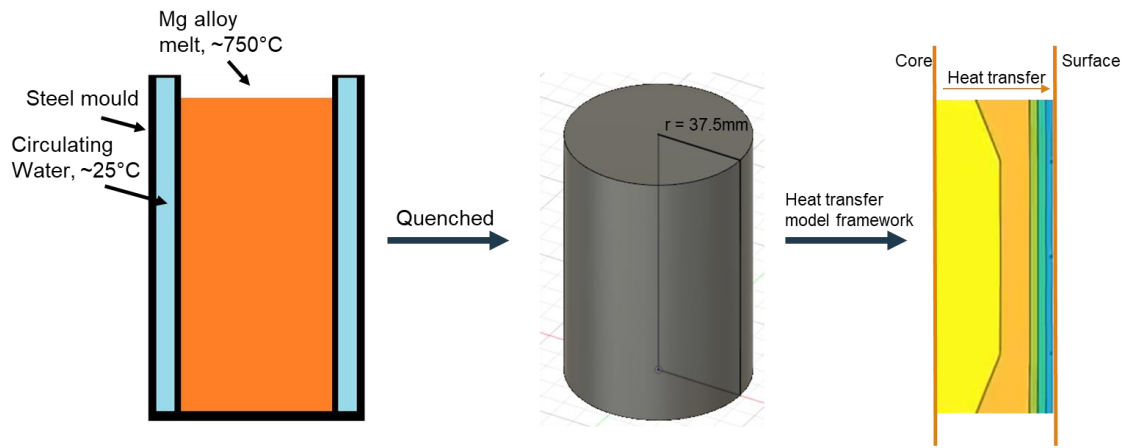


Figure 3.1 As-cast ZX10 and ZX70 samples solidification process

3.1.3 Heat Treatment

Cast Mg-Zn-Ca alloys were homogenised based on the equilibrium phase diagram calculated using Thermo-calc software and the thermodynamic database TCMG6 (Magnesium-based alloys database) shown in Figure 3.2. The ZX10 was machined into $5 \times 5 \times 10 \text{ mm}$ samples and initially homogenised at temperatures of 500°C , 520°C and 540°C for a period of 48 hours. This process was employed to identify the optimal homogenisation temperature, with the objective of preventing local melting. As shown in Figure 3.3, the ZX10 alloy displayed clear initial melting following homogenisation at a temperature of 540°C for 48 hours. However, no significant local melting was observed after homogenisation at 500°C and 520°C for the same duration. Consequently, the subsequent ZX10 alloy was homogenised at 520°C for 4 hours in order to facilitate further investigation. The label for the homogenisation process is shown in Table 3.3. For the solution treatment, extruded ZX30 alloy sheets of dimensions $5 \times 5 \times 10 \text{ mm}$ were homogenised at 370°C for 1 hour, then water quenched and subsequently underwent ageing treatment at 160°C for up to 196 hours.

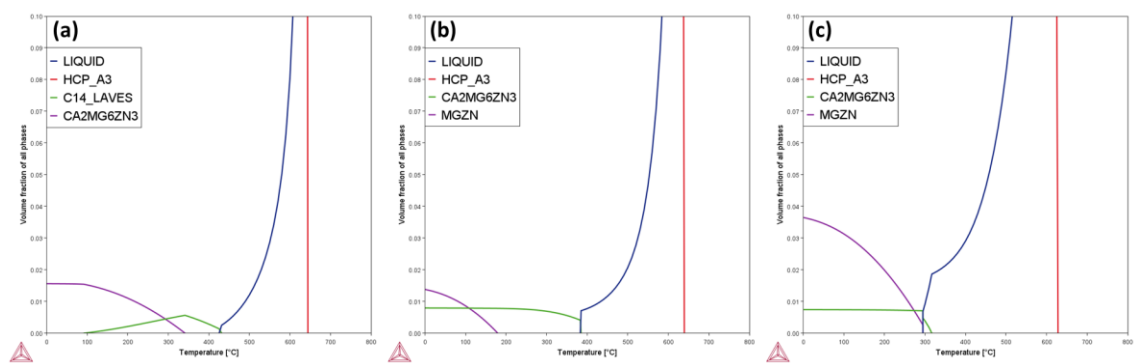


Figure 3.2 Equilibrium phase diagram of (a) ZX10, (b) ZX30 and (c) ZX70 alloys

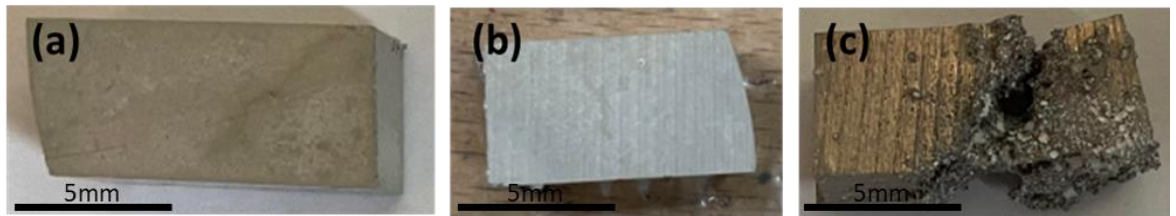


Figure 3.3 ZX10 samples after homogenisation at (a) 500°C, (b) 520°C and (c) 540°C for 48 hours

Table 3.3 Homogenisation process of ZX10 alloy

| Label | Heat treatment process |
|----------------|-------------------------------|
| H500-48 | 500°C for 48 hours |
| H520-48 | 520°C for 48 hours |
| H540-48 | 540°C for 48 hours |
| H520-4 | 520°C for 4 hours |

3.1.4 Grinding and polishing

In this study, all flat samples with varying dimensions were cold mounted into epoxy resin. This was followed by metallurgical grinding and polishing procedures, in the following steps:

1. The initial step is plane grinding, which is conducted using SiC papers of 1200, 2500, and 4000 grit to achieve a flat surface.
2. Subsequently, the specimen polished with a 1 μm and 1/4 μm diamond suspension, thereby ensuring the comprehensive elimination of any residual scratches. The polishing cloth was pre-lubricated with isopropanol to avert the suspension from clumping. Diamond suspension (1/4 μm) was added at 30-second intervals throughout the polishing process.
3. The final stage of the process is the application of a 40 nm colloidal silica suspension, which results in the creation of a mirror-like surface. To prevent the suspension from remaining on the surface and potentially influencing subsequent characterisation results, all polished specimens were subjected to an isopropanol wash, followed by an ultrasonic wash in isopropanol for a duration of five minutes.
4. For SEM-EDS and EBSD samples, Gatan's precision etching coating system (PECS™) II is employed to coat and polish the samples within a vacuum system. It is possible to perform both of these procedures on the same sample without compromising the vacuum. The PECS II system is a fully self-contained, bench-top tool that employs two wide argon beams to polish surfaces and eliminate damage. This technique is suitable

for the generation of superior-quality samples for use in scanning electron microscopes (SEM).

3.2 Phase and Composition Characterisation

3.2.1 X-ray Analysis (XRD)

A phase composition analysis was conducted on a PANalytical Aeris instrument using average Cu-K α radiation with 2θ angles spanning a range of 10° to 100° . The operating voltage and current were 30 kV and 40 mA, respectively. Upon irradiating the crystals with X-rays, diffraction patterns with specific characteristics are produced, corresponding to a particular series of lattice plane spacings and relative intensities. When combined with PDF card analysis, these patterns provide insights into the phase composition and content within the alloy. In this study, X-ray diffraction (XRD) analysis was employed for the straightforward determination of phases.

3.3 Mechanical Properties

3.3.1 Hardness Micro Indentation

Micro-hardness testing was conducted on samples that had been aged for varying periods of time in order to capture the age-hardening response. The hardness of samples is determined by means of a Vickers hardness indenter. Two Vickers hardness indenters are available for use in the microprep laboratory: the Mitutoyo and the Durascan. The Mitutoyo is employed for the purpose of taking individual hardness measurements, whereas the Durascan is better suited to the undertaking of a detailed series of measurements, the result of which is a hardness profile for the sample in a given set of circumstances. The load was set at 0.3 HV, and the dwell time was 15 seconds. To ensure the accuracy of the data, each map was composed of at least 10 indentations, and the mean value and standard deviation were calculated.

3.3.2 Tensile Test

The specimens were tensioned at room temperature on a Zwick Proline Z020 mechanical testing machine and stress and engineering strain were measured using a video extensometer coupled with testXpert Analytics software, in which tape markers were attached within the testing area of the specimen and the change in their separation was tracked in real time. The specimens were cut from extruded ZX30 alloy with dimensions of 10×40 mm using electrical discharge machining (EDM) along the extrusion direction, the tensile specimen dimensions are shown in Figure 3.4, the specimen length, width and thickness were followed for British Standards [221]. The specimens cut from the extruded ZX30 alloys were tensioned using a 5 kN load cell at a constant speed of

0.75mm/min. Finally, the extruded ZX30 samples were tested in the as-extruded and solution-treated conditions.

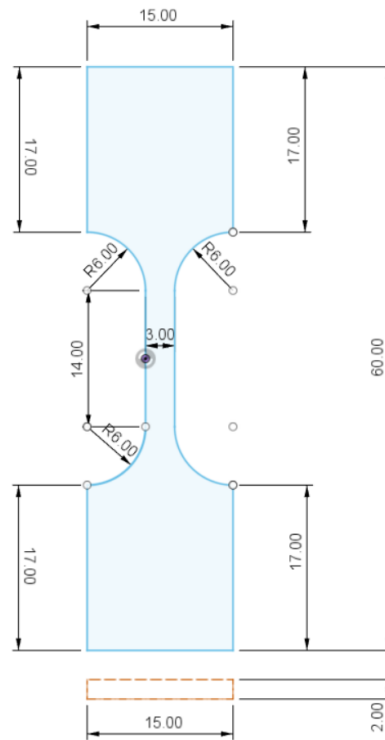


Figure 3.4 Extruded ZX30 tensile flat sample schematics with 2 mm thick dimension

The engineering stress and strain were recorded during tensile and compressive testing and subsequently plotted as stress-strain graphs. The stress σ and engineering strain ε was calculated using the following equation [222] :

$$\sigma = \frac{F}{A} \quad (3.1)$$

$$\varepsilon = \frac{\Delta L}{L_0} \quad (3.2)$$

3.4 Microstructure Characterisation

3.4.1 Optical Microscopy (OM)

Optical microscopy (OM) investigations were conducted in the Nikon microscope (Nikon, Japan) on as-received conditions and heat-treated magnesium alloys. The samples were prepared by grinding with SiC paper up to 4000 grits, with the use of water as a lubricant. Subsequently, the samples were polished using a diamond suspension (approximately 0.25 μm particle size) in isopropanol, followed by an oxide polishing suspension (OP-S),

on different Struers MD-Chem porous neoprene polishing pads. The optical microscope observations provided an overview of the distribution of precipitates, grain boundary distribution, and grain size. The average grain diameter was then calculated using ImageJ software.

3.4.2 Scanning Electron Microscopy (SEM)

The samples were prepared for scanning electron microscopy (SEM) using identical methods to those employed for optical microscopy. A scanning electron microscope (SEM) was employed to identify the presence of resolvable second phases and to analyse surface topography. This was carried out using Inspect FEI F50 and JEOL JSM-7900F Schottky field emission gun (FEG) SEM, which enabled the collection of secondary electrons (SEM-SE) and backscatter electron (SEM-BSE) images. An accelerating voltage of 20 keV for the electron beam and a working distance of 10 mm were employed. Subsequently, the data was processed using ImageJ to obtain the size, distribution, and density of the second phase particles, and using MATLAB to calculate the amount of second phase particles along the grain boundary and the area fractions of second phase particles. This analysis was conducted using 6 images, with a surface area of approximately $300 \times 250 \mu\text{m}$ per image.

3.4.3 Energy-dispersive X-ray spectroscopy based on SEM (SEM-EDS)

Scanning electron microscopy with energy-dispersive spectroscopy (SEM-EDS) is a technique used to determine the chemical composition of a specific point on a scanning electron microscope (SEM) image. This is accomplished by measuring the energy of the characteristic X-rays produced when electrons interact with the atoms in the sample. The incident electrons may excite and release bound electrons in the inner shells of atoms. The electrons in the outer shells of atoms fall into the gap left by the inner shells, thereby reducing their energy and releasing X-rays. The energy of these X-rays is dependent upon the shell from which the electrons originate and that to which they travel, and is unique to each element. Consequently, the elemental composition of a given sample can be ascertained. The use of an Inspect FEI F50 or JEOL 7900F field emission gun (FEG) with an EDS probe and an Oxford Instruments AZtec Xmax-170 detector allows for the rapid generation of information regarding the chemical composition of the sample, including the identification of elements present, their distribution within the sample, and their relative concentration. Energy-dispersive X-ray spectroscopy (EDS) is frequently conducted in backscattered electron mode concurrently with the scanning electron microscope (SEM) at an operating voltage of 20 kV. Energy-dispersive X-ray

spectroscopy (EDS) identifies the types of elements present and the percentage concentration of each element in the sample. In this study, EDS is typically employed for qualitative analysis of the distribution of alloying elements compositions. SEM observations and EDS measurements were conducted using Oxford Instruments Aztec software.

3.4.4 Electron Backscatter Diffraction (EBSD)

Electron backscatter diffraction (EBSD) was conducted using a JEOL JSM-7900F Schottky field emission scanning electron microscope, equipped with an Oxford Instruments Aztec HKL Advanced Symmetry System EBSD detector. EBSD was employed to measure the texture of the as-cast, as-extruded and annealed samples. The orientation data were plotted in polar figure (PF) and inverse polar figure (IPF) form to demonstrate the orientation distribution within the sample. The electron beam acceleration voltage was 20 keV and the working distance was 13 mm. The EBSD mapping data were analysed using Oxford Instruments AZtec Crystal software, which provides fundamental tools for processing the data.

3.4.5 Electron Probe Micro-analyser (EPMA)

The EPMA (electron probe micro-analyser) map and point data were determined using a JEOL JXA8530 Plus Hyper Probe, which is equipped with four WDS crystal spectrometers and an EDS detector. This allows for precise and accurate quantitative elemental composition analysis of composite systems on a micrometre scale. EPMA serves to supplement the visual inspection of the microstructure conducted in the scanning electron microscope by providing quantitative information regarding the chemical elements present under the electron beam. In the present study, the electron beam has an acceleration voltage of 15 keV and a working distance of 10.9 mm. The raw data is then subjected to post-processing using MATLAB, with the objective of obtaining the elemental distribution and intensity.

3.4.6 Scanning Transmission Electron Microscopes (STEM)

The transmission electron microscope (TEM) is employed for the imaging and EDS scanning of minute precipitates that are beyond the resolution capabilities of the scanning electron microscope (SEM) which is capable of identifying precipitates and second phases in experimental alloys. Furthermore, it is employed to determine the crystallographic orientation, size, habit plane, and quantitative density of precipitates. In conventional TEM operating mode, the sample is illuminated with a parallel electron beam, which is captured by a camera, with each image pixel being recorded

simultaneously. Similar to the SEM, the STEM also uses an electron beam to focus on a small probe of the sample and scan across the desired area. The STEM detector records each image pixel, thereby reducing the distortion of the image that is caused by polarization-electron interactions. In this study, data from the literature on STEM-EDS were used to observe the composition and shape of fine precipitates, thereby addressing the limitations of insufficient resolution in SEM-EDS data and optimising the precipitation model.

3.5 Error Measurements

In hardness testing, either instrumental or human error can cause the data to randomly deviate from the true value, and the variance of the data set is usually represented by the standard deviation. The standard deviation (s) is calculated by taking the square root of the value obtained by comparing the data point with the overall mean, given by the equation:

$$s = \sqrt{\frac{\sum_{i=1}^n (x_i - \bar{x})^2}{n - 1}} \quad (3.3)$$

where x_i is value of the i th point in data set, \bar{x} is the mean value of the data set, n is the number of data points in the data set.

Chapter 4: Modelling Methodology

4.1 Calculation of Phase Diagram

The Thermo-Calc thermodynamic modelling software is employed for the prediction of equilibrium phase diagrams and non-equilibrium (Scheil) solid phase diagrams. It is based on the CALPHAD method, which employs an experimental evaluation of unary, binary and ternary phase diagrams to calculate free energy functions based on thermodynamic theory. This enables the deduction of potential alloy compositions, the expected phase compositions of higher-order phase systems, predict equilibrium phases as a function of temperature. The Scheil module can be employed to simulate the solidification process and to determine the phases formed during non-equilibrium solidification, which is predicated on the assumption that there is no diffusion in the solid phase, that the liquid composition remains constant and that the solid-liquid interface is always in local equilibrium. The Thermo-Calc property module can be used to calculate a number of alloy properties such as chemical driving forces, interfacial energies, liquid and solidus temperatures and general phase transition temperatures. Prior to initiating the design experiment process, the initial phase diagram analysis of all magnesium alloys was conducted using Thermo-Calc software [192]. In the case of magnesium alloys, the current database, TCMG6, is employed for the calculation of the phase diagram and thermodynamic properties [223]. Furthermore, it is used for the prediction of phase equilibria and the simulation of the solidification process of multi-component magnesium alloys. Additionally, MOBMG1 is a thermodynamic database needed to predict kinetic data, offering kinetic evaluations for the diffusion and precipitation modules [223]. In order to calculate the second phase generation and dissolution temperatures, the second phase content, and the melting point of the Mg-Zn-Ca(-Ag) alloys under study, the Equilibrium Module was employed. This was done at equilibrium conditions. Subsequently, the Scheil module is employed to calculate the temperature at which the alloy generates second phases at non-equilibrium during actual solidification, the percentage of the alloy solidified, and the percentage of solidified phases. By analysing the phase diagrams, the temperatures and compositions necessary for the formation and dissolution of the second phases can be identified, which can assist in determining the optimal heat treatment for this alloy system.

4.1.1 Extended Scheil-Gulliver Solidification Models

The Scheil model is predicated on three fundamental assumptions: (1) The solidified phase is considered to be in a 'frozen' state, whereby reverse diffusion in the solid phase

is not taken into account; (2) diffusion in the liquid phase is assumed to be so rapid that the liquid phase always has a homogeneous composition; and (3) the liquid and solid phases are in phase equilibrium at the local interface. The classical Scheil equation provides a reasonable estimate of the solute distribution in the solid phase, as well as the proportion of the eutectic composition during solidification. This can be expressed in the subsequent equations [224]:

$$C_L = C_0(f_L)^{k-1} \quad (4.1)$$

$$C_S = kC_0(1 - f_S)^{k-1} \quad (4.2)$$

$$k = \frac{C_S}{C_L} \quad (4.3)$$

where C_L is the solute concentration in liquid, C_S is the solute concentration in solid, C_0 is the nominal composition, f_L is the liquid fraction, and f_S is the solid fraction. In the Classic Scheil model, k is taken to be constant throughout the solidification process. However, in multicomponent alloy systems such as Mg-Zn-Ca, this assumption can result in significant deviations from actual segregation behaviour. As solidification progresses, the interaction between multiple solutes leads to a dynamic partitioning environment, in which the local value of k evolves due to changing interfacial compositions. Furthermore, the assumption of complete mixing in the liquid phase may not hold near the terminal stages of solidification, where the accumulation of solute in interdendritic regions and the formation of concentration gradients limit diffusion. These breakdowns in the model's assumptions result in inaccurate predictions of solute segregation and intermetallic phase formation, especially in regions of strong solute enrichment. Farnin et al. [225] calculated the solute partition coefficient k in this equation by employing electron probe microanalysis (EPMA) grid measurements in order to analyse the redistribution of solutes that accompanies solidification. The CALPHAD method in Thermo-Calc software can also be used to determine the evolution of liquid and solid compositions during solidification, and the results can be integrated with information on the stability of the phase in order to predict the solidification process [192]. However, in the present study of the Mg-Zn-Ca ternary alloy system, discrepancies were observed between the Thermo-Calc predictions (using the TCMG6 database) and experimental results obtained by SEM-EDS experiments [223]. To address this limitation, a refined CALPHAD-based approach

tailored for ternary alloy systems has been developed. This method extends the conventional CALPHAD procedure by directly incorporating phase diagram data to calculate the Scheil solidification pathway more accurately. It is applied to describe the solidification sequence of Mg-Zn-Ca alloys with the aim of improving consistency between simulated and experimentally observed microstructures.

The Scheil solidification path predictions in CALPHAD for binary alloy system is well established [224,226]. To illustrate the approach, consider the A-B alloy system shown in Figure 4.1, with hyper-eutectic composition and at a starting temperature marked by the point X. In the event of equilibrium solidification, the composition of A and B would remain constant during cooling along the X-Y vertical line. However, in the event of far from equilibrium solidification, which adheres to the established Scheil rules, the solidification path will be that of the primary solidification of the solid B phase at point E with the liquidus temperature T_1 . It will then proceed with segregation through the red liquidus curve until it reaches point C at the eutectic point. The solid fractions at point E, $f_s(E)$, and at point C, $f_s(C)$, can be calculated by applied lever rule:

$$f_s(E) = \left| \frac{D_0D - E_0E}{D_0D} \right| = 0 \tag{4.4}$$

$$f_s(C) = \left| \frac{D_0C - E_0E}{D_0C} \right| < 1$$

It can be observed that the fraction of solids at point C is not equal to one, indicating that a eutectic reaction will occur at this composition to produce both phase A and B until complete solidification. Furthermore, by monitoring the real-time segregation of compositions, the actual real-time change in solids fraction during Scheil solidification can be determined. Assuming that the initial composition of B is $w_b(0)$, the composition at the eutectic point is $w_b(end)$, the real-time composition during solidification is $w_b(i)$, and the temperature at the i th composition is T_i at the liquidus line, the solid fraction $f_s(i)$ at the i th composition can be expressed by the following equation:

$$f_s(i) = \left| \frac{w_b(i) - w_b(0)}{w_b(i)} \right| \tag{4.5}$$

$$w_b(0) < w_b(i) < w_b(end)$$

The Scheil calculation based on Thermo-Calc, show the predicted segregated composition in each of the phases is in agreement with this solidification curve and discretisation segregation approach. As the example in Figure 4.2 shown that, although

the liquidus line primarily reached is varies with the Ca content 1 wt.%, 5 wt.%, 10 wt.% at temperature 650°C, 620°C, 580°C, respectively. The end of solidification point is same reached at the eutectic temperature. The Ca content at the eutectic point is 16.17 wt.%, and the solid fraction of each Ca content samples when reaching the eutectic point is following the Eq.(4.5) proposed in this chapter.

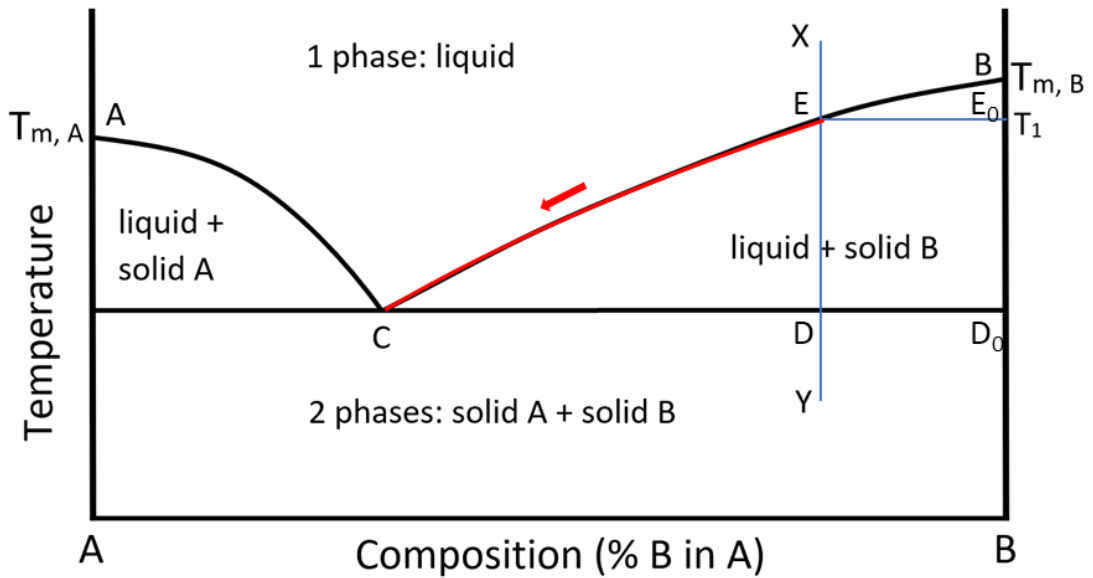


Figure 4.1 Scheil solidification path (marked in red) for a binary alloy system

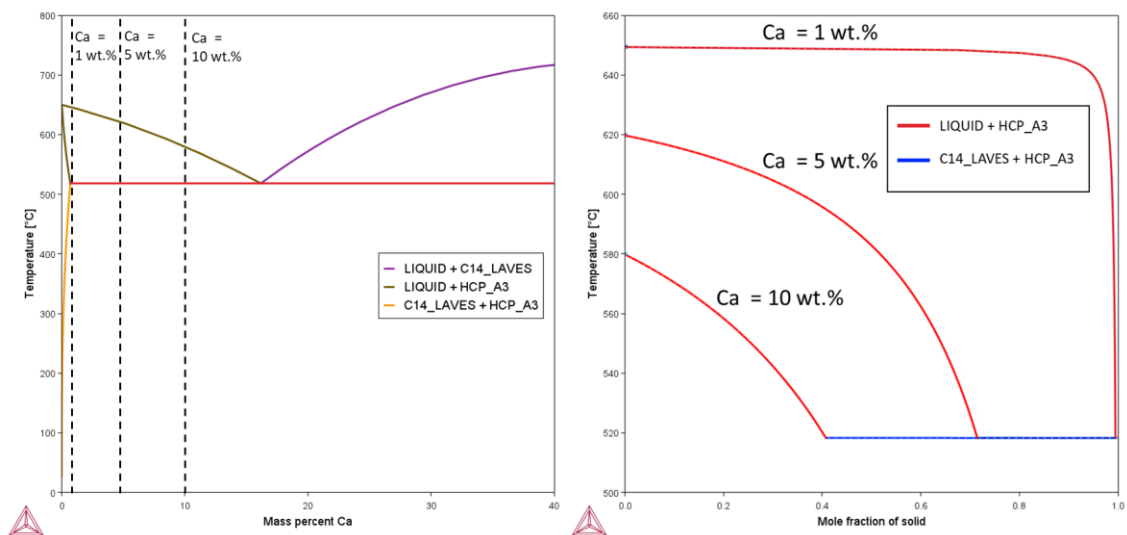


Figure 4.2 (a) Mg-Ca binary phase diagram and (b) Scheil solidification curve of Mg-1wt. %Ca, Mg-5wt. %Ca, and Mg-10wt. %Ca by Thermo-Calc

The binary system solidification path can be readily understood from the temperature-composition phase diagram in accordance with the Scheil model. However, application of such a model to the solidification process in ternary alloy system is not straight forward, since the liquidus lines in the binary phase are replaced by liquidus surfaces in the ternary

phase diagram. The work of Chen et al. and Boettinger et al. [226,227] introduced a ternary eutectic solidification model and a Scheil-based approach for ternary alloy systems, in which the newly formed solid phase remains in local equilibrium with the surrounding liquid. As solidification proceeds, mass balance is maintained by allowing the composition of the liquid phase to evolve continuously, while the composition of the solid phase remains fixed after formation, consistent with the assumption of negligible solid-state diffusion during solidification. Based on their research, the current work proposes additional assumptions to describe the ternary solidification path as an extension of binary eutectic system: (1) Scheil solidification will proceed at the liquidus surface in thermodynamic equilibrium; (2) the solidification path will follow the maximum decrease gradient of liquidus; (3) when the solidification path reaches a monovariant line, it continues along the monovariant line. For Mg-Zn-Ca ternary eutectic system, the solidification path will end at the ternary eutectic point. In this approach, the Scheil solidification pathway is constructed by following the direction of maximum liquidus gradient descent, as determined directly from the ternary phase diagram. This pathway, which represents the steepest descent in liquidus temperature towards the eutectic point, is referred to in this study as the Liquidus Minimising Scheil (LMS) pathway. An example of A-B-C ternary alloy eutectic system is shown in Figure 4.3. The initial composition and temperature start at point X_1 , the composition remains the same in the liquid state as the temperature cools to the liquidus surface (point X_2). From point X_2 to point X_3 will follow the LMS route and formed matrix phase in this stage, which will end at point X_3 , where is the monovariant line (the cross line of two liquidus surface). From point X_3 to point X_4 , the temperature will decrease following the monovariant line till the ternary eutectic point at point X_4 , and form matrix phase and first second phase in this stage. Finally, the composition will remain at point X_4 , and form matrix phase and two different second phases. It should be noticed that the segregation of A, B, C content will follow the solidification pathway as the red line in Figure 4.3 shown. The calculation of discretisation solid fraction in Eq.(4.5) for A-B binary system can be extended to the following equation for A-B-C ternary system:

$$f_s(i) = \left| \frac{\sqrt{(w_b(i) - w_b(0))^2 + (w_c(i) - w_c(0))^2}}{\sqrt{w_b(i)^2 + w_c(i)^2}} \right| \quad (4.6)$$

$$w_b(0) < w_b(i) < w_b(end)$$

$$w_c(0) < w_c(i) < w_c(end)$$

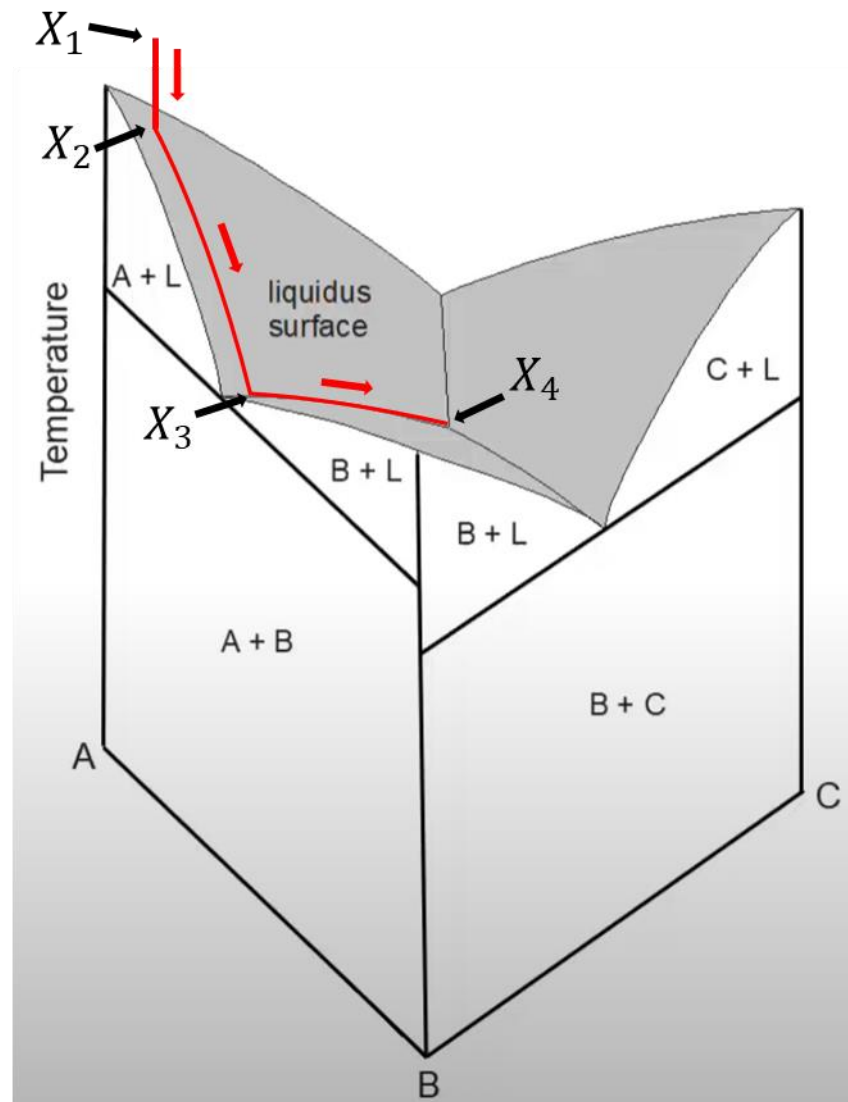


Figure 4.3 Scheil solidification path in ternary alloy system

With the calculated discretisation solid fraction, the temperature-solid fraction diagram can be drawn to describe the Scheil solidification process. Meanwhile, the segregation profile of each content can be collected from the discretisation solidification path, which can provide the local chemistry at the discretisation area. In this research, the local chemistry of the segregated alloying element can be helpful to improve the thermodynamic status of local solid state phase transition, and calculate the composition input of mean-field simulation in the following chapter.

4.1.2 Diffusion and Homogenisation (DICTRA) Simulations

The Scheil model makes different assumptions about diffusion in the solid and liquid phases. For most metal alloys with solute elements, solid-solid diffusion has a less

significant effect on solute segregation than liquid-liquid diffusion, because the solute diffusion coefficient in the solid state is usually several orders of magnitude smaller than that in the liquid state, depending on the temperature (Figure 4.4). Therefore, the assumption of no diffusion in the solid phase is not correct for most industrial or laboratory-scale solidification rates, but it can be applied to obtain an approximation of microscopic segregation during rapid cooling. In a billet with a large macroscale and a slow cooling rate, the back diffusion that occurs between solids has a greater effect on the local solute distribution of the alloy. At the microscale, the segregation of alloying elements induced by rapid cooling aligns with the predictions of the Scheil model. The resulting second phases, driven by solute enrichment, are predominantly located at dendrite tips or grain boundaries. This behaviour arises from the lower solubility of solute elements in the solid phase compared to the liquid, leading to their progressive rejection into the remaining liquid during solidification. After the segregation composition of the magnesium alloy system has been obtained using the Scheil model, a diffusion analysis of the subsequent homogenisation process can be carried out.

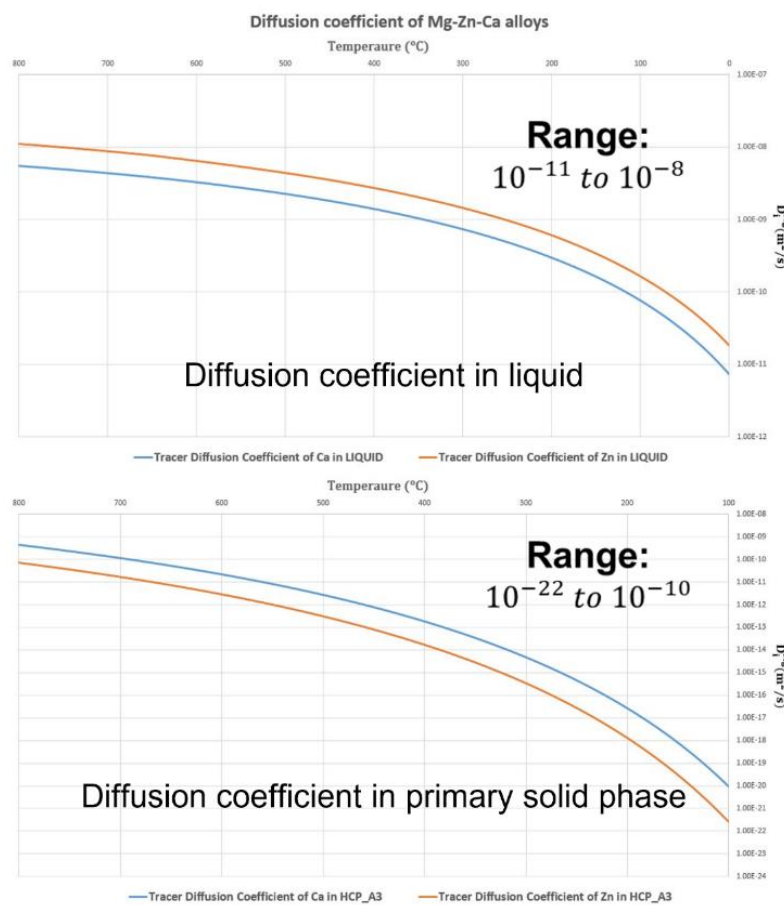


Figure 4.4 Tracer Diffusion Coefficient of Ca and Zn element in liquid and primary solid phase of Mg-Zn-Ca alloys.

Fick's laws are the classic theory for studying diffusion. Fick's first law relates the diffusive flux to the concentration gradient, assuming that the flux flows from a region of high concentration to a region of low concentration and that its magnitude is proportional to the concentration gradient, which showing in Eq.(4.7) [228,229].

$$J = -D \frac{d\varphi}{dx} \quad (4.7)$$

where J is the diffusion flux, D is the diffusion coefficient, φ is the concentration, x is position, the dimension of which is length.

Fick's first law applies to systems under steady-state conditions, where the concentration profile does not change with time. In contrast, Fick's second law is used to describe non-steady-state diffusion processes, making it more suitable for physical systems in which concentration gradients evolve over time, which can be written as Eq.(4.8) [229].

$$\frac{dc}{dt} = D \frac{d^2c}{dx^2} \quad (4.8)$$

where $\frac{dc}{dt}$ is represents the rate of change of concentration in a certain area, D is the diffusion coefficient, $\frac{d^2c}{dx^2}$ is represents the spatially rate of change in concentration curvature. For multi-component alloy systems, Zhang et al. [230] proposed the governing Fick's law equation for solute transfer in "n" alloy system.

$$\frac{\partial c_{\phi}^i}{\partial t} = \nabla \cdot \left(\sum_{j=1}^{n-1} D_{ij,n}^n \nabla c_{\phi}^j \right) + (c_L^i - c_S^i) \frac{\partial f_S}{\partial t} \quad (i = 1 \dots n - 1) \quad (4.9)$$

where c_{ϕ}^i and c_{ϕ}^j are the concentrations of the solute elements i and j in phase ϕ (ϕ take L for the liquid phase or S for the solid phase, respectively), and n is the number of elements. The n^{th} element is chosen as the solvent. $\frac{\partial f_S}{\partial t}$ represents the rate of change of the solid fraction f_S with respect to time t . $D_{ij,n}^n$ is the element of the diffusivity matrix for phase ϕ . It is calculated as follows (the subscript ϕ has been omitted for simplicity):

$$D_{ij}^n = D_{ij}^V - D_{in}^V \quad (4.10)$$

$$D_{ij}^V = \sum_{k=1}^n (\delta_{ki} - x_i) x_k M_k \frac{\partial \mu_k}{\partial x_j} \quad (4.11)$$

where D_{ij}^V is the diffusion coefficient in terms of the volume fixed reference frame, δ_{ki} is the Kronecker delta ($\delta_{ki} = 1$ if $i = k$, otherwise $\delta_{ki} = 0$), x_k and M_k are the mole fraction and atomic mobility of element k in a given phase, μ_k is the chemical potential of element k . Considering in a ternary system [230], Eq.(4.9) can be written as:

$$\frac{\partial c_i}{\partial t} = \frac{\partial}{\partial z} \left(D_{i1}^3 \frac{\partial c_1}{\partial z} \right) + \left(D_{i2}^3 \frac{\partial c_2}{\partial z} \right) + (c_L^k - c_S^k) \frac{\partial f_s}{\partial t} \quad (i = 1, 2) \quad (4.12)$$

where c_i denotes the mole fraction of component i , z is the diffusion distance, and t is the diffusion time. D_{11}^3 and D_{22}^3 are main interdiffusion coefficients, D_{12}^3 and D_{21}^3 the cross interdiffusion coefficients. D_{12}^3 and D_{21}^3 reflect the effect of concentration gradients of element 2 on the fluxes of element 1 and of element 1 on the fluxes of element 2 in sequence.

In addition, Andersson and Ågren proposed a simulation method using atomic mobility to simulate diffusion reactions in multi-component alloys according to diffusion mobility and thermodynamic factors, which has been incorporated into the DICTRA model in Thermo-Calc software [205,231]. In this theory, it is assumed that the diffusive flux of an element depends on the diffusivity and concentration gradient, and the diffusivity is a function of the atomic mobility and the thermodynamic driving force, which is expressed in Eq.(4.13).

$$D_{kj} = x_k M_k \frac{\partial \mu_k}{\partial x_j} \quad (4.13)$$

where D is the diffusivity, j is the diffusing component, k is the gradient component, $\frac{\partial \mu_k}{\partial x_j}$ is the thermodynamic factor, M_k is the atomic mobility of k , and D_{kj} is diffusion distance.

This diffusion model DICTRA of Thermo-calc software, which can be used to calculate the homogenization process within the alloy and the diffusion between different alloys, etc., and has achieved important applications in the heat treatment process of metals. In this study, the simulation of homogenised heat treatment will be carried out by DICTRA, and the distributions of the second phase and the concentration changes with time which diffuse into the primary phase by solid-solid diffusion can be studied by combining with the solute segregation parameters obtained from the Scheil model mentioned above. In this study, DICTRA is employed to describe two diffusion scenarios: (1) self-diffusion of chemistry within the matrix phase, and (2) diffusion across a moving phase boundary between the matrix and the second phase. These two mechanisms play crucial roles in the

homogenisation and phase transformation processes. The theoretical basis for these two types of diffusion models is described as follows:

1. Self-diffusion

For the self-diffusion process in matrix phase, isothermal system, the flux J_k of component k along the z -direction is governed by the gradient of its chemical potential and expressed as:

$$J_k = \sum_{i=1}^n L_{ki} \frac{\partial \mu_i}{\partial z} \quad (4.14)$$

where L_{ki} is the kinetic coefficient matrix and μ_i is the chemical potential of component i . In practice, cross-coupling terms (i.e., correlation effects with $L_{ki} = 0$ for $k \neq i$) are often neglected, reducing the expression to:

$$J_k = L_{kk} \frac{\partial \mu_k}{\partial z} = M_k c_k \frac{\partial \mu_k}{\partial z} \quad (4.15)$$

where, M_k represents the atomic mobility and c_k is the concentration of component k . This flux equation is coupled with the continuity equation for conservation of mass, which in planar form becomes:

$$\frac{\partial c_k}{\partial t} = \frac{\partial}{\partial z} (-J_k) \quad (4.16)$$

This formulation describes the local temporal evolution of c_k as a result of flux divergence. The flux can be further expanded using the chain rule in terms of concentration gradients of all components:

$$J_k = - \sum_{i=1}^n M_k c_k \frac{\partial \mu_k}{\partial c_j} \frac{\partial c_j}{\partial z} = - \sum_{i=1}^n D_{kj} \frac{\partial c_j}{\partial z} \quad (4.17)$$

where D_{kj} is the effective diffusion coefficient of component k with respect to the concentration gradient of component j , given by:

$$D_{kj} = M_k c_k \frac{\partial \mu_k}{\partial c_j} \quad (4.18)$$

This approach allows for accurate simulation of multicomponent diffusion in the matrix under the assumption of a stationary phase interface.

2. Moving phase boundary diffusion

The moving phase boundary model assumes local equilibrium at the interface, the chemical potentials of all components are continuous across the phase boundary, although their gradients may be discontinuous. Mass balance across the moving interface requires the following condition:

$$v^{\alpha/\beta} (c_k^\beta - c_k^\alpha) = J_k^\alpha - J_k^\beta \quad \text{for } k = 1, \dots, n - 1 \quad (4.19)$$

where v is the interfacial velocity, c_k^α and c_k^β are the concentrations at the α and β sides of the interface, and J_k^α and J_k^β are the corresponding fluxes.

In binary systems, the interface concentrations can be obtained directly from phase diagrams, and the interfacial velocity can be calculated once the fluxes are known. However, for ternary or higher-order systems, the interface state must be resolved through iterative numerical procedures due to additional degrees of freedom. This model allows DICTRA to simulate complex diffusion-controlled transformations and interface migration in multi-phase systems, which is essential for accurately predicting microstructural evolution during homogenisation. For further theoretical treatment and numerical implementation of this approach, refer to works by Ågren [205], Crusius et al. [232], and Höglund et al. [233].

4.2 Mean-field Theory

The mean-field model assumes that the precipitates or grains can be approximated by simplistic shapes, such as spheres, cubes or cylinders. The key attribute of mean-field approach is that the solute depletion surrounding each precipitate is averaged over the whole matrix, which is then represented as a single mean field with one average composition. This average composition evolves dynamically as the precipitate volume fraction increases. For the modelling of solidification, the lines are then discretised into a series of evenly spaced nodes, each of which is assigned a composition. For the modelling of diffusion, this composition can be a predicted value based on Schiel's calculations of chemical segregation during liquid phase cooling, or a predicted value based on measurements of the segregated composition of the alloy using SEM and EPMA. In the modelling of precipitation, this composition is assigned as the nominal composition of the alloy system.

In this study, the model assumes that only local diffusion on a microscopic scale occurs. This means that element rearrangements may occur within each node to facilitate phase transformations, but there is no diffusion between nodes. Therefore, although the model simulates each node, the logic of the model can be simplified to a single node and remains the same.

The model simulates the heat treatment process. The method used is linear interpolation of the temperature between predefined time-temperature points. In this application, the temperature is linearly increased from room temperature to the heat treatment temperature, held for the same time as the experimental sample, and then quickly reduced back to room temperature. Another assumption of the model is that the temperature at each point within the grain instantaneously reaches the heat treatment temperature, and that there is no thermal gradient throughout the sample. This assumption is considered valid given the relatively small size and high thermal conductivity of the sample on a microscopic scale.

4.2.1 Thermodynamic preparatory calculations

Thermodynamic and kinetic variables are key input variables to the mean-field model. While some values, such as interfacial energies and nucleation site concentrations are considered unknown and can be changed when calibrating the model within reasonable bounds, other variables can be calculated from the TCMG6 and MOBMG1 databases as well as the CALPHAD method [192,223].

It is convenient to calculate information regarding the equilibrium properties of the precipitate phases of interest [204]. The values extracted include the solvus temperature for each precipitate as well as the equilibrium value volume fraction, precipitate composition, phase chemical potential, and matrix diffusivity as a function of temperature. The mean-field model requires these values to be known outside of the precipitation stabilization range to capture dissolution kinetics. The equilibrium properties can be fine-tuned to improve accuracy through an energy contribution to the Gibbs free energy of the precipitate phases.

To save calculation time, the thermodynamic and mobility terms which required from mean-field model can be implement by using surrogate models in Eq.(4.20) and Eq.(4.21), the teams will introduce in following chapter 4.2.2.

$$\Delta G_c = \sum_{i=1}^n c_{ki} (\mu_{ki} - \mu_{0i}) \quad (4.20)$$

$$\theta = \frac{AR_gT}{2\sigma} = \left[\sum_{i=1}^n \frac{(c_{ki} - c_{0i})^2}{c_{0i}D_{0i}} \right]^{-1} \quad (4.21)$$

Applying the results of the surrogate model to each node of the mean-field model (each of which may have a unique composition) assumes that these values are independent of temperature. This is clearly an inaccurate assumption, since composition is a key variable in phase stability, diffusivity, and the presence of phases. However, if it is assumed that compositional variations between nodes are small (which is the same assumption made when diffusion between nodes is not taken into account), then the assumption is simplified to one that these variables are insensitive to compositional variations over a small range.

4.2.2 Mean-field Model

The spatial distribution of precipitates is influenced by local thermodynamic conditions that directly govern nucleation, growth, and dissolution of particles. Tracking the statistics of precipitate dispersion (i.e., volume fraction, particle size, number density) during complex thermo-mechanical histories is of practical importance. A highly effective method for this is the mean-field theory of precipitation. In this framework, the growth of a precipitate is driven by interfacial energy and the diffusion of chemical species toward or away from the particle. The precipitates are embedded in a matrix with an average or mean composition field. Changes in precipitate statistics are determined by solving a continuity equation for the particle size distribution. Strictly speaking, the mean-field approximation assumes low precipitate volume fractions, meaning weakly interacting diffusive fields between particles. For the magnesium alloy systems investigated in this study, the mean-field assumption is a reasonable approximation.

4.2.2.1 Continuity

The particle size distribution function $F(R, t)$ is defined such that the number of particles per volume at a time t with sizes lying in the interval R to $R + dR$ is given by $F(R, t)dR$. Key dispersion parameters can be calculated directly from the moments of $F(R, t)$. For example, the number of particles per volume, mean particle size and volume fractions are the zeroth, first and third moments of the particle size distribution:

$$N(t) = \int_0^{\infty} F(R, t) dR \quad (4.22)$$

$$\bar{R}(t) = \int_0^{\infty} RF(R, t) dR / \int_0^{\infty} F(R, t) dR \quad (4.23)$$

$$\phi(t) = \frac{4\pi}{3} \int_0^{\infty} R^3 F(R, t) dR \quad (4.24)$$

where $N(t)$ is the number density, \bar{R} the mean particle radius and ϕ the volume fraction. The Gibbs-Thompson effect will drive growth/dissolution of precipitates during the coarsening stage of precipitate evolution. Prior to this, it is the supersaturated solute and resultant composition gradients from the matrix to the precipitate interface that control growth. If each particle has a rate $\dot{R} = V(R, t)$, this will change the particle size distribution. To ensure $F(R, t)$ does not develop discontinuities a continuity condition must be imposed. This results in an advective differential equation for $F(R, t)$. Source and sink rate terms can be included to account for nucleation and dissolution rates $\mathcal{F}^+(R, t)$ and $\mathcal{F}^-(R, t)$, respectively. The continuity equation for the particle size distribution is given by:

$$\frac{\partial F(R, t)}{\partial t} + \frac{\partial [F(R, t)V(R, t)]}{\partial R} = I = \mathcal{F}^+(R, t) - \mathcal{F}^-(R, t) \quad (4.25)$$

Particle evolution over time is predicted through temporal integration of the continuity equation. It is a conserved system where particles cannot be gained or lost, unless through nucleation or dissolution events [126]. In the model applied dissolution is controlled by a boundary condition limiting the minimum radius rather than calculating the sink rate explicitly.

4.2.2.2 Growth

The growth rate in this equation $V(R, t)$ [234] is a function of the surface energy, diffusion across the precipitation boundary, the precipitation radius and the critical radius R_c , and the precipitation radius and the critical radius. It can be shown that the growth rate is a quadratic function of the curvature, and for spherical particles, can be expressed in terms of the particle radius as:

$$V(R, t) = \frac{A(t)}{R(t)} \left(\frac{1}{R_c(t)} - \frac{1}{R(t)} \right) z(R, t) \quad (4.26)$$

$$z(R, t) = 1 + R(t) \sqrt{4\pi N_v(t) \bar{R}(t)} \quad (4.27)$$

The correction factor $z(R, t)$ has been developed account for overlapping depletion zones [126,234]. The driving force for the growth of spherical particles can be expressed by the Gibbs free energy ΔG in following equation

$$\Delta G = \Delta G_s + \Delta G_v = 4\pi R^2 \gamma + \frac{4\pi}{3} R^3 \Delta G_c \quad (4.28)$$

where ΔG_s is surface energy and ΔG_v is volume energy. The relationship between the change in free energy and the particle radius is shown in the Figure 2.10. The critical radius of a particle is the smallest size at which it is thermodynamically stable. Below the critical radius, clusters are not large enough to initiate the nucleation process. Above the critical radius, particles will form and grow. From Figure 2.10 we can calculate the critical radius R_c by differentiating Eq. (2.17) to zero, then.

$$R_c = -\frac{2\gamma}{\Delta G_c} \quad (4.29)$$

where ΔG_c is Chemical driving force, γ is interfacial energy. Chemical driving force can then be derived from the particle composition and the chemical potentials and summing over all component elements, and is affect by the misfit strain energy U [234]. With these considerations, ΔG_c can be expressed as:

$$\Delta G_c = U + \sum_{i=1}^n c_{ki} (\mu_{ki} - \mu_{0i}) \quad (4.30)$$

$$U = \frac{\varepsilon^2 E}{1 - \nu} \quad (4.31)$$

where ε is misfit strain, E is Young's modulus, ν is Poisson's ratio, c_{ki} is molar concentrations of the i th alloying element in the particle phases. μ_{ki} and μ_{0i} refer to the chemical potentials of the precipitate and matrix phases considering the i th alloying element.

The diffusion across the precipitate interface is described by term $A(t)$. This variable is dependent on the effective diffusivity within the matrix, and the precipitates interfacial energy γ . The mean-field coarsening simulation is highly sensitive to define the interface energy γ . The interfacial energy γ is determined by the broken bonds separating the matrix and precipitate, and is thus a function of temperature and chemical composition [235,236], which can be obtained by fitting models' approximation [237,238], from thermodynamics [239], or first-principal

calculations [240]. The θ term arises from the matrix and precipitate compositions and diffusivity data extracted in the surrogate model.

$$A(t) = \frac{2\gamma}{R_g T} \theta \quad (4.32)$$

$$\theta = \left[\sum_{i=1}^n \frac{(c_{ki} - c_{0i})^2}{c_{0i} D_{0i}} \right]^{-1} \quad (4.33)$$

where c_{ki} and c_{0i} is molar concentrations of the i th alloying element in the particle and matrix phases, respectively. The diffusivity of the i th alloying element within the matrix is given by D_{0i} .

For non-spherical particles, the shape factor needs to be introduced into the calculation of the growth rate. The shape factor S_k and O_k is determined by Kozeschnik et al. [241] based on the aspect ratio h of the particles.

$$S_k = 0.2912h^{\frac{2}{3}} + 0.5824h^{-\frac{1}{3}} \quad (4.34)$$

$$O_k = 0.881h^{-0.122}$$

By applying this shape factor S_k and O_k , the critical radius R_c from Eq. (2.18), and $A(t)$ from Eq. (4.32) can be written as.

$$R_c = -\frac{2\gamma S_k}{\Delta G_c} \quad (4.35)$$

$$A(t) = \frac{2\gamma S_k}{R_g T O_k} \theta \quad (4.36)$$

4.2.2.3 Nucleation

Nucleation is treated using classical nucleation theory, and the transient nucleation rate is given by the following equation [242].

$$\mathcal{F}^+(R, t) = Z\beta^*(t)N_c(R, t) \exp\left(\frac{-\Delta G^*}{k_b T}\right) P_{inc} \quad (4.37)$$

where Z is the Zeldovich parameter, $\beta^*(t)$ is atomic attachment rate, $N_c(R, t)$ is nuclei radius distribution function, ΔG^* is energy barrier to nuclei formation, k_b is Boltzmann constant, and P_{inc} is nuclei incubation probability.

The Zeldovich parameter Z accounts for the likelihood that nuclei that are approaching a stable radius dissolve rather than grow to form a precipitate. It is a function of the gradient of change in free energy with radius in the region of thermal variation around the critical radius [243]. It is dependent on the atomic volume Ω , inter-facial energy γ and the critical radius R_c [203,234,243].

$$Z = \sqrt{\frac{\Omega^2 \gamma}{4\pi^2 k_B T R_c^4}} \quad (4.38)$$

where k_b is Boltzmann constant, R_c is critical particle radius. The atomic attachment rate β^* can be divided into two components [203,234,244]. The number of available sites on the precipitate surface is dependent on the critical precipitates surface area ($4\pi R_c^2$ for a spherical approximation) and the atomic density, described by Avogadro's number and the density [203] or the lattice parameter a and the molar volume V_m [244]. The attachment rate of atoms to the surface can be related to the θ term employed in the growth rate Eq. (4.33).

$$\beta^* = \frac{4\pi R_c^2}{a^4 V_m} \theta \quad (4.39)$$

$$\theta = \left[\sum_{i=1}^n \frac{(c_{ki} - c_{0i})^2}{c_{0i} D_{0i}} \right]^{-1} \quad (4.40)$$

The nuclei concentration density N_c is approximated to a Gaussian waveform [234]. This distribution is dependent on two factors: the thermal variation of radius around the critical point R_c and the number concentration of nuclei N_0 . δ is the variance of the nuclei size distribution, which can be calculated from the Zeldovich factor by Eq. (4.38), and atomic volume Ω . N_0 is dependent on the volume fraction $\phi(t)$, the equilibrium value ϕ_{eq} of which is extracted in the surrogate model. Additionally, it contains the fraction of active nucleation sites η which vary depending upon the location where the precipitates nucleate.

$$N_c(R, t) = \frac{N_0}{\delta \sqrt{2\pi}} \exp\left(-\frac{1}{2} \left(\frac{R - R_c(t)}{\delta}\right)^2\right) \quad (4.41)$$

$$N_0 = \eta \frac{3(\phi_{eq} - \phi(t))}{4\pi R_c^3} \quad (4.42)$$

$$\delta = \left(\frac{3\Omega}{2(\pi)^2} \frac{1}{Z} \right)^{\frac{1}{3}} \quad (4.43)$$

The energy barrier of nucleation can describe as ΔG^* in following equation,

$$\Delta G^* = \frac{1}{\psi^3} \frac{16\pi}{3} \frac{\gamma^3}{(\Delta G_c)^2} \quad (4.44)$$

where ψ is the sphericity of the nuclei, can be written as,

$$\psi = \frac{(3\sqrt{\pi} V_p)^{\frac{2}{3}}}{A_p} \quad (4.45)$$

where V_p and A_p refer to the particle volume and surface area, respectively.

To describe nucleation during a complex thermal cycle, an incubation probability P_{inc} is introduced. The incubation probability describes the likelihood that stable nuclei have formed. P_{inc} is defined as the ratio of the current nuclei concentration divided by the steady state nuclei concentration. τ is defined as incubation time.

$$P_{inc}(t, T, \theta, R_c, \gamma) = \exp\left(\frac{-\tau}{t}\right) = \exp\left(-\frac{1}{t} \frac{k_b T R_c^2}{2\theta\gamma a^2}\right) \quad (4.46)$$

where k_b is Boltzmann constant, R_c is critical particle radius, θ is attachment rate in Eq. (4.40). γ is interfacial energy, a is lattice parameter, T is temperature.

To describe non-isothermal conditions an equivalent time is introduced. The equivalent time t_{eq} , is obtained by rearranging the incubation probability for time,

$$t_{eq} = -\frac{\tau}{\ln(P_{inc})} \quad (4.47)$$

where $0 < P_{inc} < 1$. The temporal derivative,

$$\frac{dP_{inc}}{dt} = \frac{\partial P_{inc}}{\partial t} + \frac{\partial P_{inc}}{\partial T} \frac{dT}{dt} + \frac{\partial P_{inc}}{\partial \theta} \frac{d\theta}{dt} + \frac{\partial P_{inc}}{\partial R_c} \frac{dR_c}{dt} + \frac{\partial P_{inc}}{\partial \gamma} \frac{d\gamma}{dt} \quad (4.48)$$

Making use of the chain rule, the derivative of the incubation probability can be expressed as following equation,

$$\frac{dP_{inc}}{dt} = \frac{\tau}{t_{eq}} P_{inc} \left[\frac{1}{t_{eq}} + \left(\frac{1}{\theta} \frac{d\theta}{dT} - \frac{2}{R_c} \frac{dR_c}{dT} + \frac{1}{\gamma} \frac{d\gamma}{dT} - 1 \right) \frac{dT}{dt} \right] \quad (4.49)$$

4.3 Mechanical Properties Model

A useful approximation for estimating the strength of a material is to express it as the sum of contributions from distinct microstructural features and strengthening mechanisms. In metallic alloys, the overall yield strength σ typically arises from multiple sources, including the intrinsic strength of the matrix σ_0 , solid solution strengthening σ_s , grain boundary strengthening σ_g , precipitation strengthening σ_p , dislocation strengthening σ_d , and texture strengthening σ_t [245,246]. In samples that have undergone ageing treatment, the contributions from intrinsic strength σ_0 , grain boundary effects σ_g , dislocation effects σ_d , and texture effects σ_t remain stable. Solid solution strengthening σ_s is caused by lattice misfit of alloying elements, which hinders dislocation movement. The strengthening contribution depends on the concentration of alloying elements C_i and the solid solution strengthening coefficient of alloying elements k_i , which is expressed in the Eq. (4.50) [247]. Alloying elements that exceed the solubility limit can form second phase particles, which results in strengthening by precipitation. The strengthening contribution of the precipitated phase σ_p depends on the deformation mechanism of the interaction between dislocations and the precipitated phase, which are the shear and Orowan bowing mechanisms, respectively, and depends on the size of the precipitated phase. When the precipitates are in the early stages of ageing treatment, which is usually defined as a weak coherent precipitate, precipitate shearing is the main deformation mechanism. As the precipitates grow and coarsen, the weak coherent precipitates become strong incoherent precipitates, and Orowan bowing becomes the main deformation mechanism [248]. When the type and size of the precipitates are different, the strengthening of the precipitates can be expressed by the following equation.

$$\sigma_s = \sum_i k_i \sqrt{C_i} \quad (4.50)$$

$$\sigma_p = \sum_i \sigma_{p,i} \quad (4.51)$$

By comparing different strengthening mechanisms, the solid solution strengthening and weak precipitates strengthening are generally weaker than those of strong precipitates strengthening [249]. Therefore, in the ageing treatment process, the increase in material strength depends largely on the precipitation strengthening. The yield strength σ_{ys} from Orowan mechanisms can be described in following equation [250,251],

$$\tau_{ys} = \frac{G_s b}{\lambda} \quad (4.52)$$

$$\sigma_{ys} = M\tau_{ys} \quad (4.53)$$

where τ_{ys} is shear yield stress, G_s is shear modulus, b is Burger's vector, λ is the mean interparticle spacing and M is the Taylor factor. The mean particle spacing will be taken to be the lattice square spacing λ , which is given by [252],

$$\lambda = 1.6R \left(\sqrt{\frac{\pi}{4\phi}} - 1 \right) \quad (4.54)$$

where R is the radius of strong precipitate particle, ϕ is the volume fraction of strong precipitate particles. In a multi-dispersion alloy system with i th multiple second phase particles, the effective lattice square spacing λ can be written as,

$$\frac{1}{\lambda} = \sum_i \frac{1}{\lambda_i} \quad (4.55)$$

As described in the chapter 4.2.2, the Mean-field model can predict the nucleation, growth and coarsening of a wide range of precipitated particles in a multi-component system. Thus, the desired mean particle size \bar{R} and volume fraction of precipitates ϕ in Eq. (4.54) can be obtained from Eq. (4.23) and Eq. (4.24), respectively. The mechanical property model simulates the contribution of a variety of strong precipitates to the alloy precipitation strengthening in the Orowan mechanism. Considering the strong correlation between yield strength and hardness response in magnesium alloys [253], the model can be validated by measuring the experimental results of hardness at different ageing times and comparing them with the model predictions at the same thermal parameters.

$$Hv \propto \sigma_{ys} \quad (4.56)$$

Chapter 5: Numerical Implementation

5.1 Finite Difference Method (FDM)

The finite element method (FEM) is a common method for numerically solving differential equations that arise in engineering modelling, with typical problem areas containing heat transfer and mass transfer. The finite element method constructs a mesh of objects by discretizing a specific space, subdividing large systems into smaller parts with a finite number of points. The original complex system of equations is reduced to a system of unit equations within each subdomain, and an approximate solution to the original system of equations is derived by combining each unit equation [254]. The advantage of the finite difference method (FDM) over the finite element method (FEM) is that it is easier to perform numerical simulations when dealing with simple geometries (e.g., rectangles) [255]. This chapter focuses on the numerical implementation of the FDM framework. It starts with a description of the differential methods used to solve the continuity equation. The simulation setup is then described, giving the scenarios for applying the FDM model and the order are calculated in the following equations. The integration of the FDM code with the TQ-Fortran interface in the commercial CALPHAD software Thermo-Calc is then described. The FDM model includes the setting of the square simulation domain, the setting of the temperature and composition, the relationship between temperature and thermodynamic parameters and how they interact, and the setting of boundary conditions. Finally, the key thermodynamic parameters used in the simulation are listed.

The finite difference method is derived through the manipulation of Taylor series to obtain approximations of derivatives. A Taylor series is a method of approximating a function using a polynomial. The following equation describes a Taylor series considering a forward difference of h ,

$$f(x + h) = f(x) + \frac{\partial f}{\partial x} h + \frac{1}{2!} \frac{\partial^2 f}{\partial x^2} h^2 + \frac{1}{3!} \frac{\partial^3 f}{\partial x^3} h^3 + \dots + \frac{1}{n!} \frac{\partial^n f}{\partial x^n} h^n \quad (5.1)$$

We can rearrange this equation for first derivative $\frac{\partial f}{\partial x}$,

$$\frac{\partial f}{\partial x} = \frac{f(x + h) - f(x)}{h} + \frac{1}{2!} \frac{\partial^2 f}{\partial x^2} h + \frac{1}{3!} \frac{\partial^3 f}{\partial x^3} h^2 + \dots + \frac{1}{n!} \frac{\partial^n f}{\partial x^n} h^{n-1} \quad (5.2)$$

We can group the remaining terms into a term descriptive of the error,

$$\frac{\partial f}{\partial x} = \frac{f(x+h) - f(x)}{h} + \mathcal{O}(h) \quad (5.3)$$

For the sample solidification process in Figure 3.1, it can be approximated as a one-dimensional heat transfer process from the sample surface to the sample centre as shown in Figure 5.1a. The one-dimensional heat transfer model is meshed so that it is divided into line segments for space difference consisting of n nodes, and the i th node is selected and denoted by u_i in Figure 5.1b.

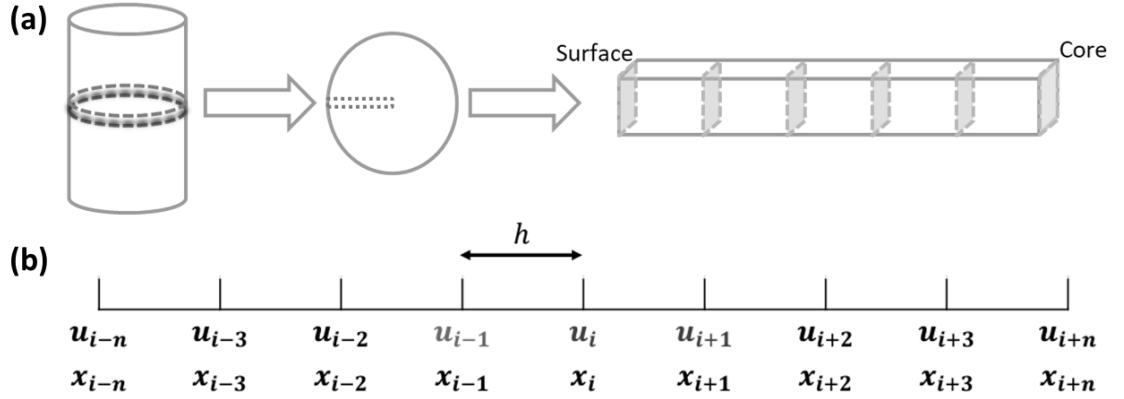


Figure 5.1 (a) One-dimensional heat transfer approximation of a three-dimensional cylindrical billet from surface to core solidification process. (b) Space difference in One-dimensional heat transfer model

From Eq. (5.3), the finite difference model in one dimension can also write as,

$$\frac{\partial u_i}{\partial x} = \frac{u_{i+1} - u_i}{h} + \mathcal{O}(h) \quad (5.4)$$

$$\frac{\partial u_i}{\partial x} = \frac{u_{i+1} - u_{i-1}}{2h} + \mathcal{O}(h^2) \quad (5.5)$$

$$\frac{\partial^2 u_i}{\partial x^2} = \frac{u_{i+1} + 2u_i - u_{i-1}}{2h} + \mathcal{O}(h^2) \quad (5.6)$$

In the one-dimension heat transfer problems, the temperature is variant with time as well, so the finite difference of time t need to be set up in Figure 5.2. Let, $u_i^p(x, t)$ refer to $u(x, t)$ at x_i and t_p where we have discretized space and time into intervals of Δx and Δt , then we have following equation,

$$\frac{\partial u_i}{\partial x} = \frac{u_{i+1}^p - u_i^p}{\Delta x} + \mathcal{O}(h) \quad (5.7)$$

$$\frac{\partial u_i}{\partial t} = \frac{u_i^{p+1} - u_i^p}{\Delta t} + \mathcal{O}(h) \quad (5.8)$$

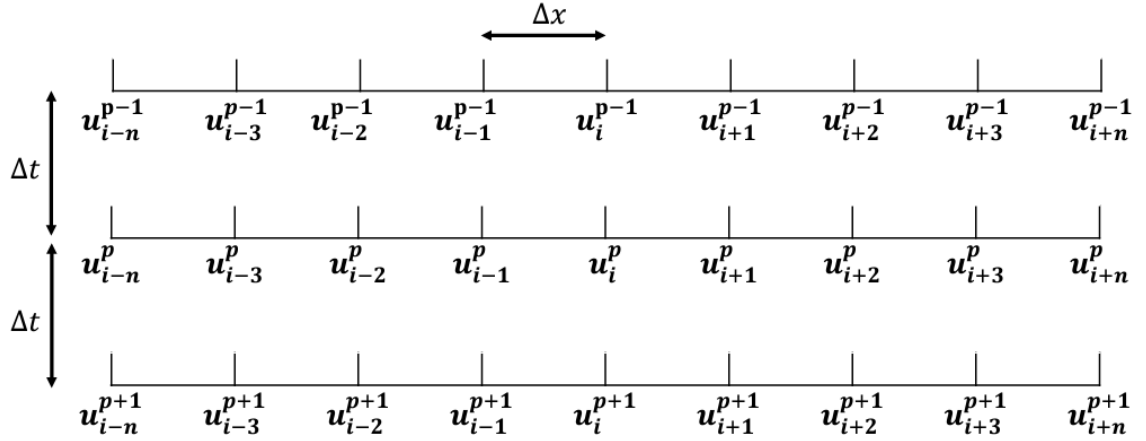


Figure 5.2 Space and time difference in One-dimensional heat transfer model

For the one-dimensional heat transfer model, focus on the temperature change of the node with the known initial temperature and boundary conditions. The surface of the sample exchanges heat with the environment by convection and radiation. For the one-dimensional heat transfer model, it is required to focus on the temperature change of the node with the known initial temperature and boundary conditions. The surface of the sample exchanges heat with the environment through convection and radiation, as described in section 2.6. The interior of the sample mainly relies on heat conduction, and heat is generated through latent heat or chemical reactions, as shown in Eq. (5.9). The heat flow on the surface of the sample is generated from conduction, convection, radiation, latent heat, and chemical reactions, as shown in Eq. 10.

$$\rho C_p \frac{\partial T}{\partial t} - k \frac{\partial^2 T}{\partial x^2} - \frac{\partial k}{\partial x} \frac{\partial T}{\partial x} = 0 \quad (5.9)$$

$$\text{sum of heat fluxes} = \sum_{i=1}^n Q_i = m C_p \frac{dT}{dt} \quad (5.10)$$

where ρ is density, C_p is specific heat, k is thermal conductivity, m is mass, Q_i is i th heat flux from conduction, convection, radiation in Eq. (2.5), Eq. (2.6), Eq. (2.7), respectively. Let $\alpha = \frac{k}{\rho C_p}$, use 1st order forward FDM scheme for temporal derivative and second order central FDM scheme for spatial derivative, and assume negligible spatial gradients in thermal conductivity, the interior heat transfer in Eq. (5.9) can be written as,

$$\frac{T_i^{p+1} - T_i^p}{\Delta t} - \alpha \frac{\partial^2 T_i}{\Delta x^2} = 0 \quad (5.11)$$

Let $F_0 = \alpha \frac{\Delta t}{(\Delta x)^2}$, T_i^{p+1} can be written as,

$$T_i^{p+1} = T_i^p + F_0(T_{i+1}^p + T_{i-1}^p - 2T_i^p) \quad (5.12)$$

Let $B_i = \frac{\Delta x h}{k}$, the T_i^{p+1} of surface heat transfer in Eq. (5.10) can be written as,

$$T_i^{p+1} = T_i^p + F_0(B_i T_a + T_{i+1}^p - (4 + B_i)T_i^p) \quad (5.13)$$

With the FDM continuity equations described above, the heat conduction in the interior can be simulated in a one-dimensional heat transfer model, and the boundary conditions on the surface are defined as convection and thermal radiation with ambient temperature T_a . The thermal parameters applied in this one-dimensional heat transfer model listed in Table 5.1. The implementation of this model allows the simulation to plot the surface to core temperature cooling over time during solidification of magnesium alloy casting, and thus to understand the difference in cooling time of each part of the casting. It is to be noted that due to the practical solidification process, the solidified component shrinks and creates voids with the mould, which changes the boundary conditions and consequently increases the cooling time. Therefore, the model is only used as a reference to simulate the fastest time for the melt to solidify to room temperature under ideal conditions.

Table 5.1 Model parameters for heat transfer calculation

| Variable | Description | Value | Units | Reference |
|---------------|-------------------------|--------------------------------|--------|-----------------|
| k_L | Thermal conductivity | 1.651517E1 + 6.732799E-2 * | W/m/K | Thermo- Calc |
| | of liquid | T | | |
| k_α | Thermal conductivity | 1.764121E2 - 6.991883E-2 * | | |
| | of solid | T | | |
| c_{pL} | Specific heat of liquid | 1.413496E3 - 1.041345E2 * T | J/kg/K | |
| $c_{p\alpha}$ | Specific heat of solid | 8.627008E2 + 5.209875E-1 * T | | |

| Variable | Description | Value | Units | Reference |
|---------------|---------------------------|--------------------------------|---------------------|-----------------|
| ρ_L | Density of liquid | $1.834740E3 - 2.580746E-1 * T$ | kg/m ³ | Thermo- Calc |
| ρ_α | Density of solid | $1.796977E3 - 1.563678E-1 * T$ | | |
| LT | Latent heat | 3.57951E5 | J/kg | [256] |
| h | Heat transfer coefficient | 600 | W/m ² /K | [257] |
| ε | Emissivity | 0.1 | - | Fitted |
| T_a | Ambient temperature | 25 | °C | Defined |

5.2 Scheil-Gulliver Solidification Model in Ternary Alloy System

The thermodynamic database can be used to obtain information about the liquidus line, solidus line, and chemistry of the equilibrium phase for a given composition. In this study, the TCMG6 thermodynamic database was used, and the TQ FORTRAN interface in the commercial software Thermo-Calc was used for coupling to capture the corresponding thermodynamic data for different compositions. The composition range selected for this study was 0 to 12 at. % Ca and 0 to 40 at. % Zn, with a composition point taken every 0.01 at. %, and a total of 4.8 million composition points of thermodynamic parameters were collected. These composition points and the liquidus temperature are imported into the numerical model to obtain the composition and liquidus map in the Mg- Zn-Ca magnesium alloy Mg-rich corner as shown in Figure 5.3. The initial composition is allocated in node $C_{i,j}$ with the corresponding liquidus temperature $T_{i,j}$, this point is recorded as the initial point in the Scheil solidification path. Through the extended Scheil methodology described in chapter 4.1.1, the temperature difference between the four neighbouring nodes around $T_{i,j}$ is dT , the liquidus minimising Scheil need to find the point with the minimum temperature around $T_{i,j}$. If the two neighbouring points have the same dT , the temperature value at the diagonal node of the two neighbouring points are taken as the next point of the Scheil solidification path, the composition and liquidus temperature of this point have been taken as new $C_{i,j}$ and $T_{i,j}$ to repeat the calculation.

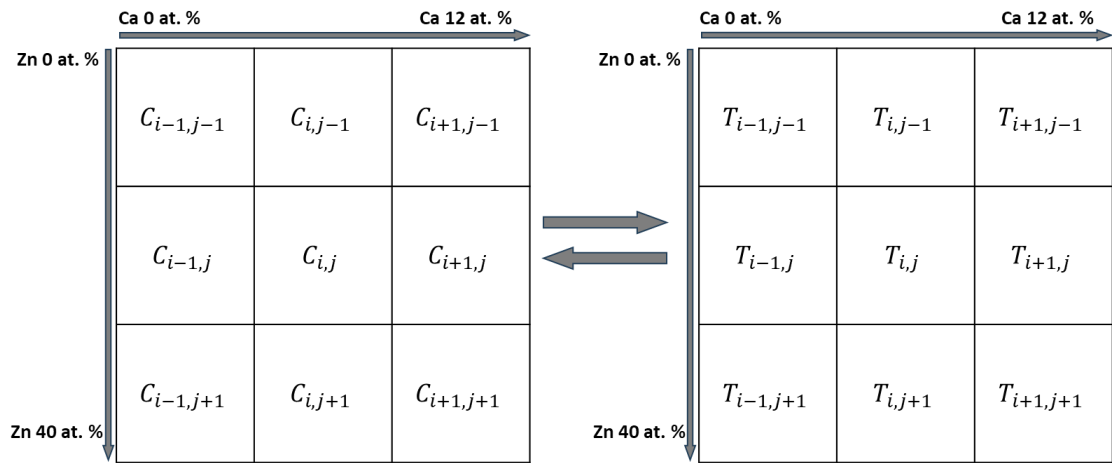


Figure 5.3 FDM model of composition and liquidus map

The liquidus minimising Scheil solidification pathway will stop when reach the boundary, which is the monovariant line. Monovariant line can be calculated by capturing thermodynamic equilibrium phases information from TCMG6 using TQ FORTRAN interface. In this study of the Mg-Zn-Ca ternary alloy, the intersection of the two monovariant lines is the ternary eutectic point. The monovariant line is also divided into n nodes, and the composition $C_{i,j}$ and liquidus temperature $T_{i,j}$ of each node are recorded. After the Scheil solidification path reaches the monovariant line, it continues in the direction of the temperature steepest decent until it ends at the ternary eutectic point.

All nodes in the solidification process are recorded and plotted as a solidification curve. Combining with the thermodynamic database TCMG6, the thermodynamic parameters at each point of the solidification curve can be obtained, thereby obtaining information such as the start and eutectic temperatures, the elemental segregation profile, and the phase fraction during solidification.

5.3 Diffusion Couple between Mg Matrix and second Phases

Diffusion-controlled phase transformations involving moving interfaces are of fundamental importance in multicomponent alloy systems. The theoretical treatment of such systems necessitates a model that accurately couples' diffusion in single-phase regions with the kinetics of interface migration. The framework described in this chapter is based on the seminal work by Ågren [258], as well as its implementation in the DICTRA software environment. It integrates thermodynamic equilibrium conditions, mass conservation principles, and advanced numerical schemes to simulate the evolution of phase boundaries with high precision.

The theoretical foundation of the moving boundary diffusion model relies on two central assumptions: local thermodynamic equilibrium at the interface and volume diffusion as the rate-controlling step. Local equilibrium implies that, at any instant, the chemical potentials (or partial Gibbs energies) of all components are equal on both sides of the interface. This allows one to define a unique set of interface compositions for each phase at the boundary. The driving force for interface migration arises not from deviations from equilibrium at the interface itself, but from the chemical potential gradients within the adjoining one-phase regions. The interface velocity is determined by the imbalance of diffusional fluxes and the difference in interfacial concentrations of the solute species. This balance is expressed as:

$$v^M (c_k^\beta - c_k^\alpha) = J_k^\alpha - J_k^\beta \quad (5.14)$$

where v^M is the interface velocity, c_k^α and c_k^β are the concentrations of component k in phases α and β at the interface, and J_k^α and J_k^β are the corresponding diffusion fluxes evaluated at the interface.

The equilibrium compositions themselves are computed from the thermodynamic description of the phases involved. If both phases contain sublattices, then the site fractions y_k^s for each component k on sublattice s must satisfy both stoichiometric constraints and equilibrium conditions. For systems where one phase is taken as a reference phase (denoted β), and the other as α , the equilibrium condition can be written in terms of partial Gibbs energies as:

$$\mu_i^\alpha = \mu_i^\beta \quad (5.15)$$

$$\frac{\partial G^\alpha}{\partial y_k^s} = \frac{\partial G^\beta}{\partial y_k^s} \quad (5.16)$$

Assuming that each component dissolves into a unique sublattice. These equations are solved numerically, often via Newton-Raphson or similar iterative methods, to determine the compositions at the interface for each timestep. The thermodynamic input for these calculations is typically derived from CALPHAD-based databases (TCMG6 and MOBGM1 in this study), which provide consistent Gibbs energy models for multicomponent phases [259]. The DICTRA tools are structured into modular components, including a preprocessor to define thermodynamic and mobility data, a

monitor for user interaction and control, a calculation engine for time stepping and interface tracking, and a postprocessor for data visualisation. The integration with thermodynamic packages such as the Gibbs Energy System (GES) allows the software to automatically evaluate chemical potentials and phase equilibria. In summary, the numerical simulation of moving boundary diffusion involves a tightly coupled solution of thermodynamic equilibrium conditions, flux balance at interfaces, and diffusion equations in one-phase regions. By discretising the spatial domain using finite elements and integrating in time with stable implicit schemes, the evolution of composition and interface position can be accurately predicted.

5.4 Mean-field Model

The mean-field model simulates the evolution of particles during solid-state heat treatment. The required thermodynamic and kinetic FORTRAN code uses the TQ FORTRAN interface of Thermo-Calc. A surrogate model in section 4.2.1 is generated using the TCMG6 and MOBMG1 databases. This model assumes that all particles have a similar composition and that their composition can be approximated by the equilibrium composition at the relevant temperature.

To run a simulation of the evolution of a dispersion of particles it is necessary to know the initial particle size distribution, material composition and the heat treatment parameters. The pre-processing includes generating thermodynamic and mobility data, creating an initial particle size distribution, the required temperature history, and inputting material parameters and simulation controls into the input key files. The material parameters for pre-processing are shown in

Table 5.2. The solver has been coded with an algorithm that runs a series of heat treatments using the initial particle size distribution and material parameters, as shown in Figure.5.4. The solver loads this information and calculates the change in particle size distribution during the heat treatment. The material parameters for the solver are shown in Table 5.3. The postprocessor then loads the generated prediction results and plots the particle size distribution. If no experimental data are available, the initial particle size distribution (PSD) is assumed to follow a Weibull distribution. This synthetic PSD defines the starting nuclei population, obtained by discretising the particle radius into bins and sampling the number density from the Weibull probability density, with the total particle volume fraction constrained by the surrogate model limits.

In order to reduce computational time, the thermodynamic and mobility terms Eq. (4.30) and Eq. (4.33) required by the mean-field model have been implemented using surrogate models. The behaviour expressed by these terms is most accurately captured by dividing kinetics into growth, sub-solvus dissolution or super-solvus dissolution states. Temperature is normalised by the solubility temperature $\Gamma = T/T_s$, term φ can describe the normalized volume fraction with following equation Eq. (5.17) and Eq. (5.18) to express growth φ_g and dissolution φ_d condition, where ϕ_{max} refers to the maximum volume fraction that can be attained prior to the complete partitioning of the element into the matrix or particle phase, assuming that the particle composition is in equilibrium, which can be used to interpolate the ΔG_c and θ in surrogate model in section 4.2.1.

$$\varphi_g = \phi/\phi_{eq} \quad (5.17)$$

$$\varphi_d = (\phi - \phi_{max})/(\phi_{max} - \phi_{eq}) \quad (5.18)$$

The numerical method for solving the continuity equation Eq. (4.25) must be able to handle the divergence of the velocity field as the particle size approaches zero. The fastest and most accurate scheme is the explicit Hamilton-Jacobi ENO scheme proposed by Osher and Fedkiw [260]. Baris Sumengen's implementation is based on this method and is adjusted to describe the coarsening dynamics of the particles in the mean field [261]. The method provides a third-order accurate approximation of the spatial derivative from the first-order accurate upwind difference. In the continuity equation Eq. (4.25) spatial derivatives, the normalised number frequency density, F of particles can be expressed in terms of the volume fraction frequency density, g in Eq. (5.19), where the term g_v occurs

and is described by u . Let the g_v in Eq. (5.19) be described by u , and the second-order accurate central difference is described by Eq. (5.5) as D_i^0, u is showing in Eq. (5.20),

$$\partial g(R, t) dr \equiv \frac{4\pi}{3} \partial F(R, t) r^3 dr \quad (5.19)$$

$$\frac{\partial g}{\partial t} + \frac{\partial(g_v)}{\partial r} = \frac{3}{r} g_v + \frac{4\pi r^3}{3} I$$

$$D_i^0, u \approx \frac{u_{i+1} - u_{i-1}}{2\Delta r} \quad (5.20)$$

The first divided difference $D_{i+\frac{1}{2}}^1, u$ can be calculated from D_i^0, u , and second divided difference D_i^2, u can be calculated from $D_{i+\frac{1}{2}}^1, u$, and then the following third divided difference $D_{i+\frac{1}{2}}^3, u$ can be calculated from D_i^2, u in following equation,

$$D_{i+\frac{1}{2}}^1, u \approx \frac{D_{i+1}^0, u - D_i^0, u}{\Delta r}$$

$$D_i^2, u \approx \frac{D_{i+\frac{1}{2}}^1, u - D_{i-\frac{1}{2}}^1, u}{2\Delta r} \quad (5.21)$$

$$D_{i+\frac{1}{2}}^3, u \approx \frac{D_{i+1}^2, u - D_i^2, u}{3\Delta r}$$

The particle size derivative can be calculated from,

$$\frac{\partial u}{\partial r} = Q'_1 + Q'_2 + Q'_3 + \mathcal{O}(h^3) \quad (5.22)$$

where Q'_1, Q'_2, Q'_3 are the coefficients determined from the first, second and third divided differences. The first coefficient is given by,

$$Q'_1(x_i) = D_{k+\frac{1}{2}}^1, u \quad (5.23)$$

where k is set to $i - 1$ or i for backward or forward differencing respectively. The second and third divided differences are given by,

$$Q'_2(x_i) = c(2(i - k) - 1) \Delta r \quad (5.24)$$

$$Q'_3(x_i) = c^*(3(i - k^*)^2 - 6(i - k^*) + 2)(\Delta r)^2 \quad (5.25)$$

where c , and k^* dependent on the absolute magnitude of the second divided difference at the positions D_k^2, u and D_{k+1}^2, u . If $|D_k^2, u| < |D_{k+1}^2, u|$, k^* is set to $k - 1$ and c is set to D_k^2, u . Otherwise, k^* is set to k and c is set to D_{k+1}^2, u . c^* depends on the value of $|D_{k+\frac{1}{2}}^3, u|$, compared with $|D_{k+\frac{3}{2}}^3, u|$. If $|D_{k+\frac{1}{2}}^3, u| \leq |D_{k+\frac{3}{2}}^3, u|$, c^* equals to $D_{k+\frac{1}{2}}^3, u$, otherwise, c^* equals to $D_{k+\frac{3}{2}}^3, u$. Then, the forward first-order accurate finite difference is applied to the time derivative, which gives the following continuity equation,

$$g^{n+1} = g^n - (Q'_1 + Q'_2 + Q'_3)dt' + \frac{3}{r} g v dt' + \frac{4\pi r^3}{3} q dt' \quad (5.26)$$

where the time step dt' can be controlled by a Courant-Friedrichs-Lewy condition,

$$dt' = \min \left[\alpha \left(\frac{|v_i| + |q_i|}{\Delta r_i} \right)^{-1} \right] \quad (5.27)$$

The part of the grid spacing that does not contain a large number of particles is not included in the adaptive time step calculation.

5.4.1 Mean-field Model in Solidification

Compositional segregation occurs during rapid solidification, and for isotopically solidified single crystals, compositional segregation usually occurs at grain boundaries. The simulation domain for the Mean-field solidification model is defined as a spherical single crystal, and compositional segregation from the core to the grain boundaries follows the distribution of the Scheil segregation profile. In this study, the nominal and maximum segregation compositions were selected as input compositions, respectively, and the thermodynamic parameters under this composition were obtained by means of the surrogate model and its databases TCMG6 and MOBMG1. The input heat treatment temperature in the solidification model is a time-dependent function of the cooling profile approximated by the FDM model in Chapter 5: . It is noted that due to the uncertainty in the actual cooling time during solidification, a time range is set in this model to describe the growth and coarsening of the second phase particles on different cooling time scales. The nucleation of second phase particles depends on the fraction of active nucleation sites, which is unknown in this study, so a range of fraction of active nucleation sites is set from 1 to 10^{-15} , which unity represents homogeneous nucleation and 10^{-15} represents

extreme heterogeneous nucleation. Magnitudes of 10^{-5} are descriptive of nucleation on dislocations, and those smaller than 10^{-10} describe grain boundary nucleation sites. The amount of sites on grain boundaries can vary if the precipitate forms on grain boundary edges, or corners. In addition to this, the growth of the second phase particles is approximately spherical to maximise the growth rate, so there is no shape factor. The interfacial energy of the second phase particles was taken from Thermo-Calc's interfacial energy calculator using the TCMG6 database and was set to a fixed value as it does not vary significantly with temperature. The details of model parameters are going to provide in following Chapter 6: .

5.4.2 Mean-field Model in Precipitation

The simulation domain of the mean-field precipitation model is not restricted to single crystals, and in this study the nominal composition was chosen as an input and the thermodynamic parameters at this composition were obtained by the surrogate model and its databases TCMG6 and MOBMG1. The input heat treatment temperature for this precipitation model was the ageing temperature, with the ramping process of the heat treatment samples and the cooling process of the subsequent water quenching ignored. This approximation was deemed to be valid given the sufficiently small size of the samples. The time of ageing treatment was defined as the heat treatment time parameter of the model, which was used to describe the growth and coarsening of second phase particles under different ageing treatments. The active nucleation sites of the second phase particles combined with their corresponding ageing hardness response were used to derive a fitted approximation by calculating the relationship between the active nucleation sites and the ageing treatment duration for a certain range. The shape factors of the different second phase particles change with the specific morphology described in the literature. The interfacial energies of the second phase particles were taken from the database of the surrogate model TCMG6 and set to fixed values, where the interfacial energies of the metastable phases and the incubation coefficient were approximated and fitted according to the parameters provided in the literature. The details of model parameters are going to be provided in following Chapter 8.

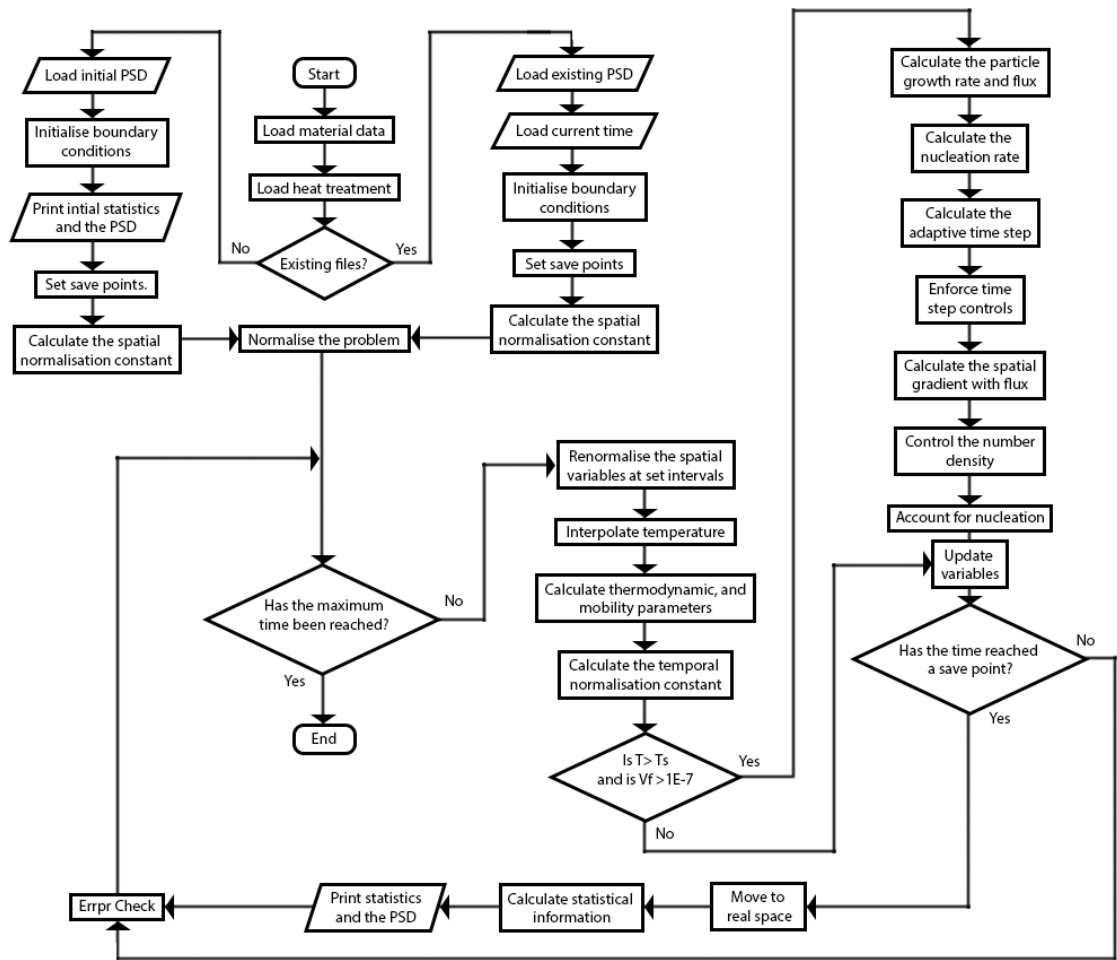


Figure.5.4 Mean-field model solver algorithm

Table 5.2 Pre-processing input key files

| | |
|--------------------------|--|
| TQ initialisation | |
| <i>NWG</i> | The size of the TQ workspace |
| <i>NWP</i> | The size of the TQ workspace |
| ΔG_p | An energy contribution to the particle phase J/mol |

| | |
|-----------------------------|---|
| Chemical composition | |
| <i>num</i> | The number of alloying elements |
| <i>charVec</i> | A list of the element names |
| <i>Conc</i> | The atomic fraction of alloying elements with a negative value for the balancing element. |

| | |
|-----------------------|--|
| Discretization | |
| n_{sub} | The number of sub-solvus temperatures examined. |
| n_{sup} | The number of super-solvus temperatures examined. |
| ϕ | The number of volume fractions per temperature examined. |

| | |
|-----------------------------------|---|
| Initialisation temperature | |
| T | The temperature used to initialise Thermo-Calc. |

Table 5.3 Solver input key files

| | |
|----------------------------|---|
| Material parameters | |
| V_m^β | Molar volume (mol/m ³) |
| k_n | The fraction of active nucleation sites |
| n_{eb} | The number of data points used to describe the interfacial energy as a function of temperature. |
| T_{eb} | A vector of length n_{eb} describing the temperatures (°C) used to define the interfacial energy. |
| | A vector of length n_{eb} of Interfacial energies (J/m ²) that link with T_{eb} . |

Material parameters

| | |
|-----------------|---|
| n_{mf} | The number of data points used to describe the lattice misfit as a function of temperature. |
| T_{mf} | A vector of length n_{mf} describing the temperatures ($^{\circ}\text{C}$) used to define the lattice misfit. |
| ε_0 | A vector of length n_{mf} describing the lattice misfit that link with T_{mf} . |
| n_e | The length of the polynomial coefficients used to describe the Young's modulus |
| E | Elastic modulus (GPa) – Polynomial coefficients (Temperature in K) |
| n_v | The length of the polynomial coefficients used to describe the Poisson's ratio |
| ν | Poisson's ratio (dimensionless) – Polynomial coefficients (Temperature in K) |
| X_{bulk} | Atomic fraction of particle forming elements in the bulk composition. |
| X_i | Atomic fraction of particle forming i th elements in the particle phase. |
| D_0 | The diffusivity coefficient. (m^2/s) |
| Q_v | The activation energy (J/mol) |
| h | The particle shape factors |
| γ | The interfacial energy (J/m^2) |
| P_{inc} | The incubation probability coefficients |

Simulation Controls

| | |
|------------------|---|
| t_{min} | The minimum time step (s) |
| t_{max} | The maximum time step (s) |
| ΔT_{max} | The maximum change in temperature ($^{\circ}\text{C}$) |
| dV_f | The maximum allowable change in volume fraction in one model calculation. |
| S_n | The number of saves (integer) |
| S_e | The save rate exponent (real) |
| i_{max} | The maximum model iterations before saving data. |

Chapter 6: Solidification, segregation and second phases formation of Mg-Zn-Ca alloys

6.1 Introduction

Mg-Zn-Ca alloys phase formation largely influenced by the Zn and Ca content. Under equilibrium conditions, when the Zn/Ca atomic ratio is below 1.2, the phases precipitated in Mg-Zn-Ca alloys include α -Mg, Mg_2Ca , and $Ca_2Mg_6Zn_3$ [262,263]. Alper and Ali [264] investigated Mg-Zn-Ca alloys with varying Zn/Ca atomic ratios and found that ZX10 (Mg-0.9%Zn-0.2%Ca), which forms fewer Mg_2Ca phases than ZX12 (Mg-0.9%Zn-1.5%Ca), exhibits superior mechanical properties, including higher tensile strength and elongation. The fine and uniformly distributed $Ca_2Mg_6Zn_3$ phase in Mg-Zn-Ca alloys contributes significantly to their enhanced mechanical properties [265]. However, the Mg_2Ca phase is a coarse and segregated intermetallic compound that is highly brittle at room temperature, and it has a high melting temperature of 715°C, significantly higher than the melting temperature of the Mg matrix, making it difficult to dissolve through heat treatment [266,267]. Oh-ishi *et al.* [80] and Yang Y. *et al.* [268] further noted that increasing Zn content in Mg-Zn-Ca systems leads to a progressive increase in binary precipitates containing Mg and Zn, which eventually stabilize as the β -MgZn phase. At the same time, an increase in the Zn content will significantly reduce the melting point of the magnesium alloy, thereby reducing the efficiency during post-treatment, when the Zn/Ca atomic ratio exceeds 1.2, the stable phases precipitated in Mg-Zn-Ca alloy are α -Mg, β -MgZn, $Ca_2Mg_6Zn_3$ [269]. The increase in MgZn reduces the ageing response of Mg-Zn-Ca alloys [270], and the segregation of $Ca_2Mg_6Zn_3$ at grain boundaries may influence electrochemical behaviour and corrosion resistance [271]. To overcome these challenges, an effective strategy involves suppressing the formation of Mg_2Ca and MgZn phases during solidification while achieving dispersed, uniform, and fine $Ca_2Mg_6Zn_3$ phases within the α -Mg matrix through optimised compositional and heat treatment design.

The work in this chapter is to investigate the influence of Mg-Zn-Ca alloy compositions and rapid cooling conditions on microstructural evolution, with a specific focus on the formation and behaviour of intermetallic phases such as Mg_2Ca , MgZn, and $Ca_2Mg_6Zn_3$ during solidification, the Liquidus-minimising Scheil model plays a crucial role in predicting the formation of these phases. Combined with the mean-field model, Scheil solidification predictions provide valuable insights into how alloy composition and cooling rates affect the resulting microstructure differences. Through experimentation and

by employing the Scheil model extended to ternary alloy systems, and integrating it with CALPHAD-based thermodynamic calculations, this study seeks to predict the segregation pathways and phase distributions under non-equilibrium solidification conditions. Furthermore, understanding the mechanisms governing the formation of the Mg₂Ca phase is critical to controlling its presence in this alloy system. By identifying the thermodynamic and kinetic factors influencing its nucleation and growth, as well as its interaction with other phases, this research aims to develop strategies to minimize its detrimental effects while tailoring microstructures for enhanced performance.

6.2 Materials and Methods

6.2.1 Methodology

To address the aim of controlling the Mg₂Ca phase and understanding its formation in Mg-Zn-Ca alloys, experimentation and modelling tools are applied to resolve uncertainties regarding the precise formation of precipitates observed in characterised microstructures. During rapid solidification, the segregation of alloying elements leads to an increasing concentration of solute elements in the liquid phase, influencing the evolution of second phase particles. Two hypotheses have been proposed to describe the formation of second phase particles in rapidly solidified castings:

- Hypothesis 1: The liquid alloy solidifies directly into both the Mg matrix and second phase intermetallic compounds simultaneously.
- Hypothesis 2: The liquid first solidifies into a supersaturated Mg matrix, and then the second phase particles precipitate from the Mg matrix.

Experiments have been performed to characterise the cast microstructures of ZX10 and ZX70. The Scheil model and the mean-field model correspond to these two hypotheses, respectively. Figure 6.1 illustrates the precipitation sequences predicted by these two models, highlighting their complementary perspectives. The distinction lies in their focus: the Scheil model emphasises phase formation during liquid-to-solid transitions as hypothesis 1, while the mean-field model examines the subsequent evolution of phases within the solid state as hypothesis 2. In reality, the precipitation of second phase intermetallic compounds in Mg-Zn-Ca alloys may result from a combination of these two mechanisms, as both liquid-phase and solid-state processes can contribute to the final microstructure. The second phase particles may nucleate during solidification, and then grow during the cool to room temperature through solid-state diffusion. Based on the model predictions from these approaches, this study seeks to bridge the gap between

theoretical models and experimental observations, providing a comprehensive understanding of phase formation and distribution in Mg-Zn-Ca alloys.

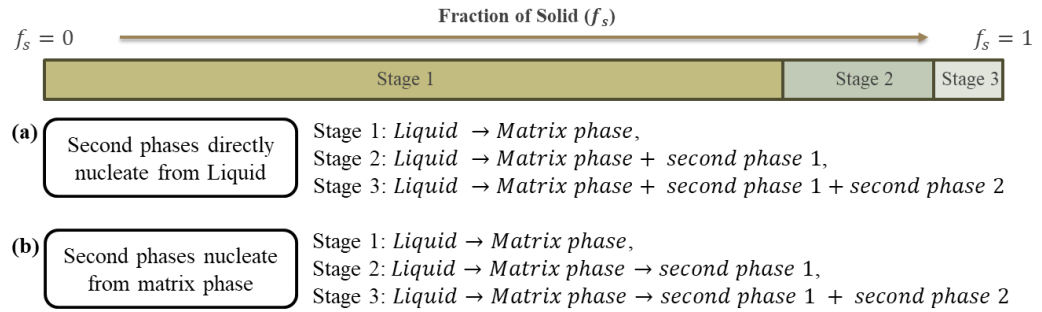


Figure 6.1. Hypothesis of precipitation sequences by (a) Scheil and (b) Mean-field model of Mg-Zn-Ca alloys.

6.2.2 Preparation of Mg alloys

The as-cast Mg-0.8Zn-0.2Ca (ZX10) and Mg-6.8Zn-0.2Ca alloys (ZX70) were provided by Luxfer MEL Technology (UK). The molten alloys were poured into a cylindrical steel mould equipped with a water-cooling system to achieve rapid solidification. The cooling water was maintained at a temperature of approximately 25°C, while the melt temperature during pouring was around 750°C. The samples were removed from the mould approximately 10 minutes after solidification and subsequently cylindrical surfaces were polished to produce cylindrical billets with a diameter of 75 mm. A disc-shaped specimen was extracted from the centre of each billet, and a 37.5 × 3 × 3 mm sample was cut from the centre to the surface of the disc. This sample was then divided into five equal-length specimens, as illustrated in Figure 6.2. The bulk compositions of both ZX10 and ZX70 alloys were measured using inductively coupled plasma optical emission spectroscopy (ICP-OES). To account for local segregation in the test specimens, multiple local compositions were analysed using scanning electron microscopy coupled with energy-dispersive spectroscopy (SEM-EDS). The compositions are measured in Table 6.1.

Table 6.1 Chemical composition of as-received Mg-Zn-Ca alloy

| Alloy | Mg (wt.%) | Zn (wt.%) | Ca (wt.%) | Measured by |
|-------------|-----------|-----------|-----------|-------------|
| ZX10 | Bal. | 0.8 | 0.2 | ICP-OES |
| ZX70 | Bal. | 6.8 | 0.2 | ICP-OES |
| ZX10 | Bal. | 0.8-1.2 | 0.2-0.5 | SEM-EDS |
| ZX70 | Bal. | 6.4-7.2 | 0.2-0.3 | SEM-EDS |

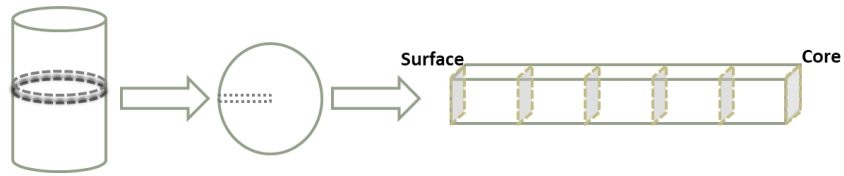


Figure 6.2 Schematic diagram of the cut area of the ZX10 and ZX70 samples

6.2.3 Thermal model set-up

To replicate the thermal history of the rapid cooling process, heat transfer calculations were conducted using the finite difference method. The casting solidifies progressively from the surface to the core, as illustrated in Figure 6.3. To simplify the analysis, the system was modelled as a one-dimensional heat transfer process from the surface to the core. The parameters used for the one-dimensional heat transfer model are detailed in Table 6.2. The approximate thermal history results obtained from these calculations are presented in Figure 6.4. It is important to note that this model describes the solidification process of a casting under ideal conditions, i.e. there is no loss of heat in transfer and there is no shrinkage gap between the ingot and the mould. In practical production, surface shrinkage of the casting can create gaps between the billet and the mould, reducing heat transfer efficiency. As a result, the actual cooling time may be longer than predicted by this model.

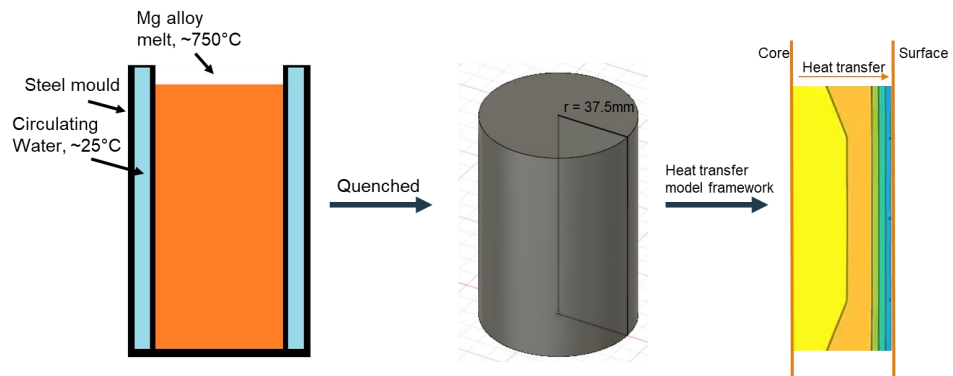


Figure 6.3. Sample rapid cooling process

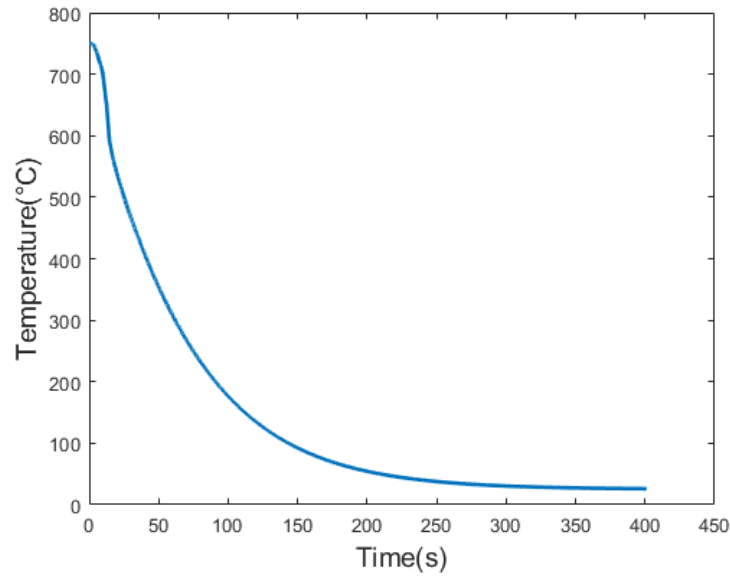


Figure 6.4. Approximate thermal history of ZX10 and ZX70 alloys cooling process in Figure 6.3

Table 6.2 Model parameters for heat transfer calculation, where Temperature is given by T with units of K

| Variable | Description | Value | Units | References | |
|---------------|---------------------------|----------------------|---------------------|-----------------|-------|
| k_L | Thermal conductivity | $16.51 + 0.07 * T$ | W/m/K | Thermo- Calc | |
| k_α | | $176.41 - 0.07 * T$ | | | |
| c_{pL} | Specific Heat | $1413.50 - 0.01 * T$ | J/kg/K | | |
| $c_{p\alpha}$ | | $862.70 + 0.52 * T$ | | | |
| ρ_L | Density | $1834.74 - 0.26 * T$ | kg/m ³ | | |
| ρ_α | | $1796.98 - 0.16 * T$ | | | |
| LT | Latent heat | 357951 | J/kg | | [44] |
| h | Heat transfer coefficient | 600 | W/m ² /K | | [272] |

6.2.4 Mean field approach

The chemical potentials and diffusion coefficients in the mean-field model were obtained from the TCMG6 database in Thermo-Calc. The compositional inputs for the mean-field model were set based on the segregation predictions from the Scheil model. The percentage of segregated area was approximated as the difference between the fraction of solids at the ternary eutectic point and at full solidification.

During rapid solidification, ZX10 and ZX70 generate a significant quantity of matrix phases at their nominal compositions, and the second phase has only very low precipitation kinetics at nominal compositions by the author's initial calculations. Consequently, the mean-field model in this study focuses on the generation of second phases during the cooling of solid with segregated composition. The model calculates the volume fraction of second phase precipitation in conjunction with the percentage of segregated compositions.

The mean-field coarsening predictions are highly sensitive to the values used for the interfacial energies, which can be obtained for each precipitate embedded in the matrix from phase calculations by Thermo-calc TCMG6 and are given in Table 6.3. The continuity equations, particle growth rates, and nucleation rates were normalized and reformulated following the approach described by Anderson *et al.* [214,216] and the advection equations are solved using the finite difference method. The nucleation of particles is carried out following the method of Jou *et al.* [203] and the size change of the stable nucleus is described using a distribution function with a finer discretisation of the particle radius.

The nucleation site fraction was determined by the dislocation density within grains, as outlined by Anderson *et al.* [217]. Grain boundary dislocations, which typically exhibit higher densities compared to the grain interior, act as nucleation sites for grain boundary precipitates. This relationship allows for the definition of the nucleation site fraction range within grains and facilitates the reverse estimation of precipitate segregation at various grain locations. When the nucleation site fraction is 1, precipitation approximates homogeneous nucleation, whereas lower nucleation site fraction values indicate a shift toward heterogeneous nucleation. In this study, the nucleation site fraction range is assumed to be between 10^{-5} and 10^{-15} , decreasing by orders of magnitude. The effects of different combinations of nucleation site fraction ranges and cooling times on the precipitation behaviour of second phases are investigated.

Table 6.3 Interfacial energy of precipitates in Mg-Zn-Ca Mg system rich corner

| Precipitates | Interfacial energy | Units | References |
|---|--------------------|------------------|-------------|
| Mg₂Ca | 0.06 | | |
| MgZn | 0.05 | J/m ² | Thermo-Calc |
| Ca₂Mg₆Zn₃ | 0.05 | | |

The concentration of nuclei, N_0 is influenced by the nucleation site fraction, η . For homogeneous nucleation, η can be approximated as 1, while for heterogeneous nucleation, η can be estimated based on the dislocation density. Anderson *et al.* [217] derived an equation describing the relationship between the nucleation site fraction η and dislocation density ρ , where b is the Burgers vector. Since the measurement of dislocation density in each part of the sample is complicated, an estimate of nucleation site fraction is required.

$$\eta = b^2\rho \quad (6.1)$$

6.3 Microstructure of As-cast ZX10 and ZX70 Alloys

The microstructure of the ZX10 and ZX70 alloys in the as-cast condition as a function of location is shown in Figure 6.5. From the SEM images and EDS element distribution maps in Figure 6.5a, significant Ca segregation is observed at the grain boundaries of the ZX10 alloy. While Zn segregation is also present at the grain boundaries, it is less pronounced compared to Ca, and the distribution of Zn appears relatively uniform within the Mg matrix, especially in regions closer to the centre of the cast sample (Figure 6.5a-6). This phenomenon can be attributed to the gradual decrease in cooling rate from the surface to the centre of the cast sample. Additionally, within the grains, a small number of spherical particles ($\sim 8 \mu\text{m}$ in radius) containing both Zn and Ca are observed. These particles are likely $\text{Ca}_2\text{Mg}_6\text{Zn}_3$ phases predicted by Thermo-Calc, which precipitated on micro-dendrites due to uneven solidification. A comparison of SEM images (Figure 6.5a-1 to Figure 6.5a-6) found that, as the cooling rate decreases, the density of particles within the grains gradually increases. This observation may suggest that the redistribution of Zn during solidification contributes to the increased particle density. The distribution of Ca and Zn elements is generally consistent, however, there are some particles and grain boundaries where Ca segregates independently. Therefore, it can be inferred that the segregated phases in ZX10 likely include both the $\text{Ca}_2\text{Mg}_6\text{Zn}_3$ phase and the Mg_2Ca phase. Furthermore, line scan composition data across dendrites in Figure 6.6a clearly show Ca enrichment at the grain boundaries and relatively flat Zn profiles within the dendrite cores, which is consistent with the thermodynamic predictions of solute segregation during solidification in the following section.

The SEM images and EDS element distribution maps of ZX70 are shown in Figure 6.5b. In ZX70, the distributions of Ca and Zn elements are generally consistent, with both segregating at the grain boundaries. However, compared to ZX10, the degree of Zn segregation at the grain boundaries in ZX70 is significantly higher, which can be attributed to the higher Zn content in the ZX70 alloy. The comparison of SEM images (Figure 6.5b-1 to Figure 6.5b-6) found that, as the cooling rate decreases, the density of second phases in ZX70 gradually increases. Unlike the spherical precipitates formed in ZX10, ZX70 forms Zn-rich intermetallic compounds. Therefore, it can be inferred that, in addition to the $\text{Ca}_2\text{Mg}_6\text{Zn}_3$ phase, ZX70 may contain a second phase that is different from the Mg_2Ca phase potentially present in ZX10. This second phase is preliminarily identified as MgZn . The corresponding line scan in Figure 6.6b shows more pronounced

Zn enrichment at the grain boundaries compared to ZX10, in agreement with the higher nominal Zn content of ZX70. While the model predictions capture the overall segregation trend, local discrepancies are observed, which may be associated with solute back-diffusion effects and microsegregation during non-equilibrium solidification.

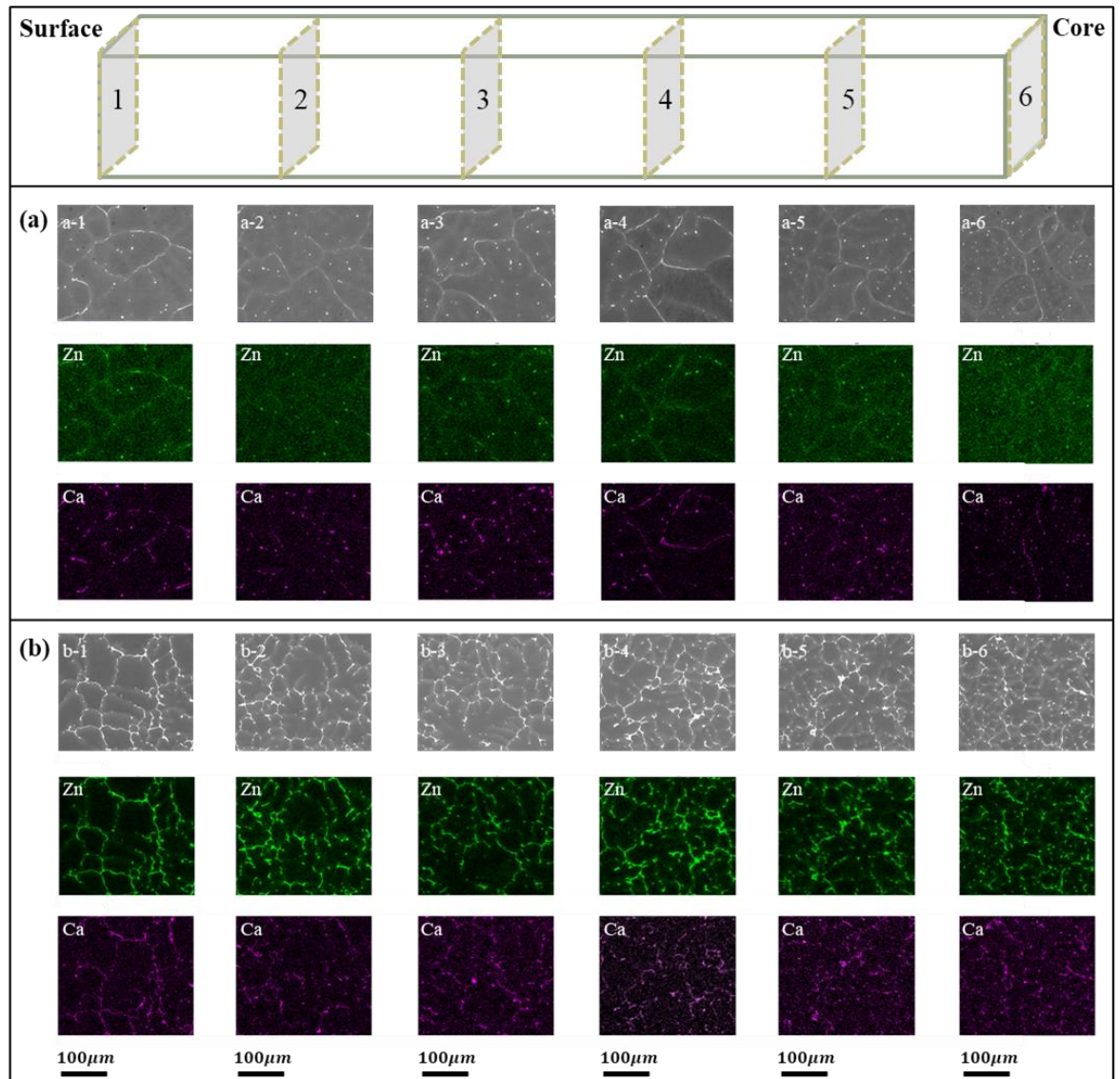


Figure 6.5. SEM-BSE and EDS map results of as-cast (a) ZX10 and (b) ZX70 alloys from surface (1) to core (6)

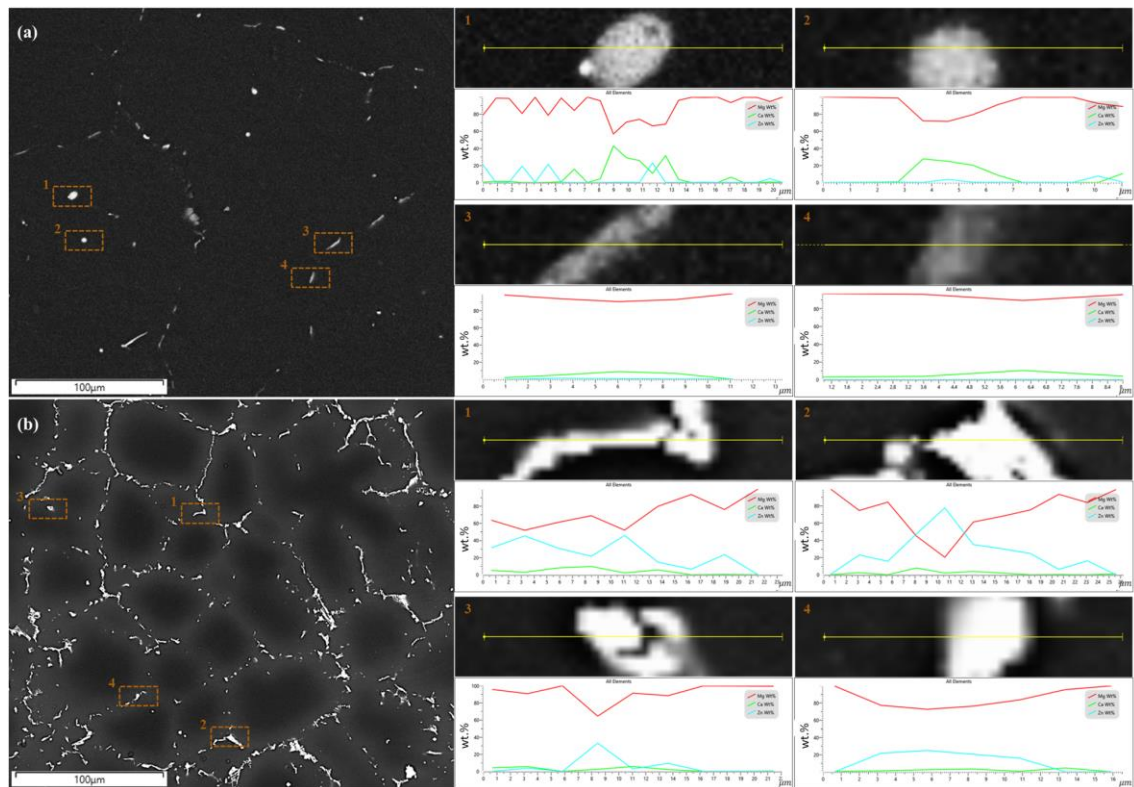


Figure 6.6. SEM-BSE and EDS line scan analysis of as-cast (a) ZX10 and (b) ZX70 alloys

6.4 Scheil solidification

Figure 6.7 illustrates the solidification paths of ZX10 and ZX70 alloys, comparing the results generated by the Liquidus-minimising Scheil model developed in this study (Figure 6.7a and 6.6c) with those from the Scheil model in Thermo-Calc software (Figure 6.7b and 6.6d). The comparison reveals significant differences in the types, amounts, and temperatures of phases formed in ZX10 between the two models. In contrast, the types of phases formed in ZX70 are consistent between the models, with only minor differences observed in the amounts and temperatures.

Figure 6.7a and 6.6b illustrate the solidification paths of the ZX10 alloy by Liquidus-minimising Scheil model and Thermo-Calc software Scheil model, respectively. It can be observed that solidification begins at approximately 647°C with the formation of the primary Mg matrix phase. In Figure 6.7a, the Mg₂Ca phase starts forming alongside the primary Mg phase at approximately 516°C and reaches the ternary eutectic point at 394°C, where the Mg matrix phase, Mg₂Ca phase, and Ca₂Mg₆Zn₃ phase solidify simultaneously. This result contrasts significantly with the findings shown in Figure 6.7b. In Figure 6.7b, the Ca₂Mg₆Zn₃ phase begins forming alongside the primary Mg phase at approximately 392°C and reaches the ternary eutectic point at 295°C, where the Mg matrix phase, Ca₂Mg₆Zn₃ phase, and MgZn phase solidify simultaneously.

Figure 6.7c and 6.6d present the solidification paths of the ZX70 alloy. In comparison, the differences between the Liquidus-minimising Scheil model and the Thermo-Calc software Scheil model are relatively minor. Both models indicate that solidification begins at approximately 628°C with the formation of the primary Mg matrix phase. Around 330°C to 340°C, the MgZn phase forms alongside the primary Mg phase, and the ternary eutectic point is reached at 295°C, where the Mg matrix phase, MgZn phase, and Ca₂Mg₆Zn₃ phase solidify simultaneously. Slight differences in temperature and solid fraction at various solidification stages can be observed between the two models. These discrepancies may arise from differences in the partition coefficients k used in the Scheil calculations or variations in the numerical methods employed by the models. These aspects will be further discussed in subsequent sections.

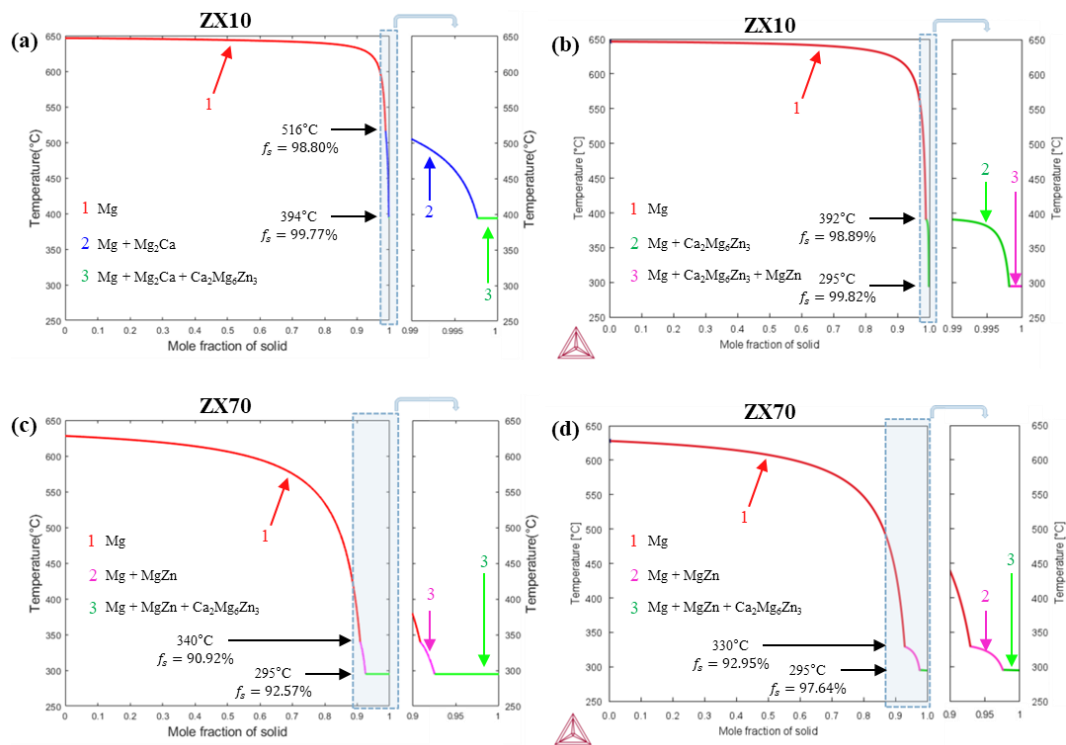


Figure 6.7. Scheil solidification curve of (a, b) ZX10 and (c, d) ZX70 alloy. Figure (a, c) are generated from the liquidus-minimising Scheil in this study, and figure (b, d) are generated from Thermo-Calc Scheil module

Based on the SEM-EDS results from Figure 6.5a, it is evident that the presence of the Mg₂Ca phase in the ZX10 alloy is more likely than the MgZn phase. To explore the significant differences observed between Figure 6.7a and 7b, the potential effects of solute redistribution on local chemical equilibrium were considered. An equilibrium phase diagram for the ZX10 alloy (Mg-0.8Zn-0.2Ca, wt.%) with compositional fluctuations within a certain range was constructed. The selected composition range was derived from local compositions measured by SEM-EDS.

As shown in Figure 6.8, the equilibrium phase diagram shows that the formation of Mg_2Ca and $MgZn$ phases is highly sensitive to compositional variations. Compared to the nominal composition of ZX10 (Mg-0.8Zn-0.2Ca, wt.%), an increase of 0.4 wt.% in Zn content may prevent the formation of Mg_2Ca during equilibrium solidification. Conversely, Ca segregation has an even more pronounced effect. An increase of 0.1–0.2 wt.% in Ca content can suppress the formation of $MgZn$ while significantly increasing the amount of Mg_2Ca at lower temperatures.

These findings suggest that the nominal composition of the ZX10 alloy lies at the critical boundary for the formation of Mg_2Ca and $MgZn$ phases. The compositional segregation caused by non-equilibrium solidification during rapid cooling amplifies the differences in phase formation. Observing the Liquidus-minimising Scheil solidification path of ZX10, Ca segregates first during the initial solidification stages, further increasing compositional differences and leading to Mg_2Ca as the first secondary phase to form. In contrast, for ZX70, Zn segregates first, causing $MgZn$ to become the initial second phase. Notably, differences in compositional segregation result in distinct solidification paths, which in turn lead to variations in the sequence, temperature, and solid fraction of second phase formation. In the Mg-Zn-Ca system magnesium-rich corner, these differing solidification paths also point to different ternary eutectic points. The phase fractions during solidification, collected from the TCMG6 database, are listed in Table 6.4, while the final solid fractions of each phase in the solid state are summarized in Table 6.5.

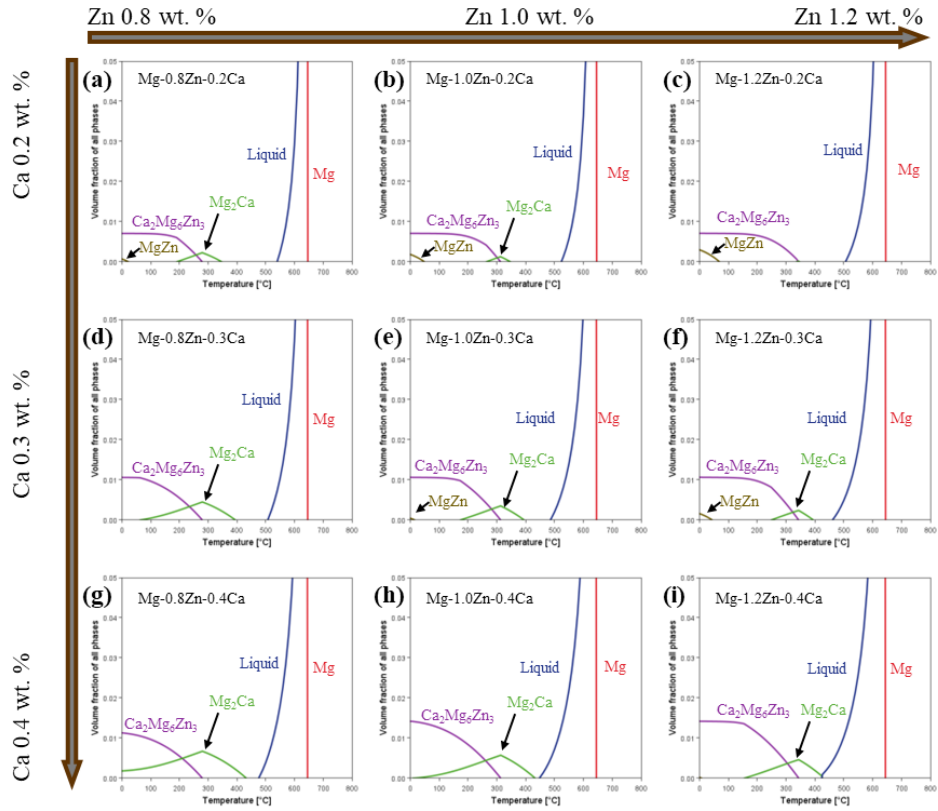


Figure 6.8. Equilibrium phase diagram of Mg- x Zn- y Ca (wt %) alloys, $x=0.8, 1.0, 1.2$, and $y=0.2, 0.3, 0.4$.

Table 6.4 Phase transition during Liquidus-minimising Scheil solidification for both ZX10 (Figure 6.7a) and ZX70 (Figure 6.7c) alloys

| | Temperature | Phase transition | Mole fraction of Solid f_s |
|------|----------------|--|------------------------------|
| ZX10 | 647°C to 516°C | $L \rightarrow 100\% \alpha(Mg)$ | $0\% < f_s < 98.80\%$ |
| | 516°C to 394°C | $L \rightarrow 64.5\% \alpha(Mg) + 35.5\% Mg_2Ca$ | $98.80\% < f_s < 99.77\%$ |
| | 394°C | $L \rightarrow 35.9\% \alpha(Mg) + 62.3\% Ca_2Mg_6Zn_3 + 1.8\% Mg_2Ca$ | $99.77\% < f_s < 1$ |
| ZX70 | 628°C to 340°C | $L \rightarrow 100\% \alpha(Mg)$ | $0\% < f_s < 90.92\%$ |
| | 340°C to 295°C | $L \rightarrow 52.4\% \alpha(Mg) + 47.6\% MgZn$ | $90.92\% < f_s < 92.57\%$ |
| | 295°C | $L \rightarrow 28.6\% \alpha(Mg) + 33.5\% Ca_2Mg_6Zn_3 + 37.9\% MgZn$ | $92.57\% < f_s < 1$ |

Table 6.5 Amount of particles simulated from liquidus-minimising Scheil solidification model

| | Phase | Mole fraction of Solid |
|------|----------------|------------------------|
| | $\alpha(Mg)$ | 0.99505 |
| ZX10 | Mg_2Ca | 0.00349 |
| | $Ca_2Mg_6Zn_3$ | 0.00145 |
| | $\alpha(Mg)$ | 0.93909 |
| ZX70 | $\beta - MgZn$ | 0.03601 |
| | $Ca_2Mg_6Zn_3$ | 0.02490 |

6.5 Mean-field Results of Second Phase Precipitation

The Scheil model is used to simulate the solidification process from the liquid to the solid phase, while the mean-field model is applied to simulate the cooling process of the solid phase from the liquid-solid transition temperature to room temperature. To simulate the solid-state phase transitions using the mean field model, a number of considerations need addressing. There is uncertainty to the exact nucleation site fraction for the second phase precipitates required by the mean field model. In addition, the exact cooling rate after solidification during the experiments is not known. In this study, the predicted range of the nucleation site fraction for second phase particles is set between 10^{-5} and 10^{-15} . Cooling times range from 5 to 120 minutes, with increments of 5 minutes.

Figure 6.9 illustrates the results of the mean-field model, showing the evolution of second phases volume fractions in the Mg matrix of ZX10 and ZX70 alloys under varying nucleation site fractions and cooling times. Figure 6.9a illustrates the formation of second phases in the ZX10 alloy. The Mg_2Ca phase is observed to form at a nucleation site fraction of 10^{-5} under the 5 min of cooling time, with its maximum volume fraction reaching approximately 2×10^{-4} . Notably, a band zone is present in Figure 6.9a, where the volume fraction of Mg_2Ca is significantly higher in the central region compared to other areas. A comparison between Figure 6.9a and 10b shows a competitive relationship, where increased formation of Mg_2Ca correlates with a decrease in $Ca_2Mg_6Zn_3$ volume fraction. In regions where Mg_2Ca forms in higher quantities, the volume fraction of $Ca_2Mg_6Zn_3$ decreases correspondingly. In areas where less Mg_2Ca formed, the volume fraction of $Ca_2Mg_6Zn_3$ remains approximately 5×10^{-4} . Additionally, by analysing the

magnified areas of Figure 6.9a and b, it can be observed that the reduction in $\text{Ca}_2\text{Mg}_6\text{Zn}_3$ volume fraction corresponds approximately to the increase in Mg_2Ca volume fraction, further confirming their competitive relationship. Interestingly, a small peak in the volume fraction of Mg_2Ca approximately 1.3×10^{-4} is noted at 30 minutes with a nucleation site fraction of 10^{-11} , after which the volume fraction of Mg_2Ca gradually decreases.

Figure 6.9c and 10d show the formation of second phases in the ZX70 alloy. Except for the region near the lower-left corner, the formation of MgZn and $\text{Ca}_2\text{Mg}_6\text{Zn}_3$ phases is relatively uniform. Upon comparing the magnified areas of Figure 6.9c and d, it is evident that both MgZn and $\text{Ca}_2\text{Mg}_6\text{Zn}_3$ phases tend to form under higher nucleation site fractions and longer cooling times, although the increase in their volume fractions is not particularly significant. The volume fraction of MgZn stabilizes at approximately 8×10^{-3} , while that of $\text{Ca}_2\text{Mg}_6\text{Zn}_3$ stabilizes at approximately 7×10^{-4} . Unlike in ZX10, no apparent competitive relationship between the formation of MgZn and $\text{Ca}_2\text{Mg}_6\text{Zn}_3$ phases is observed in the Mg matrix of ZX70. These results suggest that in ZX10, the formation of Mg_2Ca and $\text{Ca}_2\text{Mg}_6\text{Zn}_3$ phases is strongly interdependent, with significant competition affecting their respective volume fractions. In contrast, the formation of MgZn and $\text{Ca}_2\text{Mg}_6\text{Zn}_3$ phases in ZX70 appears to occur more uniformly and independently, without notable interactions between the two phases.

To provide a clearer view of the precipitation kinetics, 2D plots of volume fraction evolution with time for a selected nucleation site fraction are also presented in Figure 6.10. These curves show that Mg_2Ca and $\text{Ca}_2\text{Mg}_6\text{Zn}_3$ in ZX10 exhibit strong competitive behaviour, with the rise of one phase corresponding to the reduction of the other. In contrast, the ZX70 alloy shows smoother, nearly monotonic increases in MgZn and $\text{Ca}_2\text{Mg}_6\text{Zn}_3$ fractions, without significant mutual suppression. The shapes of the curves confirm that competitive precipitation dominates in ZX10, while more stable and independent growth occurs in ZX70.

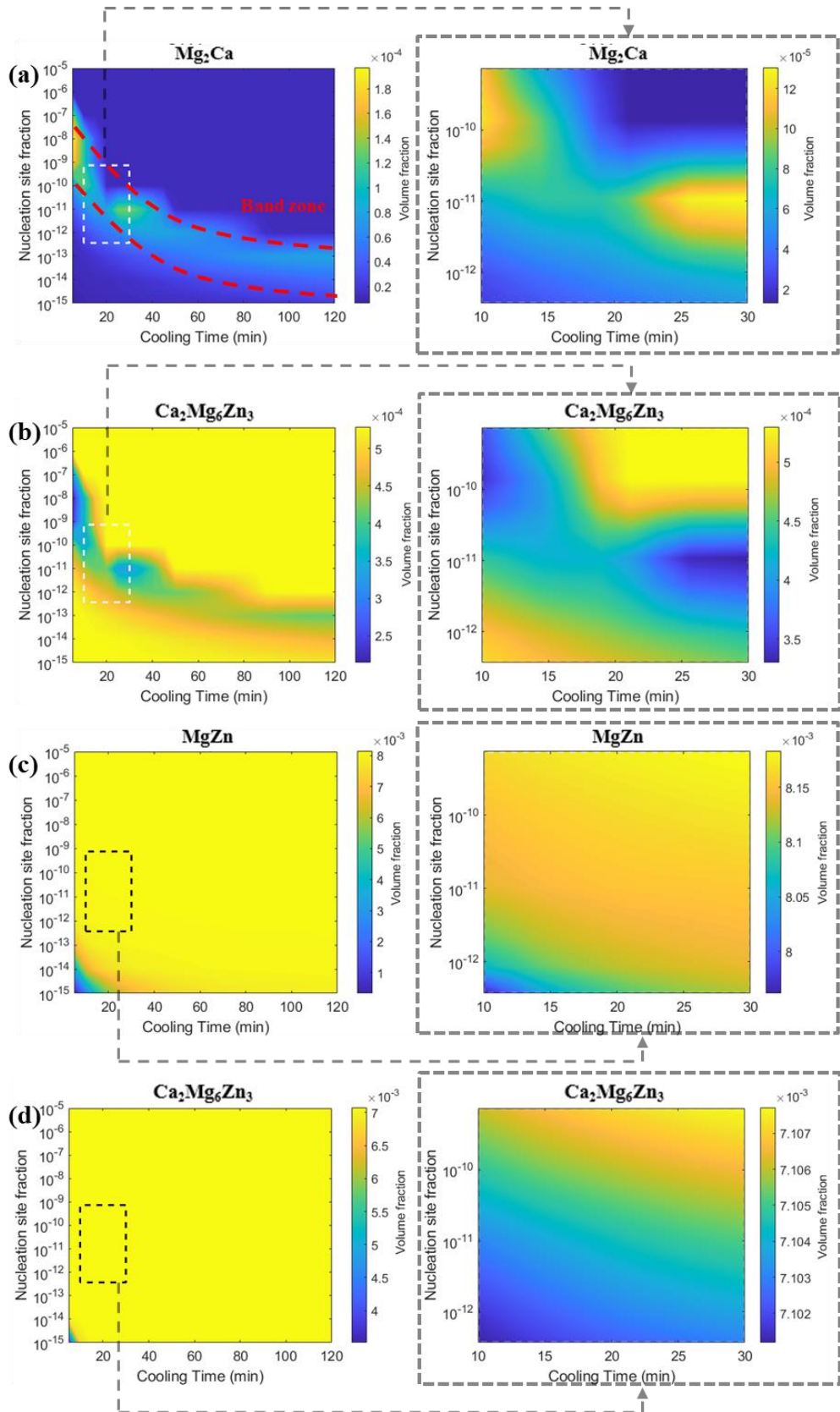


Figure 6.9. Particles volume fraction with variation of nucleation site fraction and cooling time in ZX10 (a, b) and ZX70 (c, d) alloys; (a) is Mg_2Ca phase, (b) is $Ca_2Mg_6Zn_3$ phase in ZX10; (c) is $MgZn$ phase, (d) is $Ca_2Mg_6Zn_3$ phase in ZX70

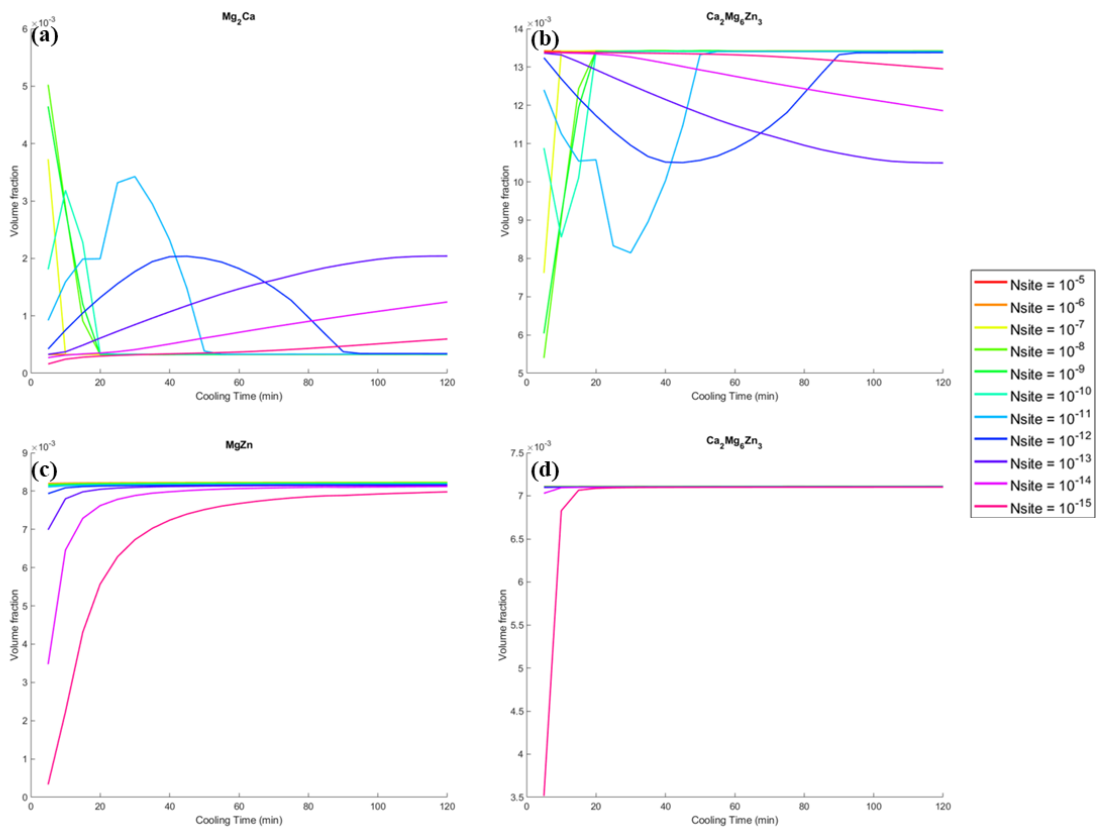


Figure 6.10. Time evolution of second phase volume fractions in ZX10 and ZX70 alloys under different nucleation site fractions: (a) Mg_2Ca and (b) $Ca_2Mg_6Zn_3$ in ZX10; (c) $MgZn$ and (d) $Ca_2Mg_6Zn_3$ in ZX70

Figure 6.11 presents the mean-field model results for the mean radius of second phase particles during the cooling process in a Mg matrix under varying nucleation site fractions and cooling times. The results indicate that all second phase particles tend to form at lower nucleation site fractions, with their mean radius increasing as the cooling duration extends. However, the particles formed in the ZX10 alloy are larger than those in the ZX70 alloy. At a nucleation site fraction of 10^{-15} , the maximum mean radius of particles in ZX10 and ZX70 are approximately 800 nm and 300 nm, respectively.

In the ZX10 alloy, as shown in Figure 6.11a and b, when the nucleation site fraction is higher than the band zone identified in Figure 10, the mean radius of Mg_2Ca and $Ca_2Mg_6Zn_3$ particles do not significantly increase with extended cooling time. Under these conditions, the mean radius of Mg_2Ca particles remains between 10 nm and 50 nm, while that of $Ca_2Mg_6Zn_3$ particles is between 100 nm and 200 nm. However, when the nucleation site fraction is lower than the band zone, the mean radius of both particles increases substantially with decreasing nucleation site fraction and longer cooling durations. At a nucleation site fraction of 10^{-15} and a cooling duration of 120 minutes, the mean radius of both Mg_2Ca and $Ca_2Mg_6Zn_3$ particles reach approximately 800 nm.

In the ZX70 alloy, as shown in Figure 6.11c and d, the particle size of MgZn and $\text{Ca}_2\text{Mg}_6\text{Zn}_3$ also increases with decreasing nucleation site fraction. At a nucleation site fraction of 10^{-15} and a cooling duration of 120 minutes, the maximum mean radius of MgZn particles reaches approximately 350 nm, while that of $\text{Ca}_2\text{Mg}_6\text{Zn}_3$ particles is approximately 300 nm. However, when comparing the mean radius of MgZn and $\text{Ca}_2\text{Mg}_6\text{Zn}_3$, MgZn particles exhibit a gradual increase in size with extended cooling time, whereas the mean radius of $\text{Ca}_2\text{Mg}_6\text{Zn}_3$ particles remains relatively unchanged.

2D plots of precipitate mean radius as a function of cooling time are shown in Figure 6.12. These curves show that in ZX10, both Mg_2Ca and $\text{Ca}_2\text{Mg}_6\text{Zn}_3$ mean radius increase rapidly at low nucleation site fractions and then grow steadily with time, producing the largest particles among all cases. By contrast, at higher nucleation site fractions the mean radius remain nearly constant, forming much finer precipitates. In ZX70, MgZn particles show a smooth and continuous growth trend with time, while $\text{Ca}_2\text{Mg}_6\text{Zn}_3$ radius reaching the peak quickly and exhibit little subsequent change. The overall shapes of these curves suggest that growth kinetics in ZX10 are strongly sensitive to nucleation site fraction, while in ZX70 they are more stable and less competitive.

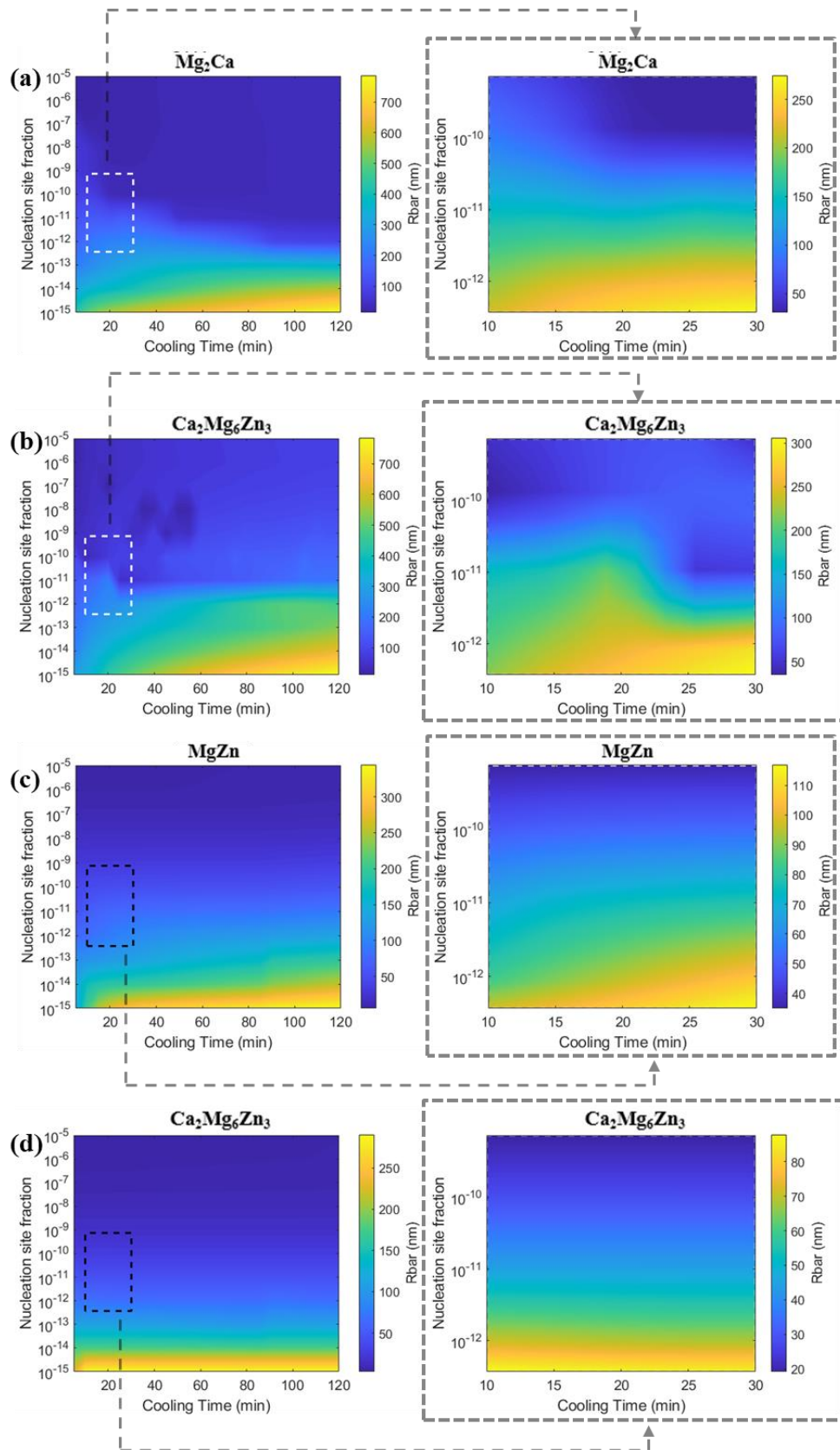


Figure 6.11. Particles mean radius with variation of nucleation site fraction and cooling time in ZX10 (a, b) and ZX70 (c, d) alloys; (a) is Mg_2Ca phase, (b) is $\text{Ca}_2\text{Mg}_6\text{Zn}_3$ phase in ZX10; (c) is MgZn phase, (d) is $\text{Ca}_2\text{Mg}_6\text{Zn}_3$ phase in ZX70

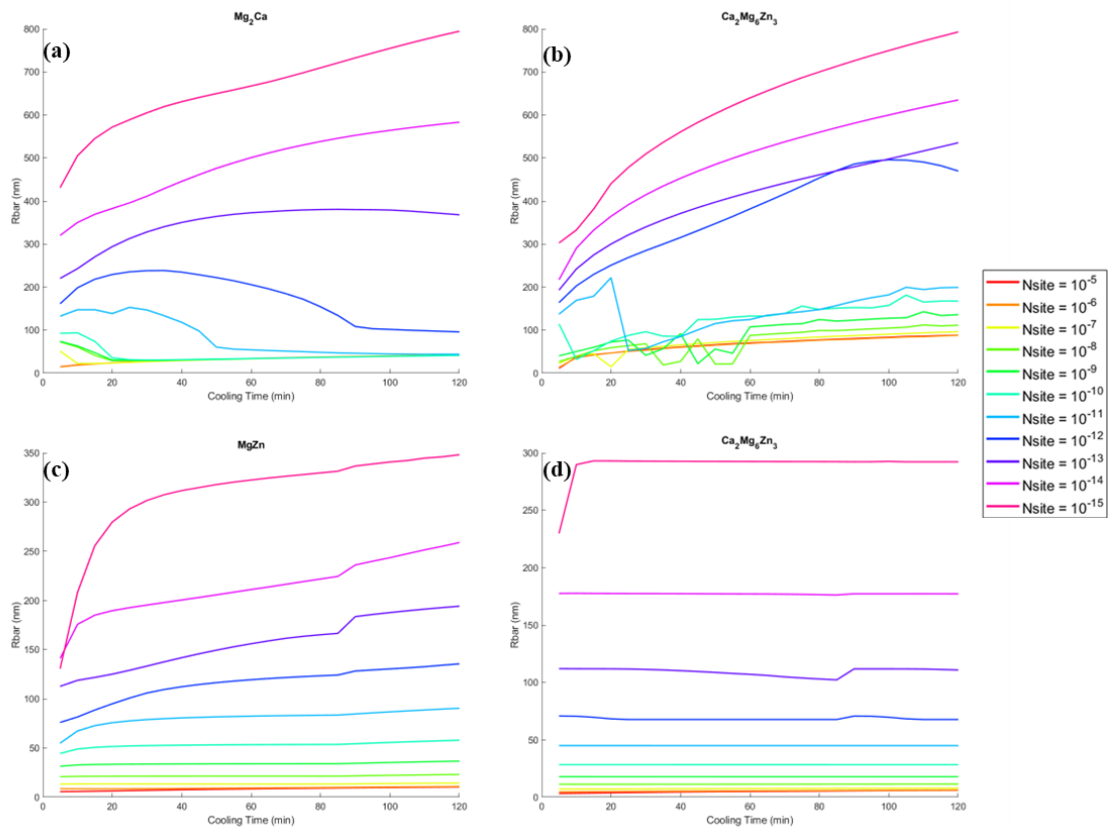


Figure 6.12. Time evolution of second phase mean radius in ZX10 and ZX70 alloys under different nucleation site fractions: (a) Mg_2Ca and (b) $Ca_2Mg_6Zn_3$ in ZX10; (c) $MgZn$ and (d) $Ca_2Mg_6Zn_3$ in ZX70

6.6 Discussion

6.6.1 Quantitative Analysis of Particles Size Distribution

To determine whether the second phases originate from the liquid or the magnesium matrix, quantitative analysis of the density and size of second phases in Figure 6.5 was performed using ImageJ software. The results were compared with the volume fraction predicted by the Scheil model and the mean-field model, which assumes a nucleation site fraction of 10^{-15} , averaged over all temperature range in Figure 6.5. The results are summarized in Table 6.6 and Table 6.7. The experimental error values are derived from the standard deviation of the second phase particle radius and volume fraction measured at different locations, and the error associated with the mean-field model results from variations in the simulations conducted under different assumed cooling rates.

Table 6.6 shows the area fraction of second phase particles at each location in Figure 6.5 for the ZX10 and ZX70 alloys, along with the mean area fraction across all locations. For ZX10, the mean area fraction is 8.86×10^{-3} while for ZX70 is 5.09×10^{-2} . The mean-field model predicts the volume fraction of second phase particles to be approximately 5.41×10^{-4} for ZX10 and 1.38×10^{-2} for ZX70. In contrast, the Scheil model predicts

volume fractions of 5.61×10^{-3} for ZX10 and 5.93×10^{-2} for ZX70. A comparison of the two models reveals that the particle volume fractions predicted by the Scheil model align more closely with the measured area fractions from Figure 6.5, suggesting that the second phase particles in ZX10 and ZX70 are more likely to have originated directly from the liquid rather than forming through precipitation from the supersaturated Mg matrix. However, it should be noted that the quantitative analysis from SEM images provides area fractions of particles on sample cross-sections, which differ from the overall volume fractions in the sample. While the Scheil and mean-field models predict the volume fraction of second phases under specific compositions, some discrepancy may arise. However, the impact of this discrepancy diminishes when the differences between the data are of an order of magnitude.

Table 6.6 Quantitative analysis of the area fraction of second phase particles, in comparison with the volume fraction predicted by the mean-field model and the Scheil model, was conducted for both ZX10 and ZX70 alloys.

| Second phases particles area fraction A_f from Figure 6.5 | | | | | | |
|--|---|--------------------------|--------------------------|--------------------------|--------------------------|--------------------------|
| Location | 1 | 2 | 3 | 4 | 5 | 6 |
| ZX10 | 8.64 $\times 10^{-3}$ | 8.36 $\times 10^{-3}$ | 9.69 $\times 10^{-3}$ | 9.24 $\times 10^{-3}$ | 8.01 $\times 10^{-3}$ | 9.22 $\times 10^{-3}$ |
| Mean area fraction A_f | $8.86 \times 10^{-3} \pm 6.3 \times 10^{-4}$ | | | | | |
| ZX70 | 4.60 $\times 10^{-2}$ | 4.95 $\times 10^{-2}$ | 4.71 $\times 10^{-2}$ | 6.70 $\times 10^{-2}$ | 5.48 $\times 10^{-2}$ | 4.11 $\times 10^{-2}$ |
| Mean area fraction A_f | $5.09 \times 10^{-2} \pm 9.1 \times 10^{-3}$ | | | | | |
| Second phases particles mean volume fraction V_f from Mean-field model | | | | | | |
| ZX10 | $5.41 \times 10^{-4} \pm 1.92 \times 10^{-6}$ | | | | | |
| ZX70 | $1.38 \times 10^{-2} \pm 2.55 \times 10^{-3}$ | | | | | |
| Second phases particles mean fraction V_f from Scheil model | | | | | | |
| ZX10 | 5.61×10^{-3} | | | | | |
| ZX70 | 5.93×10^{-2} | | | | | |

In addition, Table 6.7 shows the mean radius of second phase particles at each location in Figure 6.5 for the ZX10 and ZX70 alloys, along with the overall mean radius across all locations. The results indicate a mean radius of approximately $6.36 \mu\text{m}$ for ZX10 and $15.39 \mu\text{m}$ for ZX70. Due to the limitations of the Scheil model, it cannot provide particle size information, and thus the comparison is limited to the predictions of the mean-field model. According to the mean-field model, the predicted particle sizes are $0.64 \mu\text{m}$ for

ZX10 and $0.30 \mu\text{m}$ for ZX70. These results show that the particle sizes of second phases precipitated from the Mg matrix are significantly smaller than the observed data from Figure 6.5. Combined with the volume fraction predictions, this indicates that the second phase particles are most likely to have formed directly from the liquid phase rather than from solid state diffusion in the Mg matrix.

Table 6.7 Quantitative analysis of the mean radius of second phase particles, in comparison with the mean radius predicted by the mean-field model, was conducted for both ZX10 and ZX70 alloys.

| Second phases particles mean radius \bar{R} (μm) from Figure 6.5 | | | | | | |
|---|------------------|-------|-------|-------|-------|-------|
| Location | 1 | 2 | 3 | 4 | 5 | 6 |
| ZX10 | 7.14 | 6.24 | 7.99 | 7.76 | 5.13 | 3.91 |
| Average \bar{R} | 6.36 ± 1.60 | | | | | |
| ZX70 | 19.00 | 11.80 | 14.29 | 16.39 | 19.48 | 11.40 |
| Average \bar{R} | 15.39 ± 3.49 | | | | | |
| Second phases particles average mean radius \bar{R} (μm) from Mean-field model | | | | | | |
| ZX10 | 0.64 ± 0.12 | | | | | |
| ZX70 | 0.30 ± 0.03 | | | | | |

6.6.2 Second Phases Formation in Scheil Solidification Model

Differences in the partition coefficient k and the numerical methods employed in Scheil calculations significantly impact the accuracy of predicted solidification behavior, particularly in multicomponent alloy systems [225,226,273]. The partition coefficient k determines solute redistribution during solidification and plays a critical role in establishing phase stability, formation temperature, and phase evolution sequence. Variations in the partition coefficients used by the Liquidus-minimising Scheil model and the Thermo-Calc Scheil model can result in notable differences in predictions of phase stability and solidification sequences.

The choice of numerical methods further amplifies these discrepancies, as it governs how the precision with which local phase equilibrium is captured. The Liquidus-minimising Scheil model uses a gradient-minimising approach with a compositional gradient input step size of 0.1 at%, ensuring that the solidification path follows the fastest decreases along the liquidus surface. This approach provides a finer representation of compositional segregation and phase transformations, particularly in systems where minor compositional changes significantly affect phase equilibrium. In contrast, the Thermo-Calc Scheil model employs a more generalized algorithm that simplifies the solidification path using a temperature gradient input step size of 1 Kelvin. While sufficient for many applications, this method may underestimate or overestimate critical phase transformation

temperatures and solid fractions. For instance, as observed in the ZX70 alloy, there are slight deviations in the solidification predictions between the two models. In the ZX10 alloy, the Liquidus-minimising model predicts the formation of Mg_2Ca at $516^\circ C$, whereas the Thermo-Calc Scheil model indicates a much lower formation temperature.

The differences observed between the Liquidus-minimising and Thermo-Calc Scheil models have significant implications for Mg-Zn-Ca alloy optimisation. For compositions sensitive to segregation, such as the ZX10 alloy, even minor discrepancies in k values or numerical modelling can lead to substantial variations in phase distribution and mechanical properties. The Liquidus-minimising model's ability to capture subtle changes in phase equilibrium and segregation paths provides a more detailed understanding of solidification behaviour. In contrast, while the Thermo-Calc Scheil model is convenient for preliminary analyses, it may require enhancements to address the specific demands of complex ternary systems.

6.6.3 Solidification Segregation and Composition Map

The results of the Liquidus-minimising Scheil model indicate that ZX10 and ZX70 alloys exhibit distinct solidification paths, with the composition of ZX10 being closer to the region sensitive to changes in segregation paths compared to ZX70. The compositional diagram in Figure 6.13 illustrates the areas within the Mg-Zn-Ca magnesium-rich corner that are prone to specific elemental segregation. As shown in Figure 6.13, ZX10 is located near the region where both Zn and Ca segregate simultaneously and where Ca segregates independently. This positioning leads to pronounced Ca segregation as solidification progresses. In contrast, ZX70 is situated in the region where Zn segregates independently, making the alloy less sensitive to compositional heterogeneity during non-equilibrium solidification. Considering that the $Ca_2Mg_6Zn_3$ phase can enhance the mechanical properties of alloys [265], the compositional diagram in Figure 6.13 also provides valuable guidance for alloy design. Mg-Zn-Ca alloys with compositions located in regions where both Zn and Ca segregate simultaneously are more likely to form greater amounts of $Ca_2Mg_6Zn_3$ during solidification.

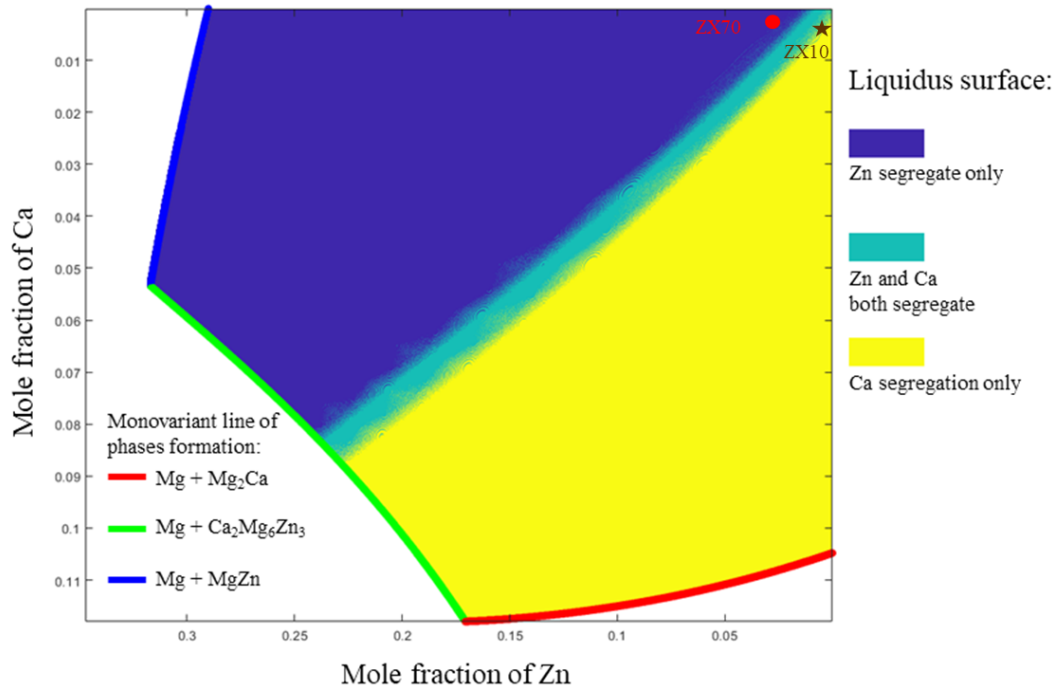


Figure 6.13. Composition map of Mg-Zn-Ca alloys solidification segregation pathway

6.6.4 Precipitation Sequences of Mg-Zn precipitates

In Mg-Zn-Ca alloy system, the precipitation sequences in Mg-Zn binary side are more complex than that of the Mg-Ca side. Figure 6.14 shows the equilibrium phases in Mg-Zn binary system, in which $Mg_{21}Zn_{25}$ also known as $MgZn$ [274]. From Figure 6.14 we can see that at the Mg-enriched corner, stable $Mg_{51}Zn_{20}$ phase will form between temperature $325^{\circ}C$ and $341^{\circ}C$, which is going to form at the eutectic point with 30 at.% of Zn before $MgZn$ phase during the cooling process [275]. In addition, different metastable binary phases are formed during the precipitation process in Mg-Zn alloys, and the generally accepted precipitation sequence is $SSSS \rightarrow GP \text{ zone} \rightarrow \beta'_1 \rightarrow \beta'_2 \rightarrow \beta$, in which β is the equilibrium phase $MgZn$ [99,276]. The GP zone has been described as a coherent nanoscale precipitate of several atomic layers on certain crystalline surfaces of the Mg matrix, however it is still not directly observable because of its small size and coherence with the matrix. Bhattacharjee et al. reported the formation of GP zone in $Mg - 2.4 \text{ at}\% \text{ Zn}$ alloy by 3-dimensional atom probe (3DAP) and observed the existence of Zn clusters [75]. β'_1 usually has a rod-like morphology vertical to the basal plane of the Mg matrix and occurs in peak-aged samples, with the currently widely accepted composition being a mixture of Mg_4Zn_7 and $MgZn_2$ phases [277,278]. β'_2 has a plate-like morphology form at basal plane of Mg matrix and occurs at over-aged samples, which has confirmed with composition as $MgZn_2$ [276,279,280]. In this study,

only stable phases exist in the phase diagram calculation because the thermodynamic database TCMG6 does not contain data on metastable phases. Considering that the focus of this study is on the segregation of alloying elements, all Mg-Zn binary phases in this study are represented by $MgZn$.

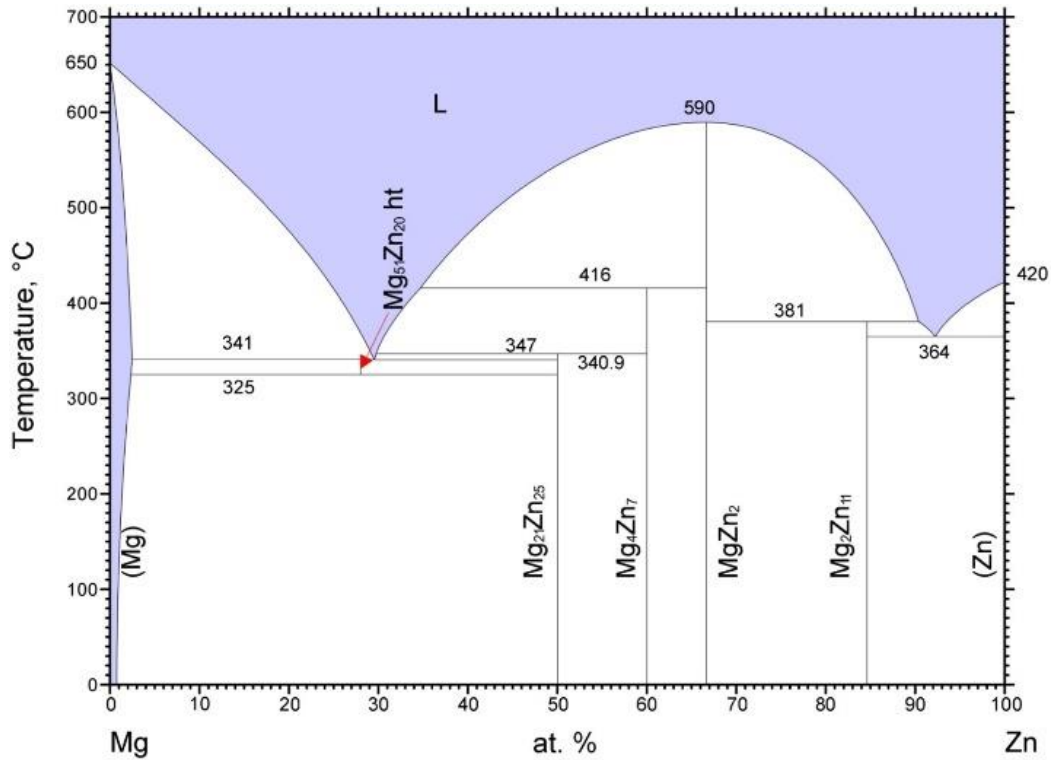


Figure 6.14. Phase diagram of Mg-Zn system [274]

6.7 Conclusion to this chapter

This study systematically explored the solidification and phase formation behaviour of the rapid cooling Mg-0.8 wt.% Zn-0.2 wt.% Ca (ZX10) and Mg-6.8 wt.% Zn-0.2 wt.% Ca (ZX70) alloys using a combination of Scheil and mean-field modelling approaches, integrated with CALPHAD thermodynamic simulations. The following conclusions may be drawn from the present study:

1. SEM-EDS analysis shows that both ZX10 and ZX70 alloys exhibit co-segregation of Ca and Zn at grain boundaries. However, ZX10 contains particles with Ca segregation alone, while ZX70 contains particles with Zn segregation alone. Based on this observation, it can be inferred that Mg_2Ca is likely to form in ZX10, whereas $MgZn$ is expected to form in ZX70.
2. A comparison of the results from the Scheil model, the mean-field model, and the quantitative analysis of SEM images shows that the second phase volume fractions (V_f) predicted by the Scheil model (5.61×10^{-3} for ZX10 and

5.93×10^{-2} for ZX70, respectively) are closer to the area fractions (A_f) obtained from the quantitative analysis (8.86×10^{-3} for ZX10 and 5.09×10^{-2} for ZX70, respectively). In contrast, the second phase particle sizes (\bar{R}) predicted by the mean-field model ($0.64 \mu\text{m}$ for ZX10 and $0.30 \mu\text{m}$ for ZX70, respectively) are significantly smaller than the particle sizes observed in the analysis ($6.36 \mu\text{m}$ for ZX10 and $15.39 \mu\text{m}$ for ZX70, respectively). These findings suggest that second phase particles are more likely to form directly from the liquid during solidification rather than precipitating from the Mg matrix. Therefore, the Scheil model provides predictions that more accurately reflect the behaviour of rapidly solidified Mg-Zn-Ca alloys compared to the mean-field model. This indicates that the laves phase must nucleate from the liquid during solidification, as there is not sufficient time for the precipitates to grow during the cooling to room temperature.

3. The Liquidus-minimising Scheil model developed in this study provides an accurate method for simulating segregation during non-equilibrium solidification, effectively capturing compositional gradient changes and predicting phase formation in both alloys. This approach is particularly effective for ternary alloys, where phase behaviour is highly sensitive to minor compositional variations. A comparison with the Scheil module in the commercial software Thermo-Calc using TCMG6 shows that, while the Thermo-Calc model predicts similar solidification trends, it exhibits differences in the formation temperatures and sequence of second phases, especially in ZX10 alloys, which are highly sensitive to compositional changes during solidification. The results underscored the critical role of compositional control. ZX10 exhibited heightened sensitivity to minor compositional variations, leading to distinct solidification paths and phase distributions, while ZX70 showed more stable phase behaviour.
4. The findings highlight the critical role of precise compositional control and the use of advanced Scheil modelling to optimise the solidification pathways of Mg-Zn-Ca alloys. The differences in the solidification paths of ZX10 and ZX70 are attributed to their varying compositional sensitivities, particularly the segregation behaviour of Zn and Ca.

Chapter 7: Homogenisation, diffusion and second phases dissolution of Mg-Zn-Ca alloys

7.1 Introduction

The presence of second phase intermetallic compounds such as Mg_2Ca and $Ca_2Mg_6Zn_3$ in Mg-Zn-Ca alloys significantly influences their mechanical properties and corrosion behaviour. As highlighted in the previous chapter, the rapid solidification of ZX10 (Mg-0.8Zn-0.2Ca) results in a competitive relationship between these two intermetallic phases, with Mg_2Ca preferentially forming due to localized Ca segregation. This phase competition leads to microstructural heterogeneity, which can negatively impact the alloy's mechanical integrity and corrosion resistance. To address these challenges, post-solidification heat treatment is often employed to homogenise the microstructure by dissolving these second phases into the Mg matrix.

Homogenisation heat treatment is a well-established method for mitigating microstructural inhomogeneity in cast alloys by promoting atomic diffusion, thereby redistributing solute elements more uniformly. In the case of ZX10, the dissolution of Mg_2Ca and $Ca_2Mg_6Zn_3$ through controlled heat treatment is expected to reduce phase segregation and refine the microstructure. However, the effectiveness of this approach depends on the thermal stability and solubility limits of these phases within the Mg matrix, as well as the kinetics of solute diffusion at homogenisation temperatures. Pulido-González et al. [281] have demonstrated that the homogenisation of Mg-Zn-Ca alloys through heat treatment can significantly reduce intermetallic phase fraction and improve corrosion resistance by promoting the dissolution of second phases. Their research emphasizes that the dissolution kinetics of Mg_2Ca and $Ca_2Mg_6Zn_3$ phases depends not only on temperature but also on composition. In as-cast ZX11 (Mg-1Zn-1Ca wt. %) alloy, the predominant intermetallic phase is Mg_2Ca , whereas in as-cast ZX30 (Mg-3Zn-0.2Ca wt. %) alloy, $Ca_2Mg_6Zn_3$ is the main intermetallic phase [282]. After solution treatment at 450°C for 24 hours, most of the $Ca_2Mg_6Zn_3$ dissolves into the Mg matrix, while the Ca-rich precipitate (Mg_2Ca) remains resistant to dissolution. This emphasizes the necessity of optimising heat treatment parameters to balance phase dissolution. Similarly, Schäublin et al. [283] investigated the precipitation behaviour in lean Mg-Zn-Ca alloys and found that binary Mg-Ca precipitates consist of Mg_2Ca containing approximately 4 at. % Zn. They also observed that the formation and dissolution of ternary Mg-Zn-Ca precipitates, such as $Ca_2Mg_6Zn_3$, are highly sensitive to heat treatment temperatures. This emphasizes the necessity of determining precipitate types based on elemental

composition and controlling the homogenisation process to achieve desired microstructural characteristics.

The aim of this chapter is to investigate the homogenisation process for ZX10, focusing on the dissolution kinetics of Mg_2Ca and $Ca_2Mg_6Zn_3$ under heat treatment conditions. Through a combination of experimental measurements and thermodynamic modelling, the evolution of phase fractions, chemical compositions, and grain boundary solute distribution will be analysed. The DICTRA model will be employed to simulate the dissolution behaviour of these phases, incorporating diffusion coefficients from TCMG6 and MOBMG1 databases. Experimental validation using SEM-EDS, EBSD, and EPMA will provide insights into the efficiency of homogenisation and the optimal processing parameters required to achieve a well homogenised microstructure. By understanding the thermal stability and dissolution mechanisms of Mg_2Ca and $Ca_2Mg_6Zn_3$ in ZX10, this study aims to provide guidelines for tailoring heat treatment schedules that enhance alloy performance.

7.2 Materials and Method

7.2.1 Methodology

To control the amount of the Mg_2Ca phase and understand its dissolution kinetics in the ZX10 alloy, a combination of advanced microstructural characterisation techniques and modelling tools was employed, which state in Chapter 4.1.2. These include phase equilibrium and diffusion simulations, which were used to address the uncertainties observed in the dissolution behaviour of the Mg_2Ca phase during homogenisation heat treatment.

During the homogenisation process, solute elements segregated at grain boundaries gradually diffuse into the Mg matrix, leading to a redistribution of alloying elements. To describe this process, the DICTRA module was used to develop a homogenisation model under two different assumptions regarding the diffusion of Mg_2Ca into the Mg matrix:

- **Mg matrix self-diffusion model:** In this scenario, the Mg_2Ca phase is treated as a segregated region of solute elements at the boundary of the Mg matrix. The initial distribution of segregated elements was derived from the Scheil model, which provides a profile of solute concentration across the solidified microstructure. As homogenisation progresses, the Mg_2Ca phase gradually dissolves into the Mg matrix, with diffusion occurring under the assumption of self-diffusion within the

Mg matrix. This model considers that the solute atoms redistribute into the matrix without significant movement of the phase boundary (Figure 7.1).

- Mg-Mg₂Ca diffusion couple model: This model assumes that the Mg₂Ca phase forms a thin intergranular layer at the grain boundaries, in direct contact with the Mg matrix, explicitly modelling the particle-matrix interface. As the homogenisation process proceeds, the interface between the Mg₂Ca phase and the Mg matrix continuously shifts, resulting in the gradual dissolution of the Mg₂Ca phase. In this scenario, the movement of the Mg-Mg₂Ca interface plays a crucial role in the dissolution kinetics, with the phase boundary retreating as diffusion progresses (Figure 7.2).

The DICTRA model employs the TCMG6 thermodynamic database and the MOBGM1 mobility database. To ensure model consistency, the geometry in DICTRA is approximated as a one-dimensional diffusion path extending from the grain centre to the grain boundary, with a total distance of 100 μm . The model domain is uniformly divided into 100 equally sized grid points. The average composition within the model domain is set to match the nominal composition of the EPMA region, as listed in Table 7.2.

In the self-diffusion model, the initial composition of the Mg matrix phase in each grid point is assigned based on the segregation profile obtained from the Scheil model in the previous chapter, replicating the as-cast compositional distribution. In the diffusion couple model, the second phase area fraction detected via high-resolution SEM-BSE image is used to define the Mg₂Ca phase region, while the remaining area is assigned as the Mg matrix phase. The Mg₂Ca phase is further divided into two categories: Zn-free Mg₂Ca and Zn-containing Mg₂Ca [283]. The compositions of these phases are provided in Table 7.1.

To validate these models and assess the redistribution of solute elements, the microstructures of both as-cast and heat-treated ZX10 alloy samples were characterised using scanning electron microscopy with energy-dispersive spectroscopy (EDS), electron backscatter diffraction (EBSD), and electron probe micro-analyser (EPMA). The as-cast data has already been reported in the previous Chapter 6. These techniques allowed for a detailed comparison of the elemental distribution before and after homogenisation. By integrating model predictions with experimental validation, this study aims to reconcile theoretical modelling with practical findings, providing a more comprehensive understanding of the homogenisation behaviour of the Mg₂Ca phase and the associated solute redistribution in ZX10 alloy.

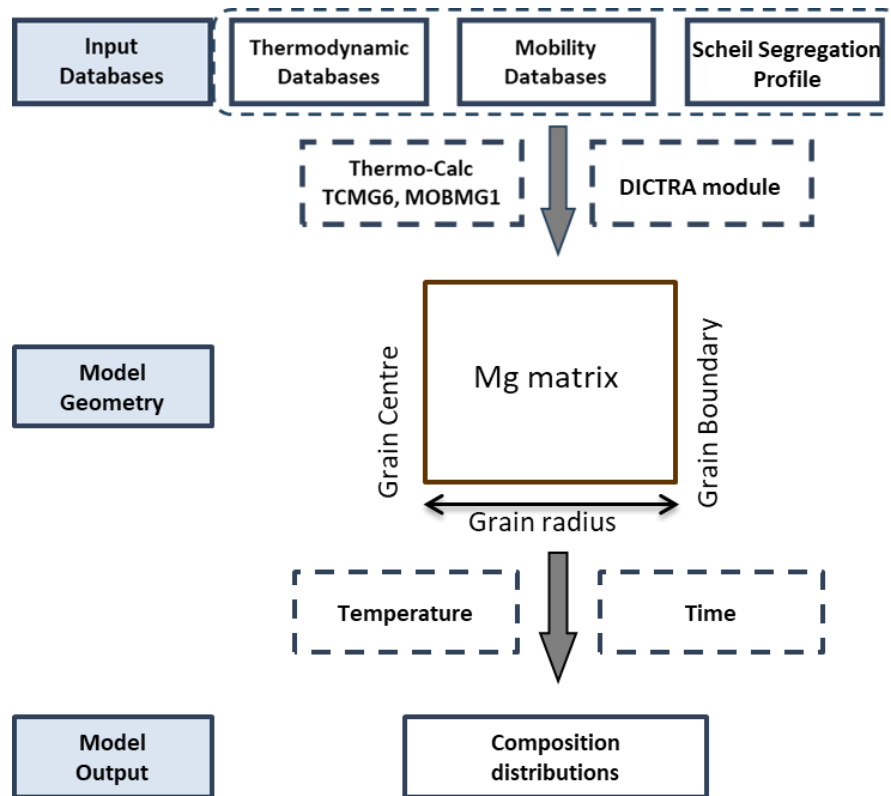


Figure 7.1. The overall process and geometry for self-diffusion DICTRA model

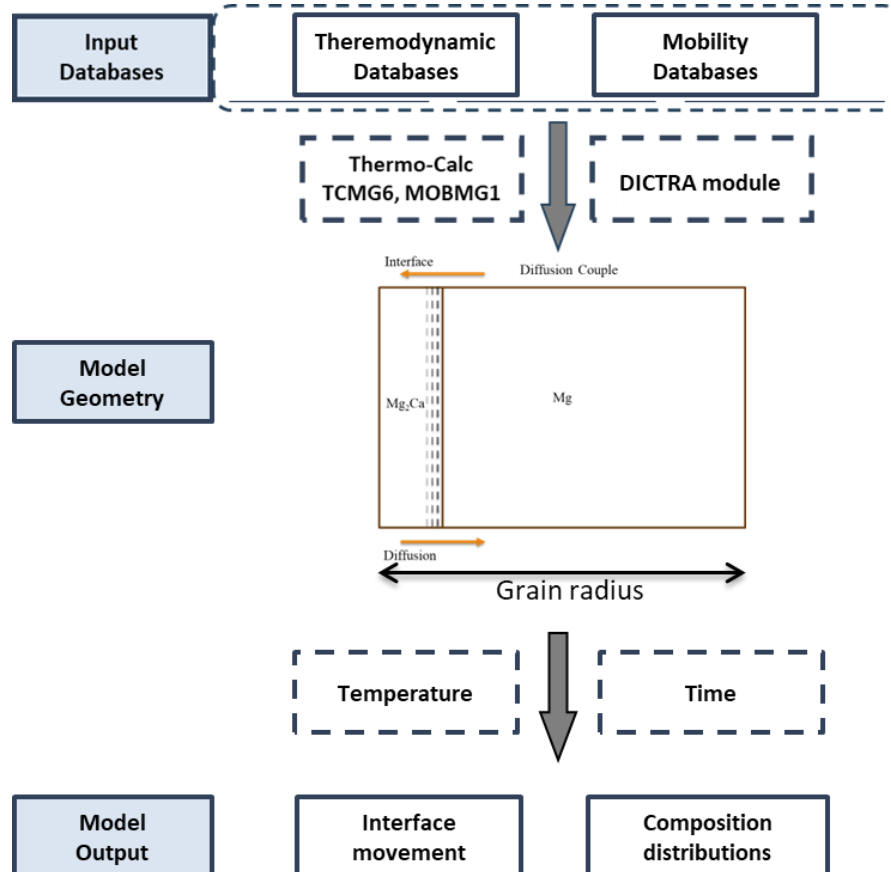


Figure 7.2. The overall process and geometry for Interface diffusion couple DICTRA model

Table 7.1 Chemical composition of Zn-free Mg₂Ca and Zn-containing Mg₂Ca phases

| Alloy | Mg (at. %) | Ca (at. %) | Zn (at. %) |
|----------------------------------|------------|------------|------------|
| Zn-free Mg ₂ Ca | 67 | 33 | - |
| Zn-containing Mg ₂ Ca | 63 | 33 | 4 |

7.2.2 Materials preparation

The as-cast Mg-0.8Zn-0.2Ca (ZX10) alloy was prepared as given in section 6.2.2. The bulk compositions of both ZX10 alloy were measured using inductively coupled plasma optical emission spectroscopy (ICP-OES). To account for local segregation in the test specimens, multiple local compositions were analysed using scanning electron microscopy coupled with energy-dispersive spectroscopy (SEM-EDS). The local composition measured by high resolution SEM was using electron probe micro-analyser. The measured compositions are presented in Table 7.2.

Table 7.2 Chemical composition of as-received ZX10 alloy

| Alloy | Mg (wt. %) | Zn (wt. %) | Ca (wt. %) | Measured by |
|-------|------------|------------|------------|-------------|
| ZX10 | Bal. | 0.8 | 0.2 | ICP-OES |
| ZX10 | Bal. | 0.8-1.2 | 0.2-0.5 | SEM-EDS |
| ZX10 | Bal. | 1.18 | 0.44 | EPMA |

7.3 Microstructure of As-Cast and Homogenised ZX10 Alloys

Figure 7.3 shows the microstructure and compositional distribution of ZX10 alloy under as-cast and homogenised conditions. The SEM images in Figure 7.3a are same as Figure 6.5a in the previous chapter, which reveal the presence of bright intermetallic phases distributed along the grain boundaries in the as-cast condition. The corresponding EDS elemental maps indicate that these phases are enriched in Zn and Ca, suggesting the formation of intermetallic compounds such as Ca₂Mg₆Zn₃ or Mg₂Ca.

After heat treatment at 520°C for 4 hours (Figure 7.3b), the microstructural evolution indicates a significant reduction in the volume fraction of intermetallic phases. The EDS maps show that the distribution of Zn in the matrix becomes more uniform, suggesting partial dissolution of the second phases and the diffusion of Zn into the α -Mg matrix. However, some residual second phase particles containing Ca remain, particularly as large particles near the grain boundaries, indicating that homogenisation is not complete under the given heat treatment conditions. The gradient of Zn and Ca distribution from the surface (position 1) to the core (position 6) provides insight into the diffusion

behaviour during homogenisation. In the as-cast state, Zn and Ca are highly concentrated in interdendritic regions, whereas after heat treatment, the elemental distribution becomes more even, implying that diffusion-driven homogenisation occurs over time. The presence of residual Ca-rich phases suggests that the dissolution kinetics of Ca-containing intermetallics are slower compared to Zn-containing phases. Therefore, it can be inferred that the Mg_2Ca particles are harder to dissolve than $Ca_2Mg_6Zn_3$ in ZX10 alloy.

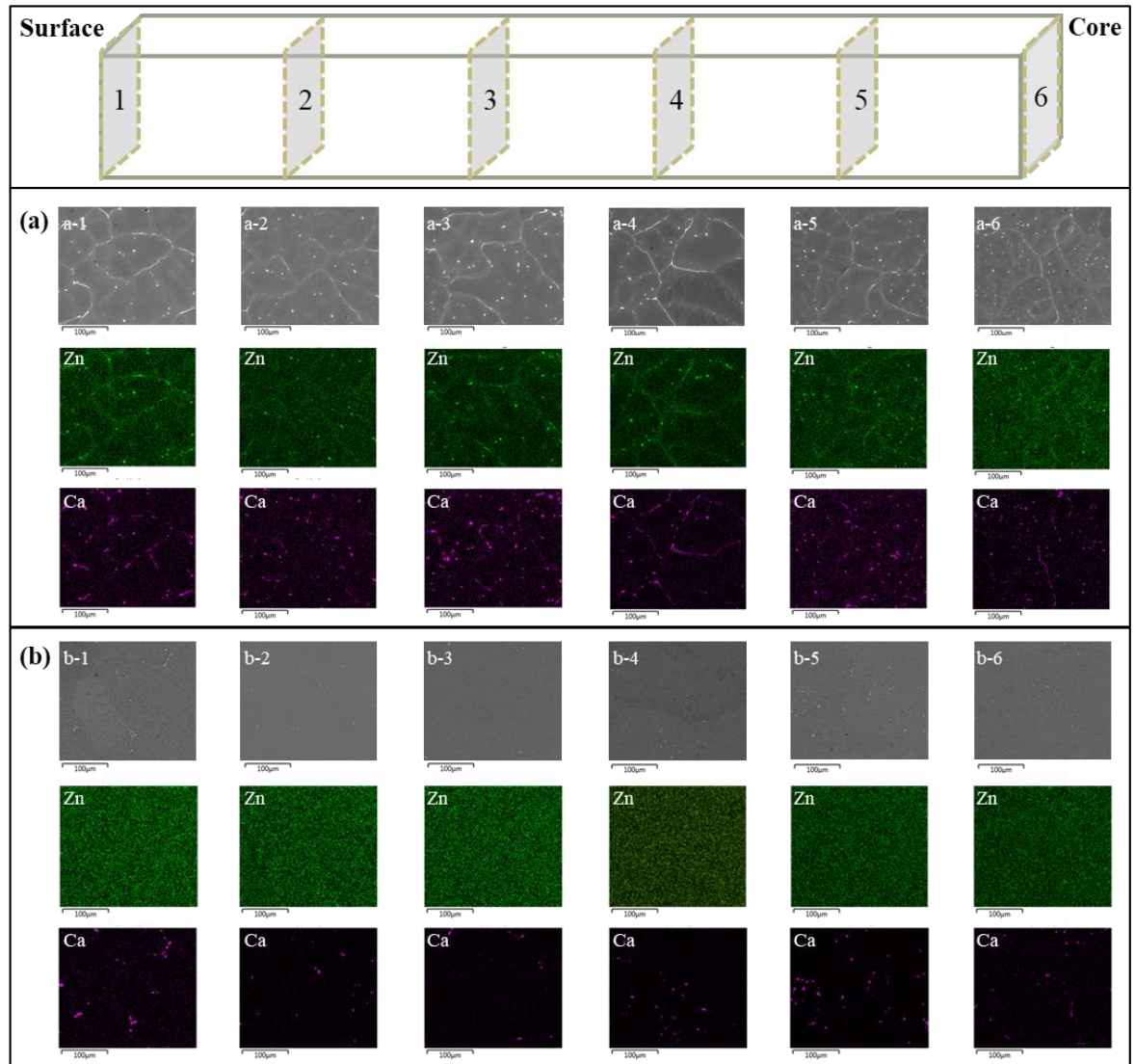


Figure 7.3. SEM-BSE and EDS map results of ZX10 alloy at (a) as-cast condition and at (b) 520 °C heat-treated for 4 hours, from surface (1) to core (6)

Figure 7.4 presents the high-resolution SEM microstructure and EBSD phase detection of the ZX10 alloy in both as-cast and homogenised conditions, with the average size and area fraction of second phase particles summarised in Table 7.3. The SEM image in Figure 7.4a shows a network of second phase particles distributed along the grain boundaries in the as-cast condition. These phases are mainly located at the grain

boundaries and interdendritic regions, indicating their formation due to solute segregation during solidification. After heat treatment at 520°C for 4 hours (Figure 7.4b), a significant microstructural transformation occurs. The second phase particles exhibit noticeable dissolution, with only a few remaining along the grain boundaries. However, some residual second phase regions persist, particularly in coarse-grained areas where diffusion-driven homogenisation is less effective. This observation is consistent with the EDS results in Figure 7.3, where Ca-rich particles remain undissolved even after prolonged heat treatment. The persistence of some coarse second phase particles suggests that complete homogenisation may require either an extended annealing duration or a higher temperature. The classic Scheil not predicting the laves phase suggests the database is underpredicting the stability of the laves phase. There are two possibilities: either the Mg_2Ca phase is thermodynamically stable at this temperature, or the dissolution kinetics are much slower than anticipated.

EBSDF phase detection of second phase particles at grain boundaries revealed that the Mg_2Ca phase could be clearly detected at grain boundaries in the as-cast condition. However, after homogenisation, only a small number of pixels corresponding to this phase remained at the grain boundaries, indicating that the homogenisation process significantly reduced the Mg_2Ca phase content in the ZX10 alloy. In contrast, the $Ca_2Mg_6Zn_3$ phase was difficult to detect in both as-cast and homogenised conditions, suggesting that its content is much lower than that of the Mg_2Ca phase or that Zn exists in small quantities within the Mg_2Ca phase [283]. To obtain a more precise Zn distribution and further investigate the evolution of Zn-containing phases, EPMA analysis was conducted in the subsequent results.

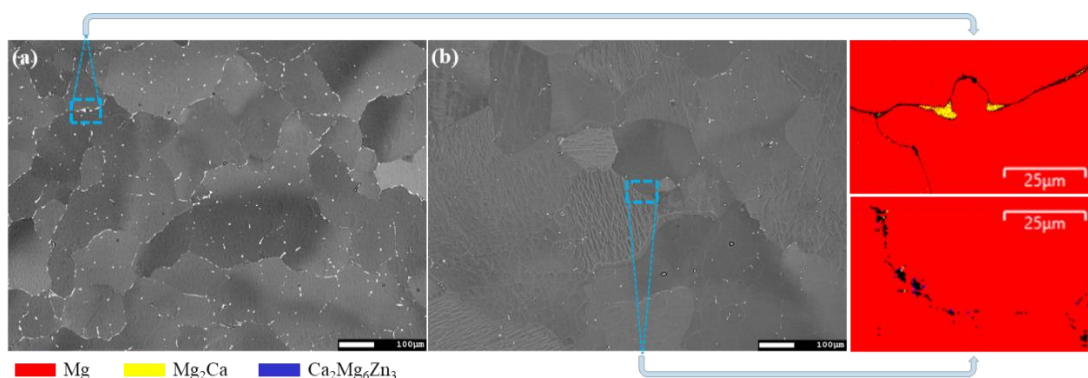


Figure 7.4. SEM-BSE images and EBSD phases index of ZX10 alloy at (a) as-cast condition and at (b) 520 °C heat-treated for 4 hours

Table 7.3 Quantitative analysis of the area fraction of second phase particles for as-cast and heat-treated at 520 °C for 4 hours in ZX10 alloys.

| Second phases particles from Figure 7.4 | | | |
|--|-----------------|--------------------------------|-------------------|
| ZX10 | Particles Count | Average Size (μm) | Area fraction (%) |
| AC | 1622 | 7.195 | 1.143 |
| HT | 871 | 2.610 | 0.223 |

Figure 7.5 presents the high-resolution compositional distribution from EPMA results of the ZX10 alloy under as-cast and homogenised conditions. The average composition in this local region display in Table 7.4. The SEM images in Figure 7.5a and Figure 7.5d illustrate the microstructure of the alloy before and after heat treatment at 520°C for 4 hours. In the as-cast condition (Figure 7.5a), second phase particles are distributed along the grain boundaries. The corresponding EPMA elemental maps (Figure 7.5b and c) confirm that these second phase particles are enriched in Ca (up to 23 at. %) and contain a small amount of Zn (up to 2 at. %), indicating the presence of intermetallic compounds, such as the Mg_2Ca phase with minor Zn incorporation.

After homogenisation (Figure 7.5d), a reduction in second phase particles is observed, leaving behind relatively larger particles. The EPMA maps (Figure 7.5e and f) show a significant decrease in Ca content in the grain boundary regions, indicating partial dissolution of the Mg_2Ca phase. Similarly, the Zn signal intensity within the second phase regions is notably reduced after heat treatment, with Zn more uniformly distributed within the α -Mg matrix. However, some residual second phase particles remain detectable, particularly in regions where the Ca concentration remains relatively high (approximately 23 at. %). These high-Ca-content particles appear resistant to dissolution in the α -Mg phase. This observation is consistent with the EBSD results in Figure 7.4, where only a small fraction of Mg_2Ca was detected after homogenisation, suggesting incomplete dissolution under the given heat treatment conditions.

The EPMA results also provide additional insight into the distribution of Zn within the alloy. As shown in Figure 7.5c, Zn-rich regions are present in the as-cast condition, though most of the Zn content remains around 1 at. %. After heat treatment, Zn appears to be more evenly distributed in the matrix (Figure 7.5f). As indicated by the EBSD analysis, no distinct $\text{Ca}_2\text{Mg}_6\text{Zn}_3$ phase was detected in either the as-cast or homogenised conditions, suggesting that Zn is most likely incorporated into the Mg_2Ca phase rather than forming a separate intermetallic phase. These results confirm that homogenisation at 520°C promotes the dissolution of second phases and enhances elemental distribution uniformity in the ZX10 alloy. However, some Ca-rich regions persist, indicating that

complete homogenisation may require an extended heat treatment duration or a higher temperature to fully dissolve intermetallic compounds.

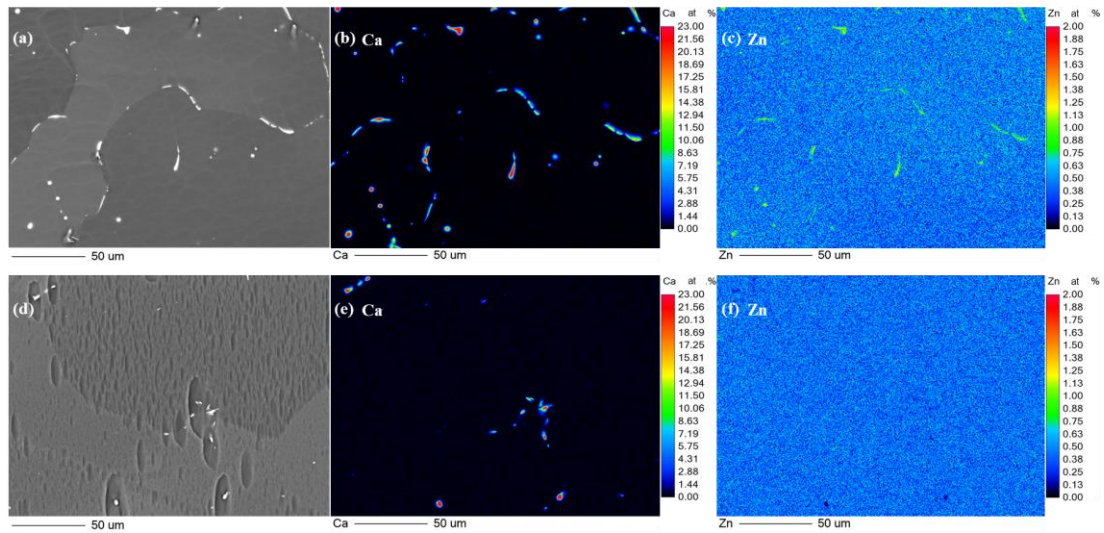


Figure 7.5. SEM-BSE and EPMA map results of ZX10 alloy at (a-c) as-cast condition and at (d-f) 520 °C heat-treated for 4 hours

Table 7.4 Average composition of as-cast and heat-treated sample in **Figure 7.5**.

| Average composition | | | |
|---------------------|-------|-------|-------|
| Zn | | Ca | |
| at. % | wt. % | at. % | wt. % |
| 0.44 | 1.18 | 0.27 | 0.44 |

7.4 DICTRA Simulation of ZX10 Alloys

Figure 7.6 to Figure 7.9 provide a computational perspective on element diffusion and phase dissolution during the homogenisation process of the ZX10 alloy at 520°C. The self-diffusion model (Figure 7.6 and Figure 7.7) highlights the gradual homogenisation of alloying elements within the Mg matrix over time, while the Mg-Mg₂Ca diffusion couple model (Figure 7.8 and Figure 7.9) emphasises the interface evolution between the Mg₂Ca phase and the Mg matrix as diffusion progresses, along with the challenges associated with the redistribution of alloying elements. These simulations, in conjunction with the experimental results, emphasize the importance of optimising heat treatment parameters to achieve a fully homogenised microstructure, as well as the limitations and potential improvements of the current model.

7.4.1 Self-Diffusion in Mg Matrix

Figure 7.6 presents the simulated compositional distribution of Mg, Ca, and Zn in the ZX10 alloy during heat treatment at 520°C for different time intervals (10 s, 100 s, 1000

s, and 10,000 s) using the self-diffusion DICTRA model. The simulation assumes that, based on predictions from the Scheil solidification model, elemental distribution in the as-cast condition is segregated along the grain boundaries. As heat treatment progresses, the concentration gradients of Ca and Zn gradually diminish, indicating element homogenisation. The diffusion profiles show that Ca exhibits slower diffusion kinetics compared to Zn, leading to more persistent segregation near grain boundaries. After 10,000 s, an almost uniform elemental distribution is observed, demonstrating the effectiveness of long-duration heat treatment in reducing microsegregation, however predicts the complete dissolution of the Mg₂Ca phase which is not seen experimentally. Figure 7.7 compares the self-diffusion compositional distributions in the as-cast and heat-treated (520°C, 4 hours) conditions. The results indicate that after 4 hours of heat treatment, Ca and Zn are more uniformly distributed within the α -Mg matrix.

According to the Scheil model predictions, Ca segregation at the grain boundary can reach up to 11.80 at. %, while Zn segregation can be as high as 17.06 at. %. However, due to the grid discretisation in this model, the grid closest to the grain boundary represents the average composition over a 1 μ m region, where Ca content is 2.39 at. % and Zn content is 11.76 at.%. As a result, this model underestimates the degree of elemental segregation at grain boundaries, particularly for Ca. Therefore, although the self-diffusion model predicts that homogenisation is achieved after 4 hours at 520°C, EPMA experimental results still reveal the presence of high-Ca content particles, indicating a discrepancy between the model predictions and experimental observations.

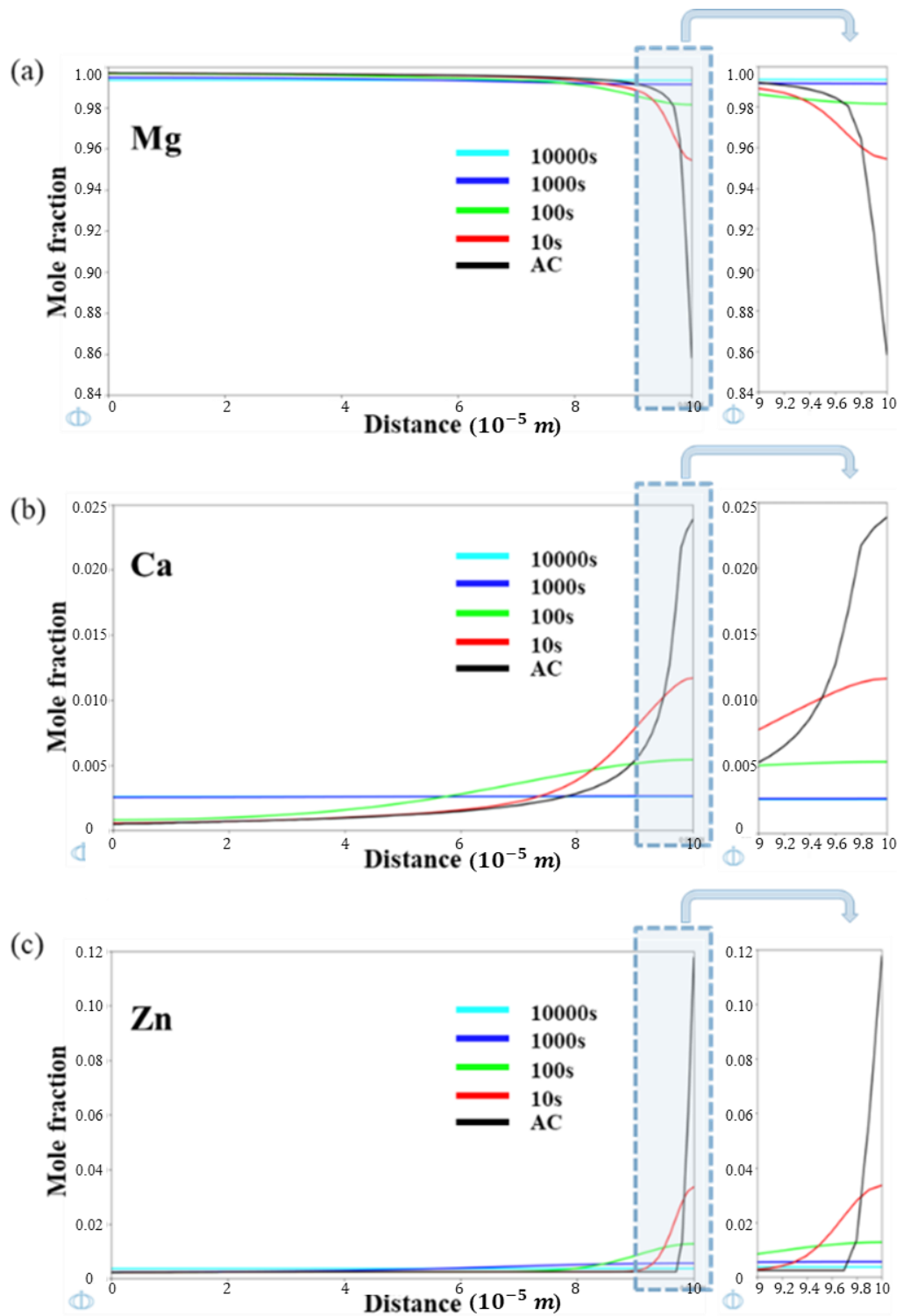


Figure 7.6. The self-diffusion DICTRA compositional distribution of (a) Mg, (b) Ca, and (c) Zn at heat-treated at 520°C conditions for 10s, 100s, 1000s, and 10000s in ZX10 alloy.

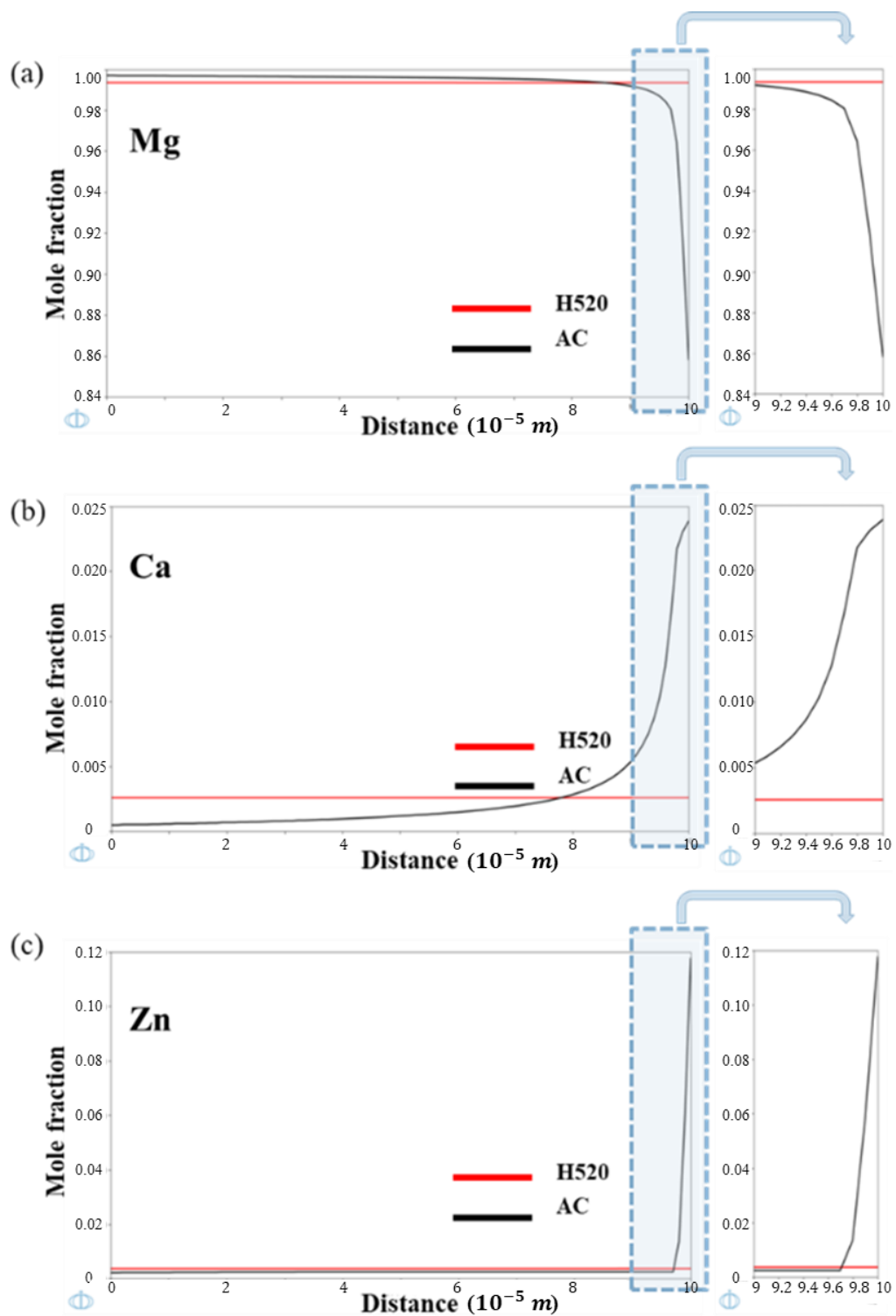


Figure 7.7. The self-diffusion DICTRA compositional distribution of (a) Mg, (b) Ca, and (c) Zn at as-cast and heat-treated at 520°C, 4 hours conditions in ZX10 alloy.

7.4.2 Diffusion Couple Between Mg Matrix and Second Phases

Figure 7.8 and Figure 7.9 present the results of the diffusion couple DICTRA model, which accounts for the interaction between the Mg matrix and grain boundary Mg_2Ca phase particles. The initial area fraction of the Mg_2Ca phase in the model is set at 1.1%, based on the results in Table 7.3. In Figure 7.8, the Mg_2Ca phase is assumed to contain 4

at. % Zn [283], whereas in Figure 7.9, it is assumed to be Zn-free. Figure 7.8b and Figure 7.8 illustrate the compositional distribution of Ca and Zn over different time intervals. The results indicate that Zn diffuses into the matrix relatively quickly, while the dissolution of Ca is significantly slower, leading to a more persistent concentration gradient. This aligns with the experimental observation that Ca-rich phases exhibit lower solubility. Figure 7.8a tracks the interface movement between the Mg₂Ca phase and the Mg matrix over time, showing that Zn-containing Mg₂Ca gradually dissolves into the matrix within approximately 2000 seconds during heat treatment. However, this is inconsistent with the experimental observations, where residual Ca-rich second phase particles persist even after homogenised.

To further investigate the dissolution kinetics of Mg₂Ca under different Zn conditions, Figure 7.9 assumes a Zn-free Mg₂Ca phase. Figure 7.9a shows the evolution of the Mg₂Ca/Mg interface, revealing a significant slowdown in dissolution over extended time durations, indicative of diffusion-limited behaviour. When the Mg₂Ca/Mg interface moves and the Mg₂Ca phase fraction decreases from 1.1% to 0.2%, further dissolution terminated. This aligns with the quantitative analysis in Figure 7.4 and Table 7.3, suggesting that a fraction of the Mg₂Ca phase remains stable under the given homogenisation conditions. Figure 7.9b presents the Ca compositional distribution over time, showing that while the Ca concentration gradually shifts as the interface moves, complete homogenisation remains challenging within practical heat treatment times. Additionally, the Ca concentration within the Mg₂Ca phase slightly increases, indicating further stabilization of this phase.

By comparing the diffusion couple DICTRA model results (Figure 7.8 and Figure 7.9) with the SEM experimental findings, it is evident that the Mg₂Ca phase cannot be fully dissolved at 520°C through an industrially relevant heat treatment. As shown in Figure 7.5, large residual Mg₂Ca particles with high Ca content persist even after heat treatment. Moreover, in conjunction with the equilibrium phase diagram in Figure 6.8, it can be observed that 520°C is near the solidus temperature, and in equilibrium conditions, Mg₂Ca should not be present. This suggests that the large Mg₂Ca particles formed during solidification may exhibit different precipitation kinetics compared to the Mg₂Ca particles along the grain boundaries. Consequently, increasing the homogenisation temperature or extending the annealing duration may not be effective in completely eliminating large Mg₂Ca particles. Additionally, Zn incorporation may alter the diffusion kinetics of the

Mg₂Ca phase, highlighting the need for more precise thermodynamic and kinetic descriptions of Zn-containing Mg₂Ca in the TCMG6 and MOBMG1 databases.

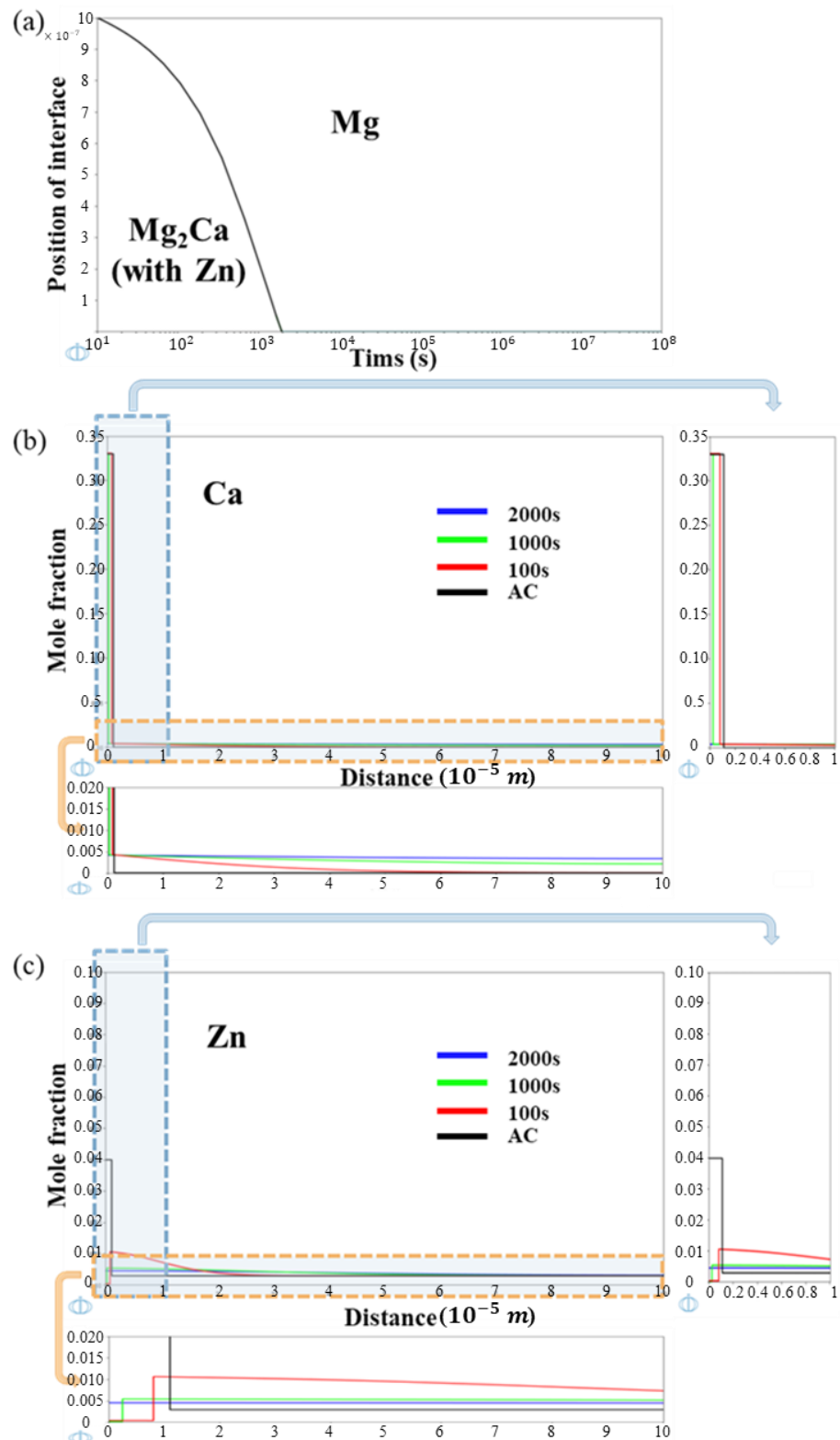


Figure 7.8. The diffusion couple DICTRA of (a) interface movement and (b,c) compositional distribution of (b) Ca, and (c) Zn at as-cast and heat-treated at 520°C for 100, 1000, and 2000 seconds conditions in ZX10 alloy.

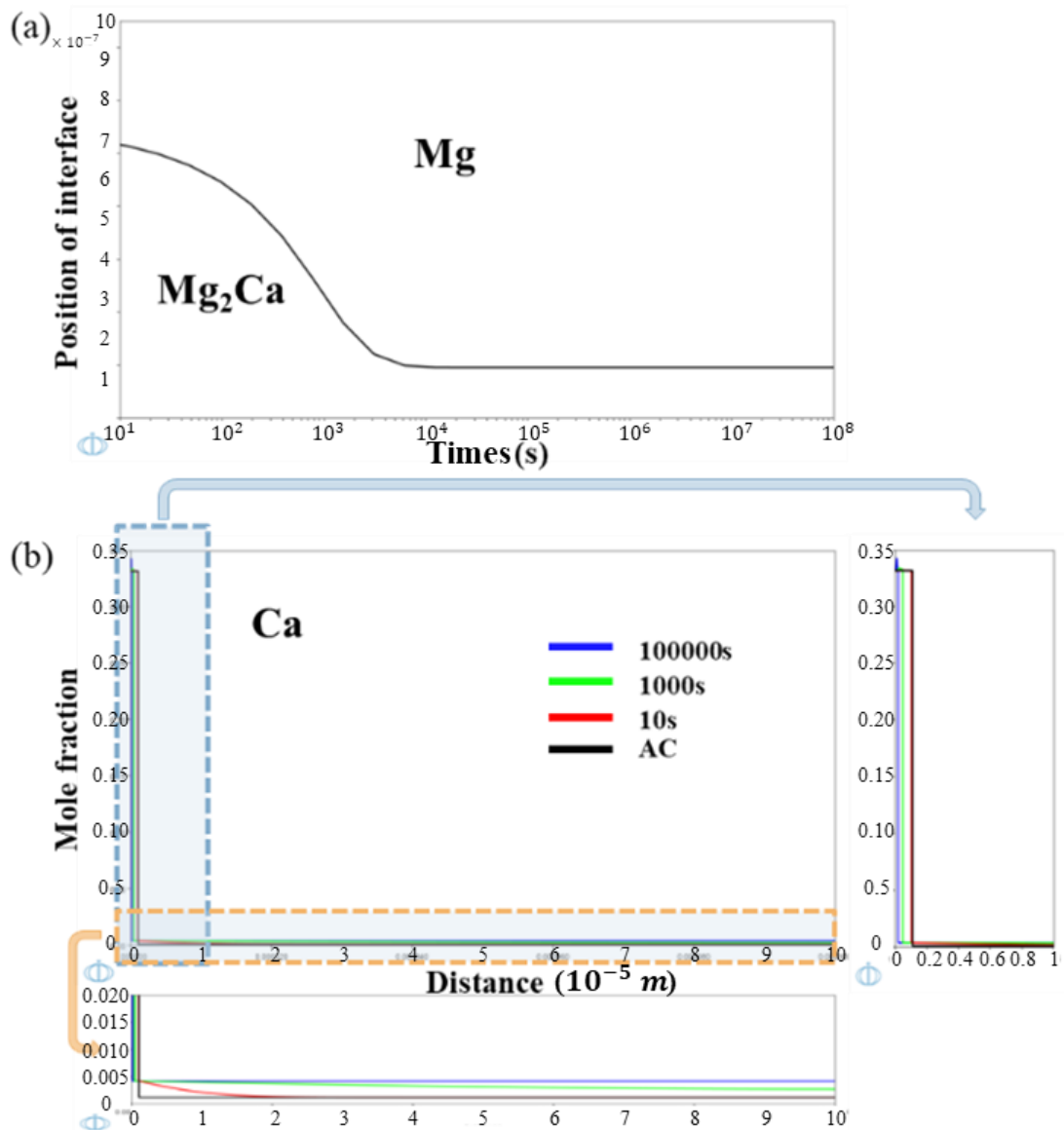


Figure 7.9. The diffusion couple DICTRA of (a) interface movement and (b) compositional distribution of Ca at as-cast and heat-treated at 520°C for 100, 1000, and 100000 seconds conditions in ZX10 alloy.

7.5 Discussion

7.5.1 Precipitates in ZX10 Alloy

The results section indicates that the primary intermetallic phases in the ZX10 alloy are Mg₂Ca and, to a lesser extent, Ca₂Mg₆Zn₃. These phases play a crucial role in the alloy's mechanical properties and thermal stability. Mg₂Ca is the dominant precipitate observed in the as-cast ZX10 alloy, primarily forming at grain boundaries due to Ca segregation during solidification. The Scheil solidification model predicted significant Ca enrichment at the grain boundaries, which was also confirmed experimentally by EPMA and SEM-EDS analysis (Figure 7.3 to Figure 7.5). The presence of this phase aligns with previous

studies on Mg-Ca alloys, where Mg_2Ca is known to form preferentially at grain boundaries and exhibit high thermal stability due to its high melting point ($711^\circ C$) [284] rather than $Ca_2Mg_6Zn_3$ with melting point at about $450^\circ C$ [285]. However, its persistence after heat treatment at $520^\circ C$ suggests that it exhibits low solubility in the α -Mg matrix, leading to incomplete homogenisation. This observation is consistent with prior research indicating that Mg_2Ca has low solubility in Mg.

The presence of Zn in the ZX10 alloy introduces additional complexity to precipitate evolution. While the DICTRA diffusion couple model (Figures 7.8 and 7.9) suggests that Zn accelerates the dissolution of Mg_2Ca , experimental observations (Figure 7.5) indicate that residual Mg_2Ca particles persist even after prolonged heat treatment. Pulido-González et al. [282] studied ZX11 and reported that in Mg-Zn-Ca alloys with a relatively low Zn/Ca atomic ratio (<1.2) after solidification, the microstructure consists of α -Mg matrix grains and intergranular $Ca_2Mg_6Zn_3$ and Mg_2Ca phases. After 24 hours of heat treatment at $450^\circ C$, only the $Ca_2Mg_6Zn_3$ phase was dissolved.

The absence of $Ca_2Mg_6Zn_3$ in the EBSD analysis suggests that Zn primarily incorporates into Mg_2Ca rather than forming a distinct phase. This finding aligns with Schäublin et al. [283], who investigated ZX20 (Mg-1.5Zn-0.25Ca wt. %) using STEM-EDS and found that binary Mg-Ca precipitates contained an average composition of 67 at. % Mg, 3 at. % Zn, and 30 at. % Ca, with STEM-EDS images provided in Figure 7.10 of their study. Their results support the hypothesis that Zn incorporation alters the dissolution kinetics of Mg_2Ca .

Another potential factor is the inherently sluggish diffusion kinetics of Ca in the Mg matrix. Even at elevated temperatures, the diffusion rate of Ca may be too slow to facilitate the rapid dissolution of the Mg_2Ca phase. This slow diffusion could result in the persistence of Mg_2Ca precipitates despite prolonged heat treatment. Additionally, the thermodynamic stability of the Mg_2Ca phase itself may play a role. The phase may possess a high dissolution temperature, necessitating heat treatment at temperatures that are impractical due to the risk of compromising the integrity of the Mg matrix or inducing other undesirable phase transformations. One possibility is that during homogenization, Ca atoms diffuse from the Mg_2Ca phase into the surrounding Mg matrix, leading to an increase in local Ca concentration. This localized enrichment could potentially lower the melting point of the adjacent Mg-rich matrix, approaching or even falling below the stability temperature of the Mg_2Ca phase. Consequently, elevating the homogenization

temperature to dissolve the Mg₂Ca phase might risk localized melting, while lower temperatures may be insufficient for complete dissolution.

The findings indicate that while homogenisation at 520°C can partially dissolve second phase precipitates, the slow diffusion kinetics of Mg₂Ca, possibly influenced by Zn, make its complete dissolution challenging. While fine Mg₂Ca particles can serve as effective grain refiners and precipitation strengthening agents, coarse Mg₂Ca particles at grain boundaries are known to promote brittle fracture and reduce ductility. Therefore, efforts should be made to control alloy composition during solidification to minimise the formation of coarse Mg₂Ca phases and improve the overall mechanical performance of the alloy.

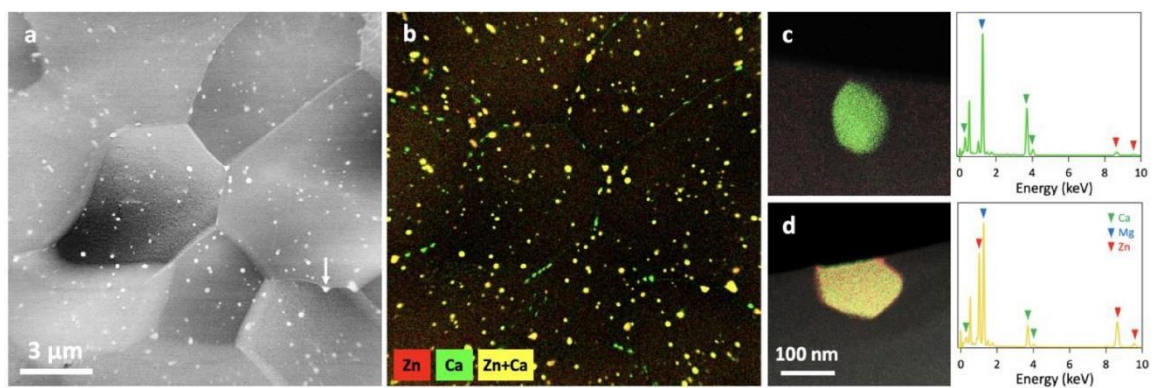


Figure 7.10. ZX20 extruded at 330°C. (a) HAADF STEM image, revealing grains of a few microns and precipitates of about 50 to 200 nm in size. The arrow points at a precipitate that pins a grain boundary, as shown by the bowing of the latter. (b) Corresponding STEM EDS map, exhibiting Zn-, Ca-, and Zn+Ca-rich regions; Mg is omitted for clarity. It reveals the (green) binary Mg–Ca and (yellow) ternary Ca–Mg–Zn precipitates. (c) Binary Mg–Ca precipitate and (d) ternary Ca–Mg–Zn precipitate, both taken at the very edge of the thin sample to avoid matrix overlap, with their corresponding EDS spectrum on the right. [283]

7.5.2 The limitation of Initial Segregation

The accuracy of diffusion modelling and homogenisation predictions in the ZX10 alloy depends significantly on how the initial segregation profile is defined. In this study, the self-diffusion and diffusion couple DICTRA models were built based on an assumed initial segregation state derived from the Liquidus-minimising Scheil solidification model. While this assumption provides a reasonable approximation of solute redistribution during casting, it does not fully capture the actual elemental segregation observed experimentally, which introduces limitations to the predictive accuracy of the simulations.

The Scheil model assumes that solid-state diffusion during solidification is negligible, leading to maximum solute enrichment at grain boundaries. However, actual cast microstructures experience partial back diffusion, particularly for elements with high diffusivity in Mg, such as Zn. EPMA and EDS mapping results (Figure 7.3 to Figure 7.5)

indicate that while Ca exhibits strong segregation at grain boundaries, Zn distribution is more homogeneous than predicted by the Scheil model. Furthermore, in the Scheil model the predicted grain boundary Ca content in the as-cast condition is as high as 11.80 at. %, while Zn is estimated at 17.06 at. %. However, in the DICTRA model, the grid closest to the grain boundary represents an average composition over a 1 μm region, which dilutes the localized segregation effect and results in lower initial concentrations (2.39 at. % Ca and 11.76 at. % Zn). This discrepancy underestimates the actual segregation intensity, particularly for Ca, and may lead to an overestimation of homogenisation rates in the model.

The inaccuracies of the initial segregation profile may contribute to DICTRA's underestimation of the time required for full homogenisation. As shown in Figure 7.6 and Figure 7.7, the self-diffusion model predicts that complete elemental homogenisation is achieved after 4 hours at 520°C, but EPMA results (Figure 7.5) reveal residual Ca-rich regions. This suggests that actual homogenisation kinetics are slower than predicted, possibly due to an underestimation of grain boundary segregation. If the model assumes a lower initial Ca content at the grain boundary, it will overestimate diffusion-driven homogenisation, as the imposed concentration gradient would be smaller than in reality.

The limitations in initial segregation modelling affect not only diffusion predictions but also precipitate dissolution behaviour. The overestimated homogenisation rate in the self-diffusion model does not fully align with the persistence of Mg_2Ca precipitates observed in experiments (Figures 7.5 and 7.8). If actual initial segregation is stronger than modelled, the dissolution of Mg_2Ca would require more time, which is consistent with experimental findings but not accurately captured in simulations. The use of the Scheil model may underestimate grain boundary segregation intensity, leading to an overestimation of homogenisation efficiency. Future improvements should integrate experimentally measured segregation profiles and finer discretisation to enhance predictive accuracy and better align with experimental observations.

7.6 Conclusion to this chapter

This chapter investigated the homogenisation, diffusion, and second phase dissolution behaviour of the ZX10 alloy (Mg-0.8Zn-0.2Ca), combining experimental characterisation and DICTRA diffusion simulations to assess the effectiveness of heat treatment in refining the microstructure. The key findings can be summarised as follows:

1. The intermetallic phases in ZX10 are Mg_2Ca and $Ca_2Mg_6Zn_3$, with Mg_2Ca being the dominant precipitate due to its preferential formation along grain boundaries as a result of Ca segregation during solidification. Zn can primarily incorporate into Mg_2Ca rather than forming a distinct phase, and it may influence the dissolution behaviour of Mg_2Ca . Heat treatment at $520^\circ C$ for 4 hours led to a significant reduction in second phase particles, particularly $Ca_2Mg_6Zn_3$, while Mg_2Ca remained partially undissolved, confirming its higher thermal stability and slower dissolution kinetics.
2. DICTRA simulations revealed that Zn diffuses faster than Ca, leading to a more homogeneous Zn distribution after heat treatment, while Ca exhibits a more persistent concentration gradient, particularly near grain boundaries. The self-diffusion model predicted complete homogenisation after 4 hours at $520^\circ C$, but experimental data (EPMA, SEM-EDS) showed residual Ca-rich regions, indicating that actual homogenisation kinetics are slower than predicted. The diffusion couple model highlighted the movement of the Mg_2Ca/Mg interface, showing that dissolution of Zn-containing Mg_2Ca is faster than Zn-free Mg_2Ca , but in both cases, residual second phase particles remained after homogenisation.
3. It is likely that the Scheil model used to define initial segregation overestimated Zn segregation while underestimating the intensity of Ca enrichment at grain boundaries, leading to an overestimation of homogenisation rates in DICTRA simulations. Since large Mg_2Ca particles are difficult to dissolve, controlling their formation during casting through alloy composition adjustments or cooling rate modifications may be more effective than relying on post-solidification heat treatment.

Chapter 8: Precipitation, mechanical properties and microstructure of Mg-Zn-Ca(-Ag) alloys

8.1 Introduction

The mechanical properties of Mg-Zn-Ca alloys are strongly influenced by the morphology, size, distribution, and stability of second phase precipitates. Controlling these precipitates through heat treatment is critical for optimising the alloy's mechanical performance. Post-extrusion heat treatments, particularly T4 solution treatment and T6 ageing treatment, are widely applied to refine the microstructure, and balance precipitation strengthening and ductility [286]. These treatments influence the alloy's texture evolution and the transformation of precipitates, including key strengthening phases such as the Mg-Zn binary precipitates ($\beta'_1, \beta'_2, \beta$), and Mg-Zn-Ca ternary precipitate ($\text{Ca}_2\text{Mg}_6\text{Zn}_3$) in Mg-3Zn-0.2Ca (wt. %) alloy [79,151,164].

Extrusion processes inherently produce a strong crystallographic texture, resulting in mechanical anisotropy in magnesium alloys [101]. To mitigate this and improve mechanical properties, T4 solution heat treatment is employed to dissolve existing precipitates and redistribute solute elements within the Mg matrix, creating a supersaturated solid solution. This homogenised state serves as a precursor for subsequent T6 heat treatment, where controlled ageing facilitates the nucleation and growth of strengthening precipitates. The effectiveness of these ageing treatments, however, is highly dependent on factors such as temperature, duration, and alloy composition, which influence both the stability and transformation of precipitates over time.

The generally accepted precipitation sequence is S.S.S.S. \rightarrow Guinier-Preston (GP) zone $\rightarrow \beta'_1 \rightarrow \beta'_2 \rightarrow \beta$ among the key precipitates in high Zn content Mg-Zn-Ca alloys [79,165]. The β -phase (MgZn) is the stable, equilibrium precipitate, which tends to form at high temperatures or long ageing durations. While the β -phase is generally coarse and less effective at impeding dislocation motion, strengthening in aged Mg-Zn-Ca alloys is provided by GP zone, with more efficient pinning of dislocations provided by the metastable β'_1 phase, which forms a fine, dispersed precipitation variant of the MgZn phase that precipitates during ageing. However, β'_1 is metastable and can transform into β'_2 during over ageing, the latter characterised as a coarser dispersion that will limit the strengthening effect of β'_1 . Therefore, understanding and optimising the precipitation kinetics of β' type precipitates is critical for achieving superior mechanical properties.

Incorporating silver (Ag) as an additional alloying element has been explored as a strategy to refine precipitate structures and further improve mechanical performance. In a previous study by Mendis et al. [167,287], it was found that the appropriate addition of Ag improves the mechanical properties of aged Mg-Zn-Ca alloys, and the ageing strengthening response time aligns with the precipitation of β' type precipitates. Therefore, the addition of Ag may modify the nucleation and growth kinetics of strengthening precipitates and stabilize finer dispersions. By adjusting the Ag content, researchers aim to achieve a more refined and thermally stable precipitate distribution, thereby increasing the alloy's strength while maintaining sufficient ductility.

From this study have also suggested a potential link between Ag addition and the recrystallisation (RX) process. Recrystallisation is driven by the rearrangement of high-density dislocation structures into more energetically favourable configurations, eventually forming new, strain-free grains through the self-organisation of dislocations [288]. This self-organisation necessitates the climb of dislocation segments, a process that involves their interaction with vacancies and requires the translation of dislocations out of their original slip planes. Since dislocation climb is diffusion-controlled, the rate of RX is closely associated with vacancy mobility. Ag additions have been observed to accelerate both precipitation kinetics and the RX process. This implies that Ag-induced precipitation may deplete solute atoms in the matrix, thereby enhancing vacancy diffusivity and facilitating dislocation climb. Consequently, higher Ag content is expected to promote faster recrystallisation by enhancing diffusion-mediated mechanisms.

To accurately predict and control the evolution of second phase precipitates during heat treatment, the Mean-field precipitation model is employed. These models are possible to estimate the alloy's mechanical response based on its precipitate distribution, which is essential for optimising heat treatment parameters and achieving a balance between strength, ductility, and thermal stability.

This chapter focuses on the texture evolution based on experimental measurement and precipitation behaviour of second phases in extruded Mg-Zn-Ca and Mg-Zn-Ca-Ag alloys subjected to T4 and T6 heat treatments, with particular emphasis on the precipitate evolution of the $\text{Ca}_2\text{Mg}_6\text{Zn}_3$ phase and its metastable β'_1 phase. The key objectives of this chapter are:

1. Investigate how the addition of Ag content and solution treatment influence the crystallographic texture of the alloys. Examine the relationship between Ag addition, texture evolution, and recrystallisation.
2. Assess how Ag additions influence precipitate nucleation, stability, and coarsening behaviour, and their role in affecting the precipitation sequence and mechanical properties. Determine the optimal ageing conditions that maximise mechanical strength and ductility while preventing over-ageing effects.
3. Apply the Mean-field precipitation model to simulate the nucleation, growth, and transformation kinetics of β' type phases during ageing. Integrate Orowan dislocation bowing models to predict precipitation strengthening contributions, evaluating how different precipitate states influence mechanical performance.

This study aims to provide a comprehensive understanding of texture evolution and second phase precipitation mechanisms, offering insights into the design of optimised heat treatment schedules for improved mechanical properties in Mg-Zn-Ca and Mg-Zn-Ca-Ag alloys.

8.2 Materials and Method

8.2.1 Methodology

This study investigates the precipitation behaviour of Mg-Zn-Ca and Mg-Zn-Ca-Ag alloys subjected to T4 solution treatment and T6 ageing (Table 8.3). Ageing treatments were carried out at 160 °C for various durations following a 370 °C solution treatment and water quenching. Microstructural characterisation was conducted using optical microscopy (OM), scanning electron microscopy (SEM), and electron backscatter diffraction (EBSD), while energy-dispersive X-ray spectroscopy (EDS) was used to identify precipitate compositions. To evaluate the mechanical response, Vickers hardness tests were performed at selected intervals during ageing, and tensile tests were used to assess yield strength, ultimate tensile strength, and elongation in solution-treated and peak-aged conditions. Precipitation behaviour was further analysed using a mean-field precipitation model incorporating CALPHAD-based thermodynamic and mobility data, allowing simulation of nucleation, growth, and coarsening. Strengthening effects were estimated via an Orowan dislocation bowing model, enabling quantitative links between precipitate evolution and mechanical performance (Figure 8.1).

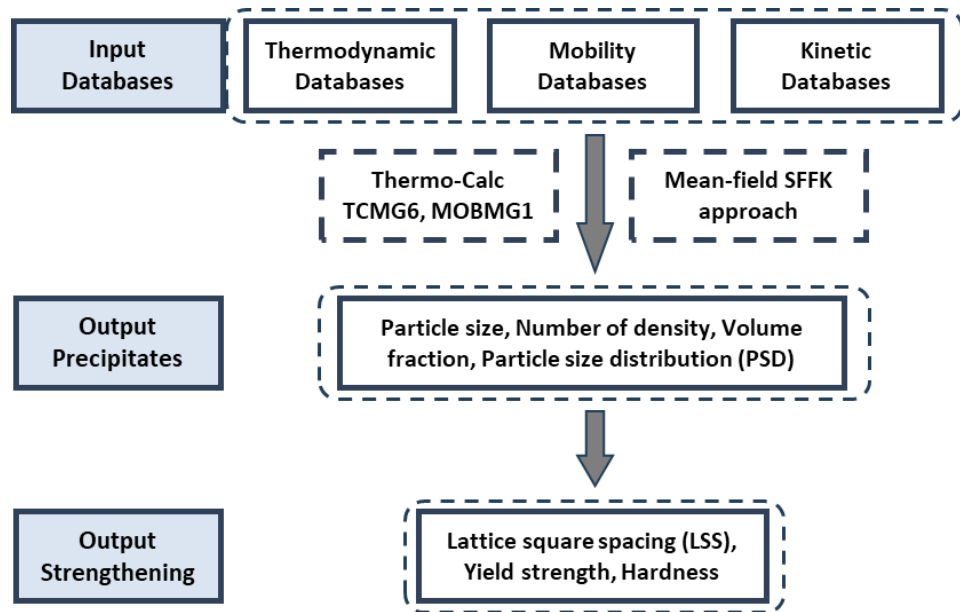


Figure 8.1. The overall framework for precipitation modelling

8.2.2 Materials Preparation

The extruded Mg-3Zn-0.2Ca (ZX30), Mg-3Zn-0.2Ca-0.1Ag (ZXQ300a), and Mg-3Zn-0.2Ca-0.3Ag (ZXQ300b) alloys was provided by Luxfer MEL Technology (UK), a composition given in Table 2.1, where the nominal Mg, Zn, Ca, Ag content was measured by Inductively coupled plasma optical emission spectroscopy (ICP-OES). ZX30, ZXQ300a, and ZXQ300b was cast at 740 °C into 3.0-inch diameters water-cooled billets, the melt was puddled and stirred in between adding additions and left for 15 minutes to settle prior to taking OES blocks and then casting. Billets were homogenised at 370 °C for 24 hours, then extruded using a 10 × 40 mm die, the extrusion parameters are shown in Table 3.2. For the solution treatment (T4), extruded ZX30 alloy sheets of dimensions 5 × 5 × 10 mm were homogenised at 370°C for 1 hour, then water quenched and subsequently undergo ageing treatment (T6) at 160°C for up to 196 hours, which shown in Table 8.3.

Table 8.1 Composition of Mg-Zn-Ca(-Ag) alloys

| Alloy | Mg (wt.%) | Zn (wt.%) | Ca (wt.%) | Ag (wt.%) | Measure by |
|---------|-----------|-----------|-----------|-----------|------------|
| ZX30 | Bal. | 3.11 | 0.22 | - | ICP-OES |
| ZXQ300a | Bal. | 3.10 | 0.21 | 0.14 | ICP-OES |
| ZXQ300b | Bal. | 3.11 | 0.21 | 0.33 | ICP-OES |

Table 8.2 Mg-Zn-Ca(-Ag) alloys extrusion parameters

| | |
|---------------------------------|---------------------------|
| Cast Temperature (°C) | 740 °C, then Water-cooled |
| Homogenisation Temperature (°C) | 370 °C for 24hrs |
| Extrusion temperature (°C) | 350°C |
| Extrusion ratio | 1:15 |

| | |
|------------------------|----------------|
| Extrusion speed | 0.2 ~ 0.3 mm/s |
|------------------------|----------------|

Table 8.3 Mg-Zn-Ca(-Ag) alloys heat-treatment parameters

| | Temperature (°C) |
|------------------------------|-------------------------|
| T4 Solution treatment | 370 |
| T6 Ageing treatment | 160 |

8.2.3 Mean-field Approach

The chemical potentials and diffusion coefficients in the mean-field model were obtained from the magnesium alloy database in Thermo-Calc. The compositional inputs of Mg-Zn-Ca and Mg-Zn-Ca-Ag alloys for the mean-field model were determined based on Table 2.1.

During the ageing process, Mg-Zn-Ca and Mg-Zn-Ca-Ag alloys nucleate β'_1 , β'_2 , and $\text{Ca}_2\text{Mg}_6\text{Zn}_3$ phases, with their growth kinetics highly dependent on ageing temperature and time. In the early stages of ageing, the β'_1 phase precipitates as fine, metastable needle-like particles, which gradually transform into β'_2 plate-like precipitates before reaching the equilibrium β -phase (MgZn). The model primarily focuses on the role of β'_1 phase during the early peak-ageing stage. However, the precipitation kinetics governing the transformation from β'_1 to β'_2 phase remain unclear; therefore, based on the experimental findings of Yang et al. [268], different interfacial energy γ values were introduced for β'_1 and β'_2 phases to adjust their respective volume fractions and average particle sizes to better align with experimental observations.

Additionally, since β'_1 and β'_2 phases exhibit different morphologies, a shape factor h which stated in Equation (4.35) was incorporated into the model to accurately represent their geometries [217]. The mean-field model primarily focuses on the nucleation, growth, and coarsening of these strengthening precipitates, considering the thermodynamic and kinetic factors governing precipitation. The volume fraction, size distribution, and morphology of precipitates were computed.

It was assumed that these precipitates nucleate on dislocations, and the site fraction N is approximated as described by Anderson et al. [217]. By correlating the time required for the β -phase to reach its peak volume fraction under different nucleation site fractions N with the experimentally observed peak ageing time of the alloy, along with the findings from Robson [289] and Xie [290], an approximate estimation of the nucleation site fractions N for β'_1 and β'_2 phases was established.

Additionally, due to the uncertainty surrounding the thermodynamic data for the GP zone precipitation sequence, this study assumes that β'_1 precipitates directly from the Mg matrix. To further refine the model, a coefficient slowing the kinetics of incubation probability P_{inc} was introduced, taking into account the ageing response times of different alloys to align the precipitation kinetics of β'_1 and β'_2 with the experimentally observed initial hardening response during ageing. The model parameters used in this study are summarized in Table 8.4.

8.2.4 Dislocation Orowan Bowing Model

To evaluate the precipitation strengthening contributions of β'_1 , β'_2 , and $\text{Ca}_2\text{Mg}_6\text{Zn}_3$ phases in Mg-Zn-Ca and Mg-Zn-Ca-Ag alloys, the Orowan bowing mechanism was employed to quantify the interaction between dislocations and precipitates. Precipitates act as obstacles to dislocation motion, and their effectiveness in strengthening the alloy depends on their size, volume fraction, spatial distribution, and morphology. The strengthening effect is particularly significant for fine, dispersed β'_1 and β'_2 precipitates, which provide precipitation hardening through the Orowan mechanism.

The yield stress contribution from precipitation strengthening was calculated using the modified Orowan equation, given by:

$$\sigma_{ys} = M \frac{G_s b}{\lambda} \quad (8.1)$$

$$\lambda = 1.6R \left(\sqrt{\frac{\pi}{4\phi}} - 1 \right) \quad (8.2)$$

where M is the Taylor factor, b is the Burgers vector, G_s is the shear modulus, r is the precipitate radius, ϕ is the precipitate volume fraction, and λ is the lattice square interparticle spacing. The mean-field precipitation model results were used to determine precipitate size distributions and volume fractions, which were then input into the Orowan equation to calculate the strengthening effect of each precipitate phase.

Since β'_1 and β'_2 phases exhibit different morphologies, a shape factor correction based on aspect ratio, which shown in Eq. (4.34) was introduced to account for the difference between needle-like β'_1 precipitates and plate-shaped β'_2 precipitates compared to the spherical particles assumed in the derivation of Equation (8.2). In addition to precipitation strengthening, other strengthening mechanisms, such as solid solution strengthening, also contribute to the overall mechanical performance of the alloy. However, at stresses that

can overcome the solid solution resistance to dislocation motion, gliding dislocation segments will interact with β'_1 and β'_2 phases and pin them, requiring an increase in the applied stress to overcome these obstacles. Thus, their strengthening contribution is significantly greater than that provided by the solid solution. Therefore, this model primarily focuses on the influence of precipitation strengthening on the mechanical performance of the alloy. Model parameters are presented in Table 8.4.

Table 8.4 Model parameters

| Mean-field model | | | | | |
|--------------------------------------|------------------------------------|---------------------------|-------------------------------------|------------------|-------------|
| Parameter | $\beta'_1(\text{Mg}_4\text{Zn}_7)$ | $\beta'_2(\text{MgZn}_2)$ | $\text{Ca}_2\text{Mg}_6\text{Zn}_3$ | Units | References |
| X_{Zn}^p | 7/11 | 2/3 | | | Thermo-Calc |
| Aspect ratio (h) | 25 | 2.5 | | | [268] |
| Interfacial energy (γ) | 0.002 | 0.015 | 0.06 | J/m ² | fitted |
| Nucleation site fraction (N) | 10^{-9} | 10^{-6} | 10^{-3} | | [289] |
| Incubation probability (P_{inc}) | 15.0 | 10.0 | 1.0 | | fitted |
| Property model | | | | | |
| Taylor factor (M) | | 2.2 | | | [289] |
| Burgers vector (b) | | 0.32 | | nm | [289] |
| Shear modulus (G_s) | | 17.2 | | GPa | [289] |

8.3 Microstructure of Mg-3Zn-0.2Ca(-xAg) Alloys

Optical micrographs for all Mg-Zn-Ca(-Ag) alloys in the as-extruded conditions are given in Figure 8.2. The microstructure is observed at both the edge and centre regions for ZX30, ZXQ300a, and ZXQ300b alloys.

In the edge region of as-extruded samples (Figure 8.2a, b, c), the microstructure exhibits significant grain elongation along the extrusion direction, with the presence of large deformed grains. The ZX30 alloy (Figure 8.2a) shows a pronounced banded structure with an inhomogeneous grain distribution, containing a considerable number of coarse grains formed after extrusion deformation. A small fraction of fine grains is observed between these coarse grains. In contrast, the ZXQ300a (Figure 8.2b) and ZXQ300b (Figure 8.2c) alloys exhibit a more refined microstructure with reduced second phase segregation. The addition of Ag in ZXQ300b appears to further suppress the coarsening of the second phase particles, resulting in a more homogeneous distribution.

In the centre region (Figure 8.2d, e, f), the microstructure is different comparing with edge region. The ZX30 alloy (Figure 8.2d) exhibits elongated grains along the extrusion direction, with a more uniform layered structure compared to the edge region. A small fraction of fine grains is observed between the layered coarse grains. The microstructures of the ZXQ300a and ZXQ300b alloys (Figure 8.2e, f) also show a uniform distribution along the extrusion direction, with a higher fraction of fine grains compared to the ZX30

alloy. Additionally, in comparison to the alloys in the edge region, the deformed grains in the centre are noticeably smaller, indicating more uniform grain deformation in this region.

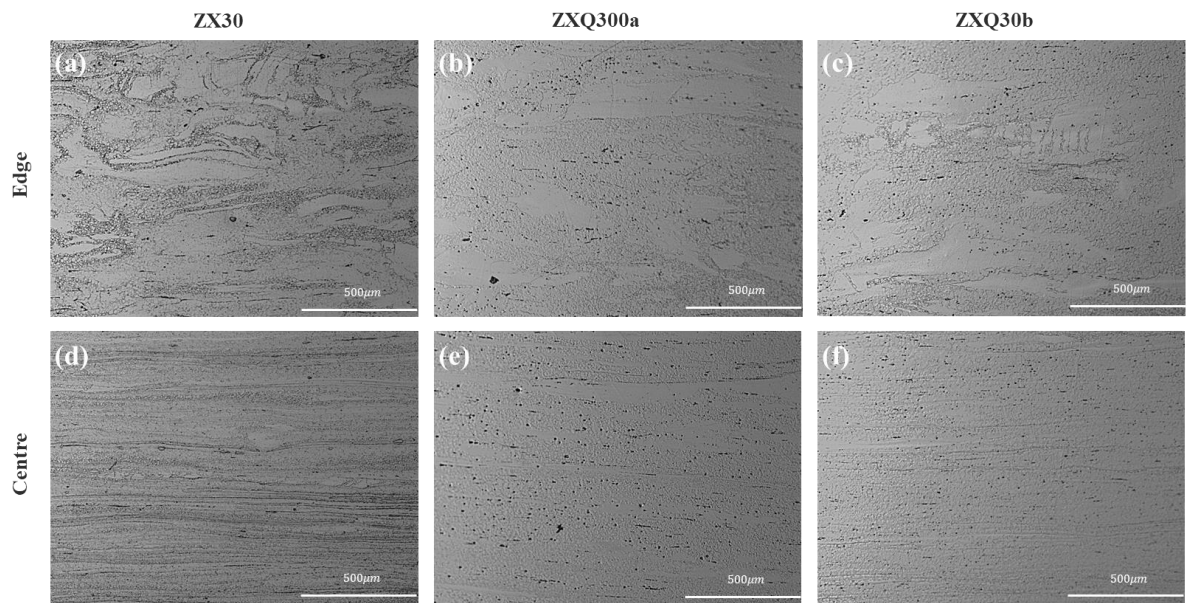


Figure 8.2. Mg-Zn-Ca(-Ag) alloy optical micrographs in the as-extruded conditions; (a,d) are ZX30, (b,e) are ZXQ300a, (c,f) are ZXQ300b; (a,b,c) are at the edge of extruded samples, (d,e,f) are at the centre of extruded samples.

EBSD maps and pole figures for all Mg-Zn-Ca(-Ag) alloys in the as-extruded condition are given in Figure 8.3. The microstructure and texture evolution of ZX30, ZXQ300a, and ZXQ300b alloys were analysed to assess the impact of alloying elements and extrusion on grain orientation and recrystallisation behaviour.

The inverse pole figure maps (Figure 8.3a, c, e) reveal significant differences in grain morphology and recrystallisation fraction among the alloys. The ZX30 alloy (Figure 8.3a) exhibits a heterogeneous microstructure with elongated grains along the extrusion direction, indicating incomplete dynamic recrystallisation (DRX). The presence of large deformed grains interspersed with smaller recrystallised grains suggests a mixed microstructure, with a relatively low fraction of fully recrystallised grains.

The ZXQ300a alloy (Figure 8.3c) exhibits a recrystallisation degree similar to that of the ZX30 alloy, with a slightly reduced proportion of large deformed grains. The orientation of these deformed large grains does not show a strong basal texture, which may be attributed to the influence of additional Ag alloying elements. However, since some regions still exhibit residual deformed grains, it indicates that complete recrystallisation has not yet been achieved.

In contrast, the ZXQ300b alloy (Figure 8.3e) exhibits the most uniform and fully recrystallised microstructure among the three alloys. The figure shows that fine equiaxed grains dominate, with minimal elongated structures, indicating that the DRX process is nearly complete. This suggests that the addition of Ag promotes more effective recrystallisation.

The pole figures (Figure 8.3b, d, f) further illustrate the texture evolution in the extruded alloys. The ZX30 alloy (Figure 8.3b) exhibits a strong basal texture, with a pronounced (0001) peak along the ND direction, indicating significant texture value increase due to the presence of elongated grains. Compared to ZX30, the ZXQ300a alloy (Figure 8.3d) shows a weaker basal texture, with the orientation of elongated grains exhibiting a $(\bar{1}2\bar{1}0)$ peak along the ED direction. This suggests that the addition of Ag promotes the randomisation of deformed grain orientations. The ZXQ300b alloy (Figure 8.3f) exhibits the weakest basal texture among the three alloys, which is consistent with its near fully recrystallised microstructure. The (0001) peak intensity in ZXQ300b is the lowest at 3.1 multiple of a random distribution (MRD), whereas the peak intensities in ZX30 and ZXQ300a exceed 10 MRD. The reduction in texture intensity indicates that the addition of Ag facilitates texture weakening by promoting more random grain orientations during DRX.

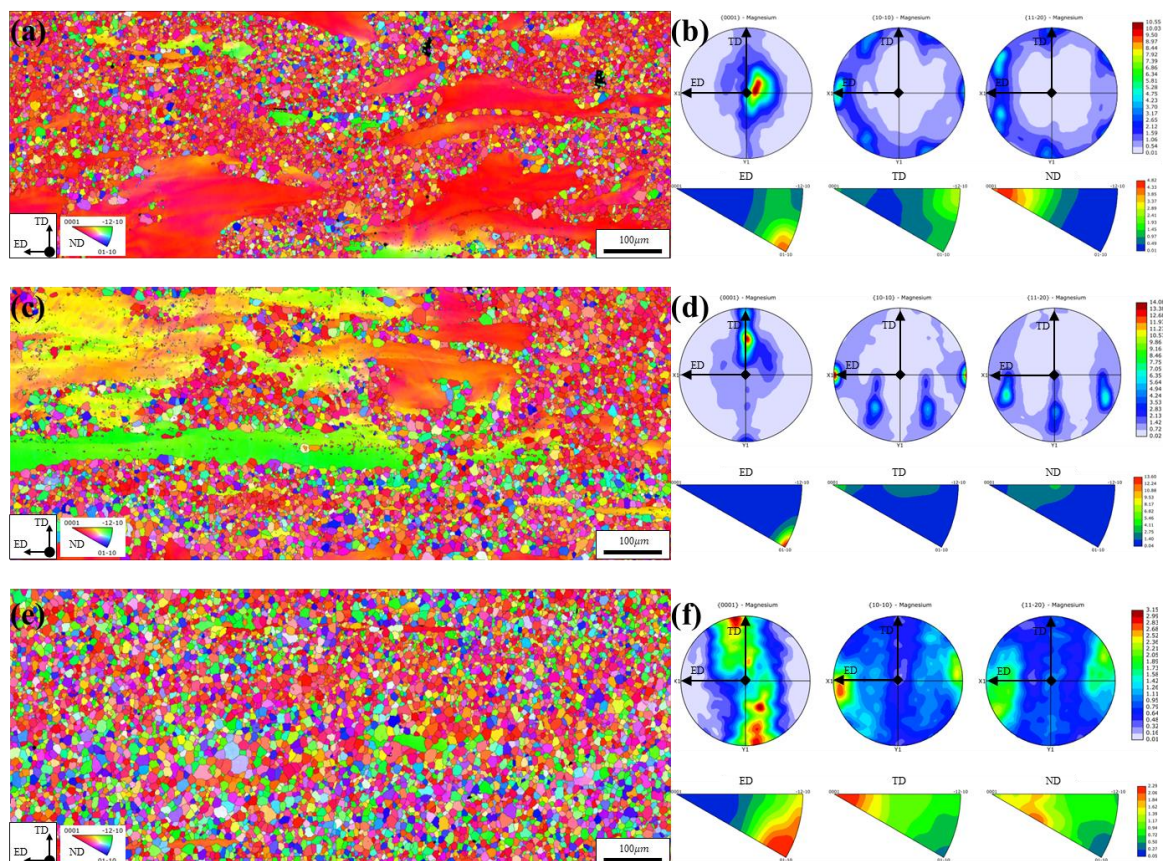


Figure 8.3. EBSD maps and pole figures for as-extruded (a) ZX30, (b) ZXQ300a, (c) ZXQ300b alloys. The extrusion direction is aligned horizontally on all EBSD maps, but the grains are coloured with respect to the crystal directions aligned parallel with the extrusion direction.

EBSD maps and pole figures for all Mg-Zn-Ca(-Ag) alloys in the solution-treated condition are given in Figure 8.4. The microstructural evolution after solution treatment was examined to assess the effects of heat treatment on grain structure, recrystallisation behaviour, and texture characteristics in comparison to the as-extruded condition.

The inverse pole figure maps (Figure 8.4a, c, e) show a significant increase in recrystallisation across the three alloys. Compared to the as-extruded condition (Figure 8.3a), the ZX30 alloy (Figure 8.4a) exhibits a more uniform and equiaxed grain structure, with a noticeable reduction in elongated grains. This indicates that solution treatment facilitates further recrystallisation, reducing internal strain and promoting grain growth. The microstructure of the ZXQ300a alloy (Figure 8.4c), compared to the as-extruded condition (Figure 8.3c), shows a significant reduction in large deformed grains, promoting more uniform grain recrystallisation and growth. However, after solution treatment, a noticeable presence of twins can be observed within the larger equiaxed grains. Compared to the as-extruded condition (Figure 8.3e), the ZXQ300b alloy (Figure 8.4e) exhibits a more uniform grain distribution, with large deformed grains completely dissolved. The grain size has increased due to coarsening. Additionally, a small number of twins can be observed within the larger equiaxed grains.

The pole figures (Figure 8.4b, d, f) illustrate the evolution of crystallographic texture after solution treatment. Compared to the as-extruded alloy (Figure 8.3b), the ZX30 alloy (Figure 8.4b) exhibits a weakened basal texture, with a reduced (0001) peak intensity along the ND direction. This suggests that solution treatment contributes to the randomisation of grain orientations and the reduction of texture intensity. For the ZXQ300a alloy (Figure 8.4d), compared to the as-extruded condition (Figure 8.3d), the basal texture is further weakened, with a more dispersed orientation along the ED direction. This confirms that solution treatment enhances orientation randomisation by further promoting recrystallisation and grain boundary mobility. The ZXQ300b alloy (Figure 8.4f) exhibits a relatively strong basal texture among the three alloys, with the (0001) peak intensity reaching approximately 7.0 MRD in the off-ND direction, whereas the ZX30 alloy shows a lower intensity of around 4.5 MRD. Compared to its as-extruded condition (Figure 8.3f), the texture intensity has unexpectedly increased. This suggests that the higher amount addition of Ag may have accelerated the recrystallisation process during solution treatment, leading to excessive grain growth.

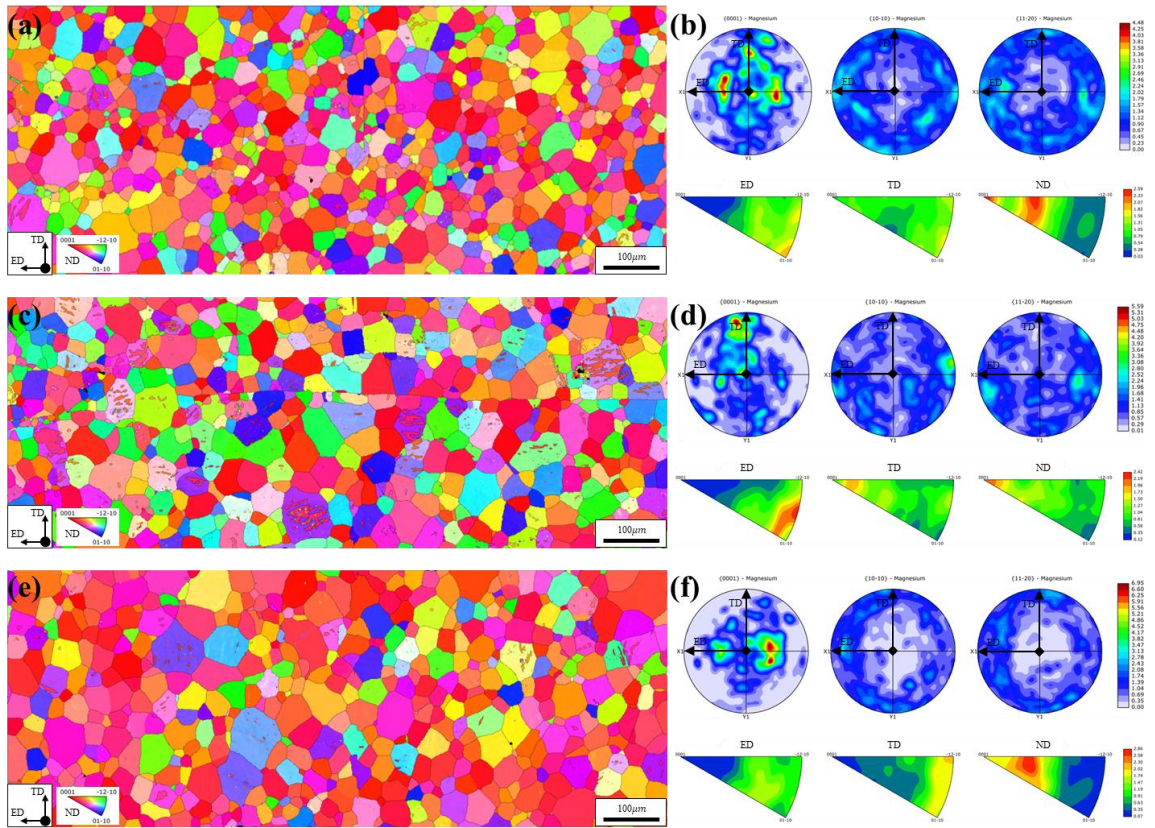


Figure 8.4. EBSD maps and pole figures for extruded and solution treated (a) ZX30, (b) ZXQ300a, (c) ZXQ300b alloys. The extrusion direction is aligned horizontally on all EBSD maps, but the grains are coloured with respect to the crystal directions aligned parallel with the extrusion direction.

Figure 8.5 and Figure 8.6 show grain boundaries (GBs) character, the corresponding grain boundary misorientation, recrystallisation distribution, and grain size distribution of the ZX30 alloy under as-extruded and solution-treated conditions. The distinction between LAGBs and high-angle grain boundaries (HAGBs) is based on a misorientation angle threshold of 15° .

In the as-extruded condition (Figure 8.5a), the grain boundary map shows that low-angle grain boundaries (LAGBs) account for approximately 22.6% of the total boundaries. Combined with the grain orientation spread (GOS) map Figure 8.5c), it is evident that LAGBs are typically located in regions with high orientation spread values, particularly in the banded areas aligned along the extrusion direction. This indicates heterogeneous deformation, where some regions are undergoing partial recrystallisation while others remain unrecrystallised. The grain diameter distribution (Figure 8.5d) further supports

this observation, showing a significant proportion of fine grains while still containing a fraction of large deformed grains.

After solution treatment (Figure 8.6), the microstructure undergoes significant changes. The grain boundary map (Figure 8.6a) reveals a sharp reduction in the fraction of LAGBs, dropping to 15.6%, with a corresponding increase in high-angle grain boundaries (HAGBs) to 84.4%. This transformation indicates that significant recrystallisation has occurred, converting previously deformed grains into fully recrystallised equiaxed grains. The misorientation distribution (Figure 8.6b) shows a more uniform distribution of grain boundary angles, further confirming the completion of recrystallisation. The GOS map (Figure 8.6c) shows a substantial decrease in high-orientation spread regions, with most grains exhibiting low internal strain. This suggests that the stored deformation energy has been largely released through static recrystallisation during solution treatment. Additionally, the grain diameter distribution (Figure 8.6d) shows a shift towards larger average grain sizes, indicating that some grain growth has occurred post-recrystallisation. However, the overall grain size remains relatively fine, suggesting that excessive coarsening has been effectively suppressed.

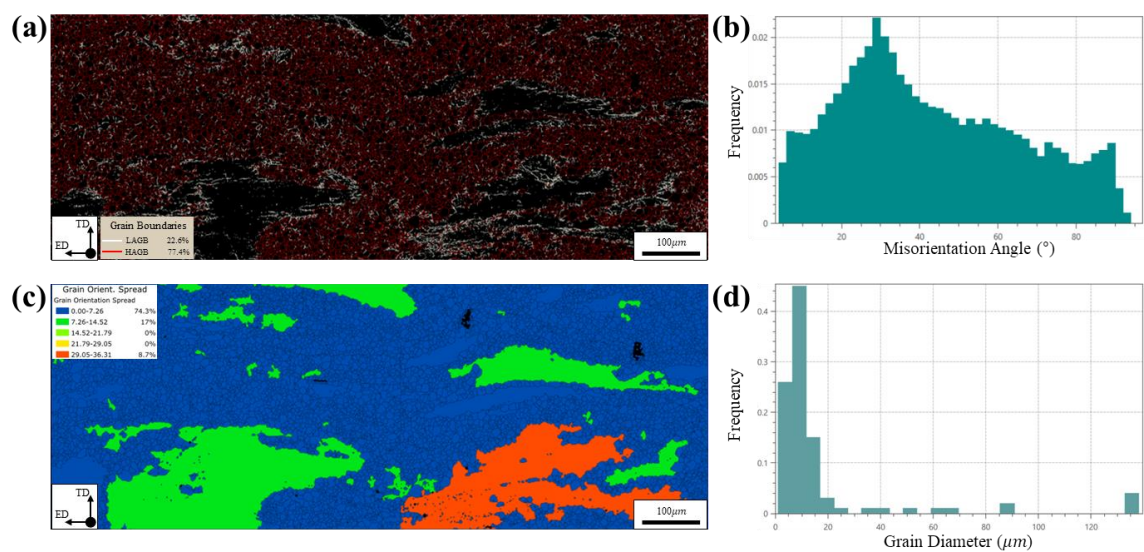


Figure 8.5. Grain boundaries (GBs) character distribution map of as-extruded ZX30 specimen, the extrusion direction is aligned horizontally on all EBSD maps. HAGBs plus LAGBs map (a), the corresponding grain boundary misorientation distribution (b), grain orientation spread (GOS) map (c), and grain diameter distribution (d).

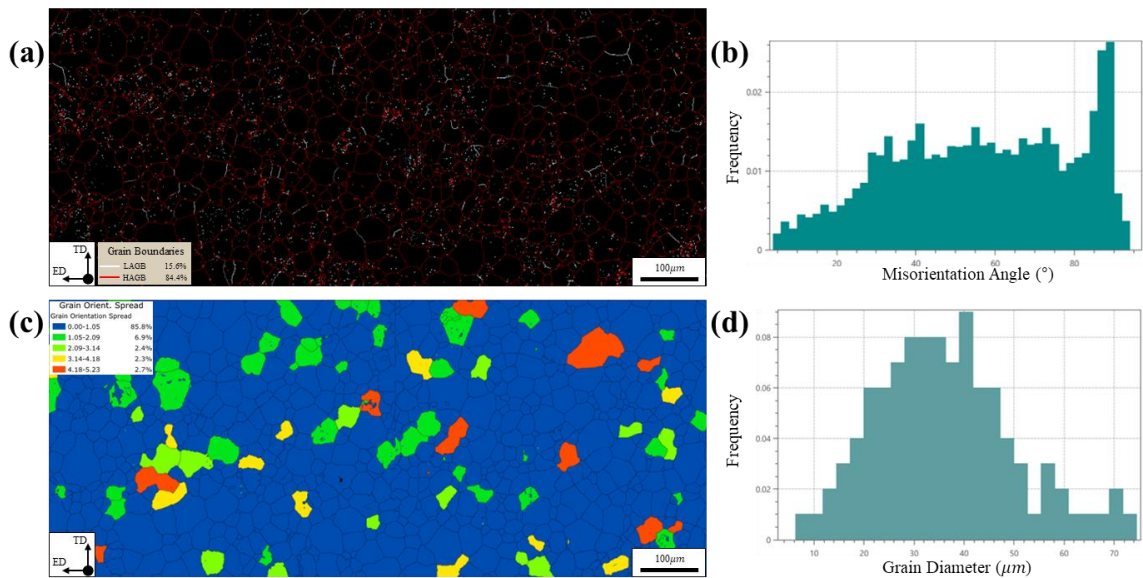


Figure 8.6. Grain boundaries (GBs) character distribution map of extruded and solution treated ZX30 specimen, the extrusion direction is aligned horizontally on all EBSD maps. HAGBs plus LAGBs map (a), the corresponding grain boundary misorientation distribution (b), grain orientation spread (GOS) map (c), and grain diameter distribution (d).

Figure 8.7 and Figure 8.8 show grain boundaries (GBs) character, the corresponding grain boundary misorientation, recrystallisation distribution, and grain size distribution of the ZXQ300a alloy under as-extruded and solution-treated conditions.

In the as-extruded condition (Figure 8.7a), the grain boundary map shows that low-angle grain boundaries (LAGBs) account for 25.8% of the total boundaries, indicating that a significant portion of the microstructure remains in a deformed state. The grain orientation spread (GOS) map (Figure 8.7c) highlights large deformed regions with high orientation spread values, particularly in the banded structures aligned along the extrusion direction. This suggests heterogeneous deformation, where some regions have undergone partial dynamic recrystallisation (DRX). The proportion of grains with GOS $< 7^\circ$ is approximately 70%, similar to that of in ZX30 (Figure 8.6c), indicating that the minor addition of Ag does not significantly enhance recrystallisation during the thermomechanical deformation of the Mg-Zn-Ca alloy. The grain diameter distribution (Figure 8.7d) further supports this observation, showing a high fraction of fine recrystallised grains while still containing large deformed grains.

After solution treatment (Figure 8.8), the microstructure undergoes significant changes. The grain boundary map (Figure 8.8a) shows that the fraction of low-angle grain boundaries (LAGBs) decreases to 17.6%, while the high-angle grain boundaries (HAGBs) increase to 82.4%, indicating extensive recrystallisation. The misorientation distribution (Figure 8.8b) exhibits a distinct peak around 85° , further confirming the enhancement of

recrystallisation. The GOS map (Figure 8.8c) reveals a substantial reduction in regions with high orientation spread, indicating that the stored deformation energy has been largely released through recrystallisation. Most grains now exhibit low internal strain, confirming the effectiveness of solution treatment in promoting microstructural recovery. The grain diameter distribution (Figure 8.8d) shifts towards larger average grain sizes, suggesting grain coarsening due to recrystallisation and subsequent grain growth. The grain structure of the ZXQ300a alloy after solution treatment is comparable to that of ZX30 (Figure 8.5 and Figure 8.6).

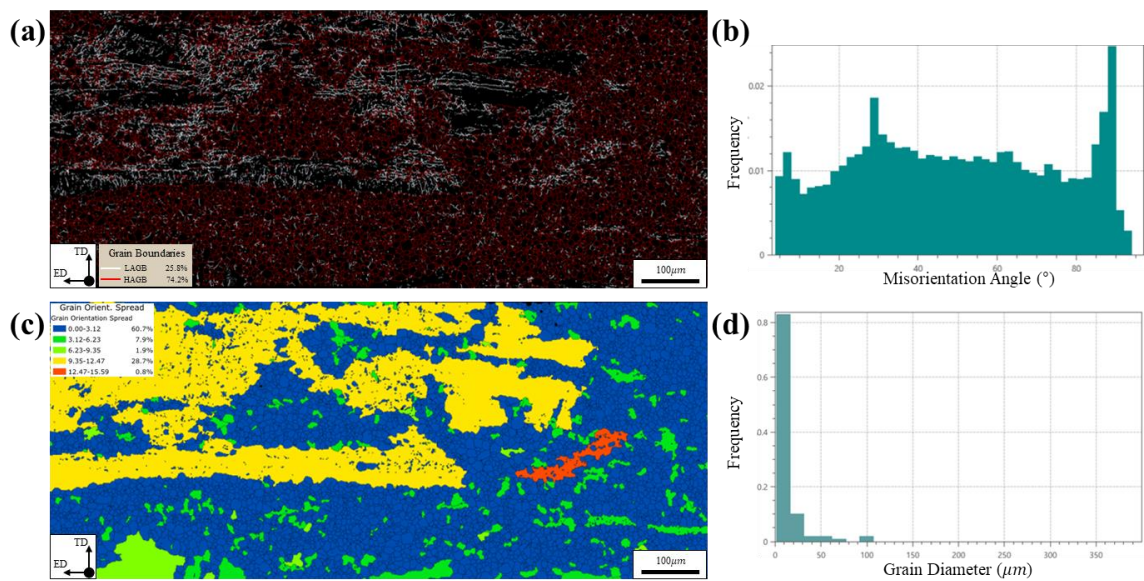


Figure 8.7. Grain boundaries (GBs) character distribution map of as-extruded ZXQ300a specimen, the extrusion direction is aligned horizontally on all EBSD maps. HAGBs plus LAGBs map (a), the corresponding grain boundary misorientation distribution (b), grain orientation spread (GOS) map (c), and grain diameter distribution (d).

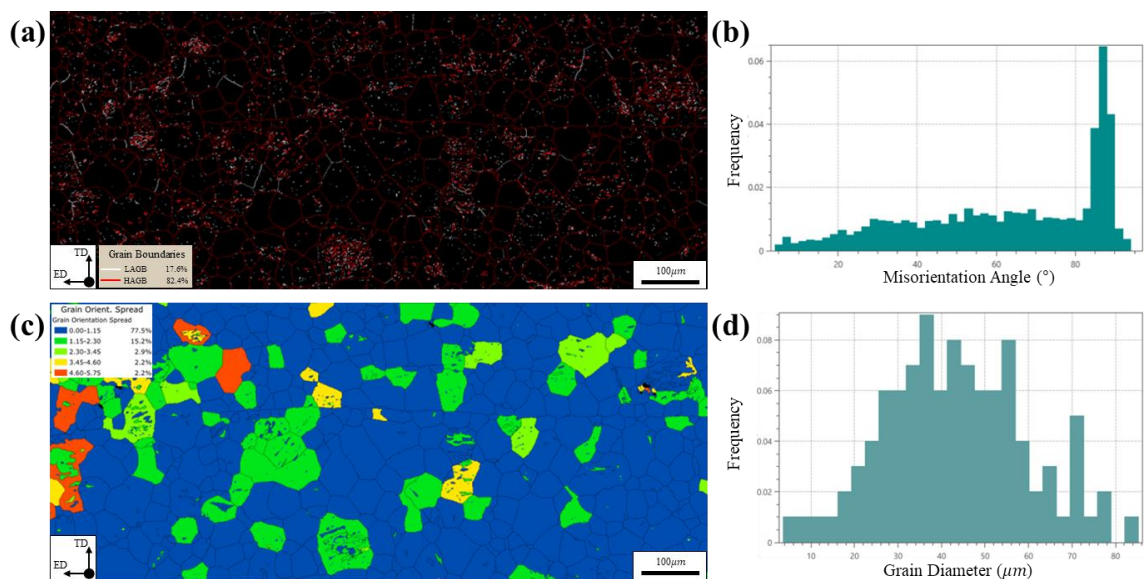


Figure 8.8. Grain boundaries (GBs) character distribution map of extruded and solution treated ZXQ300a specimen, the extrusion direction is aligned horizontally on all EBSD maps. HAGBs plus LAGBs map (a), the corresponding grain boundary misorientation distribution (b), grain orientation spread (GOS) map (c), and grain diameter distribution (d).

Figure 8.9 and Figure 8.10 show grain boundaries (GBs) character, the corresponding grain boundary misorientation, recrystallisation distribution, and grain size distribution of the ZXQ300b alloy under as-extruded and solution-treated conditions.

In the as-extruded condition (Figure 8.9a), the grain boundary map shows that low-angle grain boundaries account for 6.3% of the total boundaries, while high-angle grain boundaries dominate at 93.7%. The high fraction of HAGBs suggests that the ZXQ300b alloy has undergone extensive dynamic recrystallisation (DRX) during extrusion, leading to a highly recrystallised microstructure. The grain orientation spread (GOS) map (Figure 8.9c) further supports this observation, showing that most grains exhibit low internal strain, with 89% of grains having GOS values below 1.5° . Only a few regions display slightly higher orientation spread, with GOS values around 7° . This indicates that the stored deformation energy in the as-extruded state is already very low. The grain diameter distribution (Figure 8.9d) exhibits a unimodal distribution, with a high fraction of fine recrystallised grains, confirming that DRX is nearly complete.

After solution treatment (Figure 8.10), the microstructure remains largely recrystallised but has undergone additional grain growth. The grain boundary map (Figure 8.10a) shows that low-angle grain boundaries slightly increase to 10.6%, while high-angle grain boundaries decrease to 89.4%. This increase in low-angle grain boundaries may be attributed to the formation of substructures caused by grain growth. The misorientation distribution (Figure 8.10b) exhibits a strong peak around 85° , which is characteristic of twin boundaries, suggesting that twinning may have occurred during heat treatment [291]. The GOS map (Figure 8.10c) shows a further reduction in high-orientation spread regions, indicating that solution treatment has effectively relieved residual internal stress. However, compared to the as-extruded state, the grain diameter distribution (Figure 8.10d) shifts towards larger grain sizes, confirming that some grain coarsening has occurred. This suggests that while Ag addition in ZXQ300b promotes recrystallisation, it also accelerates grain growth during solution treatment, potentially leading to coarsening effects.

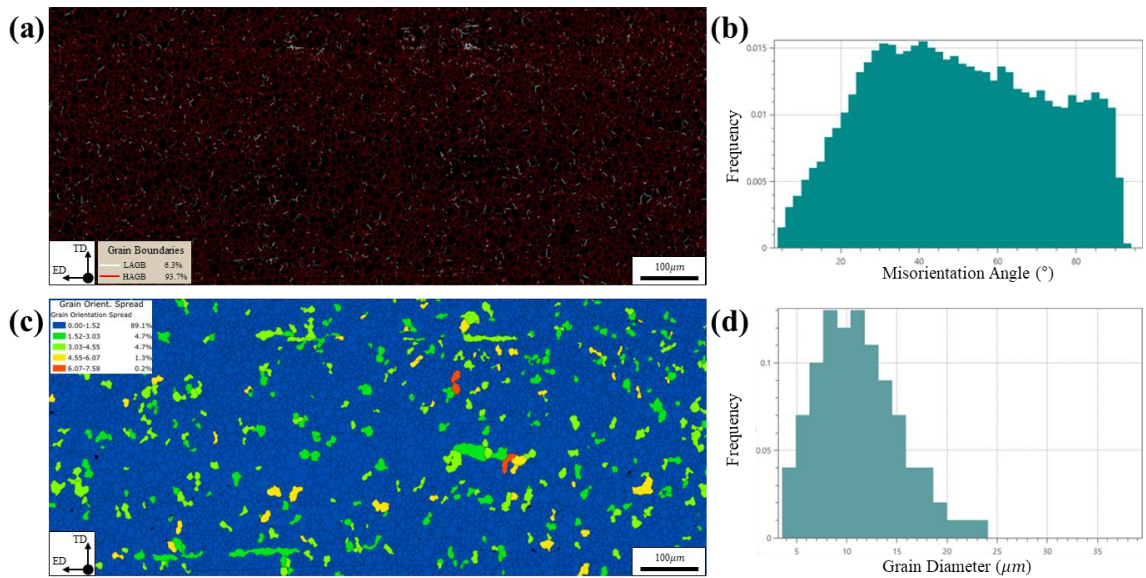


Figure 8.9. Grain boundaries (GBs) character distribution map of as-extruded ZXQ300b specimen, the extrusion direction is aligned horizontally on all EBSD maps. HAGBs plus LAGBs map (a), the corresponding grain boundary misorientation distribution (b), grain orientation spread (GOS) map (c), and grain diameter distribution (d).

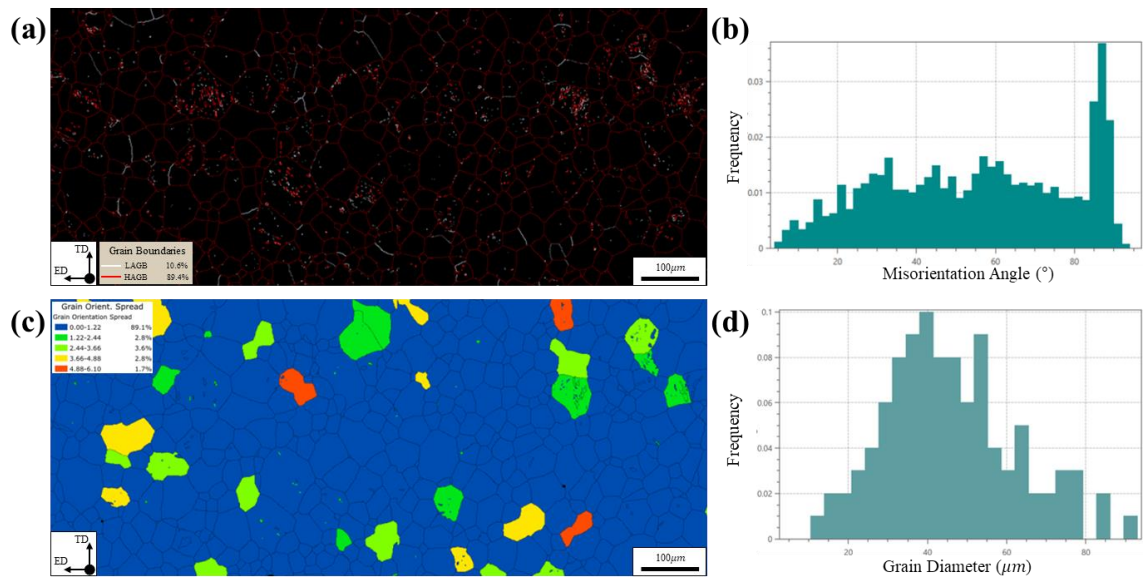


Figure 8.10. Grain boundaries (GBs) character distribution map of extruded and solution treated ZXQ300b specimen, the extrusion direction is aligned horizontally on all EBSD maps. HAGBs plus LAGBs map (a), the corresponding grain boundary misorientation distribution (b), grain orientation spread (GOS) map (c), and grain diameter distribution (d).

Figure 8.11 shows the SEM micrographs and EDS results of the ZX30, ZXQ300a, and ZXQ300b alloys in the solution-treated and peak-aged conditions. The particle analysis provides insight into the compositional variations of second phase particles before and after ageing treatment.

SEM micrographs and EDS mapping reveal that the elemental distribution of Zn, Ca, and Ag in the alloys does not show significant differences between the solution-treated and peak-aged conditions. The second phase particle size ranges between 1 μm and 3 μm , with most particles containing both Zn and Ca, while a smaller fraction exhibits only Ca segregation. Based on these observations, the predominant intermetallic phases are inferred to be $\text{Ca}_2\text{Mg}_6\text{Zn}_3$, with a minority phase of Mg_2Ca . In both ZXQ300a and ZXQ300b, Ag appears to be dispersed throughout the matrix, suggesting that a significant fraction of Ag remains in solid solution. This retained Ag may contribute to precipitation hardening during the ageing process, requiring further high-resolution STEM-EDS analysis to confirm its precise role. In Mg alloys, Ag typically forms AgMg_4 precipitates [292], however, no such precipitates were observed in either ZXQ300a or ZXQ300b. In ZXQ300b, slight Ag accumulation was detected at second phase particles, suggesting that Mg-Ag precipitates may heterogeneously nucleate on existing large particles as the Ag content increases.

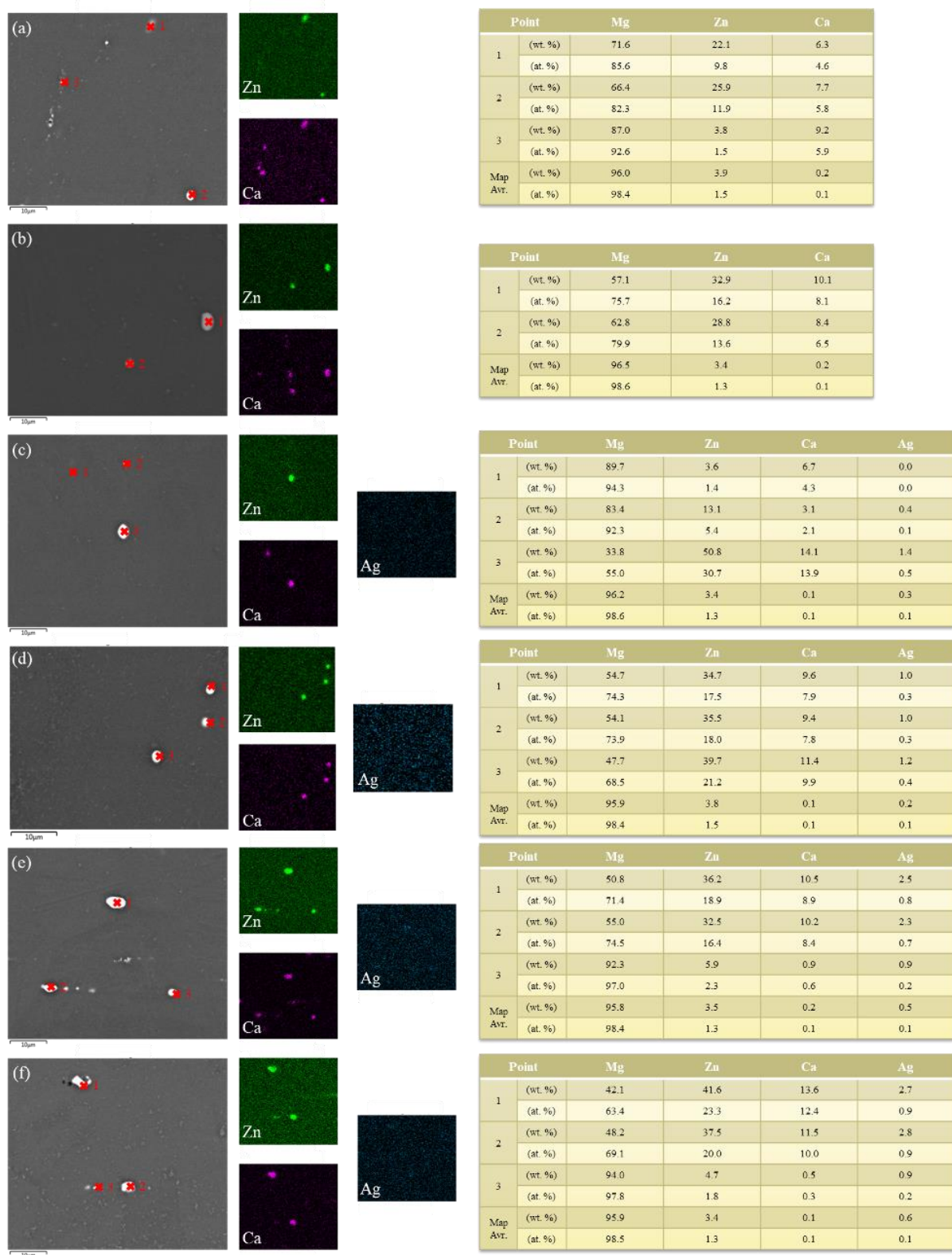


Figure 8.11. High-magnification SEM micrographs and results of EDS mapping and compositional analysis of the solution treated (a, c, e) and peak aged (b, d, f) samples. ZX30 alloy (a, b), ZXQ300a (c, d), and ZXQ300b (e, f).

8.4 Mechanical Properties of Ageing Mg-3Zn-0.2Ca(-xAg) Alloys

Figure 8.12 shows the yield stress, ultimate tensile strength (UTS), and elongation of the ZX30, ZXQ300a, and ZXQ300b alloys in the solution-treated and peak-aged conditions.

The mechanical properties of the alloys exhibit significant variations depending on the heat treatment condition, highlighting the effects of alloy composition and ageing on strength and ductility.

In the solution-treated condition (T4), all three alloys exhibit relatively low yield strength (around 100 MPa) and UTS (around 220 MPa), with moderate elongation of approximately 15%. The ZX30 alloy shows the lowest yield strength and UTS among the three alloys, indicating that the absence of Ag limits the precipitation hardening potential. The ZXQ300a and ZXQ300b alloys exhibit slightly higher yield strength, suggesting that the presence of Ag may contribute to solid solution strengthening. However, the ductility of all three alloys remains relatively high, indicating that the matrix is predominantly soft and deformable, with minimal precipitation-induced strengthening.

In the peak-aged condition (T6), the yield strength of all three alloys increases by approximately 50 to 60 MPa, while the UTS increases by only about 10 MPa, accompanied by a reduction in elongation. The increase in strength is attributed to the precipitation of strengthening phases. Compared to ZX30 and ZXQ300b, the difference between the T4 and T6 condition is less for ZXQ300a. This could be due to the distribution and coarsening of precipitates in ZXQ300a may not be as optimised as in ZXQ300b, leading to a less pronounced strengthening effect. It was also observed that in the peak-aged condition, the elongation of ZX30 decreased from 13.8% to 7.2%, whereas in ZXQ300b, the elongation only slightly decreased from 16.2% to 13.1%. This result indicates that the addition of Ag slows down the decline in ductility after ageing. One possible reason is that Ag-containing precipitates in ZXQ300b are more finely dispersed and homogeneously distributed, preventing excessive strain localization and crack initiation. Additionally, Ag may contribute to the formation of nanoscale Mg-Ag precipitates, which strengthen the material without severely compromising its ability to accommodate plastic deformation. This suggests that Ag plays a crucial role in balancing strength and ductility during the ageing process. The different shapes of the stress-strain curves in Figure 8.12a-c suggest that, in addition to precipitation, variations in recrystallization, texture, and grain size also affect the strengthening response. With increasing Ag content, the alloys show improved ductility under both T4 and T6 conditions, which consistent with the EBSD results, can be attributed to enhanced recrystallization, texture randomisation, and grain refinement induced by Ag addition.

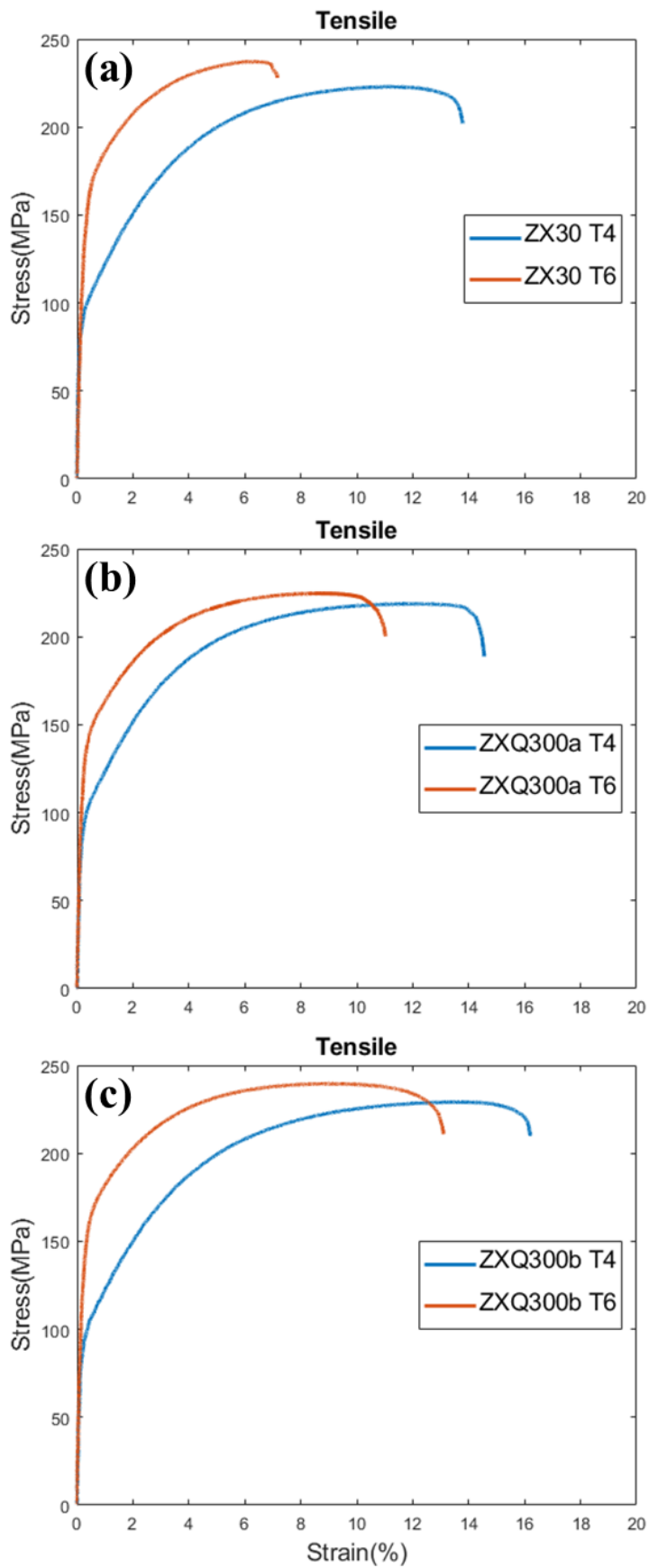


Figure 8.12. Engineering stress-strain curves for T4 treated and T6 treated (a) ZX30, (b) ZXQ300a, and (c) ZXQ300b alloys

Table 8.5 Composition of Mg-Zn-Ca(-Ag) alloys

| Alloys | YS, 0.2 offset Stress (MPa) | UTS (MPa) | EL (%) |
|------------|-----------------------------|-----------|--------|
| ZX30_T4 | 97 | 223 | 13.8 |
| ZX30_T6 | 162 | 237 | 7.2 |
| ZXQ300a_T4 | 99 | 219 | 14.6 |
| ZXQ300a_T6 | 148 | 225 | 11.0 |
| ZXQ300b_T4 | 99 | 229 | 16.2 |
| ZXQ300b_T6 | 160 | 240 | 13.1 |

Figure 8.13 shows the hardness results of the ZX30, ZXQ300a, and ZXQ300b alloys during ageing at 160°C. The hardness evolution of the three alloys highlights the effects of ageing kinetics and precipitation behaviour, providing insight into the role of alloying elements in the strengthening response.

During the early ageing stage (0 to 24 h), the hardness of all three alloys remains stable at approximately 52 HV, indicating that the strengthening precipitates are still in the incubation period and have not yet significantly contributed to hardening. As the ageing progresses, the response of each alloy varies distinctly. The ageing hardening phase for ZX30 occurs between 24 and 120 hours, reaching a hardness of 61 HV at 120 hours, followed by a slight increase to a peak hardness of approximately 62 HV. Similarly, the ageing hardening phase for ZXQ300a occurs between 24 and 96 hours, reaching 60 HV at 96 hours and then slightly increasing to a peak hardness of approximately 62 HV, showing a response similar to that of ZX30. In contrast, ZXQ300b exhibits the fastest ageing response among the three alloys, with the ageing hardening phase occurring between 24 and 72 hours. Notably, between 48 and 72 hours, the hardness of ZXQ300b increases sharply, reaching 61 HV, and continues to rise to a peak of approximately 63 HV. The peak ageing time for all three alloys is around 120 hours. The highest and most rapid peak hardness observed in ZXQ300b confirms that the certain amount addition of Ag slightly enhances and significantly accelerates the ageing hardening response.

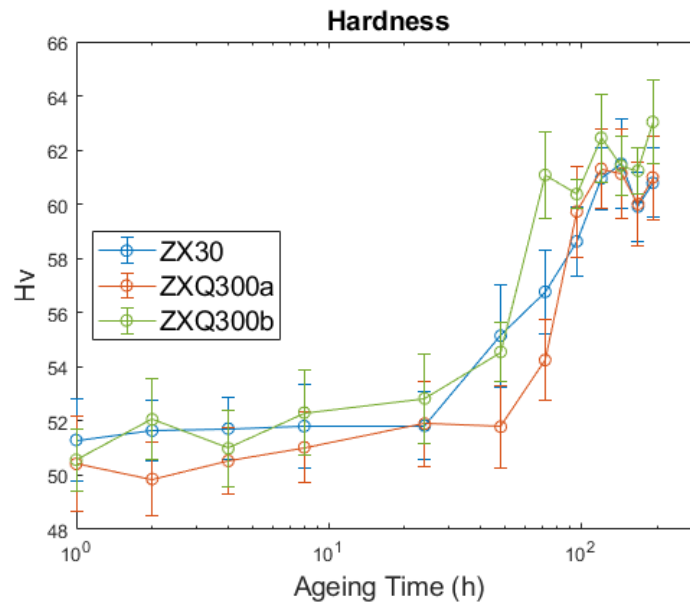


Figure 8.13. Age-hardening response curve of ZX30, ZXQ300a, and ZXQ300b alloys when aged at 160 °C.

8.5 Mean-field Predictions of Second Phase Precipitation during Ageing

The solidification behaviour of the ZX30 alloy, as illustrated in Figure 8.14, follows a non-equilibrium Liquidus-minimising Scheil solidification path. The liquidus temperature of ZX30 is observed to be approximately 650°C, where the primary Mg phase starts to solidify. As the solid fraction reaches 97.93% at 510°C, the first secondary phase, Mg₂Ca, begins to precipitate from the melt. With further cooling, at 394°C and a solid fraction of 99.49%, the Ca₂Mg₆Zn₃ phase forms, indicating the final stage of solidification. These observations highlight the influence of Zn and Ca on the formation of intermetallic compounds during solidification.

The equilibrium phase diagrams in Figure 8.15 further illustrate the stable phase formations in ZX30, ZXQ300a, and ZXQ300b alloys. In the ZX30 alloy (Figure 8.15a), Ca₂Mg₆Zn₃ and MgZn phases are expected to form at the ageing temperature (160°C), confirming their thermodynamic stability under equilibrium conditions. In ZXQ300a and ZXQ300b (Figure 8.15b and c), the introduction of Ag leads to the additional formation of AgMg₄ in ZXQ300b at the ageing temperature, whereas in ZXQ300a, this phase is not predicted to form under the same conditions. The phase fraction results indicate that at near-room temperature, AgMg₄ coexists with Ca₂Mg₆Zn₃ and MgZn, suggesting its potential influence on microstructural evolution during ageing. A comparison with EDS results implies that with prolonged ageing treatment, AgMg₄ precipitates may coarsen and become more detectable.

The combination of non-equilibrium solidification (Figure 8.14) and equilibrium phase predictions (Figure 8.15) suggests that the coarse Mg_2Ca and $\text{Ca}_2\text{Mg}_6\text{Zn}_3$ precipitates in ZX30, ZXQ300a, and ZXQ300b alloys form under non-equilibrium conditions. The finer $\text{Ca}_2\text{Mg}_6\text{Zn}_3$ and MgZn (β -type) phases formed during ageing. Additionally, AgMg_4 is expected to form in ZXQ300b but may require extended ageing times to become significant. The addition of Ag plays a crucial role in modifying the ageing kinetics of ZXQ300a and ZXQ300b alloys. It is hypothesized that Ag addition alters the nucleation site fraction of $\text{Ca}_2\text{Mg}_6\text{Zn}_3$ and MgZn (β -type) phases, thereby facilitating the precipitation of finer strengthening phases, which may contribute to the observed differences in mechanical properties after ageing.

Figure 8.16 illustrates the impact of the nucleation site fraction of the $\text{Ca}_2\text{Mg}_6\text{Zn}_3$ and MgZn (β -type) phases, revealing distinct differences in precipitation kinetics between the two phases. It is expected that the $\text{Ca}_2\text{Mg}_6\text{Zn}_3$ phase approaches its maximum volume fraction in approximately 1 hour, and MgZn takes approximately 120 hours. This corresponds to a nucleation site of 10^{-3} for $\text{Ca}_2\text{Mg}_6\text{Zn}_3$ and in the range of $10^{-9} \sim 10^{-10}$ for the MgZn phase. The volume fraction of $\text{Ca}_2\text{Mg}_6\text{Zn}_3$ remains consistently higher than that of MgZn , indicating that it is the dominant precipitate phase in the ZX30 alloy. However, the formation of MgZn follows a more delayed response, with its volume fraction gradually increasing at prolonged ageing times. This trend suggests that MgZn nucleates more sluggishly compared to $\text{Ca}_2\text{Mg}_6\text{Zn}_3$, likely due to differences in solute diffusion rates and phase stability. By correlating these findings with the ageing hardness evolution in Figure 8.13, the nucleation site fraction of $\text{Ca}_2\text{Mg}_6\text{Zn}_3$ and MgZn (β -type) phases can be estimated based on the ageing time at which their volume fractions stabilize at their maximum values in Figure 8.16. The study by Nie et al. [99] suggests that the peak ageing response time for $\text{Ca}_2\text{Mg}_6\text{Zn}_3$ occurs at approximately 1 hour. Therefore, based on Figure 8.16, the nucleation site fraction of $\text{Ca}_2\text{Mg}_6\text{Zn}_3$ is estimated to be around 10^{-3} . Meanwhile, by analysing both Figure 8.13 and Figure 8.16, the nucleation site fraction of the MgZn (β -type) phase is found to be approximately 10^{-9} , which is consistent with the findings of Robson et al. [293]. Furthermore, considering that the TCMG6 database does not include metastable phases, the initial formation of the MgZn phase in this study is described as β'_1 precipitate.

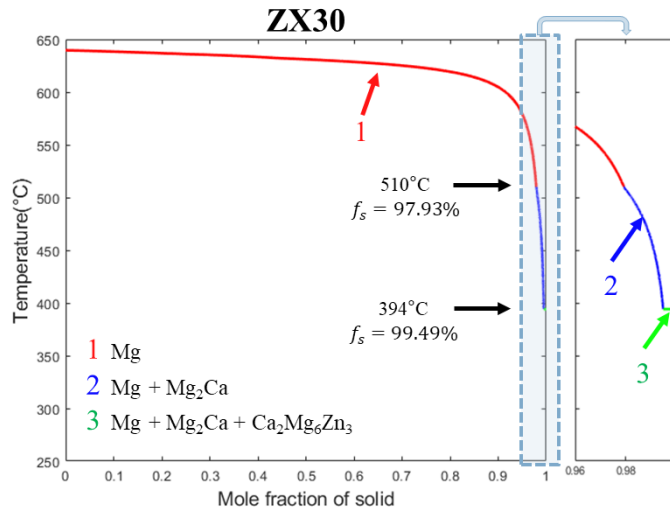


Figure 8.14. Liquidus-minimising Scheil solidification curve of ZX30 alloy.

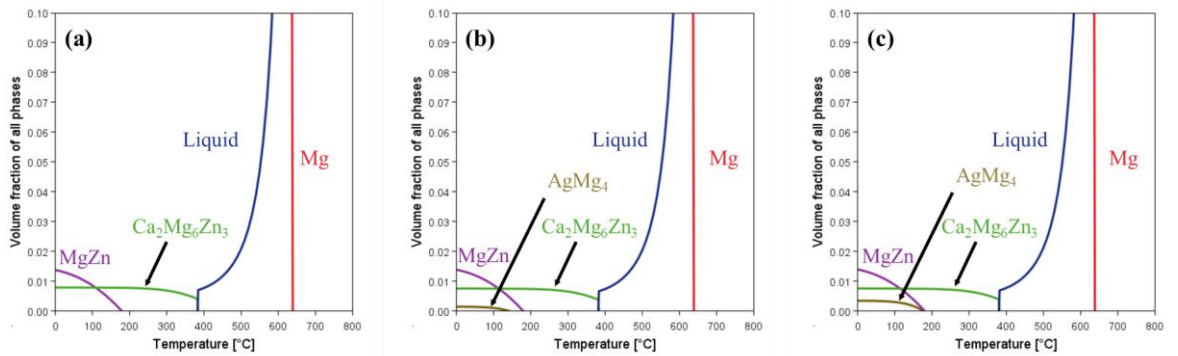


Figure 8.15. Equilibrium phase diagram of (a) ZX30, (b) ZXQ300a, (c) ZXQ300b alloys

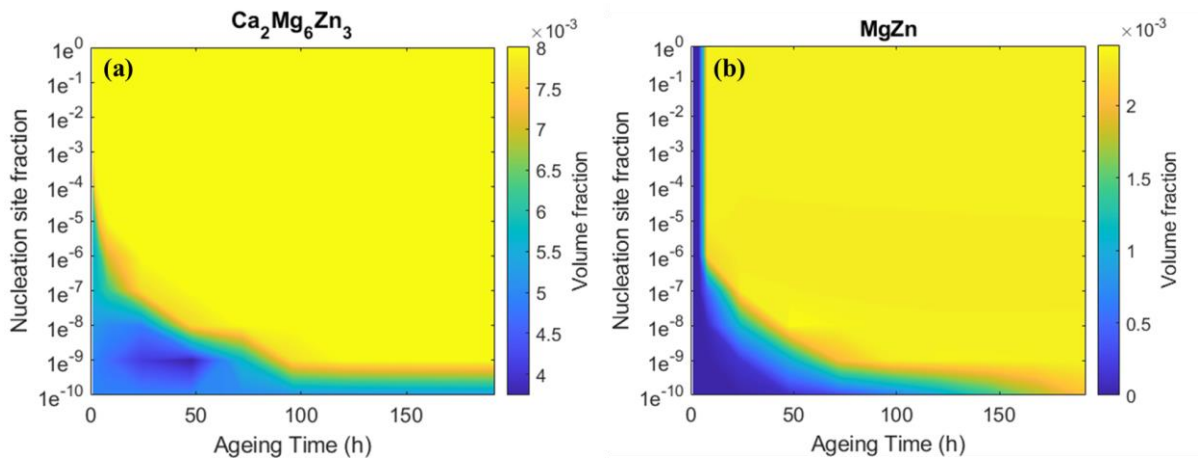


Figure 8.16. Particles volume fraction with variation of nucleation site fraction and ageing time of (a) $\text{Ca}_2\text{Mg}_6\text{Zn}_3$ phase and (b) MgZn phase in ZX30 alloy

Figure 8.17 to Figure 8.19 show the volume fraction and average particle size evolutions of the ZX30, ZXQ300a, and ZXQ300b alloys, providing insights into the precipitation kinetics and growth behaviour of different phases during ageing at 160°C. The results highlight variations in the precipitation response among the three alloys due to differences

in composition, particularly the influence of Ag on nucleation and growth mechanisms. The volume fraction of the $\text{Ca}_2\text{Mg}_6\text{Zn}_3$ phase remains nearly constant throughout the ageing process, indicating that this phase is primarily present from the early stages of precipitation.

In the ZX30 alloy (Figure 8.17c), the volume fractions of the β'_1 and β'_2 phases gradually increase over time, with β'_1 exhibiting a more pronounced growth compared to β'_2 . The mean particle size evolution (Figure 8.17d) indicates a steady increase in coarsening, with β'_2 precipitates exhibiting a larger size despite their lower volume fraction compared to β'_1 . The ZXQ300a alloy (Figure 8.18) exhibits precipitation behaviour similar to that of ZX30. However, the β'_1 phase in ZXQ300a experiences a faster increase in volume fraction, suggesting that the presence of Ag may influence its nucleation kinetics. The mean particle size evolution shown in Figure 8.18d indicates that the growth time of the β'_1 phase is delayed compared to ZX30, suggesting that Ag alters the growth kinetics of precipitates in this alloy. In contrast, the ZXQ300b alloy (Figure 8.19) displays significantly different precipitation behaviour compared to ZX30 and ZXQ300a. Both β'_1 and β'_2 phases exhibit a rapid increase in volume fraction during the early stages of ageing, with β'_2 ultimately achieving a higher final volume fraction compared to the other two alloys. This suggests that the addition of Ag in ZXQ300b promotes the transformation of β'_2 precipitates. Furthermore, the mean particle size evolution (Figure 8.19d) shows that, compared to ZXQ300a, the peak size of β'_2 precipitates is reduced, indicating that Ag addition enhances the transformation rate of β'_2 precipitates while simultaneously slowing their coarsening process.

A comparison of the results for ZX30, ZXQ300a, and ZXQ300b suggests that while Ag addition does not significantly impact the formation of $\text{Ca}_2\text{Mg}_6\text{Zn}_3$, it plays a crucial role in modifying the precipitation kinetics of β'_1 and β'_2 phases. Specifically, Ag appears to accelerate the nucleation of β'_1 precipitates and the transformation of β'_2 precipitates in ZXQ300b, leading to a higher volume fraction at earlier ageing times. This enhanced precipitation kinetics likely contributes to the improved ageing hardening response observed in ZXQ300b, as reflected in the hardness data in Figure 8.13. Ag addition affects the solute distribution and nucleation dynamics of strengthening precipitates, ultimately influencing the mechanical performance of the aged alloys.

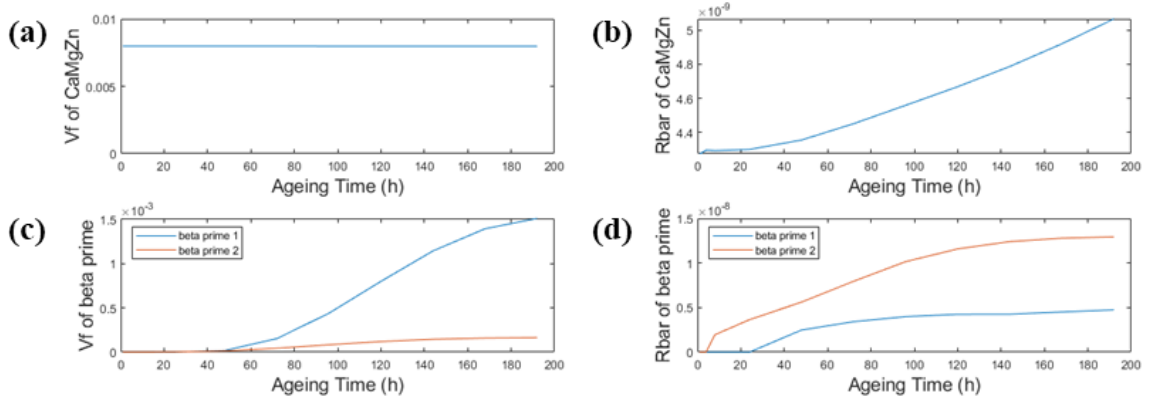


Figure 8.17. Mean-field results of (a,c) particles volume fraction and (b,d) particle mean radius in ZX30 alloy aged at 160°C; (a,b) are $\text{Ca}_2\text{Mg}_6\text{Zn}_3$ phase and (c,d) are β'_1 and β'_2 phases.

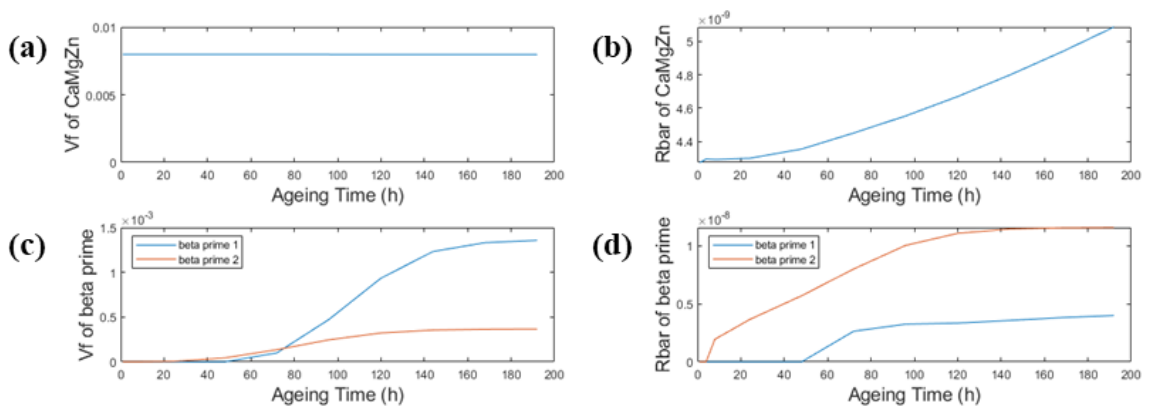


Figure 8.18. Mean-field results of (a,c) particles volume fraction and (b,d) particle mean radius in ZXQ300a alloy aged at 160°C; (a,b) are $\text{Ca}_2\text{Mg}_6\text{Zn}_3$ phase and (c,d) are β'_1 and β'_2 phases.

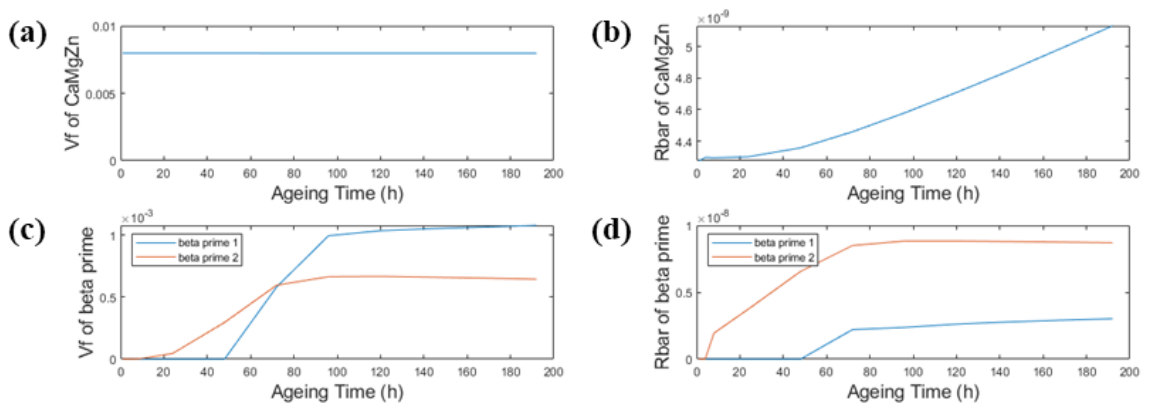


Figure 8.19. Mean-field results of (a,c) particles volume fraction and (b,d) particle mean radius in ZXQ300b alloy aged at 160°C; (a,b) are $\text{Ca}_2\text{Mg}_6\text{Zn}_3$ phase and (c,d) are β'_1 and β'_2 phases.

8.6 Precipitation-Property Model

Figure 8.20 shows the simulated strengthening curve comparing with hardness data of the ZX30, ZXQ300a, and ZXQ300b alloys. The calculated yield stress evolution aligns well

with the experimental hardness measurements, reproducing the strengthening behaviour with precipitation model.

For the ZX30 alloy (Figure 8.20a), the simulated yield stress exhibits a slow increase during the early ageing stage (0–24 h), followed by a significant rise between 24 and 120 h. The yield stress reaches its peak at approximately 144 h, which aligns with the peak ageing time observed in the hardness data. After reaching peak ageing, a slight decline in yield stress is observed, indicating the onset of over ageing, where precipitate coarsening reduces the strengthening effect. For the ZXQ300a alloy (Figure 8.20b), the strengthening trend follows a similar trajectory to that of ZX30, with an initial slow increase followed by a rapid hardening phase. However, the peak yield stress of ZXQ300a is slightly higher than that of ZX30, suggesting that the presence of Ag contributes to an improvement in strengthening. Nevertheless, the overall strengthening response remains comparable to ZX30, indicating that the Ag content in ZXQ300a is insufficient to induce a significant shift in precipitation kinetics. In contrast, the ZXQ300b alloy (Figure 8.20c) exhibits the highest peak yield stress among the three alloys, demonstrating a more pronounced strengthening effect. The rate of increase in yield stress is more rapid, with a significant rise occurring between 48 h and 72 h, reaching its peak at 96 h. This trend aligns with the rapid hardening response observed in the hardness data. However, the peak ageing time predicted by the model does not perfectly match the experimental data. This discrepancy suggests the potential presence of fine AgMg_4 precipitates in Figure 8.15 that are not accounted for in the current model at this Ag content, leading to deviations in the predicted strengthening behaviour

A comparative analysis of the three alloys reveals that Ag addition accelerates the strengthening response and enhances the overall peak strength, particularly in ZXQ300b. The improved strengthening effect in ZXQ300b can be attributed to the enhanced nucleation of β_1' precipitates and the accelerated transformation kinetics, as indicated in Figure 8.17 to Figure 8.19. These findings confirm that Ag addition alters the precipitation kinetics and strengthening mechanisms in Mg-Zn-Ca alloys, leading to superior mechanical performance.

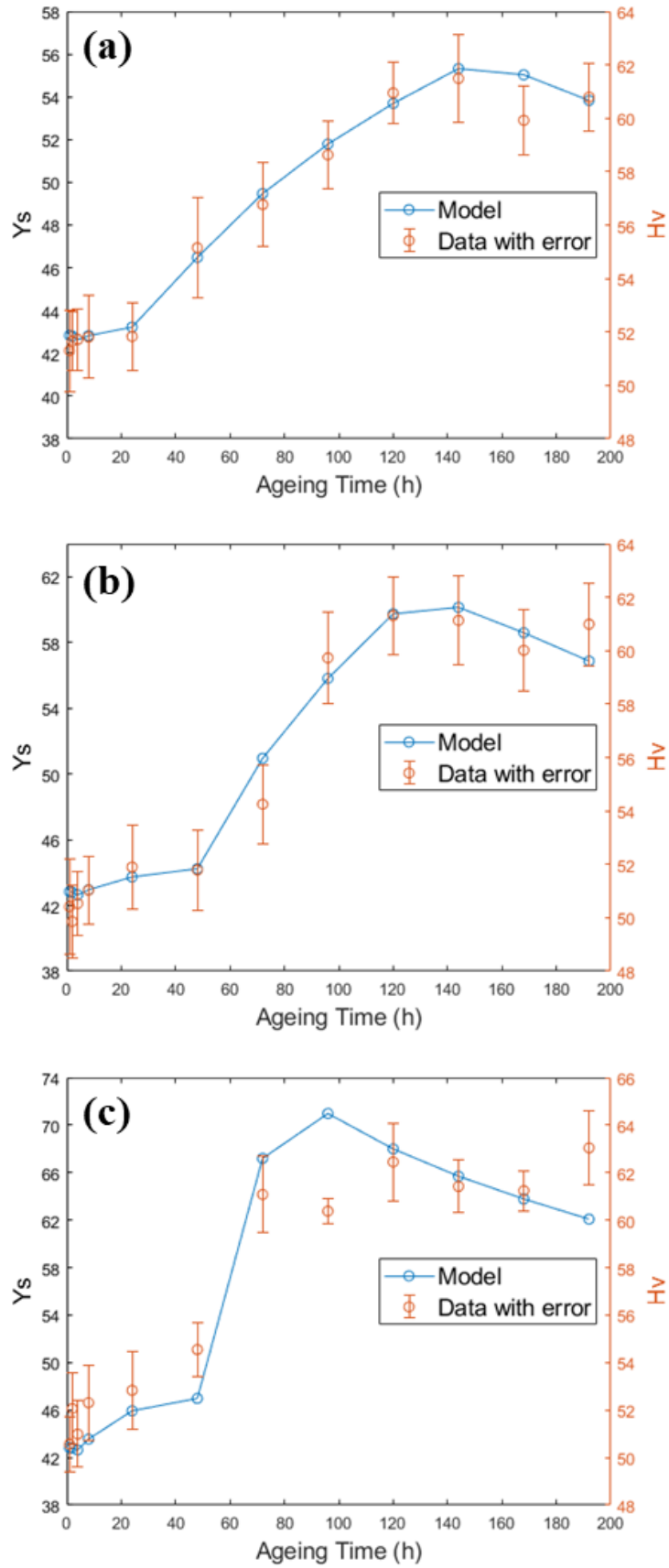


Figure 8.20. The predicted yield stress of (a) ZX30, (b) ZXQ300a, (c) ZXQ300b alloys aged at 160°C compared with the experimental hardness data.

8.7 Discussion

8.7.1 Microstructure Evolution of Mg-3Zn-0.2Ca(-xAg) Alloys

The EBSD analysis of as-extruded and solution-treated Mg-3Zn-0.2Ca(-xAg) alloys provides essential insights into their microstructure, recrystallisation behaviour, grain boundary characteristics, and texture development. Grain orientation spread (GOS) from EBSD data is widely utilised to distinguish dynamically recrystallised (DRX) grains from deformed parent grains [294].

Under the as-extruded condition, distinct differences in the extent of recrystallisation are observed among the three alloys. The ZX30 alloy exhibits a heterogeneous microstructure with elongated grains, indicating incomplete DRX. The proportion of low-angle grain boundaries (LAGBs) is 22.6%, signifying that a substantial amount of stored deformation energy remains within the microstructure. The presence of elongated grains, strong basal texture, and a pronounced (0001) peak along the normal direction (ND) further support the observation of limited recrystallisation. In comparison, the ZXQ300a alloy exhibits a recrystallisation behaviour similar to ZX30. The proportion of LAGBs is 25.8%, and GOS analysis shows that approximately 70% of grains exhibit GOS values below 7° , indicating that the minor addition of Ag does not significantly affect the extent of DRX during extrusion. In contrast, the ZXQ300b alloy exhibits the most fully recrystallised microstructure among the three compositions. The fraction of high-angle grain boundaries (HAGBs) increases to 93.7%, whereas LAGBs decrease to 6.3%, signifying that the recrystallisation process is nearly complete. The microstructure primarily consists of fine equiaxed grains with minimal internal strain, as evidenced by the low GOS values, with 89% of grains exhibiting GOS below 1.5° . In this study, the DRX critical threshold for Mg-Zn-Ca(-Ag) alloys is determined to be 2° , as the GOS threshold used to separate DRX grains from unrecrystallised grains varies between 1° and 2° in different materials [295,296]. The texture of ZXQ300b is significantly weaker than that of ZX30 and ZXQ300a, confirming that the addition of Ag strongly promotes recrystallisation and texture weakening. The enhancement of recrystallisation in ZXQ300b can be partly attributed to the formation of finely dispersed second-phase particles after the addition of Ag. These particles provide a Zener pinning effect, which delays grain boundary motion and inhibits grain growth. This helps to retain stored deformation energy and promotes nucleation of new grains, thus facilitating more complete dynamic recrystallisation.

After solution treatment, all three alloys undergo further recrystallisation and grain growth, albeit to different extents. The proportion of HAGBs in the ZX30 alloy increases

significantly to 84.4%, while LAGBs decrease accordingly, suggesting that static recrystallisation has advanced considerably. Texture intensity is reduced, as evidenced by the lower (0001) peak intensity in the pole figure, indicating that solution treatment promotes grain orientation randomisation. The ZXQ300a alloy experiences further recrystallisation, with HAGBs increasing to 82.4%. However, its overall grain structure and texture remain comparable to those of ZX30, suggesting that the presence of Ag in this composition does not induce substantial microstructural transformation during solution treatment. In contrast, the ZXQ300b alloy exhibits pronounced microstructural changes following solution treatment. Although the microstructure remains predominantly recrystallised, noticeable grain growth occurs, as indicated by an increase in LAGBs to 10.6%, suggesting the formation of substructures due to grain growth. The misorientation distribution shows a strong peak at 85° , which is characteristic of twin boundaries, indicating that twinning may have occurred during the heat treatment. This observation is consistent with the study by Leu et al. [291] and Kim et al. [110], which reported the formation of twin boundaries in Mg alloys with similar misorientation characteristics. The grain diameter distribution shifts towards larger grain sizes, confirming that recrystallisation is accompanied by grain coarsening. These findings suggest that while the addition of Ag enhances DRX and texture weakening during extrusion, it also accelerates grain boundary mobility during solution treatment, leading to excessive grain growth and potential coarsening effects.

The overall EBSD analysis reveals significant differences in the recrystallisation behaviour among the three alloys. ZX30 and ZXQ300a exhibit a mixed microstructure with partial recrystallisation after extrusion, whereas ZXQ300b undergoes nearly complete DRX. Solution treatment further enhances recrystallisation in all alloys; however, the extent of texture weakening and grain growth varies. ZXQ300b experiences substantial grain coarsening, which may be attributed to the influence of Ag on recrystallisation kinetics and grain boundary mobility [91]. The presence of a strong 85° misorientation peak in solution-treated ZX30, ZXQ300a and ZXQ300b alloys further confirms that twinning occurs during heat treatment. These findings highlight the role of Ag in influencing the microstructural evolution during thermal processing. However, its specific impact on recrystallisation requires further investigation through additional annealing EBSD experiments.

Microstructural characterization through SEM and EDS (Figure 8.11) reveals that the second phase particle distribution remains largely unchanged between the solution-

treated and peak-aged conditions. The predominant intermetallic phases in all three alloys are identified as $\text{Ca}_2\text{Mg}_6\text{Zn}_3$, with a smaller fraction of Mg_2Ca , suggesting that Zn and Ca predominantly participate in the formation of these phases. Ag is observed to be dispersed throughout the matrix in ZXQ300a and ZXQ300b, indicating that a significant portion remains in solid solution, which may contribute to subsequent precipitation hardening. However, no distinct AgMg_4 precipitates, typically expected in Mg-Ag alloys, were detected in either ZXQ300a or ZXQ300b. Instead, slight Ag accumulation was observed at second phase particles in ZXQ300b, suggesting that Ag may serve as heterogeneous nucleation sites for Mg-Ag-based precipitates upon further ageing. This microstructural observation implies that while Ag does not form distinct precipitates in its current state, it plays a crucial role in modifying precipitation kinetics. A study by Yin et al. [297] investigated Mg-2Zn-0.2Ca (wt.%) and Mg-2Zn-0.2Ca-0.5Ag (wt.%) alloys using high-resolution STEM-EDS characterization. As shown in Figure 8.21 of their work, no Mg-Ag-based precipitates were observed within precipitate particles of approximately 500 nm. Therefore, it can be inferred that Mg-Ag-based precipitates are not present in the current ageing condition of ZXQ300b. This further supports the hypothesis that Ag in ZXQ300b influences precipitation kinetics without forming distinct Mg-Ag precipitates at this stage.

The hardness evolution during the ageing process at 160°C (Figure 8.13) provides further insights into the precipitation behaviour of the alloys. In the early ageing stage (0–24 hours), the hardness remains stable at approximately 52 HV, indicating that the nucleation of precipitates is still in the incubation phase and has not yet significantly contributed to hardening. The ageing response varies distinctly among the three alloys, with ZXQ300b exhibiting the fastest age-hardening response, as evidenced by a sharp increase in hardness between 48 and 72 hours, reaching 61 HV, followed by a continued increase to a peak hardness of ~63 HV. The peak ageing time for all three alloys is approximately 120 hours, but ZXQ300b demonstrates the highest and fastest hardening response. This accelerated response in ZXQ300b can be directly linked to the role of Ag in promoting the nucleation of β -type phases. As shown in Figure 8.16, the maximum volume fraction of precipitates correlates with the nucleation site fraction, which increases with Ag content. Eq. (6.1) reveals that the nucleation site fraction is proportional to the dislocation density. Therefore, the addition of Ag likely influences the maximum dislocation density generated during hot extrusion, thereby increasing the nucleation site fraction and accelerating the nucleation of β -type precipitates during ageing. Based on the combined EDS results, although no distinct Mg–Ag-based precipitates were detected, Ag may still

facilitate the formation of β'_1 and β'_2 phases through this enhanced nucleation mechanism. The overall analysis suggests that Ag plays multiple roles in the strengthening mechanisms of Mg-Zn-Ca(-Ag) alloys. While no distinct Ag-containing precipitates were observed under the current conditions, its presence modifies the precipitation behaviour, enhances the kinetics of age-hardening, and mitigates excessive ductility loss after ageing. The superior hardening response of ZXQ300b can thus be attributed to both accelerated precipitate formation and improved microstructural stability. These findings highlight the potential of Ag-containing Mg-Zn-Ca alloys for applications requiring an optimised strength-ductility balance and improved thermal stability.

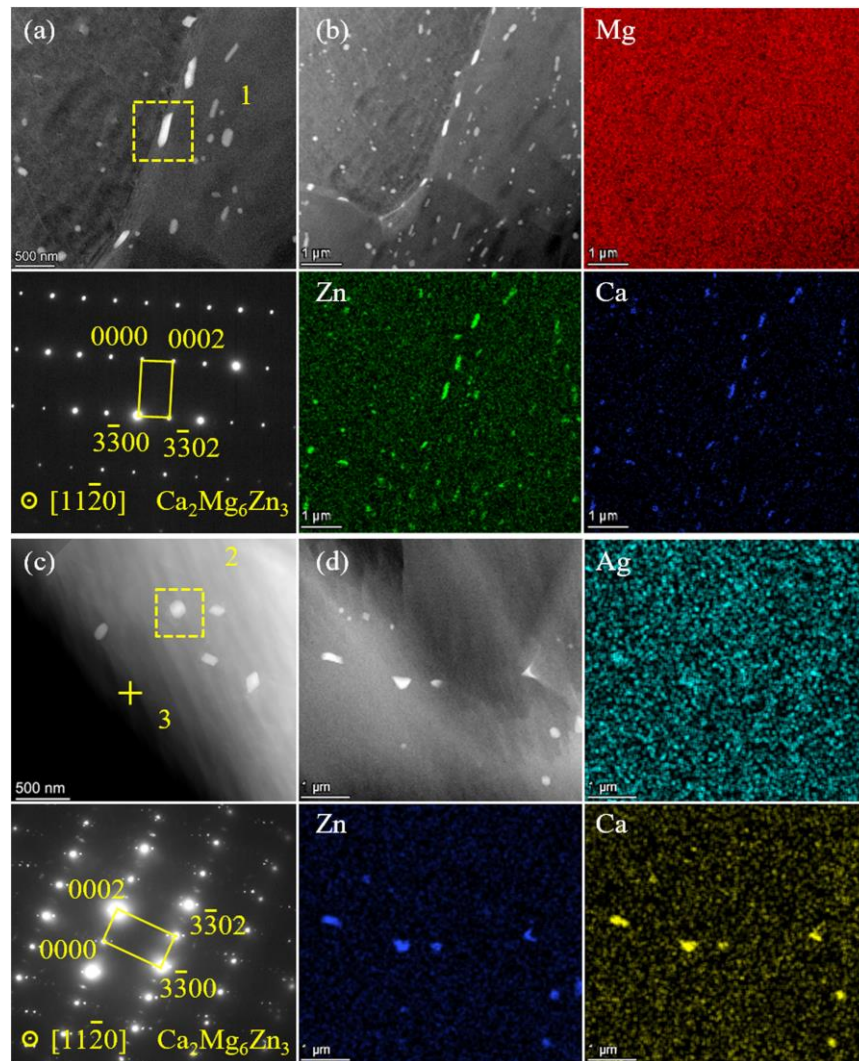


Figure 8.21. Higher magnification dark field images (a, c) with corresponding selected-area electron diffraction (SAED) images of the precipitates of yellow box, lower magnification dark field images and corresponding EDS maps (b, d): ZX20 (a, b) and ZXQ0.3 (c, d) [297].

8.7.2 Precipitation Sequences of β -type Phases

The precipitation sequence of Mg-Zn alloys has been a subject of extensive research, yet certain aspects, particularly the formation and stability of the β phase, remain uncertain.

This discussion delves into these uncertainties, drawing insights from recent studies. Traditionally, the precipitation sequence in Mg-Zn alloys is understood as: $SSSS \rightarrow GP\ zone \rightarrow \beta'_1 \rightarrow \beta'_2 \rightarrow \beta$ [99]. The GP zone in Mg-Zn-Ca alloys is a nanoscale, solute-rich monolayer, typically less than 10 nm in size. Due to its coherent nature and extremely small dimensions, it is very difficult to observe directly using conventional high-resolution microscopy techniques such as TEM or APT. Limited experimental resolution hinders accurate structural validation and comparison with simulations. For example, APT analyses show that the Zn-Ca-rich GP region is monolayered, with a size of about 8 nm and a number density of $1.3 \times 10^{23} m^{-3}$, but precise structural information remains challenging to determine [283]. Given these constraints in modelling, and considering that the formation time of GP zones (~ 1 h) is much shorter than that of the β -type phase (~ 100 h), we therefore exclude GP zone formation from our simulation and focus directly on the development of the β -type phase.

The exact nature and role of the β phase in this sequence have been the subject of debate. Recent studies have provided deeper insights into this precipitation behaviour. Cheng et al. [164] conducted first principle calculations and revealed that the β'_2 phase may form directly from the supersaturated solid solution under certain conditions, bypassing intermediate β'_1 phase. This direct transformation challenges the traditional sequential model and suggests that factors such as alloy composition, and ageing temperature significantly influence the precipitation pathway.

Moreover, the kinetic parameters governing the transformation from the β'_1 phase to the β'_2 phase remain unclear. Yang et al. [268] utilized a combination of atom probe tomography (APT) and transmission electron microscopy (TEM) to characterise the evolution of precipitate types, sizes, and volume fractions in Mg-Zn alloys during the ageing process. Based on these observations, a time-temperature-transformation (TTT) diagram was proposed for this system (Figure 8.22). Their findings revealed that β'_1 precipitates dominate in the early ageing stage, while β'_2 precipitates begin to form at approximately 100 hours at an ageing temperature of 150°C. This formation timeline closely aligns with the peak ageing time observed in the current study.

Another layer of complexity arises from the interaction between Zn and other alloying elements, which influences the precipitation behaviour of β -type phases. Elements such as Ag and Ca can modify the precipitation sequence by stabilizing or destabilizing certain phases. For example, Ca additions can promote the formation of other intermetallic compounds, potentially suppressing the precipitation of β -type phases [287].

These findings emphasize the necessity of a detailed understanding of the role of β -type phases in Mg-Zn alloys. The precipitation sequence is not universally fixed but is highly sensitive to alloy composition and processing conditions. Therefore, optimising these parameters is critical for enhancing the mechanical properties of Mg-Zn-based alloys.

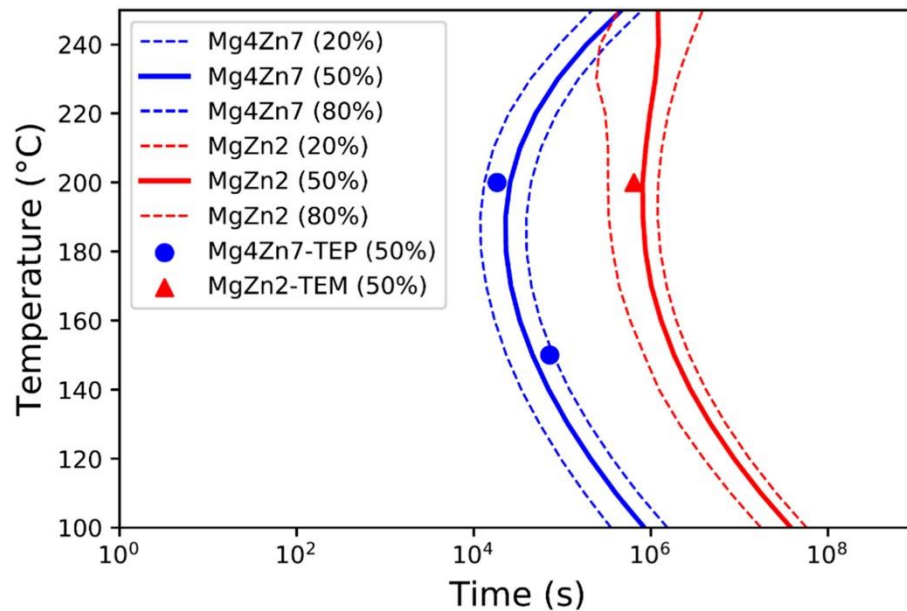


Figure 8.22. TTT diagram of the formation of Mg_4Zn_7 and MgZn_2 phases in Mg-1.7at.%Zn alloy [268].

8.7.3 Dislocation Pinning for Non-spherical Precipitates

The interaction between dislocations and precipitates plays a crucial role in determining the mechanical properties of Mg-Zn-Ca(-Ag) alloys. While spherical precipitates have been extensively studied in terms of Orowan strengthening and dislocation bypass mechanisms, non-spherical precipitates introduce additional complexity due to their anisotropic shape and heterogeneous stress distribution. In the studied alloys, the primary strengthening precipitates, including β'_1 and β'_2 phases, exhibit non-spherical morphologies, which significantly influence their ability to pin dislocations and resist deformation.

Non-spherical precipitates introduce anisotropic interactions with dislocations, making their pinning behaviour distinct from that of spherical particles. Studies on Mg-Zn alloys have shown that rod-shaped or plate-like precipitates create localized stress fields that hinder dislocation motion more effectively than spherical particles of similar volume fraction [293]. This effect is particularly relevant in Mg alloys, where basal slip is the dominant deformation mode. The presence of elongated β' phases aligned along specific crystallographic orientations can increase resistance to basal dislocation motion, thereby enhancing strength.

The effectiveness of non-spherical precipitates in dislocation pinning can be analysed using classical strengthening models. The Orowan mechanism predicts that the critical resolved shear stress (CRSS) for dislocation bowing is inversely proportional to the precipitate spacing, but this assumption is primarily based on spherical or equiaxed precipitates [131]. In contrast, for non-spherical needle-like or precipitates plate-like precipitates can increase CRSS due to their interaction with dislocations in Mg alloys, where slip anisotropy makes dislocation-pinning effects more sensitive to precipitate morphology [10]. Comparing the experimental results with strengthening predictions in Figure 8.20, it can be inferred that the ZXQ300b alloy achieves the highest strengthening efficiency due to the effects of precipitate shape, volume fraction, and distribution. The enhanced precipitation kinetics of β' phases in the presence of Ag further contributes to the observed improvements in yield strength, as seen in the predicted yield stress evolution.

8.8 Conclusion to this chapter

This chapter provided a comprehensive analysis of the microstructural evolution, precipitation behaviour, and mechanical performance of Mg-3Zn-0.2Ca(-xAg) alloys. The study focused on the role of Ag in modifying precipitation kinetics, strengthening mechanisms, and microstructural evolution, using both experimental characterisation and computational modelling approaches. The following conclusions may be drawn from the present study:

1. Extrusion followed by heat treatment significantly alters the grain structure and texture evolution. The addition of Ag was found to enhance recrystallisation in the as-extruded condition, particularly in ZXQ300b, where a higher fraction of high-angle grain boundaries (93.7%) and a weaker basal texture were observed. This enhanced recrystallisation can be attributed to the formation of fine and dispersed second phase particles induced by addition of Ag, thereby promoting more extensive dynamic recrystallisation.
2. The precipitation sequence in Mg-Zn alloys remains complex and composition-dependent. The formation of β -type phases (β'_1 and β'_2) was significantly influenced by the presence of Ag, which accelerated nucleation and modified the transformation kinetics. In ZXQ300b, an earlier formation of β'_2 was observed, suggesting that Ag promotes a more rapid transition between metastable and equilibrium precipitates, and the formation of $\text{Ca}_2\text{Mg}_6\text{Zn}_3$ was independent of Ag.

3. The precipitation strengthening contributions from ageing process were quantified through experimental hardness, which were supported by Mean-field precipitation modelling. The results showed that Ag enhances the age-hardening response by refining precipitate size and accelerate precipitate formation of β' phases, as seen in the improved hardness evolution of ZXQ300b. The predictive yield stress model closely matched experimental data, though minor discrepancies suggest that additional Ag-containing phases may exist. The β'_1 and β'_2 phases are effective barriers to dislocation motion. The addition of Ag influenced the spatial distribution of these precipitates, thereby improving the overall mechanical performance. Based on the current modelling framework, the enhanced nucleation of β -type phases in Ag-containing alloys are attributed to an Ag-induced increase in the dislocation-assisted nucleation site fraction. This implies that increasing Ag content stabilises dislocation cores, thereby promoting cross slip from basal to prismatic plane during high temperature extrusion. In consequence, the dislocation density increases resulting in a high value of η (see Eq.(6.1)), which promote faster precipitation kinetics. The Orowan bowing model confirmed that Ag-induced precipitates enhanced dislocation pinning and contributed to superior strengthening efficiency in ZXQ300b.

Chapter 9: Conclusion

This study has systematically investigated the microstructural evolution, phase transformations, and mechanical properties of Mg-Zn-Ca(-Ag) alloys using an integrated approach combining CALPHAD-based thermodynamic and kinetic modelling with comprehensive experimental validation. The research focused on three main aspects: solidification and segregation behaviour (Chapter 6), homogenisation and diffusion kinetics (Chapter 7), and precipitation mechanisms and mechanical performance (Chapter 8). Together, the results provide a coherent understanding of how alloy composition and processing routes govern the formation and transformation of second phases, and how these, in turn, affect final microstructures and mechanical properties.

In Chapter 6, the solidification behaviour of ZX10 (Mg-0.8Zn-0.2Ca) and ZX70 (Mg-6.8Zn-0.2Ca) alloys was studied using Scheil and mean-field models. SEM-EDS revealed distinct segregation behaviours: Ca segregated independently in ZX10, promoting Mg₂Ca formation, whereas Zn segregation dominated in ZX70, stabilising MgZn. Comparative analysis showed that the Scheil model provided more accurate predictions of second-phase volume fractions and formation sequences under rapid cooling conditions than the mean-field approach. A novel Liquidus-minimising Scheil model developed in this work more effectively captured the effects of composition gradients, particularly in ZX10, where minor fluctuations strongly influenced solidification paths. These modelling results confirm that intermetallic phases such as Mg₂Ca and Ca₂Mg₆Zn₃ form directly from the liquid phase and underscore the importance of composition control and advanced non-equilibrium modelling to optimise solidification outcomes.

In Chapter 7, focused on the post-solidification evolution of second phases during homogenisation heat treatment. The diffusion behaviour and dissolution of Mg₂Ca and Ca₂Mg₆Zn₃ in ZX10 were investigated through DICTRA simulations and validated experimentally. Heat treatment at 520 °C for 4 hours led to partial dissolution of Mg₂Ca and near-complete dissolution of Ca₂Mg₆Zn₃. While Zn exhibited faster diffusion and homogenised effectively, Ca showed persistent concentration gradients near grain boundaries. The diffusion simulations, particularly the self-diffusion model, overestimated the rate of homogenisation, likely due to idealised initial conditions derived from the Scheil model that underestimated Ca segregation intensity. The diffusion couple model revealed that Zn-containing Mg₂Ca dissolves faster than Zn-free variants, but significant amounts of Mg₂Ca remained in both cases. This finding highlights the limited effectiveness of post-casting heat treatment in fully removing Mg₂Ca and suggests that

mitigating its formation during solidification via alloy design and cooling rate control is a more effective strategy.

In Chapter 8, the precipitation behaviour, texture evolution, and mechanical properties of Ag-containing Mg-Zn-Ca alloys were examined. The addition Ag had a pronounced effect on precipitation kinetics, accelerating the formation of β'_1 and β'_2 phases and refining their size and distribution. These effects translated into a significantly enhanced age-hardening response and higher yield strength in Ag-containing alloys. Mean-field precipitation modelling, combined with Orowan-based dislocation strengthening predictions, closely matched experimental observations and confirmed the key role of β -type Mg-Zn precipitates in strengthening. Nonetheless, Ag addition also promoted twin formation during solution treatment, indicating a trade-off that must be managed through optimised processing schedules.

Overall, this research contributes significantly to the understanding of Mg-Zn-Ca(-Ag) alloys by providing a detailed assessment of solidification intermetallic phase formations, the effectiveness of heat treatment process, and the influence of microalloying on microstructure evolution and mechanical properties. The study advances solidification modelling through the introduction of an improved Scheil solidification approach for ternary systems, which enables more accurate predictions of phase segregation and intermetallic phase formation. It also establishes that conventional homogenisation treatments have limited success in eliminating stable intermetallics like Mg_2Ca , reinforcing the need for compositional control at the casting stage to minimise unwanted phases. Furthermore, the research highlights the potential of Ag as a microalloying element for refining precipitation behaviour and enhancing mechanical properties.

Despite these contributions, the study has limitations that should be considered when interpreting the findings. The predictive models used, particularly the Scheil and diffusion simulations, rely on simplifying assumptions that do not fully account for back-diffusion effects during solidification or the actual segregation profiles observed in experimental samples. This introduces some uncertainty in the quantitative accuracy of the homogenisation predictions. Additionally, the study focused on a limited range of compositions and processing conditions, meaning that the conclusions drawn regarding phase stability, heat treatment effectiveness, and Ag's impact may not be directly transferable to other Mg-Zn-Ca-based alloys. Furthermore, the mechanical characterisation was primarily limited to hardness and tensile testing, and did not assess other critical properties such as fatigue resistance, creep behaviour, or corrosion

performance, which are important for structural and biomedical applications. Addressing these areas in future research would provide a more comprehensive understanding of the factors governing the performance of Mg-Zn-Ca alloys. Based on these findings, several recommendations for future work can be proposed in the next chapter.

This study provides valuable insights into the microstructural evolution and mechanical performance of Mg-Zn-Ca(-Ag) alloys, offering both theoretical and practical contributions to the field of magnesium alloy development. By integrating advanced modelling techniques with experimental validation, the research enhances the understanding of phase transformations and processing-microstructure-property relationships in these alloys. The findings emphasize the importance of alloy composition, solidification control, and microalloying in optimising mechanical performance, while also identifying key challenges and directions for future research. Through continued advancements in modelling, processing techniques, and alloy design, Mg-Zn-Ca-based alloys can be further developed to meet the demands of lightweight structural materials with improved mechanical properties.

Chapter 10: Future Work

Building on the findings of this study, several research directions are proposed to further development of Mg-Zn-Ca(-Ag) alloys. These directions focus on improving computational models, expanding alloy design, integrating digital twin approaches, evaluating mechanical and environmental performance, and employing advanced characterisation techniques to deepen the understanding of microstructural evolution.

10.1 Extending computational models and alloy composition optimisation

The accuracy and applicability of computational models should be further improved, particularly by extending the Liquidus-minimising Scheil model beyond ternary systems to quaternary or higher-order alloy compositions. The current study has demonstrated that the Scheil model, when modified for ternary Mg-Zn-Ca alloys, provides more accurate phase predictions compared to conventional approaches. However, with the introduction of additional alloying elements such as Ag, the complexity of phase interactions increases, necessitating a further refinement of thermodynamic descriptions and kinetic models. Extending the solidification model to quaternary and multi-component systems will enable a more precise prediction of phase stability, elemental segregation, and intermetallic formation in increasingly complex Mg alloys. The integration of CALPHAD-based approaches with machine learning techniques could facilitate high-throughput alloy design, accelerating the discovery of new Mg-Zn-Ca-based alloys with tailored properties.

10.2 Develop multi-scale digital twin models for industrial applications

A major direction for future research lies in the development of multi-scale digital twin models, expanding the application of computational tools from experimental samples to industrial-scale manufacturing. While this study has primarily focused on laboratory-scale alloy processing and characterisation, translating these findings to real-world applications requires the integration of process simulation with materials modelling. A digital twin framework, combining thermodynamic, kinetic, and mechanical property models, could be developed to simulate alloy behaviour under various industrial processing conditions such as thermomechanical treatments (rolling, extrusion, forging) and additive manufacturing (AM). The incorporation of process-structure-property relationships within a digital twin environment would enable real-time optimisation of alloy design and manufacturing parameters, facilitating the transition from fundamental research to practical implementation in lightweight structural applications.

10.3 Expanding mechanical performance and environmental adaptability

The scope of mechanical and environmental performance evaluation can be expanded to determine the feasibility of Mg-Zn-Ca(-Ag) alloys for biomedical applications. While this study has provided insights into tensile properties and hardness, additional testing is required to fully assess the alloys' performance under application-relevant conditions. Fatigue testing should be conducted to evaluate the long-term durability of these alloys under cyclic loading, a critical requirement for structural and biomedical implants. Similarly, creep resistance at elevated temperatures should be studied to determine the stability of precipitate-strengthened alloys, particularly in applications where long-term mechanical reliability is crucial. Furthermore, the corrosion behaviour of Ag-containing Mg alloys should be thoroughly investigated, as Ag can influence the electrochemical properties of the matrix and second phases. Biodegradation studies in simulated physiological environments should be conducted to assess the suitability of these alloys for biomedical implants, ensuring that the dissolution rate and degradation mechanisms align with clinical requirements for bioresorbable materials.

10.4 Advanced characterisation techniques for microstructural evolution

Advanced characterisation techniques should be employed to gain a deeper understanding of the microstructural evolution and phase transformations in Mg-Zn-Ca(-Ag) alloys. In-situ experimental techniques, such as synchrotron X-ray diffraction (SXRD), and transmission electron microscopy (TEM), could provide real-time insights into solidification behaviour, precipitation kinetics, and phase dissolution during heat treatment. Atom probe tomography (APT) should be utilised to resolve nanoscale solute clustering and precipitation phenomena, particularly in Ag-containing alloys where the exact role of Ag in modifying nucleation and growth mechanisms remains unclear. Additionally, three-dimensional electron backscatter diffraction (3D-EBSD) can be used to study grain boundary evolution and texture development in response to thermomechanical processing. These advanced characterisation methods will not only refine our understanding of phase stability and transformation mechanisms but also provide critical input for improving computational models, thereby closing the loop between experimentation and simulation.

● References

- [1] J. Song, J. She, D. Chen, and F. Pan, Latest research advances on magnesium and magnesium alloys worldwide, *Journal of Magnesium and Alloys* 8, 1 (2020).
- [2] Wang X, Xu D, Wu R, Chen X, Peng Q, Jin L, Xin Y, Zhang Z, Liu Y, Chen X, Chen G, Deng K, Wang H, What is going on in magnesium alloys?, *J Mater Sci Technol* 34, 245 (2018).
- [3] J. Tan, S. Ramakrishna, A. M. Camacho, and F. Berto, Applications of Magnesium and Its Alloys: A Review, *Applied Sciences* 2021, Vol. 11, Page 6861 11, 6861 (2021).
- [4] W. J. Joost and P. E. Krajewski, Towards magnesium alloys for high-volume automotive applications, *Scr Mater* 128, 107 (2017).
- [5] A. A. , C. J. B. Nayeb-Hashemi, Phase diagrams of binary magnesium alloys, *ASM International* (1988).
- [6] M. Avedesian and H. Baker, *ASM Specialty Handbook: Magnesium and Magnesium Alloys*, *Corrosion Reviews* 18, 499 (1999).
- [7] R. Thamizh Selvan, P. C. Vishakh Raja, P. Mangal, N. Mohan, and S. Bhowmik, Recycling technology of epoxy glass fiber and epoxy carbon fiber composites used in aerospace vehicles, *J Compos Mater* 55, 3281 (2021).
- [8] S. Fankhauser et al., The meaning of net zero and how to get it right, *Nature Climate Change* 2022 12:1 12, 15 (2021).
- [9] S. V. S. Prasad, S. B. Prasad, K. Verma, R. K. Mishra, V. Kumar, and S. Singh, The role and significance of Magnesium in modern day research-A review, *Journal of Magnesium and Alloys* 10, 1 (2022).
- [10] J. F. Nie, K. S. Shin, and Z. R. Zeng, Microstructure, Deformation, and Property of Wrought Magnesium Alloys, *Metall Mater Trans A Phys Metall Mater Sci* 51, 6045 (2020).
- [11] J. She, J. Chen, X. Xiong, Y. Yang, X. Peng, D. Chen, and F. Pan, Research advances of magnesium and magnesium alloys globally in 2023, *Journal of Magnesium and Alloys* 12, 3441 (2024).

- [12] G. Song and A. Atrens, Understanding magnesium corrosion. A framework for improved alloy performance, *Adv Eng Mater* 5, 837 (2003).
- [13] G. L. Song and A. Atrens, Corrosion Mechanisms of Magnesium Alloys, *Adv Eng Mater* 1, 11 (1999).
- [14] A. Atrens, G.-L. Song, F. Cao, Z. Shi, and P. K. Bowen, Advances in Mg corrosion and research suggestions, *Journal of Magnesium and Alloys* 1, 177 (2013).
- [15] G. Eddy Jai Poinern, S. Brundavanam, and D. Fawcett, Biomedical Magnesium Alloys: A Review of Material Properties, Surface Modifications and Potential as a Biodegradable Orthopaedic Implant, *Am J Biomed Eng* 2, 218 (2013).
- [16] J. Davis, *Corrosion of Aluminum and Aluminum Alloys* (1999).
- [17] P. C. Banerjee, S. Al-Saadi, L. Choudhary, S. E. Harandi, and R. Singh, Magnesium Implants: Prospects and Challenges, *Materials* 2019, Vol. 12, Page 136 12, 136 (2019).
- [18] J. Chen, X. Zhou, W. Wang, B. Liu, Y. Lv, W. Yang, D. Xu, and Y. Liu, A review on fundamental of high entropy alloys with promising high-temperature properties, *J Alloys Compd* 760, 15 (2018).
- [19] M. Fracchia, M. Manzoli, U. Anselmi-Tamburini, and P. Ghigna, A new eight- cation inverse high entropy spinel with large configurational entropy in both tetrahedral and octahedral sites: Synthesis and cation distribution by X-ray absorption spectroscopy, *Scr Mater* 188, 26 (2020).
- [20] P. Kumari, A. K. Gupta, R. K. Mishra, M. S. Ahmad, and R. R. Shahi, A Comprehensive Review: Recent Progress on Magnetic High Entropy Alloys and Oxides, *J Magn Magn Mater* 554, 169142 (2022).
- [21] T. Li, J. Song, A. Zhang, G. You, Y. Yang, B. Jiang, X. Qin, C. Xu, and F. Pan, Progress and prospects in Mg-alloy super-sized high pressure die casting for automotive structural components, *Journal of Magnesium and Alloys* 11, 4166 (2023).
- [22] L. Chen, T. Ye, Y. Wang, D. Zhou, T. Suo, Q. Deng, F. Zhao, and Q. Wang, Development of mechanical properties in AZ31 magnesium alloy processed by cold dynamic extrusion, *Mater Charact* 182, 111535 (2021).

- [23] L. Feng, C. Wen, J. Li, S. Li, D. Cheng, J. Bai, and Q. Cui, Effect of $\text{Na}_4\text{P}_2\text{O}_7 \cdot 10\text{H}_2\text{O}$ as complexing agent on deposition behavior and property of electroless Ni-P coating on ZK61M magnesium alloy, *Mater Res Express* 6, 056548 (2019).
- [24] J. M. Meier, J. Caris, and A. A. Luo, Towards high strength cast Mg-RE based alloys: Phase diagrams and strengthening mechanisms, *Journal of Magnesium and Alloys* 10, 1401 (2022).
- [25] H. Shi, C. Xu, X. Hu, W. Gan, K. Wu, and X. Wang, Improving the Young's modulus of Mg via alloying and compositing – A short review, *Journal of Magnesium and Alloys* 10, 2009 (2022).
- [26] D. K. Bond, B. Goddard, R. C. Singleterry, and S. Bilbao y León, Evaluating the effectiveness of common aerospace materials at lowering the whole body effective dose equivalent in deep space, *Acta Astronaut* 165, 68 (2019).
- [27] M. Smirnova, Mars transportation vehicle concept, *Acta Astronaut* 103, 250 (2014).
- [28] J. P. ; L. F. ; B. ,Lindsey M. ; R.-S. P. Labukas, Corrosion-Mitigating, Bondable, Fluorinated Barrier Coating for Anodized Magnesium, (2016).
- [29] F. Witte, The history of biodegradable magnesium implants: A review☆, *Acta Biomater* 6, 1680 (2010).
- [30] N. Banjanin and G. Belojevic, Changes of Blood Pressure and Hemodynamic Parameters after Oral Magnesium Supplementation in Patients with Essential Hypertension—An Intervention Study, *Nutrients* 10, 581 (2018).
- [31] Y. Liu, B. Lu, and Z. Cai, Recent Progress on Mg- And Zn-Based Alloys for Biodegradable Vascular Stent Applications, *J Nanomater* 2019, (2019).
- [32] L. Wang, W. Lu, J. Qin, F. Zhang, and D. Zhang, Microstructure and mechanical properties of cold-rolled TiNbTaZr biomedical β titanium alloy, *Materials Science and Engineering: A* 490, 421 (2008).
- [33] S. Amukarimi and M. Mozafari, Biodegradable magnesium-based biomaterials: An overview of challenges and opportunities, *MedComm (Beijing)* 2, 123 (2021).
- [34] H. Zhou, B. Liang, H. Jiang, Z. Deng, and K. Yu, Magnesium-based biomaterials as emerging agents for bone repair and regeneration: from mechanism to application, *Journal of Magnesium and Alloys* 9, 779 (2021).

- [35] E. O'Neill, G. Awale, L. Daneshmandi, O. Umerah, and K. W.-H. Lo, The roles of ions on bone regeneration, *Drug Discov Today* 23, 879 (2018).
- [36] J. Chen, L. Tan, X. Yu, I. P. Etim, M. Ibrahim, and K. Yang, Mechanical properties of magnesium alloys for medical application: A review, *J Mech Behav Biomed Mater* 87, 68 (2018).
- [37] G. K. Schwalfenberg and S. J. Genuis, The Importance of Magnesium in Clinical Healthcare, *Scientifica (Cairo)* 2017, (2017).
- [38] N. Hafeez, S. Liu, E. Lu, L. Wang, R. Liu, W. lu, and L.-C. Zhang, Mechanical behavior and phase transformation of β -type Ti-35Nb-2Ta-3Zr alloy fabricated by 3D-Printing, *J Alloys Compd* 790, 117 (2019).
- [39] J. Stráský et al., Achieving high strength and low elastic modulus in interstitial biomedical Ti–Nb–Zr–O alloys through compositional optimization, *Materials Science and Engineering: A* 839, 142833 (2022).
- [40] P. Chakraborty Banerjee, S. Al-Saadi, L. Choudhary, S. E. Harandi, and R. Singh, Magnesium Implants: Prospects and Challenges, *Materials* 12, 136 (2019).
- [41] O. Jung, D. Porchetta, M.-L. Schroeder, M. Klein, N. Wegner, F. Walther, F. Feyerabend, M. Barbeck, and A. Kopp, In Vivo Simulation of Magnesium Degradability Using a New Fluid Dynamic Bench Testing Approach, *Int J Mol Sci* 20, 4859 (2019).
- [42] W. Li et al., Biomimicking Bone–Implant Interface Facilitates the Bioadaptation of a New Degradable Magnesium Alloy to the Bone Tissue Microenvironment, *Advanced Science* 8, (2021).
- [43] Z. Lin, S. Wu, X. Liu, S. Qian, P. K. Chu, Y. Zheng, K. M. C. Cheung, Y. Zhao, and K. W. K. Yeung, A surface-engineered multifunctional TiO₂ based nano-layer simultaneously elevates the corrosion resistance, osteoconductivity and antimicrobial property of a magnesium alloy, *Acta Biomater* 99, 495 (2019).
- [44] X. Yao, J. Tang, Y. Zhou, A. Atrens, M. S. Dargusch, B. Wiese, T. Ebel, and M. Yan, Surface modification of biomedical Mg-Ca and Mg-Zn-Ca alloys using selective laser melting: Corrosion behaviour, microhardness and biocompatibility, *Journal of Magnesium and Alloys* 9, 2155 (2021).

- [45] X. Niu, H. Shen, and J. Fu, Microstructure and mechanical properties of selective laser melted Mg-9 wt. %Al powder mixture, *Mater Lett* 221, 4 (2018).
- [46] K. Wei, Z. Wang, and X. Zeng, Influence of element vaporization on formability, composition, microstructure, and mechanical performance of the selective laser melted Mg–Zn–Zr components, *Mater Lett* 156, 187 (2015).
- [47] A. Pawlak, M. Rosienkiewicz, and E. Chlebus, Design of experiments approach in AZ31 powder selective laser melting process optimization, *Archives of Civil and Mechanical Engineering* 17, 9 (2017).
- [48] Y. Guo, H. Pan, L. Ren, and G. Quan, Microstructure and mechanical properties of wire arc additively manufactured AZ80M magnesium alloy, *Mater Lett* 247, 4 (2019).
- [49] J. Guo, Y. Zhou, C. Liu, Q. Wu, X. Chen, and J. Lu, Wire arc additive manufacturing of AZ31 magnesium alloy: Grain refinement by adjusting pulse frequency, *Materials* 9, (2016).
- [50] M. M. Farag and H. Yun, Effect of gelatin addition on fabrication of magnesium phosphate-based scaffolds prepared by additive manufacturing system, *Mater Lett* 132, 111 (2014).
- [51] M. Salehi, S. Maleksaeedi, S. M. L. Nai, G. K. Meenashisundaram, M. H. Goh, and M. Gupta, A paradigm shift towards compositionally zero-sum binderless 3D printing of magnesium alloys via capillary-mediated bridging, *Acta Mater* 165, 294 (2019).
- [52] M. Salehi, S. Maleksaeedi, M. A. Bin Sapari, M. L. S. Nai, G. K. Meenashisundaram, and M. Gupta, Additive manufacturing of magnesium–zinc–zirconium (ZK) alloys via capillary-mediated binderless three-dimensional printing, *Mater Des* 169, 107683 (2019).
- [53] S. Palanivel, P. Nelaturu, B. Glass, and R. S. Mishra, Friction stir additive manufacturing for high structural performance through microstructural control in an Mg based WE43 alloy, *Materials & Design (1980-2015)* 65, 934 (2015).
- [54] Y. Li et al., Additively manufactured biodegradable porous magnesium, *Acta Biomater* 67, 378 (2018).

- [55] Z. Zeng, M. Salehi, A. Kopp, S. Xu, M. Esmaily, and N. Birbilis, Recent progress and perspectives in additive manufacturing of magnesium alloys, *Journal of Magnesium and Alloys* 10, 1511 (2022).
- [56] V. A. Yartys et al., Magnesium based materials for hydrogen based energy storage: Past, present and future, *Int J Hydrogen Energy* 44, 7809 (2019).
- [57] S. K. Thandalam, S. Ramanathan, and S. Sundarajan, Synthesis, microstructural and mechanical properties of ex situ zircon particles ($ZrSiO_4$) reinforced Metal Matrix Composites (MMCs): a review, *Journal of Materials Research and Technology* 4, 333 (2015).
- [58] Z. Ding, X. Zhao, and L. L. Shaw, Reaction between $LiBH_4$ and MgH_2 induced by high-energy ball milling, *J Power Sources* 293, 236 (2015).
- [59] Ronald Redwing, *Hexagonal Close Packed Crystal Structure (HCP) | MATSE 81: Materials In Today's World*, <https://www.e-education.psu.edu/matse81/node/2134>.
- [60] D. Guan, X. Liu, J. Gao, L. Ma, B. P. Wynne, and W. M. Rainforth, Exploring the mechanism of “Rare Earth” texture evolution in a lean Mg–Zn–Ca alloy, *Scientific Reports* 2019 9:1 9, 1 (2019).
- [61] Z. R. Zeng, Y. M. Zhu, S. W. Xu, M. Z. Bian, C. H. J. Davies, N. Birbilis, and J. F. Nie, Texture evolution during static recrystallization of cold-rolled magnesium alloys, *Acta Mater* 105, 479 (2016).
- [62] D. W. Kim, B. C. Suh, M. S. Shim, J. H. Bae, D. H. Kim, and N. J. Kim, Texture evolution in Mg-Zn-Ca alloy sheets, *Metall Mater Trans A Phys Metall Mater Sci* 44, 2950 (2013).
- [63] R. Xin, C. Guo, Z. Xu, G. Liu, X. Huang, and Q. Liu, Characteristics of long {10-12} twin bands in sheet rolling of a magnesium alloy, *Scr Mater* 74, 96 (2014).
- [64] I. J. Polmear, *Light Alloys* (Elsevier, 2005).
- [65] J. Koike, R. Ohyama, T. Kobayashi, M. Suzuki, and K. Maruyama, Grain-Boundary Sliding in AZ31 Magnesium Alloys at Room Temperature to 523 K, *Mater Trans* 44, 445 (2003).
- [66] M. R. Barnett, A. Ghaderi, I. Sabirov, and B. Hutchinson, Role of grain boundary sliding in the anisotropy of magnesium alloys, *Scr Mater* 61, 277 (2009).

- [67] T. B. Massalski, J. L. Murray, and L. H. Bennet, Binary alloy phase diagrams: Volume 1, ASM International 1100 (1986).
- [68] G. Song, A. Atrens, X. Wu, and B. Zhang, Corrosion behaviour of AZ21, AZ501 and AZ91 in sodium chloride, *Corros Sci* 40, 1769 (1998).
- [69] C. H. Cáceres and D. M. Rovera, Solid Solution Strengthening in Concentrated Mg-Al alloys, *Journal of Light Metals* 1, 151 (2002).
- [70] K. Gusieva, C. H. J. Davies, J. R. Scully, and N. Birbilis, Corrosion of magnesium alloys: the role of alloying, *International Materials Reviews* 60, 169 (2015).
- [71] N. Sezer, Z. Evis, S. M. Kayhan, A. Tahmasebifar, and M. Koç, Review of magnesium-based biomaterials and their applications, *Journal of Magnesium and Alloys* 6, 23 (2018).
- [72] J. B. Clark, Transmission electron microscopy study of age hardening in a Mg-5 wt.% Zn alloy, *Acta Metallurgica* 13, 1281 (1965).
- [73] J. Jain, P. Cizek, W. J. Poole, and M. R. Barnett, Precipitate characteristics and their effect on the prismatic-slip-dominated deformation behaviour of an Mg-6 Zn alloy, *Acta Mater* 61, 4091 (2013).
- [74] C. MENDIS, K. OHISHI, Y. KAWAMURA, T. HONMA, S. KAMADO, and K. HONO, Precipitation-hardenable Mg-2.4Zn-0.1Ag-0.1Ca-0.16Zr (at.%) wrought magnesium alloy, *Acta Mater* 57, 749 (2009).
- [75] T. Bhattacharjee, C. L. Mendis, K. Oh-ishi, T. Ohkubo, and K. Hono, The effect of Ag and Ca additions on the age hardening response of Mg-Zn alloys, *Materials Science and Engineering: A* 575, 231 (2013).
- [76] M. Bornapour, M. Celikin, M. Cerruti, and M. Pekguleryuz, Magnesium implant alloy with low levels of strontium and calcium: the third element effect and phase selection improve bio-corrosion resistance and mechanical performance, *Mater Sci Eng C Mater Biol Appl* 35, 267 (2014).
- [77] Y. Wan, G. Xiong, H. Luo, F. He, Y. Huang, and X. Zhou, Preparation and characterization of a new biomedical magnesium-calcium alloy, *Mater Des* 29, 2034 (2008).
- [78] C. BETTLES, Enhanced age-hardening behaviour in Mg-4 wt.% Zn micro-alloyed with Ca, *Scr Mater* 51, 193 (2004).

- [79] J. F. Nie and B. C. Muddle, Precipitation hardening of Mg-Ca(-Zn) alloys, *Scr Mater* 37, 1475 (1997).
- [80] K. Oh-ishi, R. Watanabe, C. L. Mendis, and K. Hono, Age-hardening response of Mg-0.3at.%Ca alloys with different Zn contents, *Materials Science and Engineering: A* 526, 177 (2009).
- [81] N. Stanford, The effect of calcium on the texture, microstructure and mechanical properties of extruded Mg-Mn-Ca alloys, *Materials Science and Engineering: A* 528, 314 (2010).
- [82] B. Langelier, A. M. Nasiri, S. Y. Lee, M. A. Gharghouri, and S. Esmaeili, Improving microstructure and ductility in the Mg-Zn alloy system by combinational Ce-Ca microalloying, *Materials Science and Engineering: A* 620, 76 (2015).
- [83] Y. C. Lee, A. K. Dahle, and D. H. Stjohn, The role of solute in grain refinement of magnesium, *Metall Mater Trans A Phys Metall Mater Sci* 31, 2895 (2000).
- [84] D. Gu, J. Peng, S. Sun, and F. Pan, On the solid solution substitutional position and properties of Mg-Gd alloy, *Journal of Materials Research and Technology* 20, 2859 (2022).
- [85] K. Guan, C. Li, Z. Yang, Y. Yu, Q. Yang, W. Zhang, Z. Guan, C. Wang, M. Zha, and H. Wang, Hardening effect and precipitation evolution of an isothermal aged Mg-Sm based alloy, *Journal of Magnesium and Alloys* 11, 4619 (2023).
- [86] L. Meng, C. Ji, J. Wang, and W.-F. Rao, Thermodynamic modeling of the Mg-Nd-Sr ternary system with key experimental investigation, *Calphad* 80, 102530 (2023).
- [87] Y. Li, A. Zhang, C. Li, H. Xie, B. Jiang, Z. Dong, P. Jin, and F. Pan, Recent advances of high strength Mg-RE alloys: Alloy development, forming and application, *Journal of Materials Research and Technology* 26, 2919 (2023).
- [88] H. Pan, Y. Ren, H. Fu, H. Zhao, L. Wang, X. Meng, and G. Qin, Recent developments in rare-earth free wrought magnesium alloys having high strength: A review, *J Alloys Compd* 663, 321 (2016).

- [89] C. Li, H. Sun, X. Li, J. Zhang, W. Fang, and Z. Tan, Microstructure, texture and mechanical properties of Mg-3.0Zn-0.2Ca alloys fabricated by extrusion at various temperatures, *J Alloys Compd* 652, 122 (2015).
- [90] A. A. Luo, Magnesium casting technology for structural applications, *Journal of Magnesium and Alloys* 1, 2 (2013).
- [91] J. Feng, H. Sun, X. Li, H. Wang, and W. Fang, Effects of Ag variations on dynamic recrystallization, texture, and mechanical properties of ultrafine-grained Mg-3Al-1Zn alloys, *J Mater Res* 31, 3360 (2016).
- [92] P. SC, L. JD, E. D, and S. KW, Microstructure and mechanical properties of Mg-Zn-Ag alloys, *Materials Science Forum* 419–4, 159 (2003).
- [93] M. Mohammadi Zerankeshi and R. Alizadeh, Ag-incorporated biodegradable Mg alloys, *Materialia (Oxf)* 23, 101445 (2022).
- [94] M. Razzaghi, M. Kasiri-Asgarani, H. R. Bakhsheshi-Rad, and H. Ghayour, In Vitro Degradation, Antibacterial Activity and Cytotoxicity of Mg-3Zn-xAg Nanocomposites Synthesized by Mechanical Alloying for Implant Applications, *J Mater Eng Perform* 28, 1441 (2019).
- [95] D. Tie, F. Feyerabend, W.-D. Müller, R. Schade, K. Liefeth, K. Kainer, and R. Willumeit, Antibacterial biodegradable Mg-Ag alloys., *Eur Cell Mater* 25, 284 (2013).
- [96] Y. Ma, D. Wang, H. Li, F. Yuan, C. Yang, and J. Zhang, Microstructure, mechanical and corrosion properties of novel quaternary biodegradable extruded Mg-1Zn-0.2Ca-xAg alloys, *Mater Res Express* 7, 015414 (2020).
- [97] O. R. Myhr, O. Grong, and S. J. Andersen, Modelling of the age hardening behaviour of Al-Mg-Si alloys, *Acta Mater* 49, 65 (2001).
- [98] H. Somekawa, Effect of Alloying Elements on Fracture Toughness and Ductility in Magnesium Binary Alloys; A Review, *Mater Trans* 61, 1 (2020).
- [99] J. F. Nie, Precipitation and Hardening in Magnesium Alloys, *Metallurgical and Materials Transactions A* 2012 43:11 43, 3891 (2012).
- [100] J. Wu, L. Jin, J. Dong, F. Wang, and S. Dong, The texture and its optimization in magnesium alloy, *J Mater Sci Technol* 42, 175 (2020).

- [101] B. Zhang, Y. Wang, L. Geng, and C. Lu, Effects of calcium on texture and mechanical properties of hot-extruded Mg–Zn–Ca alloys, *Materials Science and Engineering: A* 539, 56 (2012).
- [102] A. Tehrani, B. Yin, and W. A. Curtin, Solute strengthening of basal slip in Mg alloys, *Acta Mater* 151, 56 (2018).
- [103] Y. N. Wang and J. C. Huang, The role of twinning and untwinning in yielding behavior in hot-extruded Mg–Al–Zn alloy, *Acta Mater* 55, 897 (2007).
- [104] F. Humphreys and M. Hatherly, *Recrystallization and Related Annealing Phenomena* (2012).
- [105] J. P. Hadorn and S. R. Agnew, A new metastable phase in dilute, hot-rolled Mg–Nd alloys, *Materials Science and Engineering: A* 533, 9 (2012).
- [106] I. Basu, T. Al-Samman, and G. Gottstein, Shear band-related recrystallization and grain growth in two rolled magnesium-rare earth alloys, *Materials Science and Engineering: A* 579, 50 (2013).
- [107] N. Stanford, I. Sabirov, G. Sha, A. La Fontaine, S. P. Ringer, and M. R. Barnett, Effect of Al and Gd solutes on the strain rate sensitivity of magnesium alloys, *Metall Mater Trans A Phys Metall Mater Sci* 41, 734 (2010).
- [108] T. Wang, L. Jiang, R. K. Mishra, and J. J. Jonas, Effect of Ca addition on the intensity of the rare earth texture component in extruded magnesium alloys, *Metall Mater Trans A Phys Metall Mater Sci* 45, 4698 (2014).
- [109] W. X. Wu, L. Jin, F. H. Wang, J. Sun, Z. Y. Zhang, W. J. Ding, and J. Dong, Microstructure and texture evolution during hot rolling and subsequent annealing of Mg–1Gd alloy, *Materials Science and Engineering: A* 582, 194 (2013).
- [110] D. W. Kim, B. C. Suh, M. S. Shim, J. H. Bae, D. H. Kim, and N. J. Kim, Texture evolution in Mg–Zn–Ca alloy sheets, *Metall Mater Trans A Phys Metall Mater Sci* 44, 2950 (2013).
- [111] J. Y. Lee, Y. S. Yun, W. T. Kim, and D. H. Kim, Twinning and texture evolution in binary Mg–Ca and Mg–Zn alloys, *Metals and Materials International* 20, 885 (2014).

- [112] J. Y. Lee, Y. S. Yun, B. C. Suh, N. J. Kim, W. T. Kim, and D. H. Kim, Comparison of static recrystallization behavior in hot rolled Mg–3Al–1Zn and Mg–3Zn–0.5Ca sheets, *J Alloys Compd* 589, 240 (2014).
- [113] W. X. Wu, L. Jin, J. Dong, Z. Y. Zhang, and W. J. Ding, Effect of initial microstructure on the dynamic recrystallization behavior of Mg–Gd–Y–Zr alloy, *Materials Science and Engineering: A* 556, 519 (2012).
- [114] N. Stanford, G. Sha, J. H. Xia, S. P. Ringer, and M. R. Barnett, Solute segregation and texture modification in an extruded magnesium alloy containing gadolinium, *Scr Mater* 65, 919 (2011).
- [115] N. Stanford, The effect of rare earth elements on the behaviour of magnesium-based alloys: Part 2 – recrystallisation and texture development, *Materials Science and Engineering: A* 565, 469 (2013).
- [116] D. Guan, W. M. Rainforth, J. Gao, L. Ma, and B. Wynne, Individual effect of recrystallisation nucleation sites on texture weakening in a magnesium alloy: Part 2- shear bands, *Acta Mater* 145, 399 (2018).
- [117] S. Sandlöbes, M. Friák, S. Korte-Kerzel, Z. Pei, J. Neugebauer, and D. Raabe, A rare-earth free magnesium alloy with improved intrinsic ductility, *Scientific Reports* 2017 7:1 7, 1 (2017).
- [118] D. Griffiths, B. Davis, and J. D. Robson, The Influence of Strain Path on Rare Earth Recrystallization Textures in a Magnesium-Zinc-Rare Earth Alloy, *Metall Mater Trans A Phys Metall Mater Sci* 49, 321 (2018).
- [119] D. Guan, X. Liu, J. Gao, L. Ma, B. P. Wynne, and W. M. Rainforth, Exploring the mechanism of “Rare Earth” texture evolution in a lean Mg–Zn–Ca alloy, *Sci Rep* 9, 7152 (2019).
- [120] H. Ding, X. Shi, Y. Wang, G. Cheng, and S. Kamado, Texture weakening and ductility variation of Mg–2Zn alloy with CA or RE addition, *Materials Science and Engineering: A* 645, 196 (2015).
- [121] Y. W. Zi-Kui Liu, *Computational Thermodynamics of Materials* (2016).
- [122] R. Becker and W. Döring, Kinetische Behandlung der Keimbildung in übersättigten Dämpfen, *Ann Phys* 416, 719 (1935).

- [123] M. Volmer and A. Weber, Keimbildung in übersättigten Gebilden, *Zeitschrift Für Physikalische Chemie* 119U, 277 (1926).
- [124] J. W. Gibbs and J. Tyndall, *On the Equilibrium of Heterogeneous Substances : First [-Second] Part* (Published by the Academy, [New Haven, 1874).
- [125] L. Farkas, Keimbildungsgeschwindigkeit in übersättigten Dämpfen, *Zeitschrift Für Physikalische Chemie* 125U, 236 (1927).
- [126] J. Marqusee, J. R.-T. J. of chemical physics, and undefined 1984, Theory of Ostwald ripening: Competitive growth and its dependence on volume fraction, *Pubs.Aip.Org* (n.d.).
- [127] A. Baldan, Progress in Ostwald ripening theories and their applications to nickel-base superalloys. Part I: Ostwald ripening theories, *J Mater Sci* 37, 2171 (2002).
- [128] I. M. Lifshitz and V. V. Slyozov, The kinetics of precipitation from supersaturated solid solutions, *Journal of Physics and Chemistry of Solids* 19, 35 (1961).
- [129] T. Sugimoto, CONTROL OF PARTICLE CHARACTERISTICS, *Monodispersed Particles* 368 (2001).
- [130] Thomas H. Courtney, *Mechanical Behavior of Materials, Second Edition*, by Thomas H. Courtney, <https://www.waveland.com/browse.php?t=394>.
- [131] M. R. Barnett, H. Wang, and T. Guo, An Orowan precipitate strengthening equation for mechanical twinning in Mg, *Int J Plast* 112, 108 (2019).
- [132] D. Gebauer and H. Cölfen, Prenucleation clusters and non-classical nucleation, *Nano Today* 6, 564 (2011).
- [133] Y. Gao et al., Preparation, characterization, pharmacokinetics, and tissue distribution of curcumin nanosuspension with TPGS as stabilizer, *Drug Dev Ind Pharm* 36, 1225 (2010).
- [134] T. C. Chou and T. G. Nieh, Interface-controlled phase transformation and abnormal grain growth of α -Al₂O₃ in thin γ -alumina films, *Thin Solid Films* 221, 89 (1992).
- [135] P. Dagtepe and V. Chikan, Quantized Ostwald Ripening of Colloidal Nanoparticles, *Journal of Physical Chemistry C* 114, 16263 (2010).

- [136] R. E. Smallman and A. H. W. Ngan, *Modern Physical Metallurgy: Eighth Edition*, Modern Physical Metallurgy: Eighth Edition 1 (2013).
- [137] L. K. Aagesen, J. Miao, J. E. Allison, S. Aubry, and A. Arsenlis, Prediction of Precipitation Strengthening in the Commercial Mg Alloy AZ91 Using Dislocation Dynamics, *Metall Mater Trans A Phys Metall Mater Sci* 49, 1908 (2018).
- [138] Y. D. Han, H. Y. Jing, S. M. L. Nai, C. M. Tan, J. Wei, L. Y. Xu, and S. R. Zhang, A modified constitutive model for creep of Sn–3.5Ag–0.7Cu solder joints, *J Phys D Appl Phys* 42, 125411 (2009).
- [139] W. O. Soboyejo, *Mechanical properties-of-engineered-materials*, Marcel Dekker, New York (2003).
- [140] J. M. Rosalie, H. Somekawa, A. Singh, and T. Mukai, The effect of size and distribution of rod-shaped β_1' precipitates on the strength and ductility of a Mg–Zn alloy, *Materials Science and Engineering: A* 539, 230 (2012).
- [141] Y. Lu, A. R. Bradshaw, Y. L. Chiu, and I. P. Jones, The role of beta prime precipitates in the bio-corrosion performance of Mg–3Zn in simulated body fluid, *J Alloys Compd* 614, 345 (2014).
- [142] B. Zhou, J. Chen, H. Yan, W. Xia, B. Su, H. Guo, and W. Zhu, To improve strength and bio-corrosion resistance of Mg-4Zn alloy via high strain rate rolling combined with double aging, *Mater Lett* 227, 301 (2018).
- [143] H. Pan, Y. Ren, H. Fu, H. Zhao, L. Wang, X. Meng, and G. Qin, Recent developments in rare-earth free wrought magnesium alloys having high strength: A review, *J Alloys Compd* 663, 321 (2016).
- [144] N.-E. L. Saris, E. Mervaala, H. Karppanen, J. A. Khawaja, and A. Lewenstam, Magnesium, *Clinica Chimica Acta* 294, 1 (2000).
- [145] D. Zhu et al., Mechanical strength, biodegradation, and in vitro and in vivo biocompatibility of Zn biomaterials, *ACS Appl Mater Interfaces* 11, 6809 (2019).
- [146] P. Han, M. Tan, S. Zhang, W. Ji, J. Li, X. Zhang, C. Zhao, Y. Zheng, and Y. Chai, Shape and Site Dependent in Vivo Degradation of Mg-Zn Pins in Rabbit Femoral Condyle, *Int J Mol Sci* 15, 2959 (2014).
- [147] T. M. Pollock, Weight loss with magnesium alloys, *Science* (1979) 328, 986 (2010).

- [148] H. Okamoto, Comment on Mg-Zn (magnesium-zinc), *Journal of Phase Equilibria* 15, 129 (1994).
- [149] I. Higashi, N. Shiotani, M. Uda, T. Mizoguchi, and H. Katoh, The crystal structure of Mg₅₁Zn₂₀, *J Solid State Chem* 36, 225 (1981).
- [150] M. Hida and Y. Matsui, The pseudocubic approximant Mg₅₁Zn₂₀ interpreted as a modulated crystal, *Philosophical Magazine A* 82, 831 (2002).
- [151] X. Gao and J. F. Nie, Structure and thermal stability of primary intermetallic particles in an Mg-Zn casting alloy, *Scr Mater* 57, 655 (2007).
- [152] M. Němec, V. Gärtnerová, M. Klementová, and A. Jäger, Analysis of intermetallic particles in Mg-12 wt.%Zn binary alloy using transmission electron microscopy, *Mater Charact* 106, 428 (2015).
- [153] R. Černý and G. Renaudin, The intermetallic compound Mg₂₁Zn₂₅, *Acta Crystallogr C* 58, i154 (2002).
- [154] L. Zhang, W. Wang, W. Hu, Z. Yang, and H. Ye, Nanometer-sized domain structure in complex Mg₂₁Zn₂₅ formed by eutectoid phase transformation in a Mg-Zn alloy, *J Alloys Compd* 745, 319 (2018).
- [155] Q. -B Yang and K. H. Kuo, A new description of pentagonal Frank-Kasper phases and a possible structure model of the icosahedral quasicrystal, *Urn:Issn:0108-7673* 43, 787 (1987).
- [156] J. M. Rosalie, H. Somekawa, A. Singh, and T. Mukai, Orientation relationships between icosahedral clusters in hexagonal MgZn₂ and monoclinic Mg₄Zn₇ phases in Mg-Zn(-Y) alloys, *Philosophical Magazine* 91, 2634 (2011).
- [157] J. B. Friauf, The Crystal Structure of Magnesium Di-Zincide, *Physical Review* 29, 34 (1927).
- [158] T. Ohba, Y. Kitano, and Y. Komura, The charge-density study of the Laves phases, MgZn₂ and MgCu₂, *Urn:Issn:0108-2701* 40, 1 (1984).
- [159] W. J. Kim, S. I. Hong, and K. H. Lee, Structural characterization of Laves-phase MgZn₂ precipitated in Mg-Zn-Y alloy, *Metals and Materials International* 16, 171 (2010).

- [160] A. Jain et al., Commentary: The materials project: A materials genome approach to accelerating materials innovation, *APL Mater* 1, (2013).
- [161] M. Andersson, M. De Boissieu, S. Brühne, C. Drescher, W. Assmus, S. Ohahshi, A. P. Tsai, M. Mihalkovič, M. Krajčí, and Ö. Rapp, Electronic and structural properties of Laves-phase $MgZn_2$ of varying chemical disorder, *Phys Rev B Condens Matter Mater Phys* 82, 024202 (2010).
- [162] S. Samson, Ø. Ellefsen, O. Hassel, A. Kainulainen, A. Halonen, and E. Pulkkinen, Die Kristallstruktur von Mg_2Zn_{11} . Isomorphie zwischen Mg_2Zn_{11} und $Mg_2Cu_6Al_5$., *Acta Chem Scand* 3, 835 (1949).
- [163] H. Euchner et al., Anomalous vibrational dynamics in the Mg_2Zn_{11} phase, *Phys Rev B Condens Matter Mater Phys* 83, 144202 (2011).
- [164] D. Cheng, K. Wang, and B.-C. Zhou, Crystal structure and stability of phases in Mg-Zn alloys: A comprehensive first-principles study, *Acta Mater* 242, 118443 (2023).
- [165] J. Buha, Reduced temperature (22–100 °C) ageing of an Mg–Zn alloy, *Materials Science and Engineering: A* 492, 11 (2008).
- [166] P. M. Jardim, G. Solórzano, and J. B. V. Sande, Precipitate crystal structure determination in melt spun Mg-1.5wt. %Ca-6wt. %Zn alloy, *Microsc Microanal* 8, 487 (2002).
- [167] T. Bhattacharjee, C. L. Mendis, K. Oh-ishi, T. Ohkubo, and K. Hono, The effect of Ag and Ca additions on the age hardening response of Mg–Zn alloys, *Materials Science and Engineering: A* 575, 231 (2013).
- [168] L. Y. Wei, G. L. Dunlop, and H. Westengen, Precipitation Hardening of Mg-Zn and Mg-Zn-RE alloys, *Metallurgical and Materials Transactions A* 26, 1705 (1995).
- [169] N. T. Kirkland and N. Birbilis, *Developments in Mg-based Alloys for Biomaterials*, SpringerBriefs in Materials 73 (2014).
- [170] H. R. B. Rad, M. H. Idris, M. R. A. Kadir, and S. Farahany, Microstructure analysis and corrosion behavior of biodegradable Mg–Ca implant alloys, *Mater Des* 33, 88 (2012).
- [171] M. R. Sahu, T. S. S. Kumar, and U. Chakkingal, A review on recent advancements in biodegradable Mg-Ca alloys, *Journal of Magnesium and Alloys* 10, 2094 (2022).

- [172] X. Gao, S. M. Zhu, B. C. Muddle, and J. F. Nie, Precipitation-hardened Mg–Ca–Zn alloys with superior creep resistance, *Scr Mater* 53, 1321 (2005).
- [173] R. Pâris, Contribution à l'étude des alliages ternaires, Blondel La Rougery : Gauthier-Villars (1934).
- [174] JB Clark, The solid constitution in the magnesium-rich region of the Mg-Ca-Zn phase diagram, *Transactions of the Metallurgical Society of AIME* 644 (1961).
- [175] P. M. Jardim, G. Solórzano, and J. B. V. Sande, Second phase formation in melt-spun Mg–Ca–Zn alloys, *Materials Science and Engineering: A* 381, 196 (2004).
- [176] G. Levi, S. Avraham, A. Zilberov, and M. Bamberger, Solidification, solution treatment and age hardening of a Mg–1.6 wt.% Ca–3.2 wt.% Zn alloy, *Acta Mater* 54, 523 (2006).
- [177] M. Bamberger, G. Levi, and J. B. Vander Sande, Precipitation hardening in Mg–Ca–Zn alloys, *Metall Mater Trans A Phys Metall Mater Sci* 37, 481 (2006).
- [178] J. J. Giles and J. G. Bannigan, Teratogenic and Developmental Effects of Lithium, *Curr Pharm Des* 12, 1531 (2006).
- [179] Y. Du, M. Zheng, Y. Ge, B. Jiang, and M. Shen, Microstructure and texture evolution of deformed Mg-Zn alloy during recrystallization, *Mater Charact* 145, 501 (2018).
- [180] B. Zhang, Y. Hou, X. Wang, Y. Wang, and L. Geng, Mechanical properties, degradation performance and cytotoxicity of Mg–Zn–Ca biomedical alloys with different compositions, *Materials Science and Engineering: C* 31, 1667 (2011).
- [181] M. Ramya and K. R. Ravi, Biodegradable nanocrystalline Mg-Zn-Ca-Ag alloys as suitable materials for orthopedic implants, *Mater Today Proc* 58, 721 (2022).
- [182] L. Yu, Z. Zhao, C. Tang, W. Li, C. You, and M. Chen, The mechanical and corrosion resistance of Mg-Zn-Ca-Ag alloys: the influence of Ag content, *Journal of Materials Research and Technology* 9, 10863 (2020).
- [183] J. Yin, M. Li, F. Yi, X. Zhao, D. Guan, K. Wang, Y. Gao, and C. Liu, Effects of micro-alloying Ag on microstructure, mechanical properties and corrosion behavior of extruded Mg-2Zn-0.2Ca-xAg alloys, *J Alloys Compd* 989, 174376 (2024).

- [184] D. Shin and C. Wolverton, First-principles study of solute–vacancy binding in magnesium, *Acta Mater* 58, 531 (2010).
- [185] D. Shin and C. Wolverton, First-principles density functional calculations for Mg alloys: A tool to aid in alloy development, *Scr Mater* 63, 680 (2010).
- [186] A. A. Luo, Material design and development: From classical thermodynamics to CALPHAD and ICME approaches, *Calphad* 50, 6 (2015).
- [187] P. J. Spencer, A brief history of CALPHAD, *Calphad* 32, 1 (2008).
- [188] Z. K. Liu, Thermodynamics and its prediction and CALPHAD modeling: Review, state of the art, and perspectives, *Calphad* 82, 102580 (2023).
- [189] U. R. Kattner, THE CALPHAD METHOD AND ITS ROLE IN MATERIAL AND PROCESS DEVELOPMENT, *Tecnol Metal Mater Min* 13, 3 (2016).
- [190] L. Kaufman and H. Bernstein, Computer calculation of phase diagrams. With special reference to refractory metals, (1970).
- [191] M. Hillert, Solute drag in grain boundary migration and phase transformations, *Acta Mater* 52, 5289 (2004).
- [192] *Computational Materials Engineering - Thermo-Calc Software*, <https://thermocalc.com/>.
- [193] *Pandat Software: CALPHAD-Based Materials Design – CompuTherm*, <https://compuTherm.com/software>.
- [194] *FactSage Software and Databases*, <https://factsage.com/>.
- [195] I. Toda-Caraballo, E. I. Galindo-Nava, and P. E. J. Rivera-Díaz-del-Castillo, Unravelling the materials genome: Symmetry relationships in alloy properties, *J Alloys Compd* 566, 217 (2013).
- [196] J. G.-T. C. W. of J. W. Gibbs, Ph. D., LL. D, and undefined 1957, Graphical methods in the thermodynamics of fluids, *Cir.Nii.Ac.Jp* (2010).
- [197] J. W. Gibbs, *The Collected Works of J. Willard Gibbs: Thermodynamics*, Yale University Press 1, (1984).
- [198] R. Shi and A. A. Luo, Applications of CALPHAD modeling and databases in advanced lightweight metallic materials, *Calphad* 62, 1 (2018).

- [199] H. L. Lukas, S. G. Fries, and B. Sundman, Computational Thermodynamics: The Calphad Method, Computational Thermodynamics: The Calphad Method 9780521868112, 1 (2007).
- [200] A. T. Dinsdale, SGTE data for pure elements, Calphad 15, 317 (1991).
- [201] Y.-M. Muggianu, M. Gambino, and J.-P. Bros, Enthalpies de formation des alliages liquides bismuth-étain-gallium à 723 k. Choix d'une représentation analytique des grandeurs d'excès intégrales et partielles de mélange, Journal de Chimie Physique 72, 83 (1975).
- [202] M. Hillert and L.-I. Staffansson, The Regular Solution Model for Stoichiometric Phases and Ionic Melts., Acta Chem Scand 24, 3618 (1970).
- [203] H. Jou, P. Voorhees, G. O.- Superalloys, and undefined 2004, *Computer Simulations for the Prediction of Microstructure/Property Variation in Aeroturbine Disks*, in *TMS (The Minerals, Metals & Materials Society), 2004 Superalloys, 2004* (2004).
- [204] J.-O. Andersson, T. Helander, L. Hdghmd, P. Shi, and B. Sundman, Thermo-Calc & DICTRA, computational tools for materials science, Elsevier 26, 273 (2002).
- [205] J. Ågren, Numerical treatment of diffusional reactions in multicomponent alloys, Journal of Physics and Chemistry of Solids 43, 385 (1982).
- [206] G. W. Greenwood, The growth of dispersed precipitates in solutions, Acta Metallurgica 4, 243 (1956).
- [207] C. Wagner, Theorie der Alterung von Niederschlägen durch Umlösen (Ostwald-Reifung), Zeitschrift Für Elektrochemie, Berichte Der Bunsengesellschaft Für Physikalische Chemie 65, 581 (1961).
- [208] P. Staron, R. Kampmann, and R. Wagner, Polarized Neutron Scattering Study Of Early Stage Phase Separation in a NI-13AT%AL Alloy, MRS Online Proceedings Library (OPL) 376, 707 (1994).
- [209] O. R. Myhr and O. Grong, Modelling of non-isothermal transformations in alloys containing a particle distribution, Acta Mater 48, 1605 (2000).
- [210] J. D. Robson and P. B. Prangnell, Dispersoid precipitation and process modelling in zirconium containing commercial aluminium alloys, Acta Mater 49, 599 (2001).

- [211] J. D. Robson, Modelling the overlap of nucleation, growth and coarsening during precipitation, *Acta Mater* 52, 4669 (2004).
- [212] J. Svoboda, F. D. Fischer, P. Fratzl, and E. Kozeschnik, Modelling of kinetics in multi-component multi-phase systems with spherical precipitates: I: Theory, *Materials Science and Engineering: A* 385, 166 (2004).
- [213] H. Basoalto and M. Anderson, An extension of mean-field coarsening theory to include particle coalescence using nearest-neighbour functions, *Acta Mater* 117, 122 (2016).
- [214] M. J. Anderson, C. Panwisawas, Y. Sovani, R. P. Turner, J. W. Brooks, and H. C. Basoalto, Mean-field modelling of the intermetallic precipitate phases during heat treatment and additive manufacture of Inconel 718, *Acta Mater* 156, 432 (2018).
- [215] M. J. Anderson, F. Schulz, Y. Lu, H. S. Kitaguchi, P. Bowen, C. Argyrakis, and H. C. Basoalto, On the modelling of precipitation kinetics in a turbine disc nickel based superalloy, *Acta Mater* 191, 81 (2020).
- [216] M. J. Anderson, A. Rowe, J. Wells, and H. C. Basoalto, Application of a multi-component mean field model to the coarsening behaviour of a nickel-based superalloy, *Acta Mater* 114, 80 (2016).
- [217] M. J. Anderson, J. Benson, J. W. Brooks, B. Saunders, and H. C. Basoalto, Predicting Precipitation Kinetics During the Annealing of Additive Manufactured Inconel 625 Components, *Integr Mater Manuf Innov* 8, 154 (2019).
- [218] I. J. Moore, M. G. Burke, and E. J. Palmiere, Modelling the nucleation, growth and coarsening kinetics of γ'' (D022) precipitates in the Ni-base Alloy 625, *Acta Mater* 119, 157 (2016).
- [219] E. Kozeschnik, J. Svoboda, and F. D. Fischer, Shape factors in modeling of precipitation, *Materials Science and Engineering: A* 441, 68 (2006).
- [220] J. Svoboda, F. D. Fischer, P. Fratzl, and E. Kozeschnik, Modelling of kinetics in multi-component multi-phase systems with spherical precipitates, *Materials Science and Engineering: A* 385, 166 (2004).
- [221] BRITISH STANDARD, BS EN 10002-1:2001, Metallic materials—Tensile testing (2010).

- [222] G. Dieter and D. Bacon, *Mechanical Metallurgy*, McGraw-Hill Series in Materials Science and Engineering (1976).
- [223] *Magnesium-Based Alloys - Thermo-Calc Software*, <https://thermocalc.com/products/databases/magnesium-based-alloys/>.
- [224] E. Scheil, Bemerkungen zur Schichtkristallbildung, *International Journal of Materials Research* 34, 70 (1942).
- [225] C. J. Farnin, S. Orzolek, and J. N. DuPont, A Novel Approach to Determine Variable Solute Partition Coefficients, *Metall Mater Trans A Phys Metall Mater Sci* 51, 5771 (2020).
- [226] S. L. Chen, Y. Yang, S. W. Chen, X. G. Lu, and Y. A. Chang, Solidification simulation using scheil model in multicomponent systems, *J Phase Equilibria Diffus* 30, 429 (2009).
- [227] W. J. Boettinger, The Solidification of Multicomponent Alloys, *J Phase Equilibria Diffus* 37, 4 (2016).
- [228] A. T. Conlisk, *Essentials of micro- and nanofluidics: with applications to the biological and chemical sciences*, 537 (2013).
- [229] Laura Dickson, *Diffusion - Chemistry LibreTexts*, [https://chem.libretexts.org/Bookshelves/Physical_and_Theoretical_Chemistry_Textbook_Maps/Supplemental_Modules_\(Physical_and_Theoretical_Chemistry\)/Kinetics/09%3A_Diffusion#Fick.E2.80.99s_First_Law_of_Diffusion](https://chem.libretexts.org/Bookshelves/Physical_and_Theoretical_Chemistry_Textbook_Maps/Supplemental_Modules_(Physical_and_Theoretical_Chemistry)/Kinetics/09%3A_Diffusion#Fick.E2.80.99s_First_Law_of_Diffusion).
- [230] Y. Zhang, C. Du, Y. Liu, S. Wen, S. Liu, Y. Huang, N. Hort, and Y. Du, Interdiffusion and atomic mobility in hcp Mg–Al–Sn alloys, *J Alloys Compd* 871, 159517 (2021).
- [231] J. O. Andersson, T. Helander, L. Höglund, P. Shi, and B. Sundman, Thermo-Calc & DICTRA, computational tools for materials science, *Calphad* 26, 273 (2002).
- [232] S. Crusius, G. Inden, U. Knoop, L. Höglund, and J. Ågren, On the numerical treatment of moving boundary problems, *Zeitschrift Für Metallkunde* 83, 673 (1992).
- [233] A. Engström, L. Höglund, and J. Ågren, Computer simulation of diffusion in multiphase systems, *Metallurgical and Materials Transactions A* 25, 1127 (1994).

- [234] M. J. Anderson, C. Panwisawas, Y. Sovani, R. P. Turner, J. W. Brooks, and H. C. Basoalto, Mean-field modelling of the intermetallic precipitate phases during heat treatment and additive manufacture of Inconel 718, *Acta Mater* 156, 432 (2018).
- [235] E. Clouet, M. Nastar, and C. Sigli, Nucleation of Al₃Zr and Al₃Sc in aluminum alloys: From kinetic Monte Carlo simulations to classical theory, *Phys Rev B Condens Matter Mater Phys* 69, (2004).
- [236] A. Baldan, Progress in Ostwald ripening theories and their applications to the γ' -precipitates in nickel-base superalloys Part II: Nickel-base superalloys, *J Mater Sci* 37, 2379 (2002).
- [237] A. J. Ardell, Al-L12 interfacial free energies from data on coarsening in five binary Ni alloys, informed by thermodynamic phase diagram assessments, *J Mater Sci* 46, 4832 (2011).
- [238] H. A. Calderon, P. W. Voorhees, J. L. Murray, and G. Kostorz, Ostwald ripening in concentrated alloys, *Acta Metallurgica et Materialia* 42, 991 (1994).
- [239] G. Kaptay, On the interfacial energy of coherent interfaces, *Acta Mater* 60, 6804 (2012).
- [240] C. Woodward, A. van de Walle, M. Asta, and D. R. Trinkle, First-principles study of interfacial boundaries in Ni–Ni₃Al, *Acta Mater* 75, 60 (2014).
- [241] E. Kozeschnik, J. Svoboda, and F. D. Fischer, Shape factors in modeling of precipitation, *Materials Science and Engineering: A* 441, 68 (2006).
- [242] E. Clouet, Modeling of Nucleation Processes, *Fundamentals of Modeling for Metals Processing* 203 (2009).
- [243] E. Clouet, Modeling of Nucleation Processes, *Fundamentals of Modeling for Metals Processing* 203 (2018).
- [244] J. Svoboda, F. D. Fischer, P. Fratzl, and E. Kozeschnik, Modelling of kinetics in multi-component multi-phase systems with spherical precipitates, *Materials Science and Engineering: A* 385, 166 (2004).
- [245] O. R. Myhr, O. Grong, and S. J. Andersen, Modelling of the age hardening behaviour of Al–Mg–Si alloys, *Acta Mater* 49, 65 (2001).

- [246] D. Marsetiya Utama et al., Strengthening mechanism and yield strength prediction of cold-drawn commercially pure aluminum wire, *IOP Conf Ser Mater Sci Eng* 382, 022094 (2018).
- [247] Wole. Soboyejo, *Mechanical properties of engineered materials*, (2003).
- [248] Thomas H. Courtney, *Mechanical Behavior of Materials: Second Edition* (2005).
- [249] S. Z. Han, E. A. Choi, S. H. Lim, S. Kim, and J. Lee, Alloy design strategies to increase strength and its trade-offs together, *Prog Mater Sci* 117, 100720 (2021).
- [250] C. H. Cáceres and P. Lukác, Strain hardening behaviour and the Taylor factor of pure magnesium, *Philosophical Magazine* 88, 977 (2008).
- [251] T. Gladman, Precipitation hardening in metals, *Materials Science and Technology* 15, 30 (1999).
- [252] B. F. Dyson, Microstructure based creep constitutive model for precipitation strengthened alloys: Theory and application, *Materials Science and Technology* 25, 213 (2009).
- [253] C. H. Cáceres, J. R. Griffiths, A. R. Pakdel, and C. J. Davidson, Microhardness mapping and the hardness-yield strength relationship in high-pressure diecast magnesium alloy AZ91, *Materials Science and Engineering: A* 402, 258 (2005).
- [254] F. S.-L. notes, U. of Delaware, and undefined 2008, A gentle introduction to the Finite Element Method, Team-Pancho.Github.IoFJ SayasLecture Notes, University of Delaware, 2008•team-Pancho.Github.Io (2015).
- [255] Jürgen Topper, *Option pricing with finite elements*, Wilmott (2005).
- [256] X. Yao, J. Tang, Y. Zhou, A. Atrens, M. S. Dargusch, B. Wiese, T. Ebel, and M. Yan, Surface modification of biomedical Mg-Ca and Mg-Zn-Ca alloys using selective laser melting: Corrosion behaviour, microhardness and biocompatibility, *Journal of Magnesium and Alloys* 9, 2155 (2021).
- [257] A. V. Koltygin, V. E. Bazhenov, I. V. Plisetskaya, Y. V. Tselovalnik, A. I. Bazlov, V. D. Belov, and V. A. Yudin, Susceptibility of Mg-REM-Zn-Zr Magnesium Alloys to Casting Unsoundness, *Russian Metallurgy (Metally)* 2021, 821 (2021).
- [258] J. Ågren, Numerical treatment of diffusional reactions in multicomponent alloys, *Journal of Physics and Chemistry of Solids* 43, 385 (1982).

- [259] J. O. Andersson, T. Helander, L. Höglund, P. Shi, and B. Sundman, Thermo-Calc & DICTRA, computational tools for materials science, *Calphad* 26, 273 (2002).
- [260] R. Zeytounian, and M. Platzer, Theory and Applications of Viscous Fluid Flows, *Appl Mech Rev* 57, B15 (2004).
- [261] Ian M. Mitchell, Sumengen: A Matlab toolbox implementing level set methods , Vision Research Lab. UC Santa Barbara. (2004).
- [262] S. A. Abdel-Gawad and M. A. Shoeib, Corrosion studies and microstructure of Mg–Zn–Ca alloys for biomedical applications, *Surfaces and Interfaces* 14, 108 (2019).
- [263] T. V. Larionova, W. W. Park, and B. S. You, A ternary phase observed in rapidly solidified Mg–Ca–Zn alloys, *Scr Mater* 45, 7 (2001).
- [264] A. Incesu and A. Gungor, Mechanical properties and biodegradability of Mg–Zn–Ca alloys: homogenization heat treatment and hot rolling, *J Mater Sci Mater Med* 31, 1 (2020).
- [265] G. Levi, S. Avraham, A. Zilberov, and M. Bamberger, Solidification, solution treatment and age hardening of a Mg–1.6wt.% Ca–3.2wt.% Zn alloy, *Acta Mater* 54, 523 (2006).
- [266] X. Gao, S. M. Zhu, B. C. Muddle, and J. F. Nie, Precipitation-hardened Mg–Ca–Zn alloys with superior creep resistance, *Scr Mater* 53, 1321 (2005).
- [267] J. F. Nie and B. C. Muddle, Precipitation hardening of Mg–Ca(–Zn) alloys, *Scr Mater* 37, 1475 (1997).
- [268] Y. Yang, V. Massardier, M. R. G. Ferdowsi, L. Jiang, J. Wang, T. Dorin, S. R. Kada, M. R. Barnett, and M. Perez, Revisiting Precipitation kinetics in Mg–Zn alloy – a multi-characterization and modeling study, *Acta Mater* 260, 119276 (2023).
- [269] P. Yin, N. F. Li, T. Lei, L. Liu, and C. Ouyang, Effects of Ca on microstructure, mechanical and corrosion properties and biocompatibility of Mg–Zn–Ca alloys, *J Mater Sci Mater Med* 24, 1365 (2013).
- [270] K. Oh-ishi, R. Watanabe, C. L. Mendis, and K. Hono, Age-hardening response of Mg–0.3at.%Ca alloys with different Zn contents, *Materials Science and Engineering: A* 526, 177 (2009).

- [271] N. Pulido-González, P. Hidalgo-Manrique, S. García-Rodríguez, B. Torres, and J. Rams, Effect of heat treatment on the mechanical and biocorrosion behaviour of two Mg-Zn-Ca alloys, *Journal of Magnesium and Alloys* 10, 540 (2022).
- [272] V. E. Bazhenov, Y. V. Tselovalnik, A. V. Koltygin, and V. D. Belov, Investigation of the Interfacial Heat Transfer Coefficient at the Metal–Mold Interface During Casting of an A356 Aluminum Alloy and AZ81 Magnesium Alloy into Steel and Graphite Molds, *International Journal of Metalcasting* 15, 625 (2021).
- [273] C. J. Farnin, J. M. Rickman, and J. N. DuPont, Solutions to the Scheil Equation with a Variable Partition Coefficient, *Metall Mater Trans A Phys Metall Mater Sci* 52, 5443 (2021).
- [274] D. Cheng, K. Wang, and B.-C. Zhou, Crystal structure and stability of phases in Mg-Zn alloys: A comprehensive first-principles study, *Acta Mater* 242, 118443 (2023).
- [275] H. Okamoto, Comment on Mg-Zn (magnesium-zinc), *Journal of Phase Equilibria* 15, 129 (1994).
- [276] J. Buha, Reduced temperature (22–100 °C) ageing of an Mg–Zn alloy, *Materials Science and Engineering: A* 492, 11 (2008).
- [277] J. M. Rosalie, H. Somekawa, A. Singh, and T. Mukai, Orientation relationships between icosahedral clusters in hexagonal MgZn₂ and monoclinic Mg₄Zn₇ phases in Mg-Zn(-Y) alloys, *Philosophical Magazine* 91, 2634 (2011).
- [278] Y. P. Xie, Z. Y. Wang, and Z. F. Hou, The phase stability and elastic properties of MgZn₂ and Mg₄Zn₇ in Mg–Zn alloys, *Scr Mater* 68, 495 (2013).
- [279] L. Y. Wei, G. L. Dunlop, and H. Westengen, Precipitation Hardening of Mg-Zn and Mg-Zn-RE alloys, *Metallurgical and Materials Transactions A* 26, 1705 (1995).
- [280] X. Gao and J. F. Nie, Characterization of strengthening precipitate phases in a Mg–Zn alloy, *Scr Mater* 56, 645 (2007).
- [281] N. Pulido-González, P. Hidalgo-Manrique, S. García-Rodríguez, B. Torres, and J. Rams, Effect of heat treatment on the mechanical and biocorrosion behaviour of two Mg-Zn-Ca alloys, *Journal of Magnesium and Alloys* 10, 540 (2022).
- [282] N. Pulido-González, B. Torres, S. García-Rodríguez, P. Rodrigo, V. Bonache, P. Hidalgo-Manrique, M. Mohedano, and J. Rams, Mg–1Zn–1Ca alloy for

- biomedical applications. Influence of the secondary phases on the mechanical and corrosion behaviour, *J Alloys Compd* 831, 154735 (2020).
- [283] R. E. Schäublin, M. Becker, M. Cihova, S. S. A. Gerstl, D. Deiana, C. Hébert, S. Pogatscher, P. J. Uggowitzer, and J. F. Löffler, Precipitation in lean Mg–Zn–Ca alloys, *Acta Mater* 239, 118223 (2022).
- [284] H. Okamoto, Ca-Mg (calcium-magnesium) , *Journal of Phase Equilibria* 10, (1998).
- [285] C. O. Brubaker and Z. K. Liu, A computational thermodynamic model of the Ca–Mg–Zn system, *J Alloys Compd* 370, 114 (2004).
- [286] A. Pandya, M. Shah, B. Pramod, and N. Srivastava, A Review on Heat Treatment of Magnesium Alloys and Its Effect on Various Properties, *Lecture Notes in Mechanical Engineering* 77 (2023).
- [287] C. MENDIS, K. OHISHI, Y. KAWAMURA, T. HONMA, S. KAMADO, and K. HONO, Precipitation-hardenable Mg–2.4Zn–0.1Ag–0.1Ca–0.16Zr (at.%) wrought magnesium alloy, *Acta Mater* 57, 749 (2009).
- [288] F.J. Humphreys and M. Hatherly, *Recrystallization and Related Annealing Phenomena* (Elsevier Science, 2012).
- [289] J. D. Robson and C. Paa-Rai, The interaction of grain refinement and ageing in magnesium–zinc–zirconium (ZK) alloys, *Acta Mater* 95, 10 (2015).
- [290] Y.-P. Xie, Z.-Y. Wang, and Z. F. Hou, The phase stability and elastic properties of MgZn₂ and Mg₄Zn₇ in Mg–Zn alloys, *Scr Mater* 68, 495 (2013).
- [291] B. Leu, M. Arul Kumar, Y. Liu, and I. J. Beyerlein, Deviations from Theoretical Orientation Relationship Along Tensile Twin Boundaries in Magnesium, *Minerals, Metals and Materials Series* 123 (2020).
- [292] L. Yu, Z. Zhao, C. Tang, W. Li, C. You, and M. Chen, The mechanical and corrosion resistance of Mg-Zn-Ca-Ag alloys: the influence of Ag content, *Journal of Materials Research and Technology* 9, 10863 (2020).
- [293] J. D. Robson and C. Paa-Rai, The interaction of grain refinement and ageing in magnesium–zinc–zirconium (ZK) alloys, *Acta Mater* 95, 10 (2015).

- [294] N. Allain-Bonasso, F. Wagner, S. Berbenni, and D. P. Field, A study of the heterogeneity of plastic deformation in IF steel by EBSD, *Materials Science and Engineering: A* 548, 56 (2012).
- [295] V. M. Miller and T. M. Pollock, Texture Modification in a Magnesium-Aluminum-Calcium Alloy During Uniaxial Compression, *Metall Mater Trans A Phys Metall Mater Sci* 47, 1854 (2016).
- [296] C. D. Barrett, A. Imandoust, A. L. Oppedal, K. Inal, M. A. Tschopp, and H. El Kadiri, Effect of grain boundaries on texture formation during dynamic recrystallization of magnesium alloys, *Acta Mater* 128, 270 (2017).
- [297] J. Yin, M. Li, F. Yi, X. Zhao, D. Guan, K. Wang, Y. Gao, and C. Liu, Effects of micro-alloying Ag on microstructure, mechanical properties and corrosion behavior of extruded Mg-2Zn-0.2Ca-xAg alloys, *J Alloys Compd* 989, 174376 (2024).